Cavity Control in a Single-Electron Quantum Cyclotron: An Improved Measurement of the Electron Magnetic Moment

A thesis presented

by

David Andrew Hanneke

to

The Department of Physics

in partial fulfillment of the requirements

for the degree of

Doctor of Philosophy

in the subject of

Physics

Harvard University

Cambridge, Massachusetts

December 2007

Thesis advisor

Gerald Gabrielse

Author

David Andrew Hanneke

Cavity Control in a Single-Electron Quantum Cyclotron: An Improved Measurement of the Electron Magnetic Moment

Abstract

A single electron in a quantum cyclotron yields new measurements of the electron magnetic moment, given by $g/2 = 1.001\,159\,652\,180\,73\,(28)$ [0.28 ppt], and the fine structure constant, $\alpha^{-1} = 137.035\,999\,084\,(51)$ [0.37 ppb], both significantly improved from prior results. The static magnetic and electric fields of a Penning trap confine the electron, and a 100 mK dilution refrigerator cools its cyclotron motion to the quantum-mechanical ground state. A quantum nondemolition measurement allows resolution of single cyclotron jumps and spin flips by coupling the cyclotron and spin energies to the frequency of the axial motion, which is self-excited and detected with a cryogenic amplifier.

The trap electrodes form a high-Q microwave resonator near the cyclotron frequency; coupling between the cyclotron motion and cavity modes can inhibit spontaneous emission by over 100 times the free-space rate and shift the cyclotron frequency, a systematic effect that dominated the uncertainties of previous g-value measurements. A cylindrical trap geometry creates cavity modes with analytically calculable couplings to cyclotron motion. Two independent methods use the cyclotron damping rate of an electron plasma or of the single electron itself as probes of the cavity mode structure and allow the identification of the modes by their geometries and couplings,

the quantification of an offset between the mode and electrostatic centers, and the reduction of the cavity shift uncertainty to sub-dominant levels. Measuring g at four magnetic fields with cavity shifts spanning thirty times the final g-value uncertainty provides a check on the calculated cavity shifts.

Magnetic field fluctuations limit the measurement of g by adding a noise-model dependence to the extraction of the cyclotron and anomaly frequencies from their resonance lines; the relative agreement of two line-splitting methods quantifies a line-shape model uncertainty.

New techniques promise to increase field stability, narrow the resonance lines, and accelerate the measurement cycle.

The measured g allows tests for physics beyond the Standard Model through searches for its temporal variation and comparisons with a "theoretical" g-value calculated from quantum electrodynamics and an independently measured fine structure constant.

Contents

List of Figures

List of Tables

Acknowledgments

This thesis is the seventh stemming from electron work in our lab over two decades. I am indebted to those who came before me, including Joseph Tan (thesis in 1992), Ching-hua Tseng (1995), Daphna Enzer (1996), Steve Peil (1999), and postdoc Kamal Abdullah. In particular, my own training came through close interaction with Brian D'Urso (2003), who designed the amplifiers and electron self-excitation scheme that provide our signal, and Brian Odom (2004), whose passion and dedication led to our 2006 result. It was a privilege to work with these two fine scientists.

Professor Jerry Gabrielse had the vision for an improved electron magnetic moment measurement using a cylindrical Penning trap and lower temperatures as well as the stamina to pursue it for 20 years. He has been generous with his experimental knowledge and advice, constantly available in person or by phone, and adept at acquiring support. I am grateful for the opportunity to learn from him.

Shannon Fogwell has kept the apparatus running while I analyzed results and wrote this thesis. She took much of the data contained herein, and her positron trap is the future for this experiment. Yulia Gurevich helped briefly before embarking on a quest for the electron's "other" dipole moment. I have truly enjoyed working with many graduate students and postdocs throughout my tenure, especially those in the Gabrielse Lab: Andrew Speck, Dan Farkas, Tanya Zelevinsky, David LeSage, Nick Guise, Phil Larochelle, Josh Goldman, Steve Kolthammer, Phil Richerme, Robert McConnell, and Jack DiSciacca, as well as Ben Levitt, Jonathan Wrubel, Irma Kuljanishvili, and Maarten Jansen. Each has helped this work in his or her own way, whether helping with magnet fills, letting me "borrow" cables, or simply pondering physics.

It has been a pleasure having undergraduates around the lab, including five whom I supervised directly: Verena Martinez Outschoorn, Aram Avetisyan, Michael von Korff, Ellen Martinsek, and Rishi Jajoo. They performed tasks as diverse as characterizing laboratory vibrations, designing a pump room and vacuum system, and calculating the magnetic field homogeneity and inductance matrix for a new solenoid.

The Army Research Office funded my first three years as a graduate student through a National Defense Science and Engineering Graduate (NDSEG) Fellowship. The National Science Foundation generously supports this experiment.

Numerous teachers have encouraged me throughout the years. Without the love and support of my family I could not have made it this far. My wife, Mandi Jo, has been particularly supportive (and patient!) as I finish my graduate studies.

Chapter 1

Introduction

A particle in a box is the prototype of a simple and elegant system. This thesis describes an experiment with a particle, a single electron trapped with static magnetic and electric fields, surrounded by a cylindrical metal box. The interaction between the electron and the electromagnetic modes of the box induces frequency shifts, inhibits spontaneous emission, and, with the box cooled to freeze out blackbody photons, prepares the electron cyclotron motion in its quantum-mechanical ground state.

By injecting photons into the box, we drive single cyclotron transitions and spin flips, observing both through quantum nondemolition measurements. The photons that most readily drive these transitions reveal the resonance lines and make precision measurements of the cyclotron frequency and the cyclotron–spin beat frequency. Accounting for shifts from the trapping electric field, special relativity, and the interaction between the electron and the box (or cavity) modes allows us to determine the electron g-value with a relative accuracy of 0.28 ppt.[1] Such a measurement probes the

[1] parts-per-trillion = ppt = 10^{-12}; parts-per-billion = ppb = 10^{-9}; parts-per-million = ppm = 10^{-6}

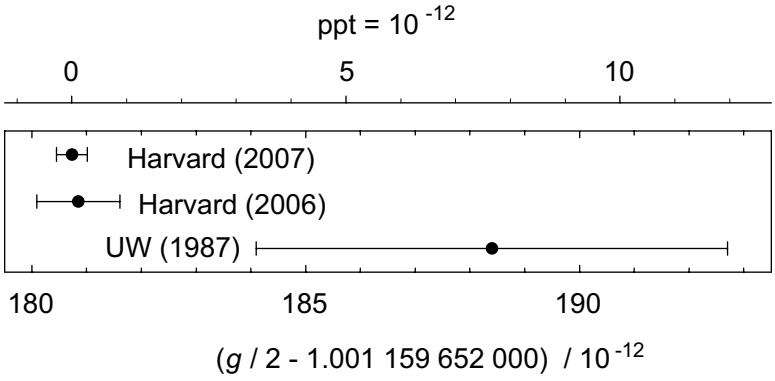

Figure 1.1: Electron g-value comparisons [1, 2].

interaction of the electron with the fluctuating vacuum, allows the highest-accuracy determination of the fine structure constant, with a precision of 0.37 ppb, and sensitively tests quantum electrodynamics.

1.1 The Electron Magnetic Moment

A magnetic moment is typically written as the product of a dimensional size-estimate, an angular momentum in units of the reduced Planck constant, and a dimensionless g-value:

$$\boldsymbol{\mu} = g\frac{-e\hbar}{2m}\frac{\mathbf{S}}{\hbar}. \tag{1.1}$$

For the case of the electron, with charge $-e$ and mass m, the dimensional estimate is the Bohr magneton ($\mu_B = e\hbar/(2m)$). For angular momentum arising from orbital motion, g depends on the relative distribution of charge and mass and equals 1 if they coincide, for example cyclotron motion in a magnetic field. For a point particle governed by the Dirac equation, the intrinsic magnetic moment, i.e., that due to spin, has $g = 2$, and deviations from this value probe the particle's interactions with the

vacuum as well as the nature of the particle itself, as with the proton, whose $g \approx 5.585$ arises from its quark-gluon composition [3].[2] The primary result of this thesis is a new measurement of the electron g-value,

$$\frac{g}{2} = 1.001\ 159\ 652\ 180\ 73\ (28)\ [0.28\ \text{ppt}], \tag{1.2}$$

where the number in parentheses is the standard deviation and that in brackets the relative uncertainty. This uncertainty is nearly three times smaller than that of our 2006 result [1] and more than 15 times below that of the celebrated 1987 University of Washington measurement [2].

1.1.1 The fine structure constant

The fine structure constant,

$$\alpha = \frac{e^2}{4\pi\epsilon_0\hbar c}, \tag{1.3}$$

is the coupling constant for the electromagnetic interaction. It plays an important role in most of the sizes and energy scales for atoms, relating the electron Compton wavelength, $\lambda\!\!\!^{-}_e$, to the classical electron radius, r_0, and the Bohr radius, a_0,

$$\lambda\!\!\!^{-}_e = \frac{\hbar}{mc} = \alpha^{-1} r_0 = \alpha a_0, \tag{1.4}$$

as well as appearing in the Rydberg constant and fine structure splittings. It is one of the 26 dimensionless parameters in the Standard Model, roughly half of which are

[2] In order to account for the proton and neutron deviations, Pauli introduced an additional term to the Dirac equation, which treated an anomalous magnetic moment as an additional theoretical parameter [4]. While this term preserves Lorentz covariance and local gauge invariance, it is not renormalizable [5]. As described in Section 1.1.2, QED and the rest of the Standard Model do a fine job quantifying anomalous magnetic moments, rendering the Pauli term obsolete.

masses, i.e., Yukawa couplings to the Higgs field [6].[3]

Being dimensionless, one might hope to calculate the value of α to arbitrary precision, much as may be done with the mathematical constant π, but no theory yet allows such computation. Anthropic arguments based on observations such as the existence of nuclei and the lifetime of the proton constrain its value to between $1/170 < \alpha < 1/80$, and anything outside a window of 4% of the measured value would greatly reduce the stellar production of carbon or oxygen [7, 8]. Some have suggested that inflationary cosmology allows the existence of a statistical ensemble of universes, a "multiverse," wherein many possible values of the fundamental constants are realized and that, beyond the truism that we find α within the anthropically allowed range, its value is in principle uncalculable [9, 10].

Because vacuum polarization screens the bare electron charge, the electromagnetic coupling constant depends on the four-momentum in any interaction and Eq. 1.3 is actually its low-energy limit. For a momentum change of $q \ll m_e c$, the "running" constant is

$$\alpha(q^2) = \alpha \left(1 - \frac{\alpha}{15\pi} \frac{q^2}{m_e^2 c^2}\right), \tag{1.5}$$

see e.g., [11, Sec. 7.5] or [12, Sec. 7.9]. Note that q^2 is negative,[4] so higher momentum interactions see a larger coupling constant—they penetrate closer to the larger, bare charge. For $q \gg m_e c$, the increase becomes logarithmic and by the energy-scale of the Z-boson, α has increased 7% to $\alpha(m_Z)^{-1} = 127.918(18)$ [13, p. 119]. In the next section, a QED perturbative expansion relates g to α in the low-energy limit of Eq. 1.3

[3] There are many ways to parameterize the electroweak terms. For example, [6] uses the weak coupling constant (g_W) and the Weinberg angle (θ_W). A parameterization using the fine structure constant is equally valid since $\alpha = g_W^2 \sin^2 \theta_W / (4\pi)$.

[4] Eq. 1.5 assumes a $(+---)$ metric and the only change is in $\mathbf{q}$.

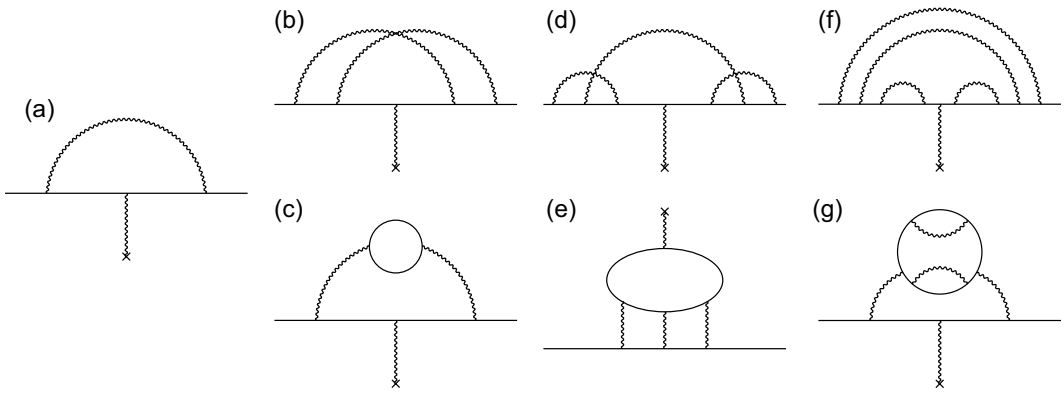

Figure 1.2: The second-order Feynman diagram (a), 2 of the 7 fourth-order diagrams (b,c), 2 of 72 sixth-order diagrams (d,e), and 2 of 891 eighth-order diagrams (f,g).

because the vacuum polarization effects are explicitly calculated.

1.1.2 QED and the relation between g and α

Vacuum fluctuations modify the electron's interactions with a magnetic field, slightly increasing g above 2. The theoretical expression is

$$\frac{g}{2} = 1 + C_2\left(\frac{\alpha}{\pi}\right) + C_4\left(\frac{\alpha}{\pi}\right)^2 + C_6\left(\frac{\alpha}{\pi}\right)^3 + C_8\left(\frac{\alpha}{\pi}\right)^4 + ... + a_{\mu,\tau} + a_{\text{hadronic}} + a_{\text{weak}}, \quad (1.6)$$

where 1 is $g/2$ for a Dirac point particle, C_n refers to the n-vertex QED terms involving only electrons and photons, $a_{\mu,\tau}$ to the QED terms involving the μ and τ leptons, and a_{hadronic} and a_{weak} to terms involving hadronic or weak interactions. Because these terms have been evaluated to high precision and assuming Eq. 1.6 is a complete description of the underlying physics, the series can be inverted to extract α from a measured g. Conversely, an independent value of α allows a test of the fundamental

theories. The first three QED terms are known exactly:

$$C_2 = \frac{1}{2} = 0.5 \qquad \text{1 Feynman diagram [14]} \tag{1.7a}$$

$$C_4 = \frac{197}{144} + \frac{\pi^2}{12} + \frac{3}{4}\zeta(3) - \frac{1}{2}\pi^2 \ln 2 \qquad \text{7 Feynman diagrams [15, 16, 17]} \tag{1.7b}$$

$$= -0.328\ 478\ 965\ 579\ldots$$

$$C_6 = \frac{83}{72}\pi^2\zeta(3) - \frac{215}{24}\zeta(5) \qquad \text{72 Feynman diagrams [18]} \tag{1.7c}$$
$$+ \frac{100}{3}\left[\left(\sum_{n=1}^{\infty}\frac{1}{2^n n^4} + \frac{1}{24}\ln^4 2\right) - \frac{1}{24}\pi^2 \ln^2 2\right] - \frac{239}{2160}\pi^4 + \frac{139}{18}\zeta(3)$$
$$- \frac{298}{9}\pi^2 \ln 2 + \frac{17101}{810}\pi^2 + \frac{28259}{5184} = 1.181\ 241\ 456\ 587\ldots,$$

with the C_6 calculations only finished as recently as 1996. Using many supercomputers over more than a decade, Kinoshita and Nio have evaluated C_8 numerically to a precision of better than 2 parts in 10^3 [19, 20],

$$C_8 = -1.9144\ (35) \qquad \text{891 Feynman diagrams.} \tag{1.8}$$

Work is just beginning on evaluation of C_{10} using a program that automatically generates the code for evaluating the 12 672 Feynman diagrams [21, 22]. Although the value of C_{10} is unknown, our high experimental precision requires an estimate, which we write as an upper bound:

$$|C_{10}| < x. \tag{1.9}$$

Following the approach of [23, App. B],[5] we will use $x = 4.6$.

[5] The authors of [23] estimate, with a 50% confidence level (CL), that the magnitude of the ratio of C_{10} to C_8 will be no larger than that of C_8 to C_6, i.e., $|C_{10}| < |C_8(C_8/C_6)|$. Converting this to the usual standard deviation (68% CL) gives an estimate of $x = 4.6$. There is no physical reason the value of C_{10} should follow this scheme, and a genuine estimate of its size is expected soon.

QED terms of fourth and higher order may involve virtual μ and τ leptons. These coefficients up to sixth order are known as exact functions of the measured lepton mass ratios and sum to [24]

$$a_{\mu,\tau} = 2.720\ 919\ (3) \times 10^{-12}. \tag{1.10}$$

Additionally, there are two small non-QED contributions due to hadronic and weak loops [25]:

$$a_{\text{hadronic}} = 1.682\,(20) \times 10^{-12} \tag{1.11}$$

$$a_{\text{weak}} = 0.0297\,(5) \times 10^{-12}. \tag{1.12}$$

The hadronic contributions are particularly interesting because the quantum chromodynamics calculations cannot be done perturbatively. Instead, one must use dispersion theory to rewrite diagrams containing virtual hadrons into ones containing real ones with cross-sections that may be measured experimentally, see e.g., [26]. One class of diagrams that prove particularly troublesome involve hadronic light-by-light scattering (as in Fig. 1.2e with hadrons in the virtual loop), which are both non-perturbative and difficult to relate to experimental data and thus involve heavily model-dependent calculations [27, Ch. 6]. This term is important when evaluating the muon magnetic moment, for reasons discussed in Section 1.1.6, and has been evaluated several ways with not entirely consistent results. Depending on the result one chooses, the total $a_{\text{hadronic}}/10^{-12}$ in Eq. 1.11 may be written as $1.682\,(20)$ [27, 28], $1.671\,(19)$ [25, 29], or $1.676\,(21)$. The last option is based on the "cautious" average adopted by the Muon $(g-2)$ Collaboration for the hadronic light-by-light contribution to the muon magnetic moment [26, Sec. 7.3]. The consequence of this difference

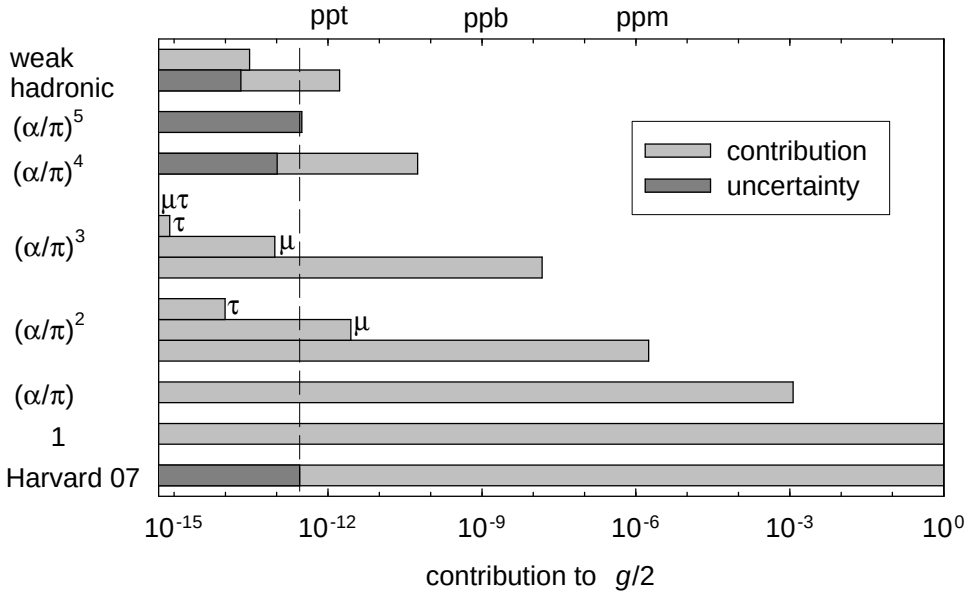

Figure 1.3: Theoretical contributions to the electron g

is negligible for our purposes; changing the value used for a_{hadronic} would only alter the last digit of α^{-1}, which corresponds to the second digit of the uncertainty, by one.

Fig. 1.3 summarizes the contributions of the various terms to the electron g-value and includes our measurement, which is just beginning to probe the hadronic contributions. Using these calculations and our measured g, one can determine α:

$$\alpha^{-1} = 137.035\ 999\ 084\ (12)(37)(33) \tag{1.13}$$

$$= 137.035\ 999\ 084\ (51)\ [0.37\ \text{ppb}]. \tag{1.14}$$

In Eq. 1.13, the first uncertainty is from the calculation of C_8, the second from our estimate of C_{10}, and the third from the measured g. For a general limit $|C_{10}| < x$, as in Eq. 1.9, the second uncertainty would be $(8x)$. With the new measurement of g, the uncertainty estimate for C_{10} now exceeds the experimental uncertainty. Eq. 1.14 combines these uncertainties and states the relative uncertainty. This result improves

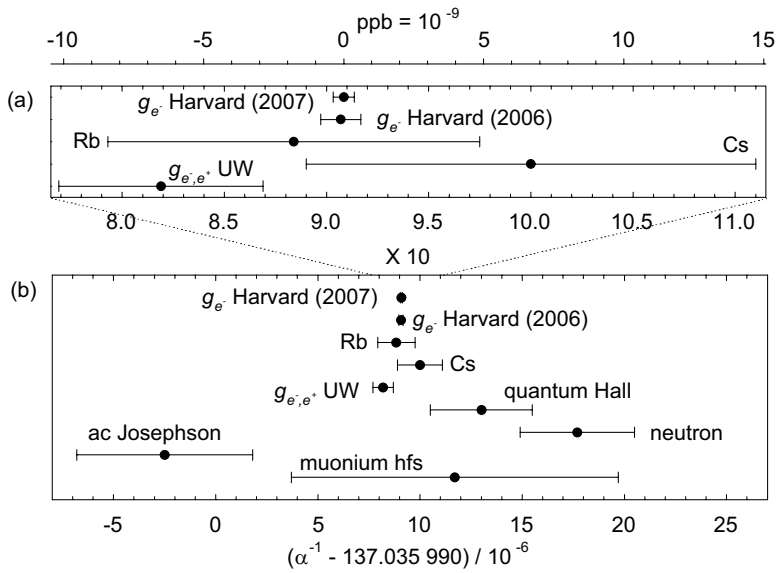

Figure 1.4: Various determinations of the fine structure constant with citations in the text.

upon our recent 0.71 ppb determination [30] by nearly a factor of two.

1.1.3 Comparing various measurements of α

The value of the fine structure constant determined from the electron g-value and QED and given in Eq. 1.14 has over an order of magnitude smaller uncertainty than that of the next-best determination. Nevertheless, independent values of α provide vital checks for consistency in the laws of physics. Fig. 1.4 displays the most precise determinations of α and includes an enlarged scale for those with the smallest uncertainty.

The least uncertain determinations of α that are independent of the free-electron g are the "atom-recoil" measurements, so-called because their uncertainty is limited by measurements of recoil velocities of ^{87}Rb and ^{133}Cs atoms. These determinations combine results from many experiments (described below) to calculate the fine struc-

ture constant using

$$\alpha^2 = \frac{2R_\infty}{c}\frac{A_\mathrm{r}(\mathrm{X})}{A_\mathrm{r}(\mathrm{e})}\frac{h}{m_\mathrm{X}}, \tag{1.15}$$

where R_∞ is the Rydberg constant and $A_\mathrm{r}(\mathrm{X})$ is the mass of particle X (either ^{87}Rb or ^{133}Cs) in amu, i.e., relative to a twelfth of the mass of ^{12}C. The Rydberg is measured with hydrogen and deuterium spectroscopy to a relative uncertainty of 6.6 ppt [25]. The mass of the electron in amu is measured to a relative uncertainty of 0.44 ppb using two Penning trap techniques: it is calculated from the g-value of the electron bound in $^{12}\mathrm{C}^{5+}$ and $^{16}\mathrm{O}^{7+}$ [25, 31] and measured directly by comparing the cyclotron frequencies of an electron and fully-ionized carbon-12 ($^{12}\mathrm{C}^{6+}$) [32]. Another set of Penning trap mass measurements determine $A_\mathrm{r}(^{133}\mathrm{Cs})$ to 0.20 ppb and $A_\mathrm{r}(^{87}\mathrm{Rb})$ to 0.17 ppb [33]. The ratio h/m_Rb is measured by trapping rubidium atoms in an optical lattice and chirping the lattice laser frequency to coherently transfer momentum from the field to the atoms through adiabatic fast passage (the equivalent condensed matter momentum transfers are called Bloch oscillations) [34, 35]. Equating the momentum lost by the field ($2\hbar k$) to that gained by the atoms (mv) yields the desired ratio, since k is known from the laser wavelength and v can be measured through velocity-selective Raman transitions. The ratio h/m_Cs is calculated from optical measurements of two cesium D_1 transitions, measured to 7 ppt [36], and a "preliminary" measurement of the recoil velocity of an atom that absorbs a photon resonant with one transition and emits resonant with the other, measured as a frequency shift in an atom interferometer [37]. The results of these two determinations are

$$\alpha^{-1}(\mathrm{Rb}) = 137.035\ 998\ 84\ (91)\ [6.6\ \mathrm{ppb}] \qquad [35] \tag{1.16}$$

$$\alpha^{-1}(\mathrm{Cs}) = 137.036\ 000\ 00\ (110)\ [8.0\ \mathrm{ppb}] \qquad [36]. \tag{1.17}$$

Using these values of α to calculate a "theoretical" g constitutes the traditional test of QED, with the results

$$\left|\frac{\delta g}{2}\right|_{\mathrm{Rb}} = 2.1\ (7.7) \times 10^{-12} \tag{1.18a}$$

$$\left|\frac{\delta g}{2}\right|_{\mathrm{Cs}} = -7.7\ (9.3) \times 10^{-12}. \tag{1.18b}$$

The agreement indicates the success of QED. Of the three contributions to these tests (measured g-value, QED calculations, and independent α), the over-ten-times larger uncertainty of the independent values of α currently limits the resolution. Higher-precision measurements are planned for both the rubidium and cesium experiments, the latter with a stated goal of better than 0.5 ppb [38].

There are many other lower-precision determinations of the fine structure constant; their values are collected in [25, Sec. IV.A] and plotted in Fig. 1.4b. Recent measurements of the silicon lattice constant, d_{220}, required for the α determination from h/m_{n}, may shift its value of α from that listed in [25], and the plotted value is one we have deduced based on the results in [39, 40].

1.1.4 Comparing precise tests of QED

Although it is the most precise test of QED, the electron g-value comparison is far from the only one, and it is worthwhile examining others. Four considerations go into determining the precision of a QED test: the relative experimental uncertainty, the relative theoretical uncertainty due to QED and other calculations, the relative theoretical uncertainty due to values of the fundamental constants, and the relative QED contribution to the value measured. The net test of QED is the fractional

uncertainty in the QED contribution to each of these quantities.

The free-electron g-value

For example, the relative experimental uncertainty in the electron g is 2.8×10^{-13}, the relative theoretical uncertainty from the QED calculation is 3.3×10^{-13} (dominated by our assumption about C_{10} in Eq. 1.9), the relative theoretical uncertainty from fundamental constants is 7.7×10^{-12} (based on α(Rb) of Eq. 1.16), and the relative QED contribution to the electron g-value is 1.2×10^{-3}, yielding a net test of QED at the 6.6 ppb level. Table 1.1 compares this test to others of note.

Hydrogen and deuterium spectroscopy

Some measurements of hydrogen and deuterium transitions look promising because of high precision in both experiment and theory [41]. As tests of QED, they are undone by the relatively low contribution of QED to the overall transition frequencies [25, App. A]. Conversely, the transitions that are dominated by QED, e.g., the Lamb shifts, tend to have higher experimental uncertainty. After the hydrogen $1S_{1/2} - 2S_{1/2}$ transition, which sets the value of the Rydberg R_∞, the deuterium $2S_{1/2} - 8D_{5/2}$ transition has the highest experimental precision (many others are close). The theoretical uncertainties are smaller than that from experiment, with the contribution from fundamental constants dominated by the uncertainty in R_∞, the deuteron radius, and the covariance between the two.[6] The QED contribution

[6]Here, we use the 2002 CODATA values [25] for the fundamental constants even though $\nu_{\rm D}(2S_{1/2} - 8D_{5/2})$ was included in that least-squares fit. We have assumed that its contribution to the relevant constants was small. We have been careful in cases where that assumption is not valid, using α(Rb) instead of α(2002) for the free-electron g-value analysis and removing $\nu_{\rm H}(1S_{1/2} - 2S_{1/2})$ from the possible tests of QED because it is the primary contributor to R_∞.

system	QED relative contribution	relative experimental uncertainty	relative theoretical uncertainty (theory)	relative theoretical uncertainty (constants)	net test of QED	Notes
free electron g	1.2×10^{-3}	2.8×10^{-13}	3.3×10^{-13}	7.7×10^{-12}	6.6 ppb	a
D: $2S_{1/2} - 8D_{5/2}$	1.4×10^{-6}	7.7×10^{-12}	2.2×10^{-13}	3.6×10^{-12}	5 500 ppb	b
H: $2P_{1/2} - 2S_{1/2}$	1.0	8.5×10^{-6}	6.2×10^{-7}	2.2×10^{-6}	8 500 ppb	b
H: $(2S_{1/2} - 4S_{1/2}) - \frac{1}{4}(1S_{1/2} - 2S_{1/2})$	0.19	2.1×10^{-6}	4.2×10^{-8}	4.2×10^{-7}	11 000 ppb	b
bound electron g ($^{12}C^{5+}$)	1.2×10^{-3}	2.3×10^{-9}	9.0×10^{-11}	8.0×10^{-12}	1 900 ppb	c
U^{91+}: $1S$ Lamb shift	0.57	1.0×10^{-2}	1.1×10^{-3}	-	1.8%	

Table 1.1: Tests of QED.
Notes:
a. The theory uses α(Rb) [35] rather than the CODATA value [25].
b. The theory uses CODATA values [25, 41] even though this measurement contributed to them. We make the valid assumption that the contribution is small.
c. The frequency ratio needed for the bound g-value has been measured to 5.2×10^{-10}, but the relative electron mass is only independently known to 2.1×10^{-9} [25].

to this frequency is only at the ppm level, undercutting the high experimental and theoretical precision.

The hydrogen Lamb shift ($2P_{1/2} - 2S_{1/2}$) is nearly entirely due to QED, but has an experimental precision at the many ppm level and a large theoretical uncertainty due to the proton radius, which is now extracted most accurately from H and D spectroscopy measurements [25]. The hydrogen $1S$ Lamb shift can be determined from a beat frequency between integer multiples of the $1S - 2S$ transition and either of the $2S - 4S$ or $2S_{1/2} - 4D_{5/2}$ transitions. In Table 1.1, we specifically analyze the difference given by $(2S_{1/2} - 4S_{1/2}) - \frac{1}{4}(1S_{1/2} - 2S_{1/2})$, the primary component of which is still non-QED. The constants part of the theoretical uncertainty is still dominated by the proton radius.

The bound-electron g-value

The bound-electron g-value has a QED calculation [25, App. D] similar to the free electron g, but a measurement using a single ion is heavily dependent on the mass of the electron, so much so that it is currently the standard for the relative electron mass ($A_\mathrm{r}(\mathrm{e})$). The relevant equation is number 48 of [25],

$$\frac{f_\mathrm{s}\left(^{12}\mathrm{C}^{5+}\right)}{f_\mathrm{c}\left(^{12}\mathrm{C}^{5+}\right)} = -\frac{g_{\mathrm{e}^-}\left(^{12}\mathrm{C}^{5+}\right)}{10A_\mathrm{r}(\mathrm{e})} \times \left[12 - 5A_\mathrm{r}(\mathrm{e}) + \frac{E_\mathrm{b}(^{12}\mathrm{C}) - E_\mathrm{b}\left(^{12}\mathrm{C}^{5+}\right)}{m_\mathrm{u}c^2}\right], \qquad (1.19)$$

where $A_\mathrm{r}(\mathrm{e})$ is determined from the measured electron spin and cyclotron frequencies (the f's) and the calculated bound g-value and binding energies (E_b).

As a potential test of QED, a single bound-electron g-value measurement must rely on a separate electron mass measurement. The experimental uncertainty is then dominated by this independent electron mass measurement, which currently is known to

2.1×10^{-9} [32]. The relevant frequency ratio has been measured to 5.2×10^{-10} [31]. The theoretical uncertainty is dominated by the theory calculations themselves, though there is a small contribution from the fundamental constants. Note that there is a measurement for $^{16}O^{7+}$ similar to the $^{12}C^{5+}$ measurement in Table 1.1 with a similar result.

Another possibility that is not as heavily dependent on the electron mass is measuring the ratio of bound g-values for two ions. This has been done, with the experimental result

$$\frac{g_{e^-}\left(^{12}C^{5+}\right)}{g_{e^-}\left(^{16}O^{7+}\right)} = 1.000\ 497\ 273\ 70(90)\ [9.0\times10^{-10}]\ [25,\ \text{Eq. } 55] \tag{1.20}$$

and the theoretical calculation

$$\frac{g_{e^-}\left(^{12}C^{5+}\right)}{g_{e^-}\left(^{16}O^{7+}\right)} = 1.000\ 497\ 273\ 23(13)\ [1.3\times10^{-10}]\ [25,\ \text{Eq. D}34]. \tag{1.21}$$

To compare its quality as a test of QED, the 0.9 ppb measurement must be reduced by the QED contribution, which cancels to first order and is only about 1 ppm, leaving a test of QED in the 900 ppm range.

High Z ions

Because the perturbative expansion of QED involves powers of $(Z\alpha)$, much work has been devoted to measuring atomic structure at high Z in search of a high-field breakdown of the theory. These experiments are designed as probes of new regions of parameter space rather than as precision tests of QED and both the experimental and theoretical uncertainties are high. For example, measurements of the X-ray spectra from radiative recombination of free electrons with fully-ionized uranium have

determined the ground-state Lamb shift of hydrogen-like uranium, U^{91+}, to 1% [42]. The theory has been calculated another order-of-magnitude better [43], and there is negligible contribution from the fundamental constants. A measurement of the $2S_{1/2} - 2P_{1/2}$ transition in lithium-like U^{89+} has a much higher precision of 5.3×10^{-5}, but the theory is not yet complete [44].

1.1.5 Limits on extensions to the Standard Model

Despite its remarkable success in explaining phenomena as diverse as the electron's anomalous magnetic moment, asymptotic freedom, and the unification of the electromagnetic and weak interactions, the Standard Model does not include gravity and does not explain the observed matter-antimatter asymmetry in the universe and is thus incomplete. The high accuracy to which we measure the electron magnetic moment allows two classes of tests of the Standard Model. The first uses the independent determinations of the fine structure constant, quantified in the comparisons of Eq. 1.18, to set limits on various extensions to the Standard Model, including electron substructure, the existence of light dark matter, and Lorentz-symmetry violations. The second looks for differences between the electron and positron g-values and searches for temporal variations of the g-value, especially modulation at the Earth's rotational frequency, to set limits on violations of Lorentz and CPT symmetries.

Electron substructure

As with the proton, deviations of the measured g-value from that predicted by QED could indicate a composite structure for the electron. Such constituent parti-

cles could unify the leptons and quarks and explain their mass ratios in the same way that the quarks unify the baryons and mesons. The challenge for such a theory is to explain how electrons are simultaneously light and small, presumably due to tightly bound components with large masses to make up for the large binding energy. Initially, one might use the inverse-mass natural scaling of magnetic moments in Eq. 1.1 to derive an additional component of the g-value that is linear in the mass ratio $\delta g/2 \sim O(m/m^*)$ [45], where m^* is the mass of the internal constituents. This theory is naive because it would also predict a first-order correction to the self-energy ($\delta m \sim O(m^*)$), which must precisely be canceled by the binding energy to explain the lightness of the electron. A more sophisticated theory suppresses the self-energy correction with a selection rule. For example, chiral invariance of the constituents removes the linear constituent-mass-dependence of both the self-energy and the magnetic moment, leaving a smaller addition $\delta g/2 \sim O(m^2/m^{*2})$ but at the cost of doubling the number of constituents required [45]. Assuming this model, the comparisons of Eq. 1.18 set a limit on the minimum constituent mass,

$$m^* \gtrsim \frac{m}{\sqrt{\delta g/2}} = 130 \text{ GeV}/c^2, \tag{1.22}$$

which suggests a natural size scale for the electron of

$$R = \frac{\hbar}{m^* c} \lesssim 10^{-18} \text{ m}. \tag{1.23}$$

(We have used $|\delta g/2| \lesssim 15 \times 10^{-12}$.) If the uncertainties of the independent determinations of α equaled ours for g, then we could set a limit of $m^* \gtrsim 1$ TeV. The largest e^+e^- collider (LEP) probes for a contact interaction at $E = 10.3$ TeV [46], [13, pp.1154-1164], with $R \lesssim \hbar c/E = 2 \times 10^{-20}$ m.

Light dark matter

The electron g-value has the potential to confirm or refute a hypothesized class of light dark matter (LDM) particles. Visible matter accounts for only 20% of the matter in the universe, and typical models for the remainder involve particles heavier than the proton. Light (1–100 MeV) dark matter has been proposed [47] as an explanation for 511 keV radiation (from e^+e^- annihilations) emitted from an extended region ($\approx 10^\circ$) about the Milky Way's galactic bulge [48]. The LDM would consist of scalar particles and antiparticles interacting via the exchange of a new gauge boson and a heavy fermion. The gauge boson, which has a velocity-dependent cross-section, would dominate interactions in the early universe and explain the observed ratio of luminous to dark matter, while the fermion would explain the presently observed 511 keV line [49]. Both would couple to electrons as well, allowing dark matter annihilations to produce electron–positron pairs; this interaction would include small shifts to the electron g-value [49]. The relative abundance of dark matter constrains the boson coupling to be far smaller than that of the fermion. Because the fermion coupling is constrained by the morphology of the 511 keV flux, the LDM theory makes a prediction for the g-value shift, equal to

$$\frac{\delta g}{2} = 10(5) \times 10^{-12} \tag{1.24}$$

times a geometric factor of order one that describes the dark matter profile in the Milky Way [50]. Our g-value precision already exceeds that of this prediction; the independent measurements of α are close to allowing observation of this size shift, and further improvements can confirm or refute the light dark matter hypothesis.

A Standard Model Extension

In order to organize various tests of violations of Lorentz-symmetry and CPT-symmetry, Colladay and Kostelecký have introduced a Standard Model extension (SME), a phenomenological parameterization of all possible hermitian terms that can be added to the Standard Model Lagrangian and that allow spontaneous CPT or Lorentz violation while preserving $\mathrm{SU}(3)\times\mathrm{SU}(2)\times\mathrm{U}(1)$ gauge invariance and power-counting renormalizability [51]. Although the terms in the SME allow spontaneous Lorentz-symmetry breaking, they maintain useful features such as microcausality, positive energies, conservation of energy and momentum, and even Lorentz-covariance in an observer's inertial frame, only violating it in the particle frame. The terms relevant to this experiment are among those that modify the QED Lagrange density,

$$\mathcal{L}^{\mathrm{QED}} = \bar{\psi}\gamma^{\mu}\left(i\hbar c\partial_{\mu} - qcA_{\mu}\right)\psi - mc^{2}\bar{\psi}\psi - \frac{1}{4\mu_{0}}F^{\mu\nu}F_{\mu\nu}, \tag{1.25}$$

and are typically parameterized as

$$\begin{aligned}\mathcal{L}^{\mathrm{SME}} = {} & -a_{\mu}\bar{\psi}\gamma^{\mu}\psi - b_{\mu}\bar{\psi}\gamma_{5}\gamma^{\mu}\psi + c_{\mu\nu}\bar{\psi}\gamma^{\mu}\left(i\hbar c\partial^{\nu} - qcA^{\nu}\right)\psi \\ & + d_{\mu\nu}\bar{\psi}\gamma_{5}\gamma^{\mu}\left(i\hbar c\partial^{\nu} - qcA^{\nu}\right)\psi - \frac{1}{2}H_{\mu\nu}\bar{\psi}\sigma^{\mu\nu}\psi \\ & + \frac{1}{2\hbar}\left(k_{\mathrm{AF}}\right)^{\kappa}\epsilon_{\kappa\lambda\mu\nu}\sqrt{\frac{\epsilon_{0}}{\mu_{0}}}A^{\lambda}F^{\mu\nu} - \frac{1}{4\mu_{0}}\left(k_{\mathrm{F}}\right)_{\kappa\lambda\mu\nu}F^{\kappa\lambda}F^{\mu\nu}.\end{aligned} \tag{1.26}$$

Here, the SME parameters are a_{μ}, b_{μ}, $c_{\mu\nu}$, $d_{\mu\nu}$, $H_{\mu\nu}$, $(k_{\mathrm{AF}})^{\kappa}$, and $(k_{\mathrm{F}})_{\kappa\lambda\mu\nu}$, and the remaining parts are the usual Dirac spinor field (ψ) and its adjoint ($\bar{\psi}$), the usual gamma matrices, the vector potential (A^{μ}), and the field strength tensor $F^{\mu\nu} \equiv \partial^{\mu}A^{\nu} - \partial^{\nu}A^{\mu}$, see e.g., [12, Ch. 7], [11, Ch. 3]. Note that the terms with an odd number of indices (a_{μ}, b_{μ}, and $(k_{\mathrm{AF}})^{\kappa}$) also violate CPT symmetry. Furthermore, each SME coefficient can have different values for each particle; we concern ourselves

here with those in the electronic sector.

Our sensitivity to QED's radiative corrections allows us to set a robust limit on the CPT-preserving photon term's spatially isotropic component: $\tilde{k}_{\rm tr} \equiv {}^2\!/_3 (k_{\rm F})^j{}_{0j0}$.[7] This component is essentially a modification to the photon propagator, and if it were non-zero, it would slightly shift the electron g-value from that predicted by QED [52]:

$$\frac{\delta g}{2} = -\frac{\alpha}{2\pi}\tilde{k}_{\rm tr}. \tag{1.27}$$

Given our limits in Eq. 1.18, we can set the bound

$$\tilde{k}_{\rm tr} \lesssim 10^{-8}. \tag{1.28}$$

This limit is almost four orders of magnitude below the prior one [53]. A tighter bound can be set if one considers the effect of this coefficient on others in the overall renormalization of the SME parameters, but this is heavily model-dependent [52].

Non-zero SME parameters would also modify the energy levels of an electron in a magnetic field producing shifts in the cyclotron and anomaly frequencies (these frequencies are defined in Chapter 2). To leading order, these shifts are [54]

$$\delta\omega_c^{\pm} \approx -\omega_c(c_{00} + c_{11} + c_{22}) \tag{1.29}$$

$$\delta\omega_a^{\pm} \approx 2(\pm b_3 + d_{30}mc^2 + H_{12})/\hbar, \tag{1.30}$$

where the $\pm$ refers to positrons and electrons. Here, the index "3" refers to the spin quantization axis in the lab, i.e., the magnetic field axis, while "1" and "2" refer to the other two spatial axes and "0" to time. The terms in the anomaly shift are

[7] Here I use the usual convention that Greek indices run over all space-time components 0, 1, 2, 3 (t, x, y, z) while Roman indices run over only the spatial ones.

conventionally combined into a shorthand,

$$\tilde{b}_j \equiv b_j - d_{j0}mc^2 - \frac{1}{2}\epsilon_{jkl}H_{kl}, \tag{1.31}$$

which acts like a pseudo-magnetic field in its coupling to spin [55]. Both c_{ij} and $\tilde{b}_j$ violate Lorentz-invariance by defining a preferred direction in space. Provided this direction is not parallel to the Earth's axis, the daily rotation of the experiment axis about the Earth's axis will modulate the couplings.[8]

In Chapter 8 we look for these modulations with anomaly frequency measurements. Because ν_a is proportional to the magnetic field, any drift in the field could wash out an effect. Since we occasionally see drifts above our sub-ppb frequency resolution, we use the cyclotron frequency to calibrate the magnetic field. In the process, we make our anomaly frequency measurement sensitive to several SME $c_{\mu\mu}$ coefficients through Eq. 1.29. Variations in the anomaly frequency are thus related to the SME parameters in the lab frame via

$$\delta\nu_a = -\frac{2\tilde{b}_3}{h} + \nu_a(c_{00} + c_{11} + c_{22}), \tag{1.32}$$

which contains three Lorentz-violation signatures: offsets between the measured anomaly frequency and that predicted by the Standard Model (c_{00} and parts of the other coefficients do not vary with the Earth's rotation) and modulations at one or two times the Earth's rotation frequency. We do not find any modulation of the anomaly frequency and set the limit

$$|\delta\nu_a| < 0.05 \text{ Hz} = 2 \times 10^{-16} \text{ eV}/h, \tag{1.33}$$

[8]Note that this modulation occurs over a sidereal day (≈ 23.93 hours) not a mean solar day (24 hours). Since the two rephase annually, one can collect data at every time of the sidereal day despite only running at "night."

an improvement by a factor of two on the previous single-electron result [56].[9] Assuming zero c_{jj}-coefficients, this limit is $\left|\tilde{b}_3\right| < 10^{-16}$ eV. Similarly, a zero $\tilde{b}_3$ coefficient yields a limit $|c_{11} + c_{22}| < 3\times10^{-10}$. For proper comparison with other measurements, the limits should be converted from the rotating lab coordinates $(1, 2, 3)$ to a non-moving frame, traditionally celestial equatorial coordinates; this is done in Chapter 8, and the results are of similar magnitude.

While these limits can provide confirmation of other results, they are not the leading constraints on the coefficients. The tightest bounds on $c_{\mu\nu}$ come from either experiments with cryogenic optical resonators [57] or astrophysical sources of synchrotron and inverse Compton radiation [58, 59], both setting limits of order 10^{-15}. The cavity-resonator experiments search for Lorentz-violating shifts in the index of refraction of a crystal due to changes in its electronic structure. They require assumptions that there are no corresponding Lorentz-violations that affect the nuclei. The astrophysical limits focus on the way the $c_{\mu\nu}$-coefficients alter the dispersion relations among an electron's energy, momentum, and velocity. For a given direction in space, an electron's velocity and energy are limited by $c_{\mu\nu}$, so measurements of large electron energies and velocities, as seen through their synchrotron and inverse Compton radiation, constrain the various $c_{\mu\nu}$ coefficients.

The tightest bound on $\tilde{b}_j$ comes from an experiment with a ring of permanent magnets suspended in a torsion pendulum [60]. The ring has a large net spin ($\approx10^{23}$ electron spins) with no net magnetic moment (the magnetic flux is entirely contained within the torus), which greatly enhances the coupling to $\tilde{b}_j$ while decreasing mag-

[9] We do not get the same order-of-magnitude improvement here that we do for the g-value because the result (also from the University of Washington) came from a dedicated Lorentz-violation experiment, optimized for detecting ν_a at the expense of poor precision of ν_c.

netic interference. Hanging with the spin vector horizontal and rotating the entire apparatus with a period on the order of an hour adds a faster modulation to any signal, which would appear as an anomalous torque on the spins. By keeping track of the apparatus orientation with respect to celestial coordinates, they place limits in the range 10^{-21}–10^{-23} eV on the components of $\tilde{b}_j$, with tighter limits for the components perpendicular to the Earth's axis because they have additional diurnal modulation [61].

Although other experiments set tighter limits on the $c_{\mu\nu}$ and $\tilde{b}_j$ parameters, our g-value experiment has a distinct advantage in the ability to replace the electron with a positron. Since the b_μ term violates CPT, this replacement changes its coupling to the particle spin, allowing a direct test of b_3 rather than $\tilde{b}_3$ [62]. Prior experiments constrained $b \lesssim 10^{-13}$–10^{-15} eV [63], with the wide range arising from a lack of data over most of the sidereal day. By extending the data-taking period and taking advantage of our improved g-value precision, future experiments using the techniques of this thesis should reduce the lower end of that limit by over an order of magnitude.

Is the fine structure constant constant?

The use of the term "constant" for α is itself subject to scientific inquiry, and there are active searches for its variation in space and time. Such an inconstancy would violate the equivalence principle but is predicted by multidimensional theories since α would be a mere four-dimensional constant and could depend on fields moving among the other dimensions [7]. The most precise techniques for measuring $\dot{\alpha}$, reviewed in [7], use either moderately precise techniques over long timescales or extremely precise

techniques over shorter timescales. Analyses of a prehistoric, naturally-occurring fission reactor at the present-day Oklo uranium mine in Gabon allow the calculation of the cross-section for a particular neutron capture resonance in ^{149}Sm as it occurred 2×10^9 years ago. Comparing these calculations with the present-day value of the cross-section and assuming any temporal variation in α is linear yields a precision on $|\dot{\alpha}/\alpha|$ of 10^{-17} yr^{-1}, although various analyses disagree on whether the result shows variation in α [64] or not [7]. Looking even further back in time, astrophysical measurements using quasar absorption spectra allow the comparison of present-day atomic lines to those from 10^{10} years ago and yield a precision on $|\dot{\alpha}/\alpha|$ of 10^{-16} yr^{-1}, although there are disagreements as to the interpretation of the results [65, 66]. High-precision laboratory spectroscopy examines pairs of atomic transitions (perhaps in different atomic species) that have different dependences on α. Monitoring their relative frequencies over several years yields limits on the present-day variation of α as good as $|\dot{\alpha}/\alpha| < 1.2 \times 10^{-16}$ yr^{-1} [67]. Although our experiment is the highest-precision measurement of α itself, we would need to monitor α over 10^6 years to achieve a similar resolution of its time-variation.

1.1.6 Magnetic moments of the other charged leptons

The magnetic moments of all three charged leptons may be written as the sum of the Dirac eigenvalue ($g = 2$), a QED expansion in powers of α/π, and hadronic and weak corrections (see Table 1.2). The contributions of a heavy virtual particle of mass M to the anomalous magnetic moment of a lepton with mass m goes as $(m/M)^2$ [26] and accounts quite well for the increasing size of hadronic and electroweak effects

	electron $g_e/2$	**muon** $g_\mu/2$	**tauon** $g_\tau/2$
Dirac	1	1	1
QED	0.001 159 652 181 1(77)	0.001 165 847 1809(16)	0.001 173 24 (2)
hadronic	0.000 000 000 001 682(20)	0.000 000 069 13(61)	0.000 003 501(48)
weak	0.000 000 000 000 0297(5)	0.000 000 001 54 (2)	0.000 000 474 (5)
total	1.001 159 652 182 8(77)	1.001 165 917 85(61)	1.001 177 21(5)

Table 1.2: Dirac, QED, electroweak, and hadronic contributions to the theoretical charged lepton magnetic moments. The dominant uncertainty in the predicted electron g is due to an independent fine structure constant (here we use Eq. 1.16). The dominant uncertainties in the muon [26] and tauon [68] g-values are from the experiments that determine the hadronic contribution.

for the heavier leptons. (The tauon hadronic contribution does not follow the ratio because its heavy mass breaks the $m \ll M$ assumption.) The heightened sensitivity to non-QED effects comes at the cost of theoretical precision because quantum chromodynamics is a non-perturbative theory and the hadronic contributions must be analyzed by relating the magnetic moment Feynman diagrams to scattering diagrams whose magnitude can be acquired from experiment. The general $(m/M)^2$ scaling may also apply to sensitivity to effects beyond the Standard Model, as seen in the electron substructure discussion of Section 1.1.5 and in [69]. Thus measurements of the charged lepton magnetic moments may be used for complementary purposes: the electron g-value, with its relatively low sensitivity to heavy particles, provides a high-precision test of QED, while the heavier leptons, with the larger but less precise contributions from hadronic and weak effects, search for heavy particles such as those from supersymmetry.

The experimental limit on the tauon magnetic moment, derived from the total cross-section of the $e^+e^- \to e^+e^-\tau^+\tau^-$ reaction, is [70]

$$0.948 < \frac{g_\tau}{2} < 1.013, \qquad 95\%\ \text{CL} \tag{1.34}$$

and has not yet begun to probe the QED correction to the Dirac g.

There is a rich history of precision measurements of the muon magnetic moment [26]. The basic premise is a measurement of the anomaly frequency for a particle in a magnetic field, just as in the electron measurement, but the experimental constraints of the middleweight lepton lead to a strikingly different apparatus. Pion decays produce spin-polarized muons, which enter a 7 m-radius storage ring. When the muon decays, it emits an electron with an energy correlated to the angle between the electron momentum and the muon spin, and the precession of that spin axis about the muon momentum occurs at the anomaly frequency. Whereas in the electron measurement we calibrate the magnetic field with the electron cyclotron frequency, the muon experiment uses a set of NMR probes on a "trolley" that traverses the storage ring. The current experimental limit on the muon g, averaged for the values from μ^+ and μ^-, is [71]

$$\frac{g_\mu}{2} = 1.001\ 165\ 920\ 80\ (63)\ [0.63\ \text{ppb}], \tag{1.35}$$

with the statistical uncertainty dominating the systematic uncertainty: 0.54 ppb to 0.33 ppb. A comparison with the theoretical value in Table 1.2 reveals a tantalizing 3.4 standard-deviation discrepancy, inspiring a proposal for another run with the goal of improving the precision by a factor of 2.5 [72, 73].

1.1.7 The role of α in a redefined SI

A system of units provides a set of common standards against which other quantities are compared. Ideally, these standards are based on an invariant of nature so that measured values change only when the measured quantity itself changes. That

unit	quantity	current reference	proposed reference
second (s)	time	$\Delta\nu(^{133}\mathrm{Cs})_{\mathrm{hfs}}$	$\Delta\nu(^{133}\mathrm{Cs})_{\mathrm{hfs}}$
meter (m)	length	c	c
ampere (A)	electric current	μ_0	e
kilogram (kg)	mass	$m(\kappa)$	h
kelvin (K)	thermodynamic temperature	T_{TPW}	k
mole (mol)	amount of substance	$M(^{12}\mathrm{C})$	N_A
candela (cd)	luminous intensity	$K(\lambda_{555})$	$K(\lambda_{555})$

Table 1.3: Current and proposed reference quantities for the SI

is, there should be no worry that the standard itself changed.[10] As presently defined the International System of Units, the SI, contains a mix of invariants of nature and other quantities. The second and the meter, defined by the ground-state hyperfine transition of cesium and the speed of light, as well as the kelvin, defined by the triple-point of water, are all based on invariants, although T_{TPW} is difficult to realize to high accuracy [74]. The kilogram, however, is defined as the mass of an artifact in a vault at the International Bureau of Weights and Measures (BIPM), and is the only remaining standard not linked to a natural invariant. The ampere, mole, and candela are currently defined relative to the vacuum permeability (μ_0), the molar mass of carbon-12 ($M(^{12}\mathrm{C})$), and the spectral luminous efficacy of monochromatic radiation of frequency 540×10^{12} Hz ($K(\lambda_{555})$—the wavelength is roughly 555 nm). While these definitions appear to be defined in terms of invariants, they each are linked to the kilogram in a manner analogous to the linking of the meter to the second by its definition in terms of a velocity.

Recent progress in relating Planck's constant to macroscopic masses through the

[10] As noted in Section 1.1.5, the "constant" nature of fundamental constants is itself subject to experimental inquiry.

moving-coil watt-balance [75] as well as improvements in the measurement of the molar volume of silicon through X-ray-crystal-density experiments [76] have led to the possibility of defining the kilogram by fixing the value of either Planck's constant (h) or Avogadro's number (N_A), both of which are invariants of nature, the latter being an integer. A recent approach [74], summarized in Table 1.3, suggests doing both and more, fixing the values of h, N_A, the positron charge (e), and Boltzmann's constant (k), while allowing the SI values of μ_0, T_{TPW}, $M(^{12}\mathrm{C})$, and the mass of the kilogram artifact to be measured quantities. In addition to the aesthetic pleasure of having a system of units defined in terms of such fundamental quantities, it will also allow higher precision measurements in the SI. For example, the Josephson constant ($K_J = 2e/h$) and the von Klitzing constant ($R_K = h/e^2$) will become exact, allowing the direct realization of the SI ampere, volt, ohm, watt, farad, and henry through the Josephson and quantum Hall effects [74]. In addition, a number of other constants will be exact in SI units as will conversions among joules, kilograms, inverse meters, hertz, kelvins, and electronvolts.

The role of the fine structure constant in such a redefined SI is twofold. First, its value will be used as part of the determination of the fixed values of the new reference quantities. For example, e will be calculated from Eq. 1.3 using the measured value of α and the recently fixed h; N_A will be calculated from

$$N_A = \frac{cA_{\mathrm{r}}(\mathrm{e})M_{\mathrm{u}}\alpha^2}{2R_\infty h}, \tag{1.36}$$

where $M_{\mathrm{u}} = 10^{-3}$ kg/mol is the molar mass constant. Second, with so many other fundamental constants fixed, the uncertainty in expressing many quantities in SI units will be greatly reduced and the precision of the measured α will set the new, lower

uncertainty scale. For example, the electron mass in kilograms is calculated from

$$m_{\mathrm{e}} = \frac{2hR_{\infty}}{c\alpha^2}. \tag{1.37}$$

With the currently dominant uncertainty in h dropped to zero and the relative uncertainty of R_{∞} two orders of magnitude lower than that in α, the fine structure constant will set the mass uncertainty. In a similar way, α will set the limits on the proton mass in kilograms (m_{p}), the Bohr magneton (μ_{B}), the nuclear magneton (μ_{N}), and the kg-amu conversion. Furthermore, with μ_0 no longer fixed, a measurement of α will set its SI value along with that of ϵ_0 and Z_0, the vacuum impedance. Lastly, since it relies on referencing its measurements to the SI units and on using the fixed value of ϵ_0, the quantum Hall effect will no longer provide a measurement of the fine structure constant; instead it will supply a direct calibration of resistance in the SI.

1.2 Measuring the g-Value

1.2.1 g-value history

The uncertainty in the measured electron g-value and that predicted by theory have been closely linked since before the development of relativistic quantum mechanics, with each providing motivation for further study in the other. The early history is reviewed in [77] and extends from atomic measurements indicating $g = 2$ and Dirac theory, to direct measurements of bound-electron g-values and the birth of QED, to measurements at the University of Michigan on bunches of free electrons using the $g - 2$ technique, a string of experiments culminating in the measurement of g at a precision of 3.5 ppb.

The trapping of a single electron [78] led to a new era in g-value measurements, eliminating many of the plasma-related systematic effects. For over a decade, a series of experiments at the University of Washington pushed down the uncertainty in g, culminating in the famous 1987 measurement at a precision of 4.3 ppt, with the interaction between the electron and the trap-electrode-cavity modes [79, 80] making the primary contribution to the uncertainty [2].[11]

A number of improvements, described below and detailed in the remainder of the thesis, have allowed two new measurements at Harvard. The first, published in 2006 [1], had a precision of 0.76 ppt, with the primary uncertainties split between cavity-shifts and the agreement between the measured cyclotron and anomaly lines and their theoretical lineshapes. A preliminary analysis of this measurement appears in [83], and we include the final analysis in Chapter 6 with additional details in the relevant chapters. The second measurement, details of which form the basis of this thesis, is at a precision of 0.28 ppt, with the cavity shift uncertainty virtually eliminated and the lineshape model uncertainty reduced. With additional work already underway, future improvements on these measurements seem likely.

1.2.2 An artificial atom

Insofar as an atom is an electron bound in the electromagnetic field of a nucleus, our system, which traps a single electron in static magnetic and electric fields, is an artificial "atom."[12] Although the 3 m-tall apparatus and rack full of electronics is

[11] A subsequent attempt at the UW used a lossy trap cavity, and thus a reduced mode-coupling, as well as a variable "magnetic bottle" (see Section 2.3.4). While it provided bottle-scaling results for several systematic effects, the g-value measurements were spread non-statistically over 14 ppt [81, 82].

[12] Hans Dehmelt coined it "geonium," an electron bound "to an external apparatus residing on the Earth" [84].

not nearly as elegant of an electron trap as a single proton, it affords precise control over the trapping potentials. Many familiar atomic features, such as well-defined quantum levels, apply to our system, and we drive transitions between levels with radio and microwaves. Our "atom" even has fine-structure, with tiny shifts from special relativity playing an important role in our analysis.

The electron is stored in a Penning trap; a strong magnetic field confines the electron radially, while a weak electrostatic quadrupole restricts the axial motion. In addition to the spin frequency ($\nu_s \approx 150.2$ GHz), the electron motion is characterized by three trap eigenfrequencies: the cyclotron frequency ($\bar{\nu}_c \approx 150.0$ GHz), the axial frequency ($\bar{\nu}_z \approx 200$ MHz), and the magnetron frequency ($\bar{\nu}_m \approx 133$ kHz). Experimentally, the g-value is twice the ratio of the spin frequency to the cyclotron frequency in free space. Since the two are within a part-per-thousand of each other, i.e., $g \approx 2$, measuring their difference frequency directly is a higher-precision technique. This beat frequency, the anomaly frequency ($\bar{\nu}_a \approx 174$ MHz), allows a sub-ppt determination of the g-value with sub-ppb precision on the frequencies. Since the frequencies used in measuring the g-value should be the free-space values not the in-trap values, we must include three corrections in our calculations:

1. Special relativity shifts the cyclotron frequency, leading to a ppt-scale correction [84].

2. The radial part of the trap's electric field shifts the cyclotron and anomaly frequencies in the trap by the magnetron frequency, giving a ppm-scale, but precisely understood, correction [84].

3. Interactions with the radiation modes of a cavity formed by the trap electrodes

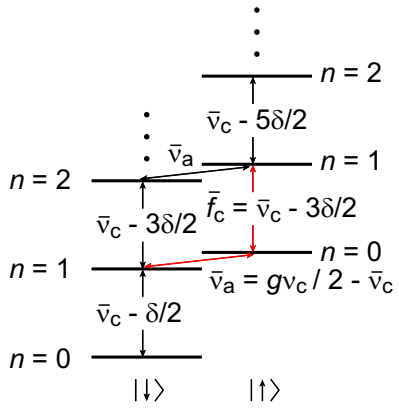

Figure 1.5: The energy levels of an electron in a Penning trap, including ppb-size shifts from special relativity. The red arrows indicate the transitions we measure to determine g.

shift the cyclotron and anomaly frequencies, yielding ppt-scale shifts that depend on the cyclotron frequency [80].

Including these corrections, the equation we use in calculating the g-value is

$$\frac{g}{2} \simeq 1 + \frac{\bar{\nu}_a - \dfrac{\bar{\nu}_z^2}{2\bar{f}_c}}{\bar{f}_c + \dfrac{3}{2}\delta + \dfrac{\bar{\nu}_z^2}{2\bar{f}_c}} + \frac{\Delta\omega_c}{\omega_c}, \tag{1.38}$$

where the barred frequencies are the eigenfrequencies of the trap, $\frac{3}{2}\delta$ is the relativistic correction, $\bar{\nu}_z^2/(2\bar{f}_c)$ is the magnetron correction, and $\Delta\omega_c/\omega_c$ is the cavity shift. The label $\bar{f}_c$ refers to the cyclotron transition between a specific pair of Fock states, as described in the next section. A derivation of Eq. 1.38 and a discussion of its leading corrections, all below our current precision, is in Chapter 4.

1.2.3 The Quantum Cyclotron

We have dubbed our apparatus a "quantum cyclotron" both because it contains a single quantum of the electron field and because a 100 mK dilution refrigerator

cools the electron cyclotron motion to the quantum ground state and we can resolve single cyclotron jumps and spin flips [85] with a quantum nondemolition (QND) measurement that couples the cyclotron and spin energies to frequency shifts of the axial motion, which we detect directly. The advantage of cyclotron-state resolution lies in the special relativistic shifts of the cyclotron frequency, which are state-dependent, as indicated by the δ terms of Fig. 1.5. By resolving the cyclotron states, we may treat these shifts exactly. In practice, we always measure the same cyclotron transition, $|0,\uparrow\rangle \leftrightarrow |1,\uparrow\rangle$, and refer to that frequency as $\bar{f}_c$.

An additional advantage of the 100 mK temperature is that it narrows the cyclotron and anomaly lines, which are primarily broadened by the same QND coupling that allows cyclotron and spin state-detection [86]. In this case, it transfers axial energy into cyclotron and anomaly frequency shifts, so a lower axial temperature reduces the linewidth. We resolve the lines via single-quantum spectroscopy by applying drives at discrete frequencies, looking for excitations, and building a histogram of the results.

The electrodes that establish the electrostatic potential form a high-Q microwave resonator at the cyclotron frequency, allowing cyclotron energy to couple into cavity modes. These coupled oscillators alter the cyclotron damping rate and shift the frequency in ways that depend on the cyclotron–mode detuning. The former can be a great advantage; by tuning the cyclotron frequency far from any cavity resonance, we inhibit spontaneous emission by up to 100 times its free-space value, allowing more time to detect cyclotron transitions before they decay. The frequency shifts, however, lead directly to shifts in the g-value and were a major part of the uncertainties

in the 1987 and 2006 measurements. In both 2006 and this thesis, we control the location of the cavity modes through the trap geometry and control the coupling of the cyclotron motion to them by adjusting the relative detuning of the cyclotron and mode frequencies. By using a cylindrical electrode geometry [87], invented precisely for our purpose, the electromagnetic modes of the cavity as well as their coupling to an electron may be analytically calculated [79, 80]. Aided by two independent techniques that use a cloud of electrons or the single electron itself to probe the cavity mode structure (Chapter 5), we measure g at four magnetic fields with cavity shifts spanning over thirty times our g-value uncertainty, demonstrate our understanding of the shifts, and at some fields nearly eliminate this once-dominant uncertainty.

Self-excitation of the electron axial motion [88], with a high signal-to-noise ratio from the resulting large but stable oscillation amplitudes, enhances our ability to detect the cyclotron state before it decays. We may thus make measurements closer to cavity modes, where the cyclotron damping rate is higher and the g-value shift larger, in order to compare measured g-value shifts to those predicted from cavity-mode calculations.

The cyclotron and anomaly lines exhibit slight departures, which we do not fully understand but attribute to magnetic field fluctuations, from their expected lineshapes, limiting our measurement by adding a model dependence to their interpretation. Our primary analysis technique uses an invariant property of the mean of the expected noise-free lineshapes to calculate g. In the presence of noise, this weighted-mean method yields identical results, provided the noise spectrum is symmetric. A second method, fitting the data to a lineshape, checks the results but requires the

adoption of a specific model for the noise distribution (we choose a Gaussian). These methods are discussed in Chapter 4, and their relative agreement quantifies a lineshape model uncertainty (Section 6.1), which dominates the measurement. In addition, data at two of the four fields at which we measure g have higher axial temperatures than the others for reasons not yet understood, though a deliberate temperature increase found no systematic shift.

With new techniques suggested to increase the magnetic field stability (Chapter 3), narrow the resonance lines, and speed-up the measurement's rate-limiting step (Chapter 7) as well as several spin-off experiments already underway (Chapter 9), many opportunities lie ahead.

Chapter 2

The Quantum Cyclotron

Our quantum cyclotron [85] consists of a single electron trapped with static electromagnetic fields and cooled to the quantum-mechanical ground state of its cyclotron motion, allowing quantum-jump spectroscopy of the cyclotron and anomaly transitions. We detect the cyclotron and spin states through a quantum nondemolition coupling to the axial motion, which is damped by a cryogenic amplifier to produce our signal. Self-excitation of the axial motion increases the signal-to-noise ratio. This chapter describes the techniques used to make a stable trapping potential and to interact with the electron.

2.1 The Penning Trap

The Penning trap confines charged particles through a combination of static magnetic and electric fields. A homogeneous magnetic field, $B\hat{\mathbf{z}}$, restricts the particle's transverse motion, pinning it in cyclotron motion about a field line. A superimposed

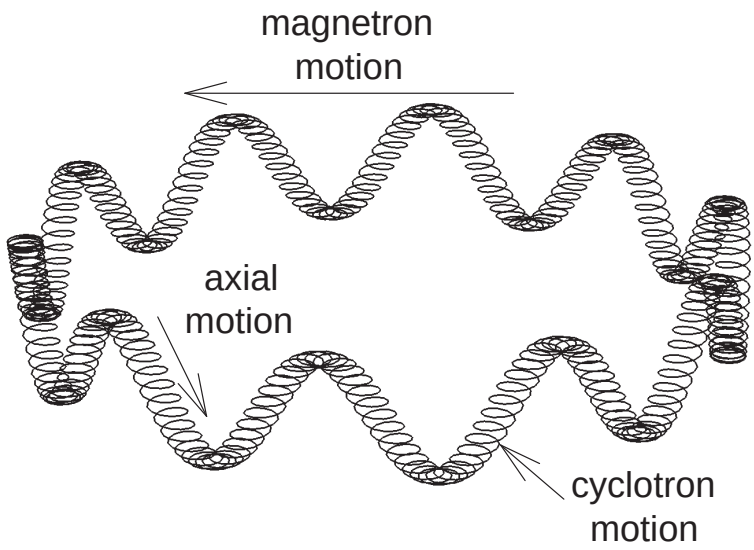

Figure 2.1: Cartoon of an electron orbit in a Penning trap. The relative amplitudes and frequencies of the motions are not to scale and the cyclotron "motion" is actually a quantum-mechanical stationary state.

electrostatic quadrupole, $V \sim 2z^2 - \rho^2$, confines its axial motion along that field line. The radial component of the quadrupole is anti-trapping; it slightly shifts the cyclotron frequency and introduces a third motion, the "magnetron" motion, that is intrinsically unstable but has a damping time so long that it is effectively stable. In addition, Section 2.3.7 discusses a technique we routinely use to reduce the radius of the magnetron motion by rolling it up the radial potential hill.

Our trap is composed of a high-homogeneity 6 T superconducting solenoid, manufactured by Nalorac Cryogenics Corporation, and five gold-plated-silver electrodes, shown in Fig. 2.2. Biases on the ring and endcap electrodes establish the electrostatic quadrupole, and the compensation electrodes allow for adjustments to its harmonicity. Section 2.4 discusses our use of feedback to allow harmonic axial motion over a large range of amplitudes. In addition to providing axial confinement, the trap electrodes form a high-Q microwave resonator, the modes of which can couple to the

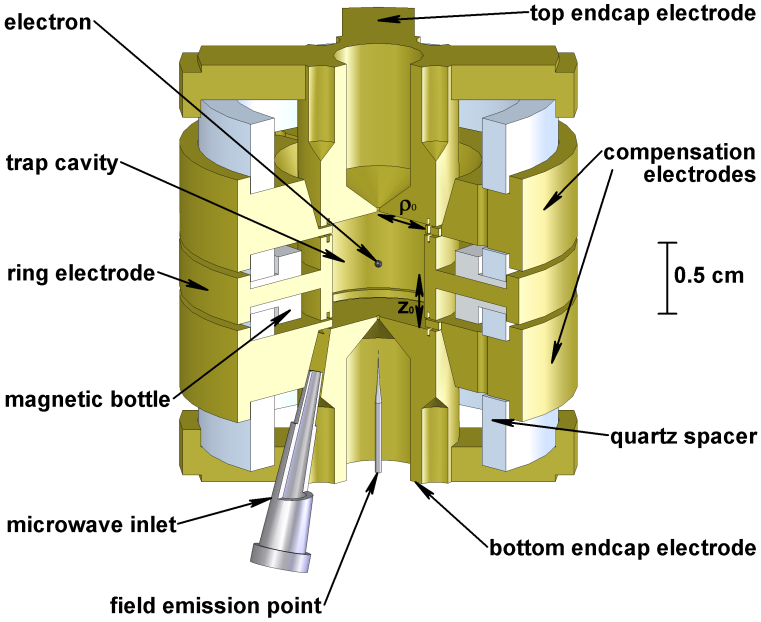

Figure 2.2: Sectioned view of the Penning trap electrodes

electron cyclotron motion. Since this coupling is an important systematic effect (see Chapter 5), we use cylindrical geometry for the trap electrode cavity, creating modes with well-defined, analytically calculable properties.

To load electrons, we put a potential of several hundred volts on an atomically sharp tungsten rod, which field-emits high energy electrons through a hole in the bottom endcap electrode. These electrons hit the top endcap electrode, releasing some gas. Through collisions with this gas, some electrons lose enough energy to fall into the trap. Trapping a single electron often begins with loading many electrons then follows an iteration of inverting the electrostatic potential to discard them and reloading with a lower voltage on the field-emission point or for a shorter time. Once

parameter	**value**	**coefficient**	**value**
ρ_0	4549 μm	$C_2^{(0)}$	0.125
z_0	3833 μm	D_2	-0.0003
Δz_c	766 μm	$C_4^{(0)}$	-0.023
d	3538 μm	D_4	-0.066
B	5.36 T	c_1	0.784
V_R	101.4 V	c_3	0.320
V_{comp}	74 V		

Table 2.1: Typical trap parameters and anharmonicity coefficients, with definitions and relationships defined in the text. The magnetic field and electrode biases are adjusted to change the trap frequencies. The trap dimensions include thermal contraction to 0.1 K.

the appropriate loading parameters have been characterized, it is often easier to load a single electron by beginning with the field-emission-point potential too low and increasing it until loading "something." We ensure it is only one by measuring its axial signal strength, axial damping rate, and the change in its magnetic moment with a single cyclotron jump, each of which changes in discrete steps for low numbers of electrons.

2.1.1 Trap frequencies and damping rates

The typical electrode bias configuration has the endcaps grounded, the ring at potential V_R, and the compensation electrodes at potential V_{comp}.[1]

The axial frequency is given by

$$\nu_z = \frac{1}{2\pi}\sqrt{\frac{eV_R}{md^2}(1+C_2)}. \tag{2.1}$$

[1]Here, we define the potentials V_R and V_{comp} as we apply them in the experiment. Other articles, e.g., [84], define the trapping potential in terms of V_0 and V_c that are related to our potentials by $V_0 = -V_R$ and $V_c = V_{\text{comp}} - V_R/2$.

Here, d is a characteristic trap dimension calculated in terms of the trap radius, ρ_0, and half-height, z_0,

$$d^2 = \frac{1}{2}\left(z_0^2 + \rho_0^2/2\right), \tag{2.2}$$

and C_2 is the coefficient of the second-order term in an expansion of the trapping potential in spherical coordinates:

$$V = -V_R \frac{z^2 - \rho^2/2}{2d^2} - \frac{V_R}{2}\sum_{\substack{k=0\\ \text{even}}}^{\infty} C_k \left(\frac{r}{d}\right)^k P_k(\cos\theta). \tag{2.3}$$

The expansion uses both cylindrical (ρ) and spherical (r) radii, and $P_k(x)$ are Legendre polynomials. The C_k depend on the trap geometry and the ratio of the ring and compensation electrode potentials. It is convenient to make this dependence explicit by writing

$$C_k = C_k^{(0)} + D_k\left(\frac{1}{2} - \frac{V_{\text{comp}}}{V_R}\right), \tag{2.4}$$

where the $C_k^{(0)}$ and D_k now depend only on the trap geometry. The relevant expressions for calculating the coefficients may be found in [87, 84]; Table 2.1 lists some values for our trap. A useful trick when designing a trap is to make the aspect ratio and compensation electrode height, Δz_c, such that $D_2 = 0$. In such an "orthogonalized" trap, C_2 (and thus ν_z) is independent of V_{comp}, which is used to tune the leading anharmonicity coefficient, C_4, to zero [87].

In general, the anharmonic terms in the electrostatic potential add a small dependence on axial amplitude, A, to the axial frequency ([84, Sec. IX] and [89, Sec. 2.2]):

$$\nu_z(A) \approx \nu_z\left[1 + \frac{3C_4}{4\left(1+C_2\right)}\left(\frac{A}{d}\right)^2 + \frac{15C_6}{16\left(1+C_2\right)}\left(\frac{A}{d}\right)^4\right]. \tag{2.5}$$

Here, ν_z is the zero-amplitude axial frequency of Eq. 2.1, and we have assumed that $C_4^2 \ll \left(1+C_2\right)C_6$, which is typically valid.

motion	**frequency**	**damping**
magnetron	$\nu_m \approx 133$ kHz	$\gamma_m^{-1} \approx 4$ Gyr
axial	$\nu_z \approx 200$ MHz	$\gamma_z^{-1} \approx 0.2$ s
cyclotron	$\nu_c \approx 150.0$ GHz	$\gamma_c^{-1} \approx 5$ s
spin	$\nu_s \approx 150.2$ GHz	$\gamma_s^{-1} \approx 2$ yr

Table 2.2: Trap frequencies for the parameters listed in Table 2.1. The magnetron and spin damping rates are calculated from radiative decay and are too small to measure. The axial damping rate reflects its coupling to a detection circuit and not the free-space radiative damping, which has a timescale of days. The cyclotron decay time is controlled by tuning the cyclotron frequency relative to the radiation modes of the trap cavity, greatly altering its 90 ms free-space value.

In free-space, a magnetic field, B, determines the cyclotron and spin frequencies, given by

$$\nu_c = \frac{1}{2\pi}\frac{eB}{m} \tag{2.6}$$

$$\nu_s = 2\mu B/h = \frac{g}{2}\nu_c, \tag{2.7}$$

where Eq. 2.7 uses the definition of the electron magnetic moment given in Eq. 1.1. The electrostatic quadrupole leaves the spin degree of freedom unchanged but separates the radial motion into two degrees of freedom with frequencies given by [84]

$$\nu_\pm = \frac{1}{2}\left(\nu_c \pm \sqrt{\nu_c^2 - 2\nu_z^2}\right), \tag{2.8}$$

which are a slightly modified cyclotron frequency and the aforementioned magnetron frequency

$$\nu_c' = \nu_c - \nu_m \tag{2.9}$$

$$\nu_m = \frac{\nu_z^2}{2\nu_c'}. \tag{2.10}$$

Of the four electron degrees of freedom, only the cyclotron motion has a natural damping rate at an experimentally-relevant timescale. Cyclotron motion decays through synchrotron radiation with a free-space rate of

$$\gamma_c = \frac{1}{4\pi\epsilon_0}\frac{4e^2\omega_c^2}{3mc^3}, \tag{2.11}$$

which is around 90 ms for a typical cyclotron frequency. As discussed in Chapter 5, we use the electromagnetic modes of the trap cavity to alter this rate by controlling the density of states into which the cyclotron motion can radiate. By tuning the cyclotron frequency between mode frequencies, for example, we can inhibit spontaneous emission by factors of over 100, producing lifetimes of excited cyclotron states that exceed 10 s. We also alter the free-space damping rate of the axial motion with a resonant detection circuit and feedback (Section 2.3.3 and Section 2.4).

2.1.2 The Brown–Gabrielse invariance theorem

The discussion thus far has assumed an ideal Penning trap with a quadrupole described exactly by $V \sim 2z^2 - \rho^2$ and perfectly aligned with the magnetic field. A real trap will have some misalignments of the electrodes, both with the magnetic field and with each other, as well as machining imperfections. After relaxing some of these assumptions and examining a trap whose quadrupole is elliptical and misaligned with respect to the magnetic field, Brown and Gabrielse derived an invariance theorem in which the free-space cyclotron frequency can be expressed in terms of the measured eigenfrequencies of the trap (here denoted with bars), irrespective of the degree of ellipticity or misalignment [90], [84, Sec. II.D]:

$$\nu_c^2 = \bar{\nu}_c^2 + \bar{\nu}_z^2 + \bar{\nu}_m^2. \tag{2.12}$$

In addition, for a well-spaced hierarchy of trap frequencies,

$$\bar{\nu}_c^2 \gg \bar{\nu}_z^2 \gg \bar{\nu}_m^2, \tag{2.13}$$

the free-space cyclotron frequency may be approximated as

$$\nu_c = \bar{\nu}_c + \frac{\bar{\nu}_z^2}{2\bar{\nu}_c} \tag{2.14}$$

with relative corrections of the order $(\bar{\nu}_z/\bar{\nu}_c)^4 \approx 10^{-12}$ times the square of the misalignment or ellipticity $\approx (10^{-2})^2$. While Eq. 2.14 is strikingly similar to Eq. 2.9, it is important to recognize the underlying hierarchy assumption, which may not be satisfied in cases such as trapped ions. For a single electron, however, it relieves us of the necessity of a precision measurement of the magnetron frequency.

2.2 Cooling to the Cyclotron Ground State

In order to perform single-quantum-jump spectroscopy, we must cool the electron cyclotron motion to its ground state. Since that motion is coupled radiatively to the trap electrodes, we simply cool the electrodes far below the energy spacing between cyclotron levels, $h\nu_c/k_B \approx 7.2$ K. Removing the blackbody photons from that part of the spectrum reduces the average cyclotron occupation number, $\langle n \rangle$. Mounting the electrodes on a dilution refrigerator running at 100 mK cuts $\langle n \rangle$ to 10^{-32}, a level at which we would expect thermal cyclotron excitations to be spaced by times longer than the age of the universe.

Fig. 2.3 is a diagram of the assembled apparatus. The superconducting solenoid is entirely self-contained, with a bore that can operate from room temperature down to

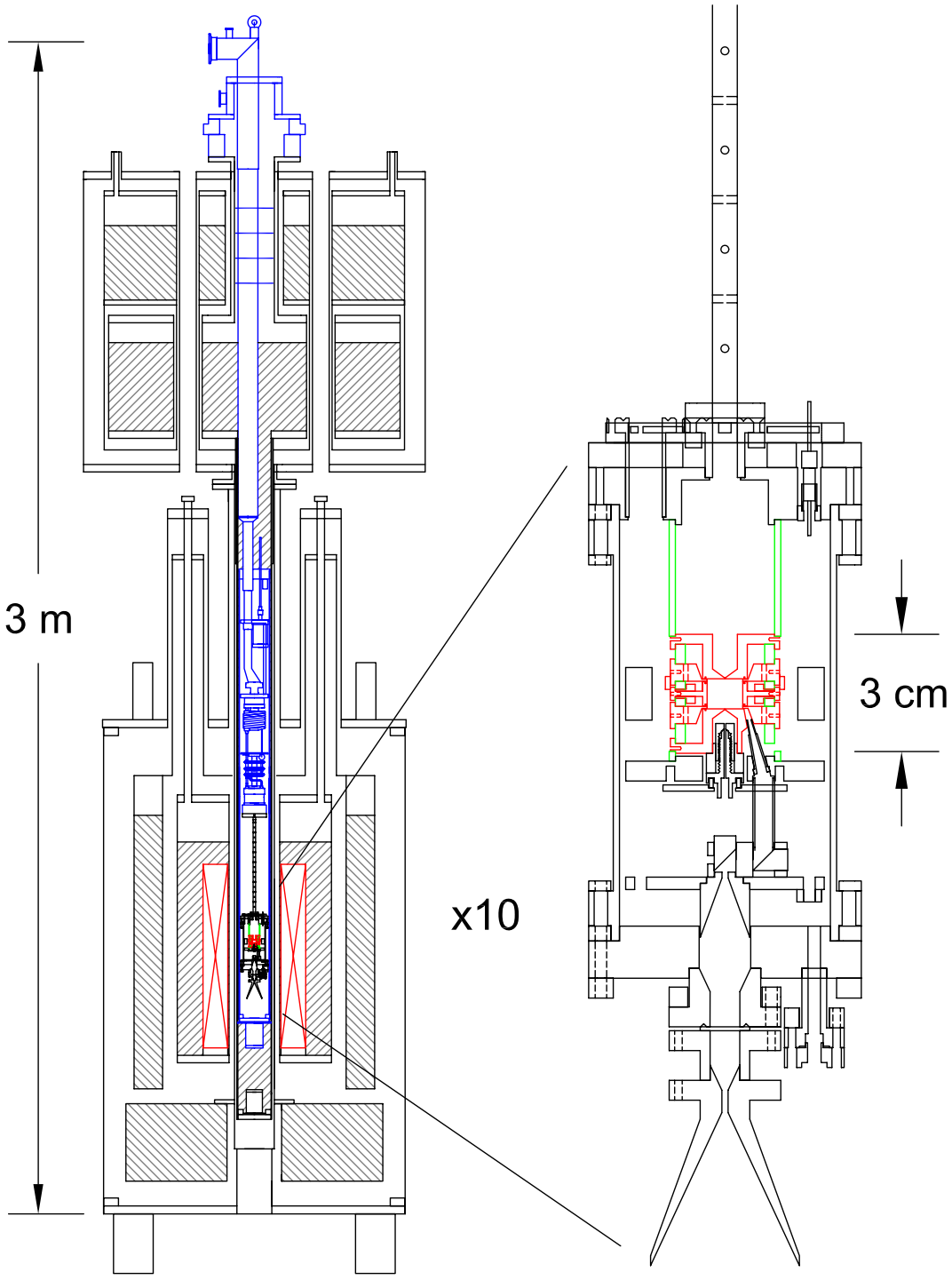

Figure 2.3: The entire apparatus

77 K. It possesses shim coils capable of creating a field homogeneity better than a part in 10^8 over a 1 cm^3 volume and has a special "shield" coil that reduces fluctuations in the ambient magnetic field by over 150 (see Section 3.1 and [91]). When properly energized, it achieves field stability better than a part in 10^9 per hour, and we regularly observe drifts below 10^{-9} per night.

The trap electrodes are mounted in thermal contact with the mixing chamber of a custom-designed Oxford Instruments Kelvinox 300 dilution refrigerator. They are housed within a separate vacuum enclosure that is entirely at the base temperature. Measurements on an apparatus with a similar design but at 4.2 K found the vacuum in the enclosure to be better than 5×10^{-17} torr [92]; our lower temperature should further reduce any background gas, allowing the retention of the same electron indefinitely. Sitting atop the magnet is a large bath of liquid helium with a tail to lower the bore temperature to 4.2 K and a 115 L volume that allows continuous operation of the refrigerator with five to seven days between liquid helium fills.

2.3 Interacting with the Electron

2.3.1 Biasing the electrodes

To ensure stability of the axial frequency, we take great care with all connections to the electrodes. Floating supplies source all DC biases on twisted pairs, which pass through numerous LC and RC filters to eliminate any noise that might heat the axial motion. In order to avoid ground loops, all ground connections are made on the trap vacuum enclosure's top flange, the pinbase, which contains the electrical feedthroughs

into the enclosure. Fig. 2.4 contains the overall wiring diagram for the trap electrodes.

As mentioned above, the typical bias configuration minimizes the number of power supplies by keeping the endcaps grounded and raising the ring to approximately 100 V. Since the axial frequency goes as the square root of the trapping potential (Eq. 2.1), the relative voltage stability need only be half the desired frequency stability. In order to keep the 200 MHz axial frequency stable to within the 1 Hz axial line width, we require voltage stability at the 10 ppb level (1 μV). Our primary voltage source is a Fluke 5720A voltage calibrator, which has a specified stability of 500 ppb over 24 hours. The Fluke charges a 10 μF metalized polypropylene film capacitor, which is kept at the refrigerator's base temperature and provides the short-term stability for the axial potential. Along with the capacitor, two resistors form a large RC filter (time constant over 15 min); a 1 MΩ resistor is at 100 mK and a 100 MΩ resistor is at room temperature so it can be bypassed for quick voltage changes. We monitor the ring voltage through the axial frequency and actively adjust the bias by charge-pumping the capacitor with 50 ms pulses from a BiasDAC [93], a low-drift, computer-controlled digital to analog converter (DAC) that is manufactured in-house at the Harvard Electronics Instruments Design Lab. Normally at 0 V except during the pulse, the BiasDAC voltage is stacked on top of the Fluke output, which is updated after the charge-pump to maintain long-term stability. Because of the large resistances in the ring RC filter, any leakage resistance must be eliminated or it will form a voltage divider with the 100 MΩ resistor.

With an orthogonalized trap configuration, the compensation electrode potentials are important for making the trap harmonic, but their affect on the axial frequency is

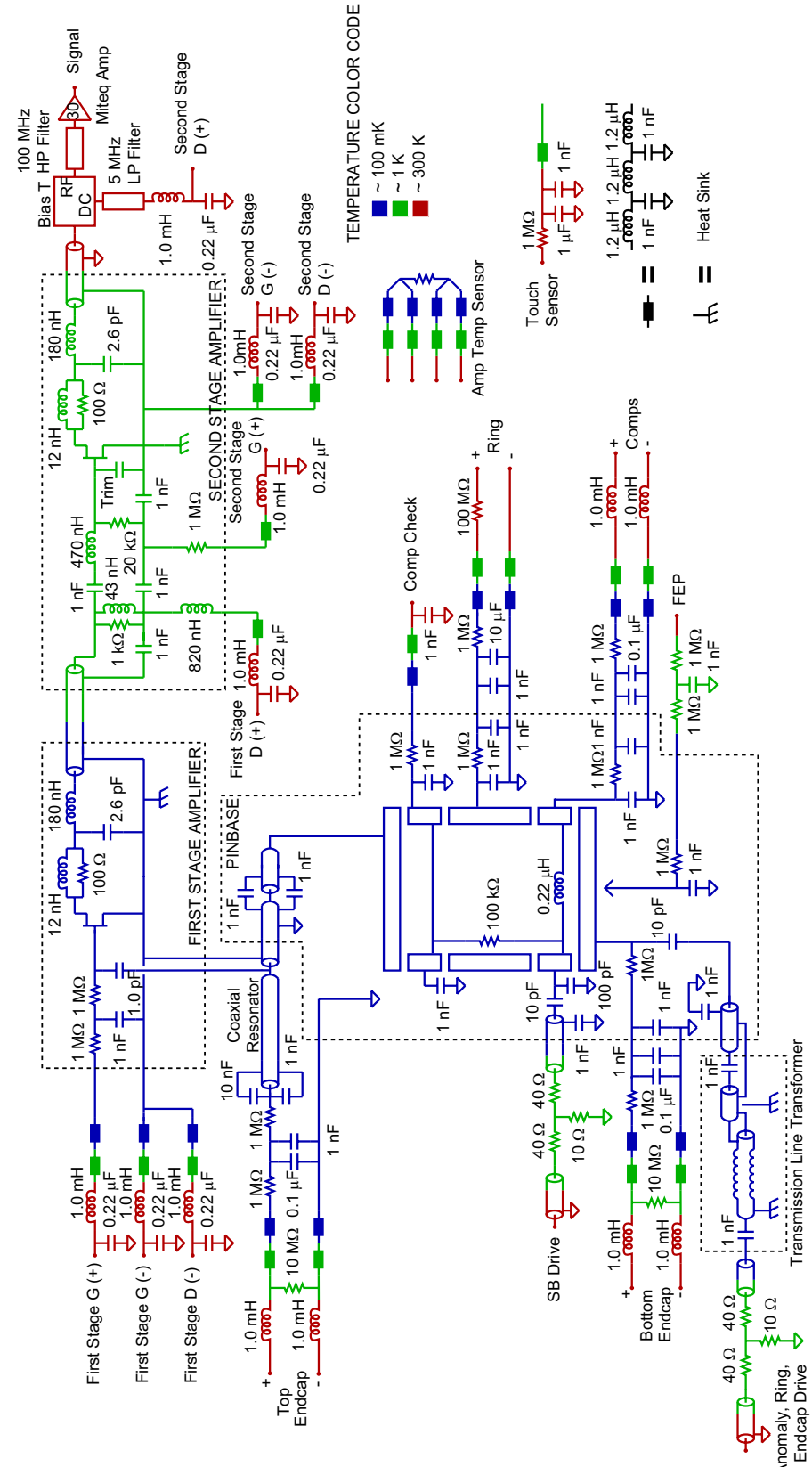

Figure 2.4: Trap electrode wiring diagram

small, reducing their stability requirement. With the measured frequency dependence of -2.00 Hz/mV, they need only be stable to 500 μV out of 74 V (7 ppm). To bias the compensation electrodes, we stack three BiasDAC channels on top of the Fluke output, providing a range for $V_{\rm comp}$ of within 50 V above or below V_R.

While the endcaps are normally grounded, we raise their potential above the ring's whenever removing electrons from the trap in order to prevent hysteretic effects in the ring's 10 μF capacitor. The endcap bias filters have shorter time constants (100 ms) than the ring's to allow for rapid changes of the axial potential. For example, an equal bias on each endcap allows detuning of the axial frequency from the tuned circuit resonance to decrease the axial damping rate. We have found that hysteresis in the endcap capacitors during rapid detuning can be overcome by briefly overcompensating upon retuning. For example, when switching from the endcaps detuned at $-0.1\ V_R$ to the endcaps grounded, one might spend 0.5 s at $0.1\ V_R$. The actual magnitude and length of this pre-retune bias is determined by trial and error. The detuning and retuning is done via relay[2] so that the endcaps can be retuned simply by shorting them to ground.

Oppositely biasing each endcap offsets the potential minimum and moves the electron along the axis of the trap. A pair of 10 MΩ resistors, with resistances matched to better than 500 ppm at 4.2 K, facilitates an antisymmetric bias by allowing a single potential, V_A, to be applied between the "high" leads of each electrode, while the "low" leads are left unconnected, forcing the same current to flow through both resistors, which are grounded at the pinbase (see Fig. 2.5). This current sets the endcap biases of $\pm V_A/2$; since the resistors are well-matched, any noise in V_A affects

[2]Coto Technology reed relay, P/N 3501-05-511

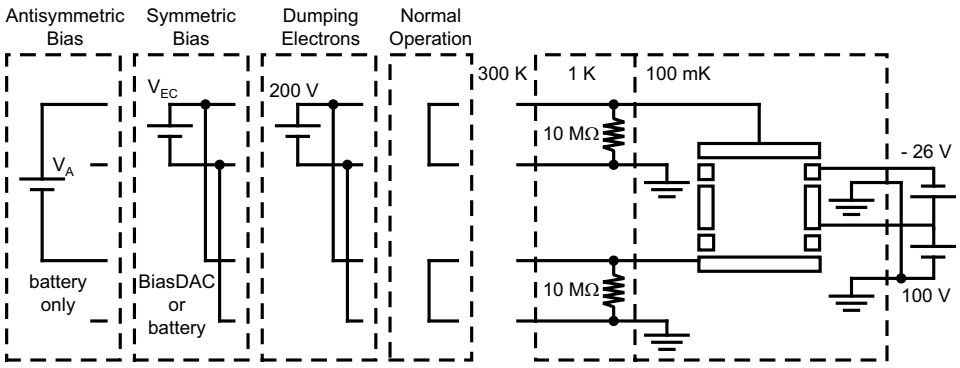

Figure 2.5: Typical bias configurations for the top and bottom endcaps. For simplicity, only components affecting DC operation are shown. The complete wiring schematic is shown in Fig. 2.4

both electrode biases, yielding a more stable potential than if each had its own voltage source. We typically source V_A with a battery because the BiasDAC "low" is isolated from ground by a 1 MΩ resistor and not truly floating.

The electrostatic potential of an antisymmetric bias my be expanded in a manner similar to Eq. 2.3 [87, 84]:

$$V = \frac{V_A}{2} \sum_{\substack{k=1 \\ \text{odd}}}^{\infty} c_k \left(\frac{r}{z_0}\right)^k P_k(\cos\theta). \tag{2.15}$$

There is a similar expansion for an antisymmetric potential applied to the compensation electrodes, but we do not use that configuration in this work. To first order, the shifted potential minimum, z_e, is given by [87, 84]

$$\frac{z_e}{z_0} = \frac{1}{2}\left(\frac{d}{z_0}\right)^2 \left(\frac{V_A}{V_R}\right) c_1 \frac{1}{1+C_2}. \tag{2.16}$$

The altered electrostatic potential shifts the axial frequency, given by [87, 84]

$$\frac{\Delta\nu_z}{\nu_z} = -\frac{3}{4}\left(\frac{d}{z_0}\right)^4 \frac{c_1 c_3}{(1+C_2)^2} \left(\frac{V_A}{V_R}\right)^2. \tag{2.17}$$

2.3.2 Driving the axial motion

Driving the electron at radio frequencies is accomplished by modulating the electrode potentials. We wish to avoid any perturbation to the ring potential and we use the top endcap electrode for detection (see the next section), so we apply most rf drives to the bottom endcap. One may write a bottom endcap modulation of magnitude V_D and frequency ω_D as the sum of two modulations applied to both endcaps: a symmetric drive, $-V_D\cos(\omega_D t)/2$, and an antisymmetric drive, $V_D\cos(\omega_D t)$ (these cancel at the top endcap). The antisymmetric drive produces the potential of Eq. 2.15 near the trap center. In particular, it creates an oscillating electric field that, for $\omega_D \approx \omega_z$, is capable of driving the axial motion directly.

The symmetric drive adds a modulation to the axial potential, which has a time-dependent depth of $V_R + V_D\cos(\omega_D t)/2$. When substituted for V_R in Eq. 2.1, the axial frequency becomes time-dependent,

$$\omega_z^2 \to \omega_z^2\left(1+\frac{V_D}{2V_R}\cos(\omega_D t)\right) = \omega_z^2\left(1+h\cos(\omega_D t)\right), \tag{2.18}$$

where we have introduced a dimensionless frequency modulation strength $h \equiv V_D/(2V_R)$. We have used such frequency modulation in two ways. First, a slow drive with $\omega_D \ll \omega_z$ produces sidebands at $\omega_z \pm \omega_D$, and driving at one of these sidebands can excite the axial motion. This slow modulation technique is one way to avoid an axial drive feeding through to the top-endcap detection circuit because one can arrange the sideband to be far from the circuit resonance. Second, a strong modulation at $\omega_D \approx 2\omega_z$ can excite a parametric resonance displaying a wealth of phenomena including threshold energies and spontaneous symmetry breaking; we explore this technique further in Section 5.2.

The drive signals are carried from room temperature to the electrodes via 50 Ω semi-rigid coaxial transmission lines, which are heat-sunk at several temperatures to reduce the heat load on the dilution refrigerator. To avoid heating the axial motion with room-temperature 50 Ω Johnson noise, we include 20 dB attenuators at 1 K (see Fig. 2.4). A transmission-line transformer ensures that the center conductor is well heat-sunk.

2.3.3 Detecting the axial motion

The axial motion is the only degree of freedom that we detect directly. At 200 MHz, it lies in the radio-frequency (rf) range, which is more experimentally accessible than the microwave (sometimes called millimeter-wave) range of the 150 GHz cyclotron and spin frequencies. Nevertheless, the standard rf techniques must be carefully tailored for our low-noise, cryogenic experiment. The electron axial oscillations induce image currents in the trap endcaps. We send this current through an effective resistor, damping the motion and creating a voltage signal that we amplify with two single-transistor cryogenic amplifiers.

The current, I, induced in the endcap electrodes is proportional to the electron velocity, $\dot{z}$ [84, Sec. III],

$$I = \frac{ec_1}{2z_0}\dot{z}, \tag{2.19}$$

where c_1, often called κ in this context, is the same antisymmetric expansion coefficient seen in Eq. 2.15. An effective resistance, R, arises from intrinsic losses in an LC circuit that is tuned to resonate at the axial frequency and composed of the capacitance between trap electrodes, C, and a home-made inductor, L, which is connected

to the top endcap. The losses in the inductor give the LC circuit a finite Q. On resonance, the inductor and capacitor reactances cancel, and the circuit has a purely resistive impedance of magnitude [94, Ch. 2]

$$R = \frac{Q}{\omega_z C} = Q\omega_z L. \tag{2.20}$$

Since the electron signal is the voltage $V = IR$ and the primary noise source, Johnson noise, only goes as $R^{1/2}$, increasing the circuit Q increases the signal-to-noise. Dissipation of the image currents in the tuned circuit resistance damps the electron axial motion at a rate [84, Sec. III]

$$\gamma_z = \left(\frac{ec_1}{2z_0}\right)^2 \frac{R}{m}. \tag{2.21}$$

In our first-stage amplifier, whose input network is the LC circuit above, the 200 MHz axial frequency and 13 pF trap capacitance would require a traditional inductor coil of a turn or two, a design incompatible with our tunability and high-Q requirements. Instead, we use the distributed inductance of a coaxial transmission line less than a quarter-wavelength long. The Q of the tuned circuit is around 600. The signal is amplified by a single-gate high electron mobility transistor (HEMT).[3] The HEMT output impedance is matched to a 50 Ω transmission line via a "π-network" and a resistor and inductor in parallel form a suppression circuit to add loss at high frequencies. (The amplifier schematics appear in Fig. 2.4 and complete details may be found in [89, Ch. 4].) In order to avoid feedback in the amplifier, it is crucial that the input network be tuned slightly above the output network resonance.

Two other crucial features of our first-stage amplifier relate to its cryogenic environment. First, since the dilution refrigerator can tolerate a heat-load of only 50 μW

[3] Fujitsu FHX13LG

at 100 mK, the HEMT is operated three orders of magnitude below its 10 mW intended power output. Second, the HEMT must be reliably heat-sunk because the coupling of the electron and the tuned circuit keeps the electron in thermal equilibrium with the amplifier. Our precision measurements require the axial temperature to rapidly cool when the amplifier is turned off. In practice, the HEMT is heat-sunk using indium/tin solder to directly connect a source lead to a large block of silver, which is mounted on the silver tripod that hangs below the mixing chamber.

A second-stage cryogenic amplifier, mounted on the refrigerator still, counteracts the attenuation of the thermally-isolating but lossy stainless steel transmission lines and boosts the signal above the noise floor of the first room-temperature amplifier. Its design is conceptually similar to that of the first-stage amplifier, though the second-stage input network uses surface-mount components and has a correspondingly lower Q and higher bandwidth. The still can handle a much higher heat-load, and we typically dissipate 250 μW with the second-stage amplifier.

At room temperature, immediately after exiting the refrigerator's inner vacuum chamber but still within an rf-shielded box, the signal passes through a bias-T (to allow the second-stage drain to be biased down the signal line), a 100 MHz high-pass filter, and a commercial broadband amplifier.[4] It then follows the detection chain pictured in Fig. 2.6, passing through additional stages of broadband amplification with the bandwidth restricted via commercial filters[5] and a home-made filter with a 2 MHz bandwidth. For easy detection via a signal analyzer[6] or data acquisition card,[7]

[4]Miteq AU-2A-0110-BNC
[5]Mini-Circuits BHP-200 and BLP-200
[6]HP 3561A
[7]National Instruments PCI-4454

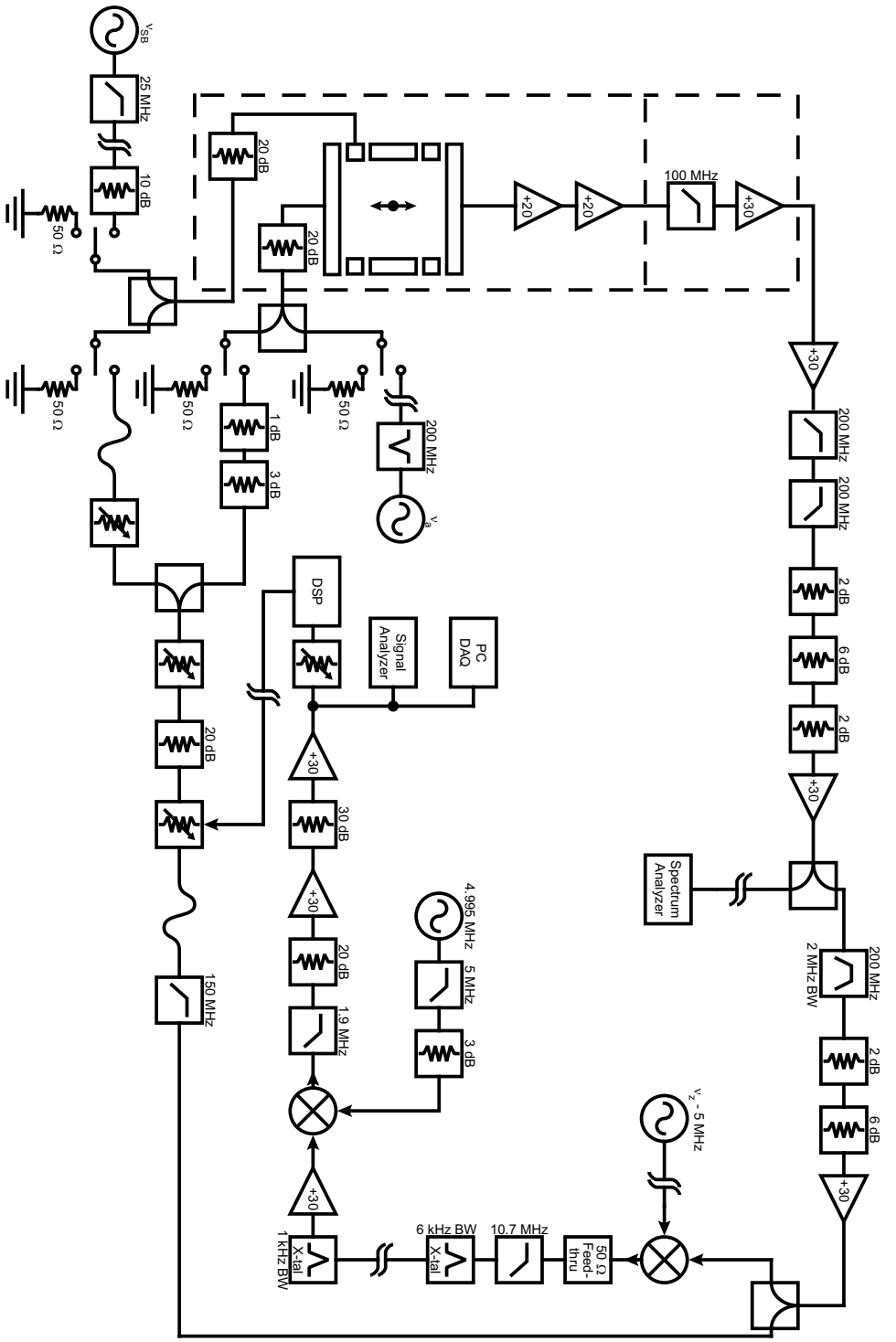

Figure 2.6: Radiofrequency detection and excitation schematic. Detailed schematics for the components within the dashed lines may be found in Fig. 2.4.

the 200 MHz signal is mixed down twice: first with a local oscillator[8] at $\nu_z - 5$ MHz and then with a local oscillator[9] at 4.995 MHz to a final frequency of 5 kHz.

In order to produce a detectable signal, the electron must be driven high above its thermal amplitude. Indeed, driven by the tuned circuit's Johnson noise alone, the electron appears on the amplifier resonance as a dip of width γ_z [95, 84]. In the past, axial excitation has been created by modulating the potential on the bottom endcap with an independent oscillator that also serves as a reference in a phase-sensitive detection scheme, see e.g., [84, 96]. We now use the electron itself as the oscillator, feeding the detected signal back as a drive [88]. This self-excited oscillator allows us to get much larger signal-to-noise and is discussed separately in Section 2.4. With either excitation scheme, it is important to avoid the feedthrough that arises when the first-stage amplifier picks up the drive and saturates. This can be eliminated by simultaneously driving two electrodes, e.g., the bottom endcap and a compensation electrode, with their relative amplitudes and phases adjusted to destructively interfere at the top endcap. Alternately, we have applied a slow modulation, e.g., 5 MHz, to the bottom endcap, allowing us to drive the axial motion at the sideband $\nu_z - 5$ MHz, far enough away from the amplifier resonance to decrease the feedthrough. In order to control the application and removal of the drives, all rf lines have switches[10] that may be toggled via software[11] or a timing pulse.

[8] Programmed Test Sources PTS-250
[9] SRS DS345
[10] HP 8765A
[11] Using an HP 87130A switch driver

2.3.4 QND detection of cyclotron and spin states

Since the cyclotron and spin frequencies are too high for practical direct observation, we apply a weak perturbation to the magnetic field that couples these states to the axial potential. Called a "magnetic bottle," a pair of nickel rings, shown in Fig. 2.2, saturate in the magnetic field with magnetization $\mu_0 M_{\mathrm{Ni}}/(4\pi) = 0.0485$ T [84]. To lowest order, the rings offset the magnetic field by approximately -0.7%. This is important when comparing NMR measurements of B with those from the electron cyclotron frequency, but for our present purposes it merely redefines the magnetic field strength. More important is the next-order perturbation; for a bias field $\mathbf{B} \parallel \hat{\mathbf{z}}$, it is [84, Sec. VI]

$$\mathbf{B}' = B_2 \left[\left(z^2 + \rho^2/2 \right) \hat{\mathbf{z}} - z\rho\hat{\boldsymbol{\rho}} \right], \tag{2.22}$$

with B_2 calculated to be 1474(31) T/m^2 and measured to be 1540(20) T/m^2 (Fig. 2.7). A different magnetic bottle of nominally identical geometry was measured to have $B_2 = 1539(12)$ T/m^2 [96, Sec. 4.1]. The disagreement between calculated and measured values suggests that the magnetization number above, M_{Ni}, may be off by a few percent. High-precision knowledge of B_2 is not required for our measurement.

The perturbation from the magnetic bottle alters the axial potential, making it dependent on the total electron magnetic moment:

$$H_z' = -\boldsymbol{\mu} \cdot \mathbf{B}'. \tag{2.23}$$

Since the electron is always near the center of the trap and its magnetic moment is always parallel to the bias field, we can set $\rho = 0$ and $\boldsymbol{\mu} \parallel \hat{\mathbf{z}}$ to get

$$H_z' = B_2 \mu_B z^2 \left(2n + 1 + g m_s \right), \tag{2.24}$$

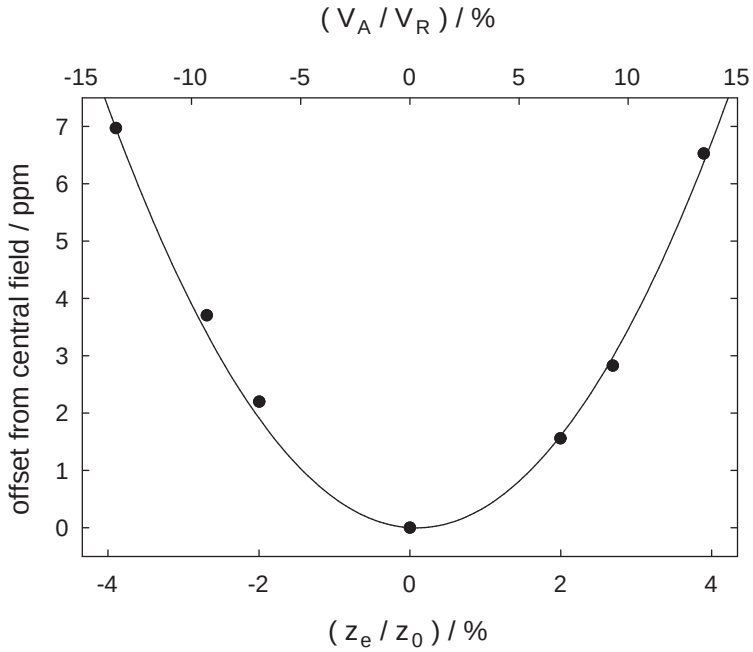

Figure 2.7: Displacing the electron axially shows the field of the magnetic bottle.

where the magnetic moment has been written in terms of the Bohr magneton and the orbital (from cyclotron motion) and intrinsic (from spin) quantum numbers $n = 0, 1, 2, \ldots$ and $m_s = \pm 1/2$; we have neglected a small contribution from the magnetron motion. The total axial potential is thus

$$H_z = \frac{1}{2} m\omega_{z0}^2 z^2 + 2B_2\mu_B z^2 \left(n + \frac{1}{2} + \frac{g}{2} m_s \right), \tag{2.25}$$

where ω_{z0} is 2π times the axial frequency in Eq. 2.1. Thus the axial frequency depends on the cyclotron and spin states, shifting from its bottle-free value by

$$\frac{\Delta\nu_z}{\nu_z} = \frac{2B_2\mu_B \left(n + \frac{1}{2} + \frac{g}{2} m_s \right)}{m\omega_{z0}^2} \approx 2 \times 10^{-8} \left(n + \frac{1}{2} + \frac{g}{2} m_s \right), \tag{2.26}$$

where we have made the assumption that $B_2\mu_B / \left(m\omega_{z0}^2 \right) \approx 10^{-8} \ll 1$. A cyclotron jump ($\Delta n = 1$) or a spin flip ($\Delta m_s = 1$) shifts the axial frequency by 20 ppb, about

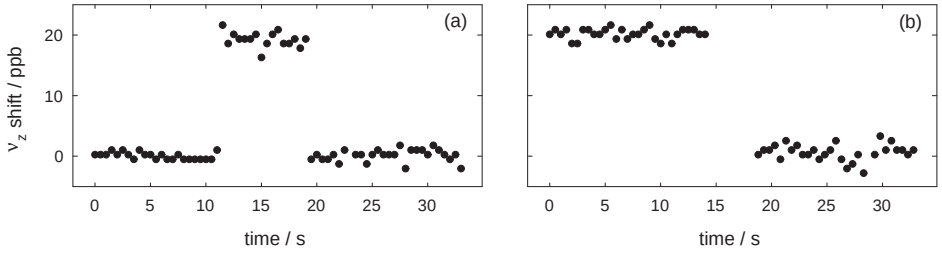

Figure 2.8: Two quantum leaps: A cyclotron jump (a) and spin flip (b) measured in a QND manner through shifts in the axial frequency.

4 Hz, as seen in Fig. 2.8. The shifts are different by the part-per-thousand difference between g and 2, but we cannot currently resolve the axial frequency to the 4 mHz level. In addition to coupling the axial frequency to the cyclotron and spin energies, the magnetic bottle couples the cyclotron and spin frequencies to the axial energy, at topic explored in detail in Section 4.2.

The perturbation Hamiltonian of Eq. 2.24 formally commutes with the cyclotron and spin Hamiltonians, so the determination of the cyclotron and spin states via the axial frequency is a quantum nondemolition (QND) measurement. In practice, this means that observing ν_z does not destroy the state $|n, m_s\rangle$, and repeated measurements of the cyclotron and spin states will return the same value unless they are altered through other means, e.g., a cyclotron drive or spontaneous emission.

2.3.5 Making cyclotron jumps

The cyclotron motion, with its frequency nearly a thousand times that of ν_z, cannot be driven with rf techniques like modulating the trapping potential because the coaxial lines would attenuate the drive to nothing. Instead, we use a semi-optical setup, depicted in Fig. 2.9, in which electromagnetic radiation travels through

waveguides and is broadcast between microwave horns mounted at room and base temperatures, focused by teflon lenses.

A drive at ν_c begins in an Agilent E8251A Performance Signal Generator (PSG) as $\nu_c/10 \approx 15$ GHz. The PSG was purchased with a special low-phase-noise, 10 MHz oven-controlled crystal oscillator (OCXO) that serves as the timebase for all frequency synthesizers in the experiment.[12] It can also perform amplitude, frequency, and phase modulation and has a pulse function that is useful for ensuring uniformity of cyclotron drive lengths. After exiting the PSG, the 15 GHz travels to a microwave circuit mounted beneath the magnet, passing along the way through a section of waveguide that removes all subharmonics.

In the circuit, manufactured by ELVA-1 Millimeter Wave Division, an impact ionization avalanche transit-time (IMPATT) diode multiplies the frequency by ten and outputs the ν_c drive at a power of 2 mW. The IMPATT diode was chosen for its high-power capabilities, which are required for attempts to drive the sidebands of the cyclotron frequency (Chapter 7). A direct cyclotron excitation, however, takes a single photon, so the power must be much lower. In order to allow rapid switching between high and low power, we have several voltage-controlled attenuators in the waveguide; each pair can nominally attenuate 100 dB, and we have at various times included one or two pairs. At this level of attenuation, however, the amount of power leaking through waveguide flanges and elsewhere becomes significant. To plug these leaks, we use carbon-loaded foam, which attenuates at 150 GHz due to its

[12]Since our measurement goal is a frequency ratio, we need not trace our timebase to the SI cesium second but we must still refer all frequencies to a common standard. To aid us in this task, we use a Spectra Dynamics (SDI) distribution amplifier, P/N HPDA-15RM/A, which distributes the 10 MHz clock on isolated channels with minimal additional noise.

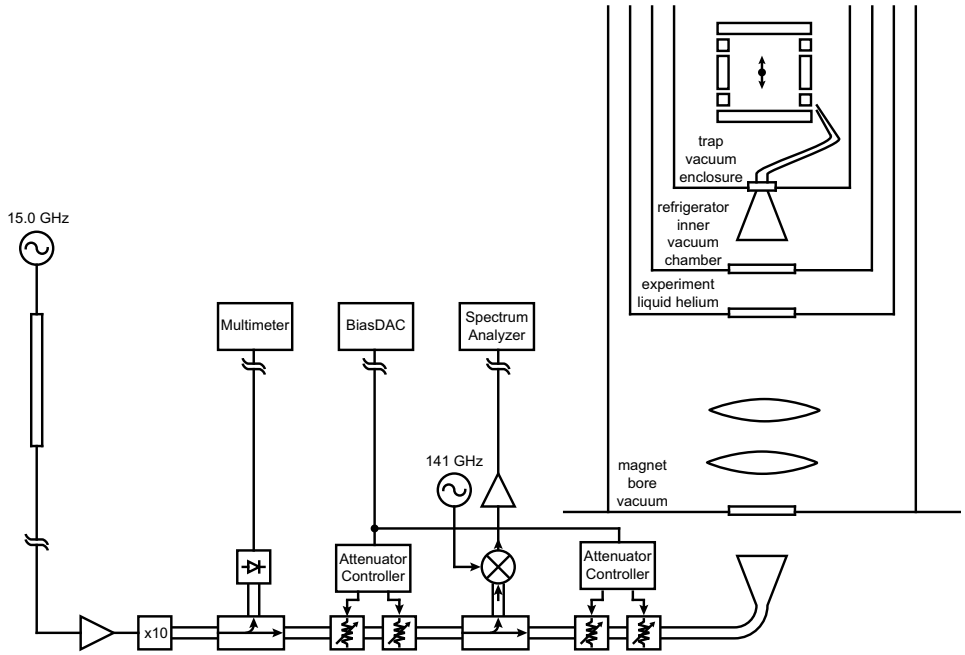

Figure 2.9: The microwave system. The transmission lines are a combination of cables (single lines) and waveguides (double lines) and long runs between the experiment and the electronics rack are indicated by a break.

high resistivity. Quarter-inch thick sheets from Cuming Microwave Corp.[13] stuck directly on the multiplier and other components are particularly useful, though we also employ large panels from Emerson & Cuming Microwave Products Inc.[14] to arrest any reflections from nearby materials.

We monitor the microwave power level on a diode immediately after the multiplier. The system is also equipped with a 141 GHz oscillator and frequency mixer to allow monitoring the significantly lower power after the first pair of attenuators. In practice, the 141 GHz oscillator has not proved stable enough for routine use.

The drive exits the multiplier assembly via a horn, which broadcasts the signal through a window into the magnet bore vacuum. There, several teflon lenses focus

[13]C-RAM MT 26 / PSA
[14]ECCOSORB CV-3, unpainted

it through a window in the tail of the experiment liquid helium dewar. The signal travels through the liquid helium into the refrigerator's inner vacuum chamber and is guided by another horn into a waveguide and finally into the trap electrode cavity. The last portions of this path can be seen in Fig. 2.3 and Fig. 2.2. Based on the nominal 2 mW multiplier output and the ability of a full-strength drive to heat the mixing chamber by tens of microwatts, the drive reaching the low-temperature horn is attenuated by roughly 20 dB.

The amount that actually makes it into the trap electrodes is much harder to quantify and likely to be significantly lower. As mentioned in Section 2.1 and discussed fully in Chapter 5, the trap electrodes themselves form an important part of this microwave circuit. They are designed to be a high-Q microwave resonator, including such features as $\lambda/4$ choke-flanges at the gaps between electrodes to reflect leaking power back into the cavity. Since we typically operate at cyclotron frequencies between cavity modes, one would expect most of the drive power to be reflected.

The main limitation of our current g-value measurement lies in our model of the cyclotron and anomaly lines, which appear slightly blurred compared to their expected shape (Section 4.2). We model the blurring as magnetic field noise, but phase noise on the drive could cause the same effect. Calculations of the expected frequency deviations based on the signal generator's specified phase noise and additional noise from an ideal multiplier, see e.g., [97], suggest they should be over two orders of magnitude below the level required to explain the blurring. In addition, our prior measurements [1] saw a similar broadening using different microwave systems [98, Sec. 2.6] and [83, Sec. 2.3], including a GaAs-Schottky-barrier-diode-based harmonic

mixer as the frequency multiplier, suggesting that any noise is not from the cyclotron drive itself.

2.3.6 Flipping the spin

As mentioned in the experimental overview (Section 1.2), we achieve greater precision by measuring the electron anomaly frequency directly rather than measuring the thousand-times larger spin frequency. This simultaneous spin-flip and cyclotron jump is driven with an oscillating transverse magnetic field near the center of the trap. Since the electron radius vector, $\boldsymbol{\rho}$, is changing direction at the trap cyclotron eigenfrequency, $\bar{\nu}_c$, the combination of transverse drive and cyclotron motion produces beat frequencies at $\bar{\nu}_c$ plus and minus the drive frequency. The spin flips when the beat frequency equals the spin frequency,

$$\nu_s = \bar{\nu}_c + \bar{\nu}_a, \tag{2.27}$$

where $\bar{\nu}_a$ is the anomaly frequency measured in the Penning trap. It is related to the free-space anomaly frequency through

$$\bar{\nu}_a = \nu_s - \bar{\nu}_c = \nu_s - \nu_c + \frac{\bar{\nu}_z^2}{2\bar{\nu}_c} = \nu_a + \frac{\bar{\nu}_z^2}{2\bar{\nu}_c} \tag{2.28}$$

$$\nu_a = \bar{\nu}_a - \frac{\bar{\nu}_z^2}{2\bar{\nu}_c}, \tag{2.29}$$

where we have used the approximation for $\bar{\nu}_c$ of Eq. 2.14.

There are two standard methods for producing the transverse magnetic drive, see e.g., [99, 81]. The first, which we do not use, splits the compensation electrodes in half and drives the four halves with relative phases such that they form two effective current loops producing the desired field. The second drives the electron axially

through the $z\rho\hat{\boldsymbol{\rho}}$ portion of the magnetic-bottle gradient, producing the required oscillating radial field. Although we have split our compensation electrodes in half for other purposes (see Section 2.3.7), we have solely used the bottle technique.

In the paper for their famous 1987 g-value measurement [2], Van Dyck, Schwinberg, and Dehmelt describe the superiority of the electrode current-loop method over the bottle-driven method, which was limited by the size drive they could apply before the increased liquid helium boil-off caused instabilities [99]. Our dilution refrigerator restricts us to even lower powers; nevertheless, we use the bottle-driven method because our axial frequency is closer to ν_a, allowing an 8 dB weaker drive to achieve the same transition rates, and our over-ten-times-lower axial temperature narrows the anomaly line, decreasing the required drive power by an additional 20 dB.

2.3.7 "Cooling" the magnetron motion

Other than as a correction factor between the cyclotron and anomaly frequencies in the trap and in free space, we have thus far ignored the magnetron frequency. With its slow speed and long damping time, it plays little role in our measurement provided its radius is negligibly small. Because an arbitrarily loaded electron will have some finite magnetron radius and because various perturbations damp the motion, increasing the radius, we need a method to add energy to the magnetron degree of freedom to reduce its radius (it is unbound, so reducing the radius corresponds to adding energy). This "cooling" is accomplished by coupling the magnetron motion to the axial motion through a spatially inhomogeneous drive at their sum frequency [84, Sec. IV]. Using half of a split compensation electrode, the drive at $\bar{\nu}_z + \bar{\nu}_m$ creates an

xz-gradient in the electric potential at the trap center. The cooling continues until the temperature ratio is equal in magnitude to the frequency ratio,

$$\frac{T_m}{T_z} = -\frac{\nu_m}{\nu_z}, \tag{2.30}$$

or, equivalently, until their thermally averaged quantum numbers are equal. The sideband cooling increases the energy in the axial motion as well as the magnetron motion, but the former stays in thermal equilibrium with the first-stage amplifier on timescales longer than $\gamma_z^{-1} \approx 0.2$ s. The other sideband of the axial motion, $\bar{\nu}_z - \bar{\nu}_m$ increases the magnetron radius in a similar manner.

An analogous technique can couple the cyclotron motion to the axial and magnetron motions. This has the potential to reduce the axial motion to its quantum-mechanical ground state but only if it is first decoupled from the amplifier by detuning the axial frequency or physically breaking the electrical connection. Producing a drive with the required gradient at a sideband of the cyclotron frequency is challenging, and attempts at simply using a high-powered drive from the microwave system showed excitation at the sideband frequency but low cooling rates. It may be possible to use cavity modes with the appropriate geometry to build up the electromagnetic fields. These ideas are further explored in Chapter 7.

2.4 The Single-Particle Self-Excited Oscillator

Since the electron signal is proportional to its axial velocity, $\dot{z}$ (Section 2.3.3), feeding this signal back as a drive alters the axial damping rate. For a noiseless feedback loop, the fluctuation-dissipation theorem [100] relates a decreased damping

rate to lower temperature [101]. An increased feedback gain can excite the electron to large amplitudes that can be stabilized electronically. Such a self-excited oscillator (SEO) is ideal for resolving the small frequency shifts caused by cyclotron jumps and spin flips because it is always resonant and because the large amplitudes increase the signal-to-noise ratio [88].

The feedback can be analyzed by including a drive force, $F_d(t)$, in the axial equation of motion,

$$\ddot{z} + \gamma_z \dot{z} + \omega_z(A)^2 z = F_d(t)\,/m, \tag{2.31}$$

which includes the damping, γ_z, from the tuned circuit (Eq. 2.21) and the amplitude-dependent axial frequency $\omega_z(A)$ (Eq. 2.5). It is convenient to parameterize the drive force as

$$F_d(t)\,/m = G\gamma_z \dot{z} \tag{2.32}$$

so unit feedback gain ($G = 1$) corresponds to exact cancellation of the tuned circuit damping. Allowing for a relative phase ϕ between the signal and feedback drive, e.g., due to a time delay in the feedback loop, the damping cancellation occurs when [89, Sec. 6.1]

$$G\cos\phi = 1 \tag{2.33}$$

at a frequency

$$\nu(A,\phi) \approx \nu_z(A) + \frac{\gamma_z}{4\pi}\tan\phi. \tag{2.34}$$

The self-excitation frequency is a useful diagnostic for adjusting the feedback phase. For properly-tuned feedback, slowly increasing the gain above $G = 1$ will initiate self-excitation at the same frequency as the center of the dip.

Assuming a well-adjusted feedback phase, $\phi = 0$, any deviation from unit gain leads to exponential growth or decay of the axial amplitude. Since there is nothing intrinsically stable about $G = 1$, a useful SEO requires an amplitude-dependent gain $G(A)$ in order to maintain a fixed amplitude A_0. Substituting this gain into Eq. 2.31 yields

$$\dot{A} = -\frac{1}{2}\gamma_z A\left[1 - G(A)\right] \tag{2.35}$$

for the time evolution of the amplitude [102].

We regulate the feedback gain by adjusting a voltage-variable attenuator (VVA)[15] in response to amplitude deviations from A_0. The SEO amplitude is continuously monitored by a digital signal processor (DSP).[16] It reads the 5 kHz mixed-down axial signal (Section 2.3.3), calculates its discrete Fourier transform, and declares the signal amplitude to be the height of the bin with the largest magnitude. The DSP then outputs a voltage, used to control the VVA, that depends on the difference between this amplitude and the desired amplitude A_0. The effective gain is a cubic polynomial of this difference,

$$G(A) = 1 + a_1\left(A_0 - A\right) + a_2\left(A_0 - A\right)^2 + a_3\left(A_0 - A\right)^3, \tag{2.36}$$

with the polynomial coefficients, a_i, set in the DSP code. For a linear response function ($a_2 = 0 = a_3$), small deviations away from A_0 exponentially damp back. We have found that adjustments to the a_3 coefficient aid in decreasing the SEO rise time from $A = 0$ to A_0, a time that is especially important when attempting to detect cyclotron jumps with short lifetimes.

[15] Mini-Circuits RVA-2500

[16] Texas Instruments TMS320F2812

Since it ignores all Fourier transform bins except that with the highest amplitude, the DSP acts as a filter with an effective bandwidth of 8 Hz (the width of each bin) and a central frequency that tracks the axial frequency. This dynamic filtering reduces the technical noise in the feedback loop. The total usable bandwidth of the DSP depends on the number of frequency bins, limited by the physical memory and available processor time. In our current implementation, we have 64 bins, spaced at 1 Hz intervals to ensure adequate overlap for a smooth response, for a total usable bandwidth of approximately 64 Hz.

Although we have our choice of oscillation amplitude, a particularly useful one is the amplitude at which the effects of the C_4 and C_6 terms of Eq. 2.5 cancel (C_4 and C_6 are of opposite sign). At this amplitude, often exceeding a few percent of the trap height, the axial frequency is at a maximum and the oscillation is locally harmonic despite the anharmonic potential. To a high degree, the axial frequency loses its amplitude-dependence, and thermal amplitude fluctuations arising from the detection circuit no longer correspond to frequency fluctuations. Since C_4 and C_6 depend on the compensation electrode potential, the stable oscillation amplitude may be changed by adjusting V_{comp}.

The large amplitude increases the signal-to-noise ratio (S/N), which may be estimated as the ratio of the signal power, I^2R from Section 2.3.3 with $|\dot{z}| = \omega_z A$, and the noise power, derived from the Johnson noise of the amplifier acting over a bandwidth Δf:

$$S/N = \frac{P_{\mathrm{signal}}}{P_{\mathrm{noise}}} = \frac{I^2R}{4kT\Delta f} = \frac{A^2\omega_z^2\gamma_z m}{4kT\Delta f}. \tag{2.37}$$

The anticipated frequency uncertainty, $\Delta\nu$, for a given signal averaging time Δt can

be estimated from the frequency-time uncertainty principle ($\Delta\nu\,\Delta t \geq 1/(4\pi)$) and the S/N as [103, Eq. 63]

$$\Delta\nu\,\Delta t \cong \sqrt{\frac{3}{2\pi^2\,(S/N)}} = \frac{1}{\omega_z A}\sqrt{\frac{6kT\Delta f}{\gamma_z m\pi^2}}. \tag{2.38}$$

This uncertainty is a reasonable estimate for the resolution we actually observe, although the predicted increase in precision with increasing amplitude eventually breaks down as the next-order anharmonicity components to Eq. 2.5 become important.

2.5 Summary

Our quantum cyclotron allows detection of single cyclotron jumps and spin flips via a quantum nondemolition coupling to the axial frequency. Measuring the axial frequency involves specialized cryogenic amplifiers, enhanced signal from electron self-excitation, and high stability and careful filtering of all electric potentials and radio-frequency drives. Magnetic field stability is crucial to maintaining clean cyclotron and anomaly resonances and forms the topic of the next chapter.

Chapter 3

Stability

Since the cyclotron and anomaly frequencies are both proportional to magnetic field, their ratio in Eq. 1.38 is, in principle, independent of the field value. In practice, it takes several hours to measure both frequencies and any magnetic field variation on shorter timescales will add noise to the measurement. Such fluctuations could arise from changes in the ambient magnetic field, including the motion of cars and the powering of the local subway; from the solenoid itself, including flux jumps and internal stresses; from the motion of the trap electrodes in an inhomogeneous magnetic field, including apparatus vibration and expansion of the dewar under room temperature changes; or from the varying magnetic susceptibility of materials.

In this chapter, we discuss our techniques for lowering these fluctuations. We wish to keep field noise far below 1 ppb, which corresponds to 1 ppt in the g-value. Despite the efforts described in this chapter, we see noise (discussed in Chapter 4 and Chapter 6) at the 0.5–1 ppb level, and only careful systematic checks allow us to beat this noise limit in determining the resonant frequencies. We conclude the chapter by

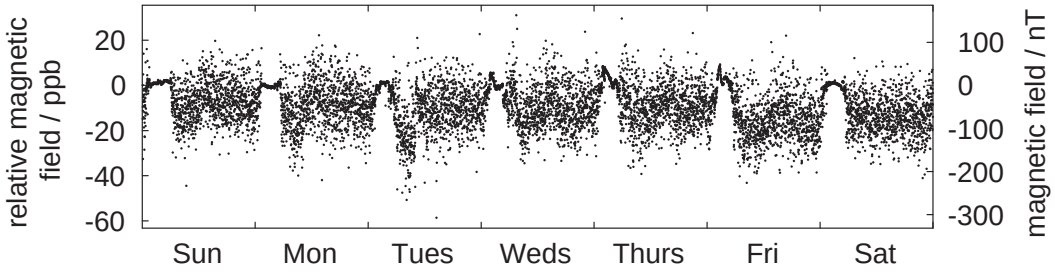

Figure 3.1: The subway effect, as measured by a flux-gate magnetometer in the lab. Were it not for our self-shielding magnet design, these 10 ppb fluctuations would limit our cyclotron and anomaly frequency resolution.

suggesting ways to further improve the field stability.

3.1 Shielding External Fluctuations

Our primary defense against external field fluctuations is a high magnetic field, which makes them relatively smaller. Current solenoid designs limit our field to the few-teslas range, with order-of-magnitude increases impractical, and we typically run at 5–6 T. Our largest source of magnetic noise is the local subway. It runs daily from approximately 05:00 to 01:00 and produces normally-distributed field fluctuations of width ≈ 50 nT (10 ppb) in our lab. Figure 3.1 shows a week of the daily fluctuations and nightly quiet periods.

These 10 ppb fluctuations would limit us to four hours of data per day if we could not shield them from the electron. Typical mu-metal techniques are impractical because the large solenoid field would saturate the shields unless they were placed far away. Eddy currents in the high-conductivity aluminum and copper cylinders of the dewars, magnet bore, and fridge help shield high-frequency fluctuations [104]. A

passive, self-shielding solenoid design cancels the long-term (seconds to hours) ambient fluctuations [91]. This design uses the coil geometry to make the central field always equal to the average field over the coil cross-section, thus making the basic solenoid property of flux conservation identical to central-field conservation. While it is possible to make a single solenoid with a self-shielding geometry, such a coil cannot simultaneously be optimized for homogeneity. We employ a set of superconducting solenoids that are designed for high-homogeneity and add one additional coil, inductively coupled to the others, with the geometry appropriate for making the entire network self-shielding. The shielding-factor for our magnet has been measured to be 156 [105], which means the electron only sees 0.06 ppb field fluctuations from the 10 ppb subway noise.

3.2 High-Stability Solenoid Design

Details of the solenoid construction such as superconducting wire choice and winding method are crucial to the field stability. While some published information exists, e.g., [106], much of these details lie in the realm of old-magnet-winders' lore and trade secrets. Our magnet uses single-core superconducting wire, which facilitates making the persistent joint that turns the wire into a loop. Any resistance in this joint will lead to field-decay with an L/R time constant. The use of single-core wire rather than the now-industry-standard multi-filament wire increases the solenoid's susceptibility to flux-jumps [106, Ch. 7] and their resulting field-jumps or magnet quenches, so care must be exercised in wire selection and coil design to minimize this risk.

Even with a well-designed persistent coil, the simple act of charging the magnet or

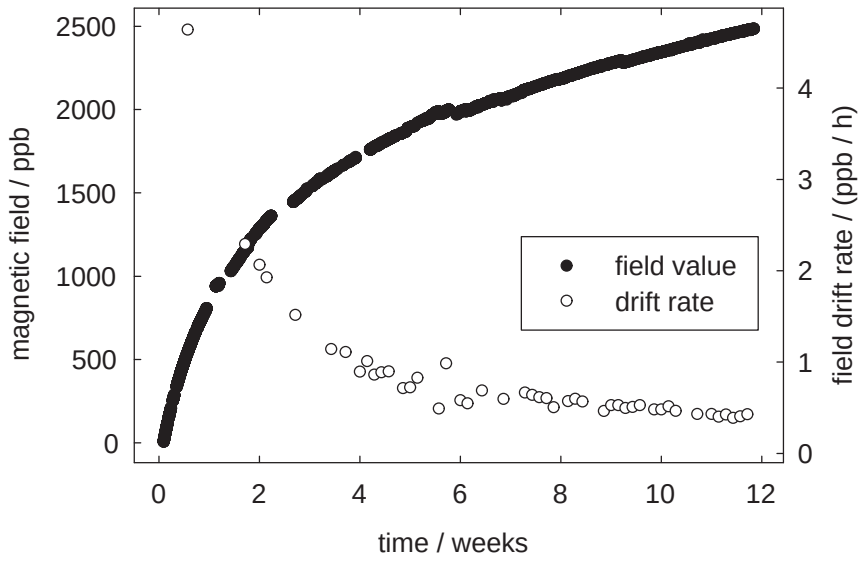

Figure 3.2: The time it takes the magnetic field to settle after charging strongly depends on the energization technique. This plot shows a particularly bad drift, which takes over a month to decay below 1 ppb/h. The magnetic field was measured with the electron cyclotron frequency, while the drift rate is calculated from linear fits.

changing its field alters the forces in the solenoid itself and the resulting stresses can take months to stabilize. Figure 3.2 shows a particularly large charging drift. With care, this drift can be minimized by "over-currenting" the magnet—when changing the field, overshoot the target value by a few percent of the change, then undershoot by a similar amount, then move to the desired field, pausing for several minutes at each point.[1] This slow ringing-in to a field presumably helps to pre-stress the magnet. It was not used during the charging that resulted in the drift of Fig. 3.2, and such an enormous drift has not been seen any time we have over-currented during a field change. For most of our g-value data runs, magnet settling has not been a

[1]We have left the persistent switches energized during these pauses, with the magnet power supplies continuing to source the solenoid current.

major source of field drift, and on a typical night the field remains fairly constant, see e.g., Fig. 4.6.

Many groups have seen improved field stability by regulating the pressure of the liquid helium around the solenoid [107, 108, 109]. This vapor-pressure regulation serves to stabilize the temperature of the helium bath and thus of the solenoid itself. In addition, due to our historical apparatus design (see the next section), temperature changes that alter the length of certain dewar parts can move the solenoid relative to the trap electrodes, which could change the field seen by the electron. To minimize such effects, we regulate the pressures of all five cryogen reservoirs [83] to ≈ 50 ppm.

3.3 Reducing Motion in an Inhomogeneous Field

Our superconducting magnet is equipped with nine shim coils that allow the field homogeneity at the center to be tuned to better than 10^{-8} over a 1 cm diameter sphere. We have built an adjustable-height spacer that allows us to position the refrigerator such that the trap electrodes sit in this homogeneous region [110]. With the magnet well-shimmed and the electrodes in the flattest field region, if the residual field gradient is linear, the electron will see a 0.1 ppb field shift if the trap electrodes move 100 μm.[2]

Our apparatus is particularly susceptible to such motions because the two parts of the Penning trap, the solenoid and the electrodes, are supported in vastly different

[2]Although the amplitude of the electron axial motion routinely exceeds 100 μm when self-excited, this motion through a linear gradient would appear as a fast modulation of the magnetic field which would only add axial-frequency sidebands on the cyclotron and anomaly lines rather than blurring them. A quadratic gradient would merely redefine the magnetic bottle strength of Section 2.3.4. We are concerned here with motion on timescales slow compared to the inverse-linewidths of Section 4.2.

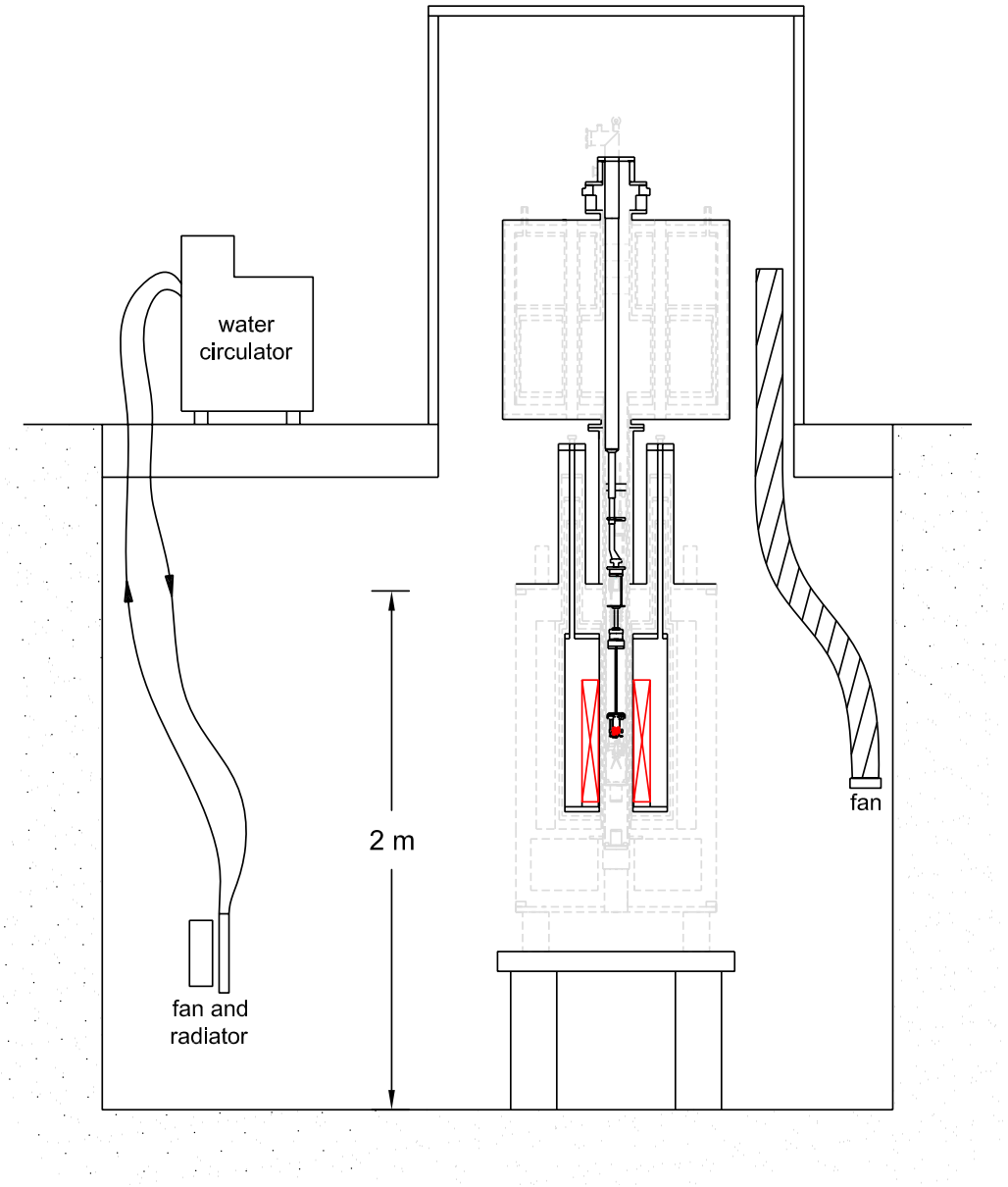

Figure 3.3: The separate support structure of the magnet and electrodes allows for their relative movement with room temperature or cryogen pressure fluctuations. Here, the electrodes and magnet windings are shown in red and their support structure in black. The entire apparatus is housed in a chamber with the air temperature actively regulated via a refrigerated circulating bath. Several fans increase convection and couple the water temperature to the air via a radiator.

ways. As shown in Fig. 3.3, the superconducting solenoid sits on the bottom of the magnet helium dewar, which hangs from two 304 stainless steel stacks extending from the magnet top plate. The trap electrodes hang 2.2 m below the mounting-plate of the dilution refrigerator. That plate sits on an aluminum dewar, which sits on the aluminum magnet bore. This peculiar arrangement results from the evolutionary assembly of the apparatus and is not a design "feature." In Section 3.5, we discuss a new apparatus, currently under construction, explicitly designed to lock the solenoid and electrodes together.

3.3.1 Stabilizing room temperature

Because some of the structure establishing the relative location of the trap electrodes and the solenoid is at room temperature, changes in room temperature will alter this structure and move the electron in the magnetic field. Based on the materials involved, the estimated expansion coefficient is 30 μm/K, which, assuming the well-shimmed field mentioned above, corresponds to a field-change of 0.03 ppb/K. This low field–temperature correlation would be negligible; unfortunately, we have at various times measured it to be 0.7 ppb/K, 2.7 ppb/K, and 5.3 ppb/K, indicating a range in our ability to shim the field and to position the electrodes in the flattest field region (the last number was deliberately measured in a high-gradient region).

The temperature in our lab routinely cycles 1–2 K daily, so we house the apparatus in a large, insulated, buffer air-mass that we actively regulate to 0.1 K. The boundary of the regulated zone is a concrete pit, $10' \times 10'$ and $8'$ deep, sunk into the earth, and covered with a plywood floor, along with an insulated shed sitting atop a hole

in the plywood floor. The lower part of the apparatus sits on a large table in the pit, and the upper part rises above the floor into the shed. Four fans and tubes force airflow through the hole coupling the pit to the shed and help to keep a uniform temperature throughout. A refrigerated circulating bath,[3] located above the pit and outside the regulated zone, pumps water into the pit and through an automobile transmission fluid cooler, heating and cooling the water to maintain constant air temperature. The transmission cooler was chosen for its ready availability and lack of ferromagnetic parts. A fan mounted behind the cooler couples the water and air temperatures. A similar system is described in [111].

3.3.2 Reducing vibration

Vibration can directly move the electrode position, and a 100 μm motion can arise from movement along the apparatus axis or from a 0.0026° swing of the 2.2 m-long moment-arm of the refrigerator. In addition to their noise and heat, the dilution refrigerator vacuum pumps create large vibrations. We have gone to great lengths to isolate these vibrations from our apparatus, including mounting the pumps on springs[4] and installing them in a different room at the end of a 12 m pipe run. The pump room is located in a free-standing tower that is structurally not well connected to the remainder of the building, and the vacuum tubes are encased in concrete within the wall of the tower, coupling the tubes and wall and damping any residual vibration.

Figure 3.4 shows typical vibration levels on the pit floor after moving the pumps, as

[3] ThermoNeslab RTE-17

[4] We have found the wire-rope-isolator design particularly effective, e.g., Enidine Inc. WR5-900-10-S.

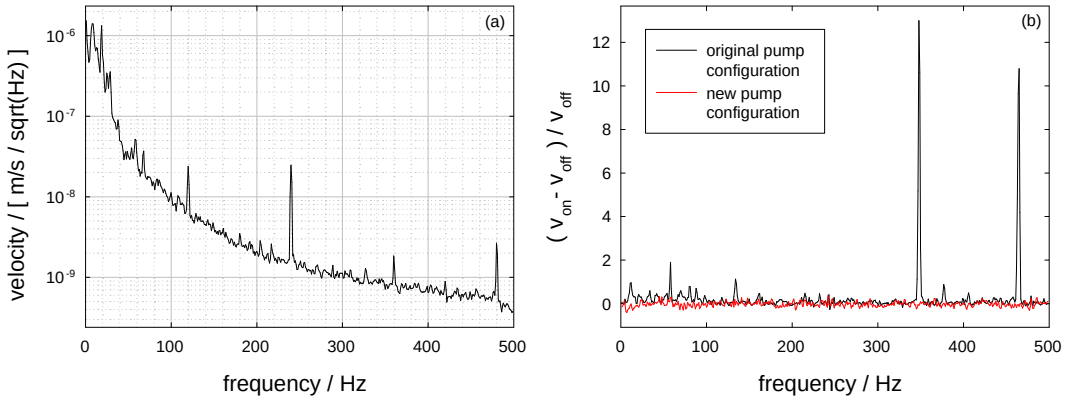

Figure 3.4: Typical vibration levels of the floor on which the experiment stands (a) and the relative improvement in vibration from mounting the refrigerator vacuum pumps on springs far away from the experiment (b). Here, $v_{\rm on}$ and $v_{\rm off}$ refer to the velocity spectral density (as in (a)) with the pumps running or off.

well as the reduced vibration resulting from the move.[5] Order-of-magnitude vibration reductions are seen at frequencies related to the pump motion, though we have seen no obvious improvement in the quality of our g-value data. The typical vibration spectrum of Fig. 3.4a indicates a root-mean-square floor displacement of 0.4 μm. This size displacement could not by itself cause a 0.5 ppb blurring of the resonance lines, indicating that any vibration-induced field noise must come from a resonance in the apparatus such as the refrigerator swinging.

One additional source of noise is plotted in Fig. 3.5. It appears as sharp drops in the electron cyclotron frequency and occurs daily from 06:00 to 15:00 except on Sundays and holidays. Since it is uncorrelated with ambient magnetic field readings of a flux-gate magnetometer,[6] its origins are presumed to be vibrational. This noise limits us to taking data for only 60% of the day.

[5]The measurements in Fig. 3.4 were made with an accelerometer (PCB Piezotronics 393A03). We independently measured the vibration using a Geospace Geophone GS-11D, which gave comparable results.

[6]Macintyre Electronic Design Associates (MEDA) FVM-400

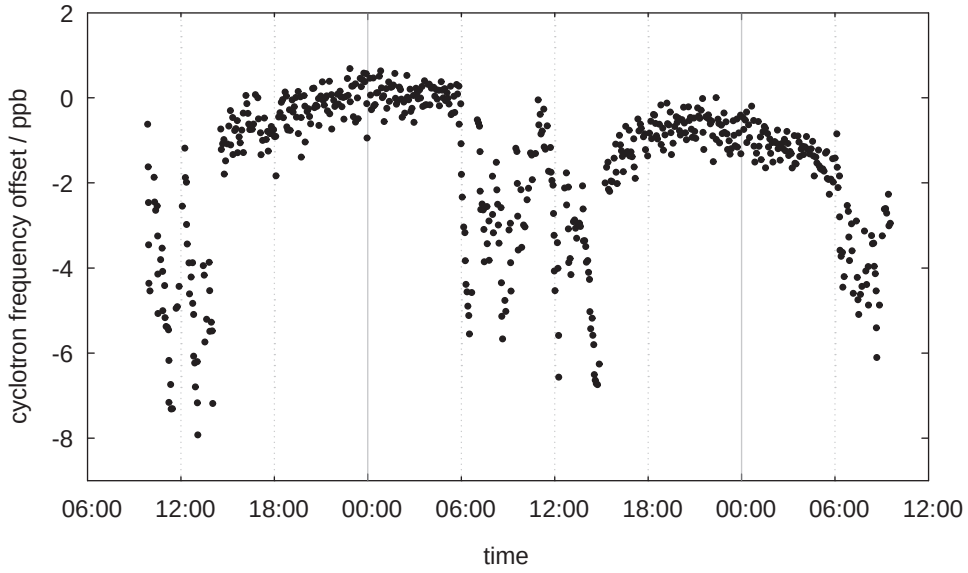

Figure 3.5: Daytime field noise, seen from 06:00 to 15:00 except Sundays and holidays. Plotted is the electron cyclotron frequency, offset from an arbitrary value and with a 2 ppb/h linear drift removed.

3.4 Care with Magnetic Susceptibilities

Temperature-dependent paramagnetism is another source of potential field drift. Others have documented woes related to the electronic paramagnetism of G-10 that was not well-anchored thermally [109]. For our apparatus, the most important concern is nuclear paramagnetism [83]. The T^{-1} dependence of the nuclear magnetization from the Curie law leads to a T^{-2} dependence of dM/dT, which can be quite large at dilution-refrigerator temperatures. We have taken great care to use only low-Curie-constant materials at base temperature. The electrodes are gold-plated silver, which has a Curie constant nearly 300 times lower than the usual copper. The insulating spacers are quartz, 70 times better than the usual MACOR. The remainder of the pieces are primarily titanium and molybdenum, with silver used where high thermal

conductivity is important. For details of the trap materials and a table of the relevant Curie constants, see [83, Sec. 3.3]. Temperature-dependent magnetizations only matter if the temperature fluctuates, and we minimize the base-temperature changes by regulating the mixing chamber to better than 1 mK with a LakeShore Cryogenics 370AC Resistance Bridge.

3.5 Future Stability Improvements

We currently see magnetic-field noise at the 0.5–1 ppb level, as can be seen in the nighttime section of Fig. 3.5 and is discussed fully in Chapter 4 and Chapter 6. Pushing the frequency resolution below our current level will require additional techniques for stabilizing the magnetic field. In addition to the passive shielding from external field changes described above, an additional shielding factor of 50 to 80 may be attained by actively monitoring the ambient field and feeding back to a pair of Helmholtz coils to compensate for the fluctuations [109]. Adding a small heater to each cryogen reservoir would allow flow regulation in addition to pressure regulation and would keep the exhaust system, parts of which are structural in our current apparatus, at a constant vapor-cooled temperature.

The major change required for improved stability is locking the relative positions of the superconducting solenoid and the trap electrodes. To accomplish this goal, we have designed an entirely new dilution refrigerator, magnet, and dewar, which is compared to our existing apparatus in Fig. 3.6. In the new apparatus, the dilution refrigerator stands on the magnet itself rather than hanging from the top of the dewar. The axial alignment of the trap electrodes in the magnetic field depends only on the

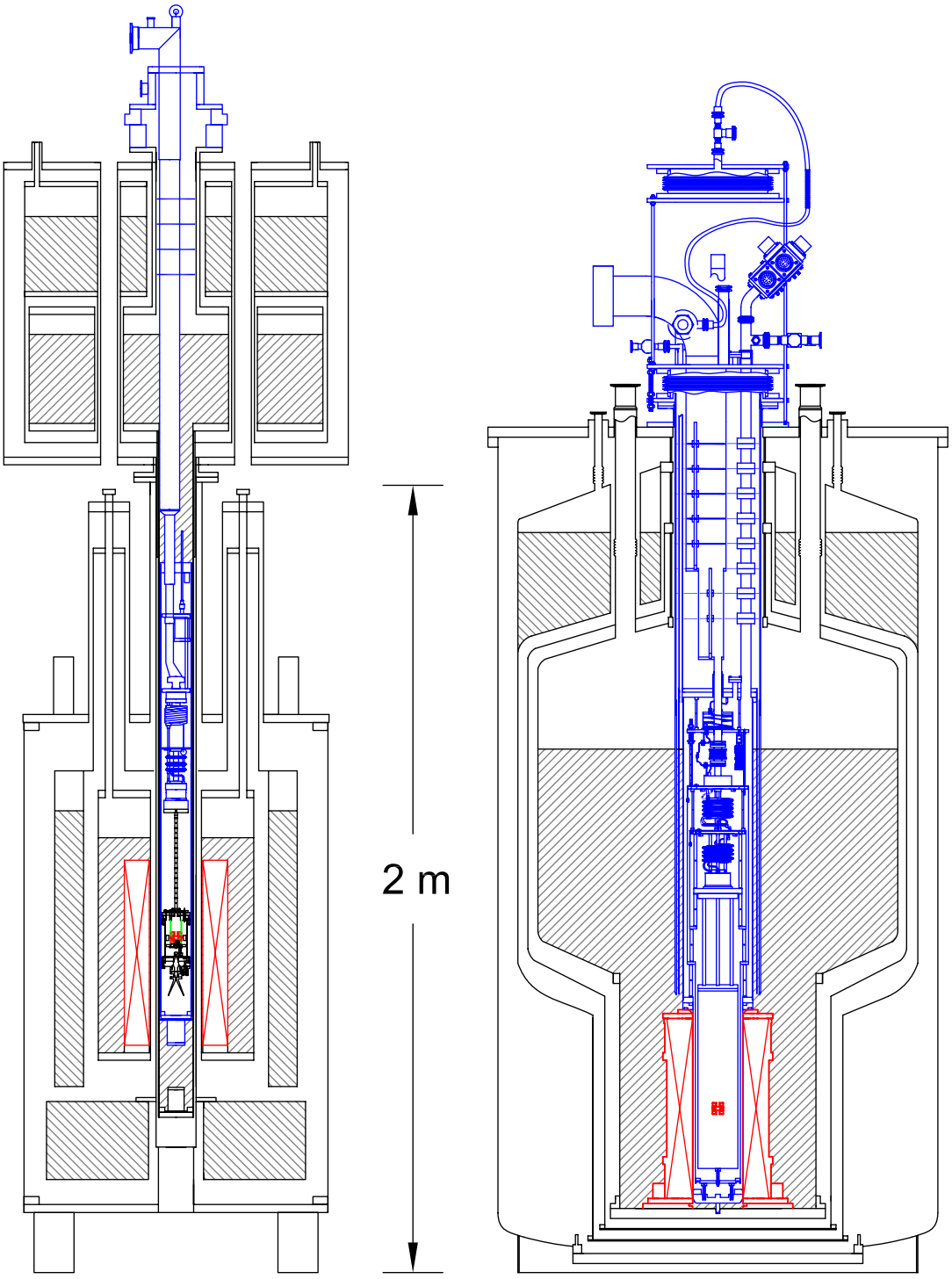

Figure 3.6: Side-by-side comparison of a new, high-stability apparatus (right) and the current one (left). (New apparatus figure courtesy of Janis Research Company.)

height of 4 K-to-100 mK carbon-fiber supports and of material at base temperature. For the first time, we also have radial alignment of the trap electrodes, maintained through a series of pins that center the trap electrodes with respect to the thermally-floating radiation shield, then to the refrigerator inner-vacuum chamber, and finally to the dewar bottom-plate. Additional stability comes from a reduction in the number of cryogen spaces from five to two, with a helium space large enough to reduce pressure-destabilizing fills from once every five days to once every few weeks. The refrigerator is surrounded by a closed cylinder that allows differential pressurization in the dewar, forcing liquid helium up the side of the IVC where it can be maintained at a constant level. The dilution refrigerator, manufactured by Janis Research Company, and the dewar, manufactured by Precision Cryogenic Systems, are complete; the magnet, manufactured by Cryomagnetics, is nearing completion. After testing at Janis, we expect an early 2008 delivery.

Chapter 4

Measuring g

4.1 An Experimenter's g

What must we actually measure to determine the g-value? Experimentally, it is convenient to measure frequency, which has well-developed techniques for attaining high precision. A free-space electron interacts with a magnetic field through its intrinsic and orbital angular momenta, providing an experimenter's definition of g in terms of the spin and cyclotron frequencies. Since the two are within a part-per-thousand of each other, directly measuring their beat frequency, the anomaly frequency, is a higher-precision technique. Thus, in free-space,

$$\frac{g}{2} = \frac{\nu_s}{\nu_c} = \frac{\nu_c + \nu_a}{\nu_c} = 1 + \frac{\nu_a}{\nu_c}. \tag{4.1}$$

There is a small but significant correction to this equation at the ppt-level in g (ppb in $\bar{\nu}_c$) due to special relativity, which modifies the cyclotron and spin frequencies in a state-dependent way. The resolution of single quantum transitions, allowing exact treatment of this shift, is one of the key advantages of the quantum cyclotron over

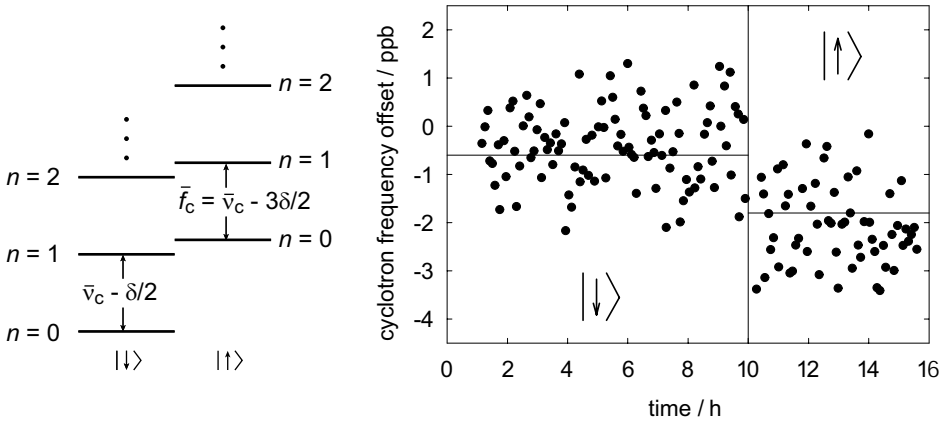

Figure 4.1: Special relativity alters the cyclotron frequency in a state-dependent manner, appearing as a ppb-scale shift between the frequencies of the lowest cyclotron transition in the spin-down and spin-up ladders. The horizontal lines are separated by the predicted relativistic shift. An overall 0.61 ppb/h drift has been removed from this data.

previous measurements [2], which excited a distribution of cyclotron states [99], each with a different relativistic shift. The shift can be thought of as a relativistic mass correction, whereby states with larger cyclotron energy have a reduced ν_c due to the frequency's inverse-mass dependence. Quantitatively, the Dirac-equation solution for the transition between $|n, m_s\rangle \leftrightarrow |n+1, m_s\rangle$ shows a reduction in frequency given by [84, Sec. VII.B]

$$\Delta\nu_c = -\delta(n + 1 + m_s), \tag{4.2}$$

where

$$\frac{\delta}{\nu_c} = \frac{h\nu_c}{mc^2} \approx 10^{-9} \tag{4.3}$$

and $m_s = \pm\frac{1}{2}$. Since this ppb-scale shift is state-dependent, we must be consistent in which pair of energy levels we use for measuring ν_c. The difference between $|0, \downarrow\rangle \leftrightarrow |1, \downarrow\rangle$ and $|0, \uparrow\rangle \leftrightarrow |1, \uparrow\rangle$ is on the order of our linewidth and easily resolved, as shown

in Fig. 4.1.[1] So that we may account for the relativistic shift exactly, we have chosen always to measure the spin-up transition, whose frequency we designate f_c. The selection of this transition over the spin-down one is primarily for convenience—it allows us to begin all measurement cycles in the $|0,\uparrow\rangle$ state. The anomaly frequency has no relativistic shift, as the modifications of the cyclotron and spin frequencies cancel.

The addition of the Penning trap's electrostatic quadrupole makes two further modifications to the equation for g. First, using the invariance theorem discussed in Section 2.1.2, we replace the free-space cyclotron frequency with the trap eigenfrequency and its calculated-magnetron-frequency correction. The free-space anomaly frequency is similarly replaced with the measured frequency using Eq. 2.29. Second, we correct for the shift in the cyclotron frequency arising from the radiation modes of the trap electrode cavity. The spin frequency is unchanged by these cavity modes, but the anomaly frequency, through its definition in terms of the spin and cyclotron frequencies, is also shifted. This cavity shift is the topic of Chapter 5 and is included below as $\Delta\omega_c/\omega_c$, a term defined in Eq. 5.20. The equation we will use in the g-value measurement is

$$\frac{g}{2} \simeq 1 + \frac{\bar{\nu}_a - \dfrac{\bar{\nu}_z^2}{2\bar{f}_c}}{\bar{f}_c + \dfrac{3}{2}\delta + \dfrac{\bar{\nu}_z^2}{2\bar{f}_c}} + \frac{\Delta\omega_c}{\omega_c}. \tag{4.4}$$

All the barred frequencies indicate those actually measured in the trap. Although $\bar{\nu}_a$, $\bar{f}_c$, δ, and $\Delta\omega_c/\omega_c$ vary with the magnetic field, their combination in Eq. 4.4 does not,

[1] Directly measuring δ and ν_c in SI units, together with the Rydberg constant, is an alternate route to the fine structure constant (it is an h/m measurement like the atom-recoil methods of Section 1.1.3). The data in Fig. 4.1 give $\delta/\nu_c = 1.7(3)$ ppb, near agreement with the calculated 1.2 ppb, but far from the high precision required for an α determination.

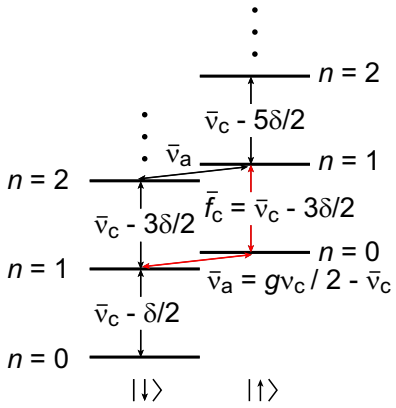

Figure 4.2: The energy levels of an electron in a Penning trap, including ppb-size shifts from special relativity. The red arrows indicate the transitions we measure to determine g.

provided the measured $\bar{\nu}_a$ and $\bar{f}_c$ correspond to the same field. Corrections to Eq. 4.4 from higher-order terms in the invariance theorem expansion of Section 2.1.2 are of the order 10^{-16}, while those from applying the cavity shift to $\bar{\nu}_a$ and not $\bar{f}_c$ are of order $(\bar{\nu}_a/\bar{f}_c)(\Delta\omega_c/\omega_c) \lesssim 10^{-14}$. Both are below our current precision but straightforward to include should our resolution increase.

The remainder of this chapter contains the procedure for measuring the three required frequencies ($\bar{f}_c$, $\bar{\nu}_a$, $\bar{\nu}_z$). The combination of these frequencies with the cavity shift to extract the g-value is the topic of Chapter 6.

4.2 Expected Cyclotron and Anomaly Lineshape

We measure $\bar{f}_c$ and $\bar{\nu}_a$ by resolving their resonance lines, relying on an invariant property of the expected lineshapes (their mean frequency) to determine the frequencies with uncertainties less than the linewidths. The same magnetic bottle that makes a QND coupling of the cyclotron and spin energies to the axial frequency

(Section 2.3.4) couples the axial energy to the cyclotron and anomaly frequencies so that the distribution of axial states broadens the cyclotron and anomaly lines, which we shall see are two limits of the same nontrivial lineshape. Brown [86] derived the lineshape treating the coupling of the axial state to the amplifier as random, thermal, Brownian motion. D'Urso [89, Ch. 3] treated axial degree of freedom quantum-mechanically through a density matrix with a thermal distribution of states. The results of both Brown and D'Urso are in the low cyclotron damping limit.[2] As we shall see, our resolution of the anomaly line is fine enough that we may no longer ignore the broadening from the finite lifetime of the $|1,\downarrow\rangle$ state, and we present the result as a function of cyclotron damping rate, γ_c. Since the derivation including γ_c is straightforward when following the detailed analyses in [86] and [89, Ch. 3], we state the result without proof.

The drives used to excite the cyclotron and anomaly transitions are described in Section 4.3. Assuming that they are left on for a time much longer than the inverse linewidth and inverse axial damping rate, γ_z^{-1}, at an amplitude low enough that the transition rate remains small, the probability, P, that a transition will have occurred after a time, T, is linear in that time,

$$P = \frac{1}{2}\pi T \Omega^2 \chi(\omega). \tag{4.5}$$

Here Ω is the Rabi frequency, whose specific value depends on the strength of the

[2] In one case, Brown does keep a non-zero cyclotron damping rate, with a result [86, Eq. 6.12] identical to that presented here. Because the anomaly excitation technique employed at the time involved maintaining a large cyclotron radius with a nearly-resonant drive, see e.g., [2], Brown derives the anomaly lineshape with the radial coordinate ρ determined by the strength of this drive. In the limit that the drive is white noise, i.e., its time-time correlation is a δ-function, the $\gamma_c \ll \gamma_z$ approximation is not necessary. Although our excitation technique, described in Section 2.3.6, is different than the one used for Brown's derivation, the only effect is a redefinition of the Rabi frequency, as described in [112].

drive. The factor of $\frac{1}{2}$ applies exactly in the case of the anomaly transition, but the radiative decay of cyclotron excitations will decrease its value for the cyclotron transition if there is any delay between the end of the drive and the measurement of the state. This effect is explored further in Section 4.2.4 along with a relaxation of the weak-drive assumption. The last factor in Eq. 4.5 is the lineshape, $\chi(\omega)$, to which we now turn.

For an electron on axis ($\rho = 0$), the magnetic bottle adds a z^2 dependence to the magnetic field (see Eq. 2.22) and thus to the cyclotron and anomaly frequencies, here collectively ω:

$$\omega(z) = \omega_0(1 + \frac{B_2}{B}z^2). \tag{4.6}$$

Our goal in understanding the lineshape is to take measurements of a cyclotron line and an anomaly line and extract a pair of cyclotron and anomaly frequencies that correspond to the same average z and thus the same magnetic field. These may then be used to calculate the g-value. The conventional choice is $z = 0$, i.e., find ω_0 in Eq. 4.6, but we shall see that the root-mean-square (rms) thermal amplitude, z_{rms}, is also convenient.

It is useful to define a linewidth parameter[3] in terms of this average, $\langle z^2 \rangle$,

$$\Delta\omega \equiv \omega_0 \frac{B_2}{B} \langle z^2 \rangle = \omega_0 \frac{B_2}{B} \frac{kT_z}{m\omega_z^2}, \tag{4.7}$$

where in the last step we have used the equipartition of energy, $\frac{1}{2}m\omega_z^2 \langle z^2 \rangle = \frac{1}{2}kT_z$, to express the rms amplitude of the axial oscillation in terms of the axial temperature. This substitution is allowed because the axial motion is in thermal equilibrium

[3]This linewidth parameter, $\Delta\omega$, is not to be confused with the relative cavity shift, $\Delta\omega_c/\omega_c$, of Eq. 4.4 and Chapter 5.

with the detection amplifier. The axial damping constant, γ_z, sets the timescale of the thermalization, and it is useful to examine the lineshape when this timescale is much shorter or much longer than that set by the linewidth parameter $\Delta\omega$ and the uncertainty principle.

4.2.1 The lineshape in the low and high axial damping limits

For $\gamma_z \ll \Delta\omega$, the axial motion is essentially decoupled from the amplifier during the inverse-linewidth coherence time. During that time, the electron remains in a single axial state and the lineshape is a Lorentzian with the natural linewidth, γ_c, and centered on the frequency given by Eq. 4.6 with the rms axial amplitude of that state as z. We do not know which axial state that is, however, and since excitation attempts occur on timescales longer than γ_z^{-1}, subsequent attempts will be in different states. Thus, the composite lineshape after many attempts is the convolution of the instantaneous lineshape, the narrow Lorentzian, and the Boltzmann distribution of axial states. That is, the lineshape is a decaying exponential with a sharp edge at ω_0. The cyclotron line is close to this "exponential" limit and should have a sharp edge at the zero-axial-amplitude cyclotron frequency that is useful for quick field measurements such as tracking drifts.

For $\gamma_z \gg \Delta\omega$, the axial motion is strongly coupled to the amplifier. During the time required to resolve the line, the axial amplitude relaxes to the thermal z_{rms} yielding a lineshape that is a natural-linewidth Lorentzian offset from ω_0 by $\Delta\omega$. This limit is approached through a Lorentzian centered on $\omega_0 + \Delta\omega$ with a full-width of $\gamma_c + 2\Delta\omega^2/\gamma_z$. The anomaly line is near this Lorentzian limit.

In both of these limits, the lineshape's average frequency is $\omega_0 + \Delta\omega$ and corresponds to the magnetic field given by the rms thermal axial amplitude in the magnetic bottle (Eq. 4.6). This average frequency is the same for all γ_z between these limits as well, and this invariant forms the heart of the weighted-mean line-splitting method introduced in Section 4.4.1.

4.2.2 The lineshape for arbitrary axial damping

The lineshape, for arbitrary γ_z and $\Delta\omega$, is given by three equivalent solutions,

$$\chi(\omega) = \frac{4}{\pi}\mathrm{Re}\left[\gamma'\gamma_z \int_0^\infty dt \frac{e^{i(\omega-\omega_0)t}e^{-\frac{1}{2}(\gamma'-\gamma_z)t}e^{-\frac{1}{2}\gamma_c t}}{(\gamma'+\gamma_z)^2 - (\gamma'-\gamma_z)^2 e^{-\gamma' t}}\right] \tag{4.8a}$$

$$= \frac{4}{\pi}\mathrm{Re}\left[\frac{\gamma'\gamma_z}{(\gamma'+\gamma_z)^2}\sum_{n=0}^{\infty}\frac{(\gamma'-\gamma_z)^{2n}(\gamma'+\gamma_z)^{-2n}}{(n+\frac{1}{2})\gamma' + \frac{1}{2}(\gamma_c-\gamma_z) - i(\omega-\omega_0)}\right] \tag{4.8b}$$

$$= -\frac{4}{\pi}\mathrm{Re}\left[\frac{\gamma_z\ {}_2F_1\left(1, -K; 1-K; \dfrac{(\gamma_z-\gamma')^2}{(\gamma_z+\gamma')^2}\right)}{K(\gamma_z+\gamma')^2}\right], \tag{4.8c}$$

where

$$\gamma' = \sqrt{\gamma_z^2 + 4i\gamma_z\Delta\omega}, \tag{4.9}$$

$$K = \frac{2i(\omega-\omega_0) + \gamma_z - \gamma' - \gamma_c}{2\gamma'}, \tag{4.10}$$

and ${}_2F_1(a, b; c; z)$ is a hypergeometric function. The integral definition in Eq. 4.8a plainly shows the effect of the cyclotron lifetime. The lineshape is the Fourier transform of the product of a lifetime-independent term and the finite-lifetime correction. The Fourier transform convolution theorem, see e.g., [113, Sec. 15.5], says the result is the convolution of the Fourier transforms of the two terms. That is, the finite-lifetime

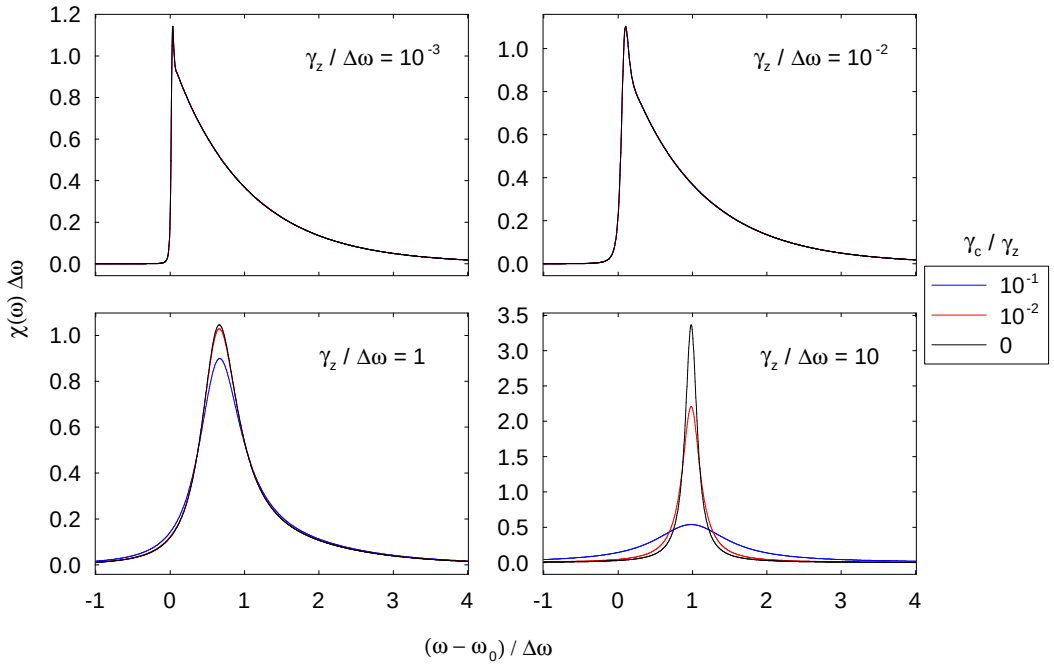

Figure 4.3: The theoretical lineshape for various $\gamma_z/\Delta\omega$ and γ_c/γ_z. The cyclotron line has $\gamma_z/\Delta\omega \approx 10^{-2}$. The anomaly line has $\gamma_z/\Delta\omega \approx 10$. For our γ_z, $\gamma_c/\gamma_z = 10^{-1}, 10^{-2}$ correspond to 1.6 s and 16 s lifetimes. The infinite-lifetime limit is $\gamma_c/\gamma_z = 0$.

lineshape is the convolution of the infinite-lifetime lineshape with a Lorentzian of full-width γ_c.

Figure 4.3 plots this lineshape for a range of $\gamma_z/\Delta\omega$ and γ_c/γ_z. The exponential and Lorentzian limits are clearly visible, as is the broadening due to the cyclotron damping rate.

Invariance of the lineshape mean from γ_z

An important feature of this lineshape, which we use in our primary line-splitting technique (Section 4.4.1), is the independence of its mean from γ_z [86]. The average frequency of the lineshape, $\langle\omega\rangle = \int_{-\infty}^{\infty} \omega\,\chi(\omega)\,d\omega$, always corresponds to that given

by the thermal $z_{\rm rms}$ in the magnetic bottle field (Eq. 4.6). That is,

$$\langle\omega\rangle = \omega_0 + \Delta\omega \tag{4.11}$$

or

$$\langle(\omega - \omega_0)\rangle = \Delta\omega. \tag{4.12}$$

The second-moment of $\omega - \omega_0$ is also independent of γ_z and in the limit $\gamma_c \to 0$ is given by [86]

$$\left\langle(\omega - \omega_0)^2\right\rangle = 2\Delta\omega^2. \tag{4.13}$$

A finite cyclotron lifetime broadens the line, and the second moment above is no longer correct. The first moment is unchanged.

In Section 4.4.1, we will introduce a method for calculating the mean of a measured resonance. These means will be our primary measurements of $\bar{f}_c$ and $\bar{\nu}_a$ and will be used directly in Eq. 4.4.

4.2.3 The cyclotron lineshape for driven axial motion

We have thus far assumed a thermal distribution of axial states. The case of driven axial motion added to this thermal motion is also of interest because it corresponds to what one measures with the self-excited oscillator running. While we turn off the SEO and allow the axial motion to thermalize before g-value measurements, it is necessarily driven during detection, and we make extensive use of this driven lineshape in Section 5.4 for calibrating the absolute amplitude of the self-excited axial motion. The driven lineshape for an arbitrary $\gamma_z/\Delta\omega$ appears as an integral in [86, Eq. 7.14].

In the weak-coupling limit ($\gamma_z \ll \Delta\omega$) that corresponds to our cyclotron line, it is

$$\chi_d(\omega) = I_0\left(\frac{2\sqrt{(\omega-\omega_0)\Delta_d\omega}}{\Delta\omega}\right)\theta(\omega-\omega_0)\frac{1}{\Delta\omega}\exp\left(-\frac{\omega-\omega_0+\Delta_d\omega}{\Delta\omega}\right), \tag{4.14}$$

where

$$\Delta_d\omega = \omega_0\frac{B_2}{B}\frac{A^2}{2}, \tag{4.15}$$

A is the driven axial amplitude, $\theta(x)$ is the Heaviside step function, and $I_0(x)$ is the order-zero modified Bessel function. Note that if the drive goes to zero ($\Delta_d\omega \to 0$), we recover the exponential limit of $\chi(\omega)$. If the driven amplitude is much larger than the thermal one ($\Delta\omega \to 0$), the lineshape goes to a δ-function centered at $\omega_0 + \Delta_d\omega$, corresponding to a cyclotron frequency shift given by the rms driven amplitude in the magnetic bottle.

The mean frequency of the driven line for an arbitrary $\gamma_z/\Delta\omega$ is also invariant from γ_z and equal to $\omega_0 + \Delta\omega + \Delta_d\omega$.

4.2.4 The saturated lineshape

We have thus-far assumed that the transition is driven for a long time compared with the inverse-linewidth and γ_z^{-1} and at an amplitude that produces a low transition rate. If we relax the amplitude condition [86],

$$P = \frac{1}{2}\left[1 - \exp\left(-\pi T\Omega^2\chi(\omega)\right)\right]. \tag{4.16}$$

The transition probability saturates at $\frac{1}{2}$ for large Rabi frequencies, Ω, or long drive times, T, indicating equal chance to finish in either of the two states. For two states coupled only by the drive, such as the anomaly transition, this saturation level is observed. It must be modified for the cyclotron line because of possible cyclotron

decays and transitions to states above $|1\rangle$. The state $|1\rangle$ decays back to $|0\rangle$ and may do so after the drive is complete but before the amplifiers are on to look for a transition. The $\frac{1}{2}$ must therefore be multiplied by $e^{-\gamma_c t}$, where t is the warm-up time between the end of the cyclotron pulse and the beginning of the data acquisition. Furthermore, the cyclotron degree of freedom has a whole ladder of states and routinely driving the electron above $|1\rangle$ would increase the saturation value to 1. The relativistic anharmonicity of the cyclotron states helps some, but the cyclotron line is broader then these ppb-shifts, so the exponential tail of the $|1\rangle \leftrightarrow |2\rangle$ line extends into the $|0\rangle \leftrightarrow |1\rangle$ line. We account for these possibilities by including the exponential factor, $e^{-\gamma_c t}$, in the cyclotron lineshape model and by keeping transition rates low enough that excitations to $|2\rangle$ are rare.

Saturation also invalidates the relation of the frequency mean to $\Delta\omega$ by making it dependent on γ_z, Ω, and T. For example, the mean frequency for saturated lines in the Lorentzian limit ($\gamma_z \gg \Delta\omega$) remains $\omega_0 + \Delta\omega$, while that for saturated lines in the exponential limit ($\gamma_z \ll \Delta\omega$) increases with the leading correction equal to $\pi T\Omega^2/8$. In practice, we keep both the cyclotron and anomaly peak transition probabilities below 20% to avoid the effects of higher cyclotron states and saturation as well as to maintain the invariant frequency mean. At $P = 20\%$, we expect the saturation-shift of the cyclotron mean to be smaller than the uncertainty in our weighted-mean calculation. Nevertheless, we check the "unsaturated lines" assumption of the weighted-mean method by fitting the data to the saturated lineshape (we must include a model of magnetic field noise) and comparing both the resulting g-value and the numerically integrated means of the fitted lines. This agreement between calculated means and

fits quantifies a lineshape model uncertainty, which is analyzed in Section 6.1.

4.2.5 The lineshape with magnetic field noise

Although the cyclotron line is in the exponential lineshape limit ($\gamma_z \ll \Delta\omega$) and should have a sharp low-frequency edge, all of our data show an edge-width of 0.5–1 ppb. We model this discrepancy as fluctuations in the magnetic field, which could arise from any of the instabilities discussed in the previous chapter. In this section, we show that any source of noise that is not correlated with the thermal axial fluctuations modifies the noise-free lineshape of the previous sections by convolving it with a noise function. Provided the noise fluctuates symmetrically, the lineshape mean frequency remains $\omega_0 + \Delta\omega$.

In general, the lineshape, $\chi(\omega)$, is the Fourier transform of a correlation function, $\tilde{\chi}(t)$, which first-order perturbation theory shows is related to the statistical average of a fluctuating magnetic field, $\omega(t)$ [86]:

$$\tilde{\chi}(t) = \left\langle \exp\left[-i\int_0^t dt'\omega(t')\right]\right\rangle. \tag{4.17}$$

For the Brownian-motion lineshape of the previous sections and Eq. 4.8, $\omega(t)$ fluctuates due to the thermal axial motion in the magnetic bottle and is given as a function of $z(t)^2$ in Eq. 4.6. To model additional magnetic field noise, we add a noise term, $\eta(t)$, to the fluctuating field,

$$\omega(t) = \omega_0\left(1 + \frac{B_2}{B}z(t)^2 + \eta(t)\right), \tag{4.18}$$

so that the lineshape is given by the Fourier transform of

$$\tilde{\chi}(t) = \left\langle \exp\left[-i\int_0^t dt'\omega_0\left(1 + \frac{B_2}{B}z(t')^2 + \eta(t')\right)\right]\right\rangle. \tag{4.19}$$

For magnetic field noise that is not correlated with the axial fluctuations, the average factors into

$$\tilde{\chi}(t) = e^{-i\omega_0 t}\left\langle \exp\left[-i\omega_0 \frac{B_2}{B}\int_0^t dt' z(t')^2\right]\right\rangle \left\langle \exp\left[-i\omega_0 \int_0^t dt' \eta(t')\right]\right\rangle . \qquad (4.20)$$

The first two factors are the Brownian-motion lineshape and the third is an additional noise broadening. Because of the Fourier transform convolution theorem, the resulting noisy lineshape is the noise-free lineshape of Eq. 4.8 convolved with a noise function. Provided the noise fluctuates symmetrically, i.e., the mean frequency of the noise function is zero, the mean frequency of the lineshape is unchanged by the convolution and our weighted-mean method remains a valid analysis technique.

Further analysis of magnetic field noise in the lineshape requires the adoption of a specific model for $\eta(t)$. If there is a timescale associated with the noise (akin to γ_z^{-1} for the axial fluctuations), then the average involving $\eta(t)$ will take different values depending on the timescale's relation to the inverse-linewidth coherence time. For rapid fluctuations, the average quickly relaxes to its mean value and no noise-broadening occurs. For slow fluctuations, the field remains constant during a single excitation attempt and many excitation attempts build a lineshape broadened by a distribution of field values. These limits are analogous to the Lorentzian ($\gamma_z \gg \Delta\omega$) and exponential ($\gamma_z \ll \Delta\omega$) limits of the Brownian-motion lineshape. By attributing the broadening of the cyclotron edge to magnetic field noise, we assume that the noise fluctuates slower than the inverse-linewidth time of the cyclotron line, ≈ 200 μs. In Section 4.3.3 we discuss a technique for tracking the cyclotron edge as a function of time; we determine its location once every few minutes, and adjacent determinations are uncorrelated, suggesting field fluctuations on timescales faster than minutes. This

range of allowed timescales constrains the possible fluctuation mechanisms.

4.3 A Typical Nightly Run

With a model of the expected resonance lineshapes and their properties in place, we give an overview of the data collection techniques used to resolve them. Both the cyclotron and anomaly lines are probed with quantum jump spectroscopy, in which we apply a drive in discrete frequency steps, checking between applications for a cyclotron jump or a spin flip and building a histogram of the ratio of excitations to attempts at each frequency. A typical g-value measurement consists of alternating scans of the cyclotron and anomaly lines and lasts 14.5 h, from 15:30 to 06:00 the next morning, with daytime runs only possible on Sundays and holidays when the ambient magnetic field noise is lower (see Chapter 3). Interleaved among these scans are periods of magnetic field monitoring to track any long-term drifts in the field so we may account for them during data analysis. In addition, we continuously monitor over fifty environmental parameters such as refrigerator temperatures, cryogen pressures and flows, and the ambient magnetic field in the lab so that we may screen data for abnormal conditions and troubleshoot problems.

4.3.1 Cyclotron quantum jump spectroscopy

We drive cyclotron transitions by broadcasting microwaves into the trap cavity (Section 2.3.5). Since the drive wavelength (≈ 2 mm) is much longer than any electron

motion,[4] we may make the dipole approximation and write the interaction Hamiltonian between the electron and the drive $\mathbf{E}(t)$ without z-dependence:

$$H = -\mathbf{d} \cdot \mathbf{E}(t). \tag{4.21}$$

For a drive polarized along $\hat{\mathbf{x}}$, $\mathbf{E}(t) = E_0 \cos(\omega_d t)\hat{\mathbf{x}}$, this becomes

$$H = exE_0 \cos(\omega_d t). \tag{4.22}$$

When acting on a state $\binom{|n\rangle}{|n-1\rangle}$, the Hamiltonian in matrix notation is

$$H = -\hbar\Omega_c \boldsymbol{\sigma}_\mathbf{y} \cos(\omega_d t), \tag{4.23}$$

where $\boldsymbol{\sigma}_\mathbf{y}$ is a Pauli matrix and the Rabi frequency,

$$\Omega_c = eE_0 \sqrt{\frac{n}{2m\hbar(\omega_c' - \omega_m)}}, \tag{4.24}$$

may be derived from the harmonic oscillator formalism of [84, Sec. II.B].

We probe the cyclotron line with discrete excitation attempts spaced in frequency by approximately 10% of the expected linewidth. A quantum jump to the first excited cyclotron state indicates success, and we detect it via a quantum nondemoltion coupling of the increased cyclotron energy to a 20 ppb axial frequency shift (see Section 2.3.4). Prior to each excitation attempt, we apply a magnetron cooling drive (Section 2.3.7) to reduce the magnetron radius. We turn off the amplifiers during the excitation attempt to reduce the axial temperature and thus, through Eq. 4.7, the linewidth. To keep the conditions identical during both cyclotron and anomaly excitation, we apply a detuned anomaly drive during the cyclotron pulse. This extra

[4] We estimate the cyclotron and magnetron radii to be tens and hundreds of nanometers and the thermal axial amplitude to be 2 μm.

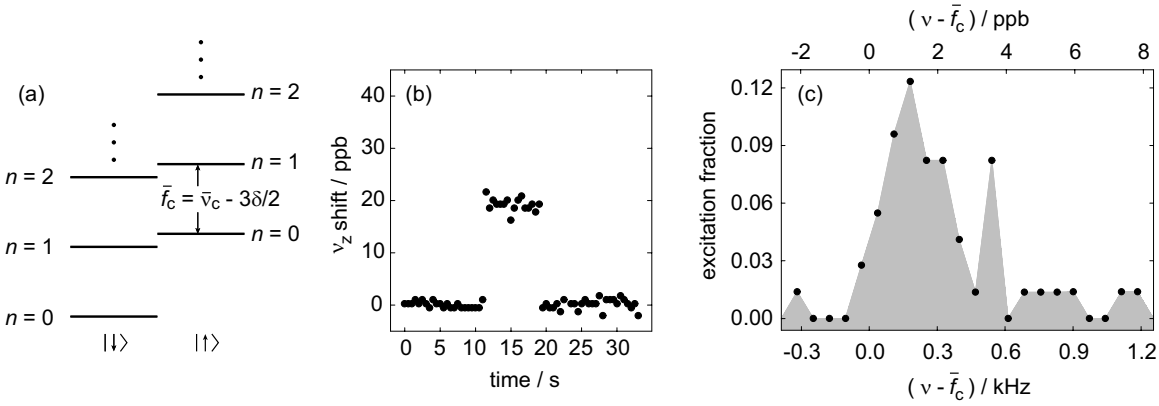

Figure 4.4: Cyclotron quantum jump spectroscopy proceeds through discrete interrogations of the lowest cyclotron transition in the spin-up ladder (a). A successful excitation appears as a shift in the axial frequency (b), a quantum nondemolition measurement technique. Multiple attempts at different frequencies may be binned into a histogram (c) to reveal the overall cyclotron line.

drive ensures the axial amplitude, and therefore the magnetic field seen by the electron as it moves in the bottle, remains the same for both frequency measurements; as discussed in the next section, the effect on the lineshape is negligible. To aid in accounting for the relativistic shift, we always drive between the same pair of cyclotron levels, $|0,\uparrow\rangle \leftrightarrow |1,\uparrow\rangle$, as indicated in Fig. 4.4.

The following is the sequence for a single cyclotron excitation attempt. The times listed are typical values, and the timing is done in hardware with a pulse generator. The "Event Generator" is manufactured in-house at the Harvard Electronics Instruments Design Lab; it has twelve channels and a 10 μs resolution with sub-nanosecond reproducibility, which is more than adequate for the timescales in our timing sequence. We always begin in $|0,\uparrow\rangle$.

1. Turn the self-excited oscillator off and the magnetron cooling drive on. Wait 0.5 s.

2. Turn the amplifiers off. Wait 1.0 s.

3. Turn the magnetron cooling drive off. Wait 1.0 s ($\approx 6\gamma_z^{-1}$).

4. Apply the cyclotron drive and a detuned anomaly drive for 2.0 s.

5. Turn the amplifiers on and start the self-excited oscillator. Wait 1.0 s to build up a steady-state axial oscillation.

6. Trigger the computer data-acquisition card (DAQ).

Once triggered, the DAQ reads data continuously and a LabVIEW software routine Fourier transforms this data in 0.25 s chunks. Based on the central frequency of each chunk, the computer looks for the roughly 4 Hz axial frequency shift that corresponds to a cyclotron excitation. If it sees one, it declares a successful excitation and waits for the cyclotron state to decay back to $|0,\uparrow\rangle$. Once the electron is in $|0,\uparrow\rangle$, the sequence is repeated at the next frequency. The entire process is automated.

4.3.2 Anomaly quantum jump spectroscopy

We create anomaly transitions by driving the axial motion in the $\mathbf{B} \sim z\rho\hat{\boldsymbol{\rho}}$ gradient of the magnetic bottle. The interaction Hamiltonian is

$$H = -\boldsymbol{\mu} \cdot \mathbf{B_d}, \tag{4.25}$$

where the drive $\mathbf{B_d} = B_2 z_a \cos(\omega_d t)\rho\hat{\boldsymbol{\rho}}$ comes from a driven axial amplitude, z_a. Using Eq. 1.1 for $\boldsymbol{\mu}$, the Hamiltonian acting on a state $\binom{|n-1,\uparrow\rangle}{|n,\downarrow\rangle}$ is [112]

$$H = \hbar\Omega_a \boldsymbol{\sigma_y} \cos(\omega_d t) \tag{4.26}$$

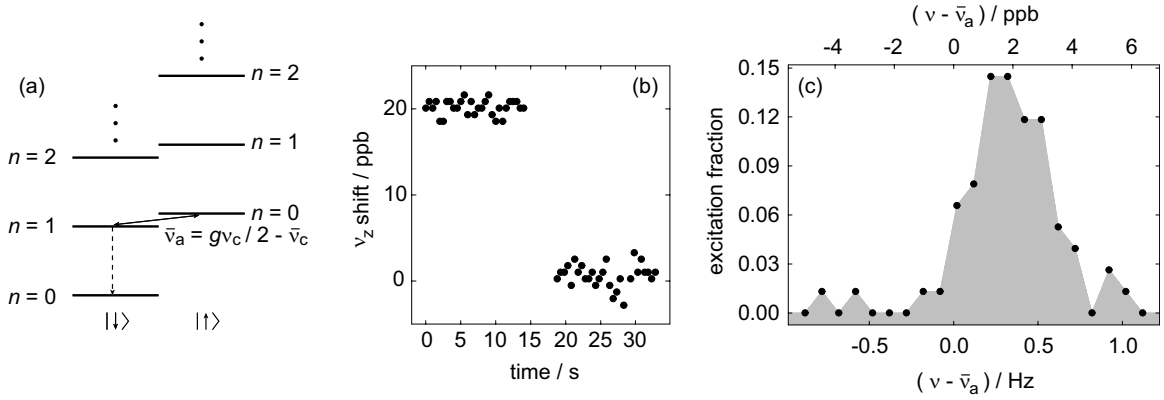

Figure 4.5: Anomaly quantum jump spectroscopy proceeds through discrete interrogations of the $|0,\uparrow\rangle \leftrightarrow |1,\downarrow\rangle$ transition (a). A successful transition appears as a shift in the axial frequency when the $|1\rangle$ state radiatively decays to the ground state (b). This frequency shift is a quantum nondemolition measurement. Multiple attempts at different frequencies may be binned into a histogram (c) to reveal the overall anomaly line.

where $\boldsymbol{\sigma_y}$ is a Pauli matrix and the Rabi frequency is

$$\Omega_a = \frac{g}{2}\frac{e\hbar}{2m}B_2 z_a \sqrt{\frac{2n}{m\hbar(\omega_c' - \omega_m)}}. \tag{4.27}$$

The anomaly procedure is similar to the cyclotron procedure described above and is done with quantum jump spectroscopy looking for single spin-flips, which appear as 20 ppb shifts in the axial frequency (see Section 2.3.4). Although there is no relativistic shift of the anomaly frequency, we always drive the $|0,\uparrow\rangle \leftrightarrow |1,\downarrow\rangle$ transition starting in the $|0,\uparrow\rangle$ state because it does not require a simultaneous cyclotron excitation. We do, however, apply a detuned cyclotron drive to keep identical conditions for both the anomaly and cyclotron excitations.

By comparing the measured peak excitation fraction to the lineshape and Rabi frequency, we estimate that our anomaly drive excites an axial amplitude $z_a \approx 100 - 250$ nm. This estimate agrees with that calculated from the drive voltage

applied on the bottom endcap based on our calibration of losses in the anomaly transmission line. This low amplitude has a minimal effect on the lineshape, as seen by the ratio of lineshape parameters $\Delta_d\omega/\Delta\omega \approx 10^{-2}$–$10^{-3}$ and the ten-times-larger thermal amplitude. We revisit frequency shifts from the anomaly drive in Chapter 6.

A single anomaly excitation attempt begins in $|0,\uparrow\rangle$ and follows the exact procedure listed for the cyclotron excitation sequence above with the exception that the anomaly drive is resonant and the cyclotron drive detuned in step 4. Once the excitation sequence finishes and the DAQ begins reading data, the LabVIEW software routine looks for a 4 Hz downward shift indicating a transition to $|1,\downarrow\rangle$ followed by a spontaneous decay to $|0,\downarrow\rangle$. If no decay occurs after waiting several cyclotron lifetimes, the attempt is declared a failure and the sequence is repeated at the next frequency. If the decay does occur, resonant cyclotron and anomaly drives pump the electron back to the $|0,\uparrow\rangle$ state before continuing to the next frequency. Again, the entire process is automated.

4.3.3 Combining the data

Magnetic field drift

Over the course of several hours, the magnetic field seen by the electron can drift due to pressure and flow changes in the cryogen reservoirs, room temperature changes, stresses in the solenoid, and other reasons discussed in Chapter 3. Typical drifts are at the level of a few 10^{-10} h^{-1}, though a poorly energized solenoid can drift several ppb per hour for months (see Fig. 3.2) and the pressure and flow changes in the hours following a liquid helium fill can cause field changes too rapid to track.

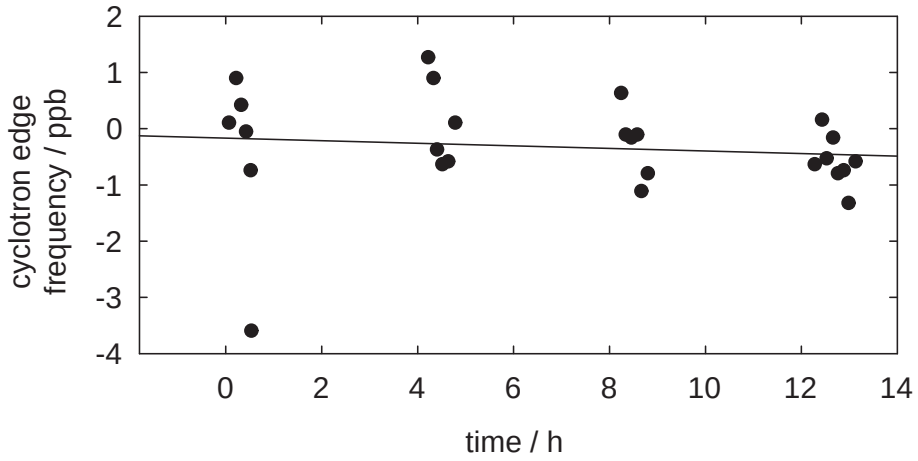

Figure 4.6: Periodically monitoring the cyclotron edge throughout a g-value scan allows the removal of any field drift. In this example, a linear fit to the edge data reveals a mild -0.02 ppb/h field drift to be removed during analysis.

We employ two techniques to deal with magnetic field drifts. First, we take cyclotron and anomaly data as close to simultaneously as we can, interleaving scans of the the two lines by making one attempt at each frequency in the cyclotron histogram then one at each frequency in the anomaly histogram. Second, we use the electron itself to monitor the magnetic field throughout the night and adjust for any drifts in our post-run analysis.

To accomplish this field-normalization, we take advantage of the sharp left edge of the cyclotron line. For a half-hour at the beginning and end of the run and again every three hours throughout, we alter our cyclotron spectroscopy routine by applying a stronger drive at a frequency below the edge. We use the same timing as in Section 4.3.1 but with a ten-times-finer frequency step, continuing to increase the excitation frequency until we observe a successful transition. We declare that

frequency to be "the edge," jump back 60 steps and begin again. In this manner, we may quickly track the cyclotron frequency throughout the night.[5] After the run, we model the magnetic field drift by fitting a first or second-order polynomial to these edge points. Since we time-stamp every cyclotron and anomaly excitation attempt, we use the smooth curve to remove the field drift. Figure 4.6 shows a typical night's drift and our fit. A particularly large drift and its removal from some cyclotron data are shown in [83, Fig. 4.5]. This edge-tracking adds a 20% overhead, but provides a valuable service not only on nights that happen to have large drifts but in enabling us to combine data from different nights.

The axial frequency

The axial frequency is the last frequency required for determining the g-value, and we measure it throughout the night as we determine the cyclotron and spin states. The anharmonic terms in the axial potential cause an important shift between the frequencies of the high-amplitude, self-excited electron during detection and the low-amplitude, thermally-excited electron during the cyclotron and anomaly pulses (see Eq. 2.5). We cannot directly measure the axial frequency under the pulse conditions because the amplifiers are off. We come close by measuring the frequency dip with the amplifiers on and the axial drives off; the shift between SEO-on and off, shown in Fig. 4.7, is typically a few hertz. It is the SEO-off axial frequency that we use in calculating g. The amplitude difference between amplifiers on (≈ 7 μm) and off

[5]Because of magnetic field noise, the edge frequencies are typically distributed across 0.5–1 ppb and offset below the cyclotron frequency. The value of the offset and the distribution of edge points about it depend on the particular edge-tracking technique, e.g., pulse power and frequency step size, but we consistently use the same excitation parameters so the edge frequency tracks ν_c.

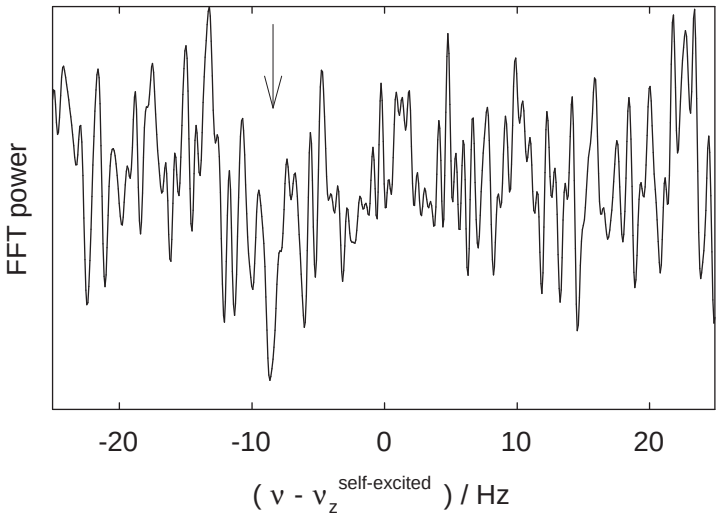

Figure 4.7: A dip in the amplifier noise spectrum at the axial frequency reveals a few-hertz shift between the self-excited and thermal frequencies.

(≈ 2 μm) is minuscule compared to the ≈ 100 μm self-excited amplitude. Since the frequency shift at low amplitudes goes as the amplitude-squared, the frequency difference between the two thermally-excited amplitudes is negligible.

The dip can at times be difficult to resolve because of drifts in the ring voltage while averaging. Additionally, when we tune the SEO for stability at a large amplitude, the non-zero C_4 coefficient can transform thermal amplitude fluctuations into axial frequency fluctuations. As these approach the size of the dip width, the dip can get lost in the background noise.

The rate-limiting step

The most time-consuming step of the nightly scan is discriminating between the $|1,\downarrow\rangle$ and $|0,\uparrow\rangle$ states after applying an anomaly pulse. The signal is the $|1,\downarrow\rangle \rightarrow |0,\downarrow\rangle$ decay. The drive is low enough that the state after the pulse usually remains $|0,\uparrow\rangle$,

which does not decay, and our confidence in that state-assignment grows as $1 - e^{-\gamma_c t}$ after waiting a time t with no decay. Since we want this confidence to be high, we typically wait several cyclotron lifetimes before proceeding. For example, if we wait five cyclotron lifetimes and make 100 attempts on a peak frequency with a 20% chance of flipping the spin, then far fewer than one of the final states will be misdiagnosed. If we wait only three cyclotron lifetimes, then on average one successful attempt would be mistakenly declared unsuccessful. Since the lifetimes can stretch upwards of five seconds, this wait time can be long indeed. Unfortunately, since inhibited sponteneous emission and cavity-shifts are closely linked, the cyclotron frequencies with the smallest cavity-shift uncertainty are also those with the longest lifetime and thus the fewest scans per night. While a typical night with a 1 s lifetime has over 70 scans, one at 7 s has fewer than half that number.

Multi-night composite scan

A single night of data yields resonances with signal-to-noise comparable to that shown in Fig. 4.4c and Fig. 4.5c. With several nights of data at the same magnetic field, we may average the results to reduce the uncertainty in g. We have used two methods for this averaging. In the first, used in our 2006 result [1], we analyze each night's data separately and average the resulting g-values. In the second, used in the new measurement presented in this thesis, we combine all the data into a single cyclotron and a single anomaly resonance, from which we extract g. To create a single pair of histograms, we extend the field-drift normalization technique above to longer timescales. After using the above edge-fitting procedure to remove the drift

from each night's data, we normalize all nights to a common field. At the same time, we account for any changes in $\bar{\nu}_z$ from night to night (we hold the axial potential constant throughout a nightly scan (see Section 2.3.1), but it may drift several ppb between scans). The resulting composite lines have much higher signal-to-noise ratios than the individual nightly scans, as shown in Fig. 4.8 and Fig. 6.2.

4.4 Splitting the Lines

After collecting sufficient cyclotron and anomaly data, we may use the signal-to-noise on the resonances to "split the lines" using our knowledge of the lineshapes and their properties to extract values for the frequencies with uncertainties smaller than the resonance linewidths. Our primary analysis technique exploits the invariance of the lineshape mean frequency from γ_z; we bin the data into a histogram and calculate its weighted mean to determine the resonance frequencies corresponding to the thermal rms axial amplitude: $\bar{\nu}_c^{z_{\rm rms}}$ and $\bar{\nu}_a^{z_{\rm rms}}$. As a check on the assumptions inherent in the weighted-mean method (discussed in the following section), we also fit the theoretical lineshape to the individual attempts and determine the resonance frequencies corresponding to zero axial amplitude: $\bar{\nu}_c^0$ and $\bar{\nu}_a^0$.

Since these two frequency pairs correspond to the cyclotron and anomaly frequency at different magnetic fields, they are related by the ratio ν_a/ν_c, which should be field-independent. When used to calculate g in Eq. 4.4, they should yield nearly identical values with the difference going as the product of $\Delta\omega/\omega_0 \sim 10^{-9}$ and $\nu_m/\nu_c \sim 10^{-6}$, far below our current precision. The agreement of the fits and the weighted-mean methods quantifies a "lineshape model uncertainty," which will be discussed in

Section 6.1.

4.4.1 Calculating the weighted mean frequencies

During the spectroscopy, we keep the transition rate low so the lines do not saturate and the average frequency of the lineshape is $\omega_0 + \Delta\omega$, independent of γ_z (see Eq. 4.11). This mean frequency corresponds to the magnetic field seen by the electron at its rms thermal axial amplitude, $\bar{\nu}^{z_{\rm rms}}$, and we may calculate g using the means of the measured cyclotron and anomaly lines. In addition, the mean of the measured data remains easily calculable even if the signal-to-noise of the measured resonance lines is poor, a concern particularly when analyzing a single night of data taken at a long-lifetime cyclotron frequency. The average frequency of the lineshape is unchanged by any magnetic field noise as long as the noise spectrum is symmetric about $\omega = 0$. This invariance is important because we see such noise through broadened cyclotron edges. Fits to noisy lines require the adoption of a full noise model. Because the weighted mean works with the relatively mild assumption of a symmetric noise distribution and does not require a determination of γ_z, we adopt it as our primary analysis technique.

The calculation of the mean involves discretizing the integral

$$\bar{\nu}^{z_{\rm rms}} = \langle\nu\rangle = \frac{\int \nu\chi(\nu)d\nu}{\int \chi(\nu)d\nu} \tag{4.28}$$

into the weighted sum

$$\bar{\nu}^{z_{\rm rms}} = \langle\nu\rangle = \frac{\sum_{i=1}^{N} w_i\nu_i}{\sum_{i=1}^{N} w_i}, \tag{4.29}$$

where the w_i are the weights. (Simulations of data for lineshapes with the parameters we experimentally observe show that any error introduced by this discretization

is smaller than the uncertainty calculated in the weighted mean and/or the lineshape model uncertainty.) Ideally, the summation index i would run over all individual excitation attempts. In practice, absent large overnight field drifts, the drift-corrected attempt frequencies tend to cluster around the original attempt frequencies and attempts to integrate across the large gaps between clusters, e.g., with a linear interpolation function, tend to be heavily dependent on the particular attempts that happen to lie nearest the gaps. We have found it much more reliable to bin the attempts into histograms, with the summation index i running over the histogram bins. While making a histogram discards information about individual attempt frequencies, the calculation becomes insensitive to results at a single attempt. We check to make sure the weighted mean is independent of the number of histogram bins.

For a histogram bin centered on ν_i with x_i excitations in n_i attempts, we define the excitation fraction

$$\xi_i \equiv \frac{x_i}{n_i}. \tag{4.30}$$

For bins that are evenly-spaced in frequency, Eq. 4.29 may be evaluated with weights equal to these excitation fractions. With arbitrarily-spaced bins, we may integrate a linear interpolation function between the histogram points, i.e., use the trapezoid rule, by assigning the weights

$$w_i = \begin{cases} \xi_1(\nu_2 - \nu_1) & \text{for } i = 1 \\ \xi_i \frac{1}{2}(\nu_{i+1} - \nu_{i-1}) & \text{for } i \neq 1 \text{ and } i \neq N \\ \xi_N(\nu_N - \nu_{N-1}) & \text{for } i = N \end{cases}, \tag{4.31}$$

where the endpoints are treated in such a way that it produces results identical to $w_i = \xi_i$ for equal bin-spacing. The shaded regions in Fig. 4.4c and Fig. 4.5c indicate

areas corresponding to $\sum w_i$.

The uncertainty in the average frequencies may be calculated with

$$\sigma_{\bar{\nu}\,z_{\rm rms}} = \sigma_{\langle\nu\rangle} = \sqrt{\sum_{i=1}^{N}\left(\frac{\langle\nu\rangle - \nu_i}{\sum_{j=1}^{N} w_j}\,\sigma_{w_i}\right)^2}. \tag{4.32}$$

The uncertainty in the weights is entirely due to uncertainty in the excitation fraction:

$$\sigma_{w_i} = \begin{cases} \sigma_{\xi_1}(\nu_2 - \nu_1) & \text{for } i = 1 \\ \sigma_{\xi_i}\dfrac{1}{2}(\nu_{i+1} - \nu_{i-1}) & \text{for } i \neq 1 \text{ and } i \neq N \\ \sigma_{\xi_N}(\nu_N - \nu_{N-1}) & \text{for } i = N \end{cases}. \tag{4.33}$$

This, in turn, is derived from the uncertainty in the number of excitations x_i. Assuming that the measured excitation fraction represents the actual probability of excitation, we may use the variance of the binomial distribution to write the excitation fraction uncertainty,

$$\sigma_{\xi_i} = \frac{\sigma_{x_i}}{n_i} = \sqrt{\frac{\xi_i(1-\xi_i)}{n_i}}. \tag{4.34}$$

4.4.2 Fitting the lines

As an additional analysis method to check the weighted-mean results, we fit the data to the lineshapes themselves. This analysis requires an estimate of γ_z, which at $\approx 2\pi(1\text{ Hz})$ is difficult to resolve precisely. In the presence of magnetic field noise faster than our edge-tracking method is capable of removing (minutes to hours) but slower than the coherence times given by the inverse-linewidths (200 μs–200 ms), it requires the adoption of a noise model. The section below is written for the noise-free expected lineshapes of Section 4.2, but we typically fit to these lineshapes convolved with a Gaussian noise model whose width is a fit parameter.

When fitting to the expected, noise-free cyclotron and anomaly lines, there are five parameters for which we lack independent determinations and thus must fit: the zero-axial-amplitude cyclotron and anomaly frequencies, $\bar{\nu}_c^0$ and $\bar{\nu}_a^0$; the axial temperature, T_z; and the Rabi frequencies, Ω_a and Ω_c. The axial temperature determines the width of the cyclotron line and both the width and a shift in the central value of the anomaly line. Since there is no feature on the anomaly lineshape to indicate the size of this shift and since the width can also have a large component from γ_c, the anomaly line is much less sensitive to T_z. Thus, we typically start by fitting the cyclotron line to determine $\bar{\nu}_c^0$, Ω_c, and T_z, then use that value for T_z in fitting the anomaly line for $\bar{\nu}_a^0$ and Ω_a. Because T_z determines the offset between the anomaly line and $\bar{\nu}_a^0$, any uncertainty in T_z contributes to uncertainty in $\bar{\nu}_a^0$. (If instead we fit the two lines simultaneously, the T_z and $\bar{\nu}_a^0$ parameters have a high correlation coefficient, which increases their uncertainties.) Below we discuss the fit routine for the cyclotron line. The routine used for the anomaly line is identical but with one fewer parameter.

Although we apply the drives at discrete frequencies, our drift-correction technique shifts the effective application frequency and, in general, these frequencies are no longer exactly the same. Rather than binning the attempts into a histogram, which would discard the information stored in these slightly different application frequencies, we fit to the individual attempts using the "maximum-likelihood method," see e.g., [114, Ch. 10] or [115, Ch. 5]. This point-by-point fitting is less critical for the multi-night composite lines, which have histogram bin widths comparable in size to the resulting frequency uncertainties; we include several histogram fits in the lineshape model analysis of Section 6.1.

For a given excitation attempt at ν_i and particular values for the fit parameters $\bar{\nu}_c^0$, Ω_c, and T_z, the probability p_i of a successful excitation is given by the lineshape in Eq. 4.16

$$p_i = P(\nu_i; \bar{\nu}_c^0, \Omega_c, T_z). \tag{4.35}$$

For repeated attempts at the same frequency, the probability of x_i successes in n_i attempts is given by the binomial distribution

$$P_B(x_i; n_i, p_i) = \frac{n_i!}{x_i!(n_i - x_i)!} p_i^{x_i} (1 - p_i)^{n_i - x_i}, \tag{4.36}$$

and for our point-by-point fitting, n_i is always 1 and x_i is either 0 or 1. For a given set of fit parameters, the total probability that N independent attempts would have the outcome recorded is the product of their individual probabilities. We define this product as the "likelihood function,"

$$\mathcal{L}(\bar{\nu}_c^0, \Omega_c, T_z) = \prod_{i=1}^{N} p_i^{x_i} (1 - p_i)^{1 - x_i}, \tag{4.37}$$

and fitting the line consists of maximizing it. In practice, the product of many probabilities, each less than 1, makes $\mathcal{L}$ very small, and we maximize the logarithm of the likelihood function,

$$M = \ln \mathcal{L} = \sum_{i=1}^{N} \ln(p_i^{x_i} (1 - p_i)^{1 - x_i}). \tag{4.38}$$

With M maximized, the uncertainty in the parameters is determined by the curvature in the vicinity of the maximum. For example, if there are no correlations among parameters the uncertainty in $\bar{\nu}_c^0$ is

$$\sigma_{\bar{\nu}_c^0} = \left(-\frac{\partial^2 M}{\partial \bar{\nu}_c^{0\,2}} \right)^{-1/2}. \tag{4.39}$$

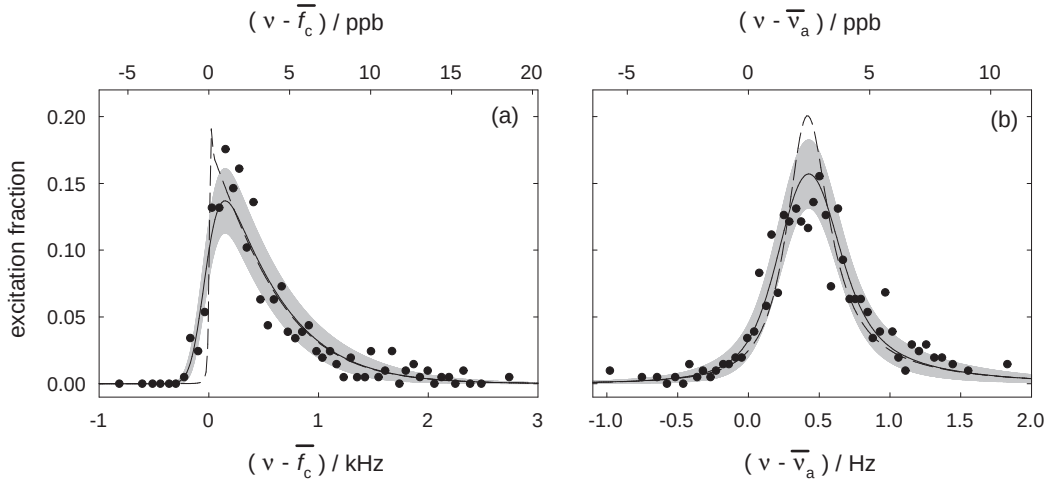

Figure 4.8: Results from maximum-likelihood fits to all of the 147.5 GHz cyclotron (a) and anomaly (b) data. To test the goodness of the fit, the individual attempt data have been binned into histograms (points). The gray bands indicate 68% confidence limits for distributions of measurements about the fit values. The dashed curves show the best-fit line with the Gaussian width set to zero.

In general, uncertainties in correlated parameters may be handled by inverting a curvature matrix, see e.g., [114, Ch. 7].

Figure 4.8 shows a pair of composite cyclotron and anomaly data sets binned into histograms. The edge of the exponential cyclotron line appears blurred by 0.5–1 ppb, indicating the presence of some magnetic field fluctuations. This blurred edge is seen in all of the g-value data (see Fig. 6.2 for similar plots from each field). Some possible sources of such fluctuations are discussed in Chapter 3. To produce meaningful fits, we must include a model of these fluctuations in the lineshape. We model the noise as normally distributed in frequency, producing a lineshape that

is the noise-free $\chi(\omega)$ convolved with a Gaussian resolution function.[6] The g-value calculated from fits to the Gaussian-noise lineshape provide a check on the weighted-mean calculation, and comparisons between the methods at each field quantify a lineshape model uncertainty, discussed in Section 6.1.

Also in Fig. 4.8 are comparisons of the histogrammed data to the best-fit Gaussian-noise lines. The gray confidence bands indicate where 68% of the histogram points should lie, given the number of excitation attempts and the fit results.[7] To emphasize the blurring of the cyclotron edge, the dashed line shows the lineshape corresponding to the best-fit parameters with the Gaussian width set to zero.

4.5 Summary

To measure g, we must determine the free-space cyclotron and anomaly frequencies. Using the cyclotron, anomaly, and axial trap eigenfrequencies, we can calculate the free-space values by applying three corrections: a special relativistic cyclotron frequency correction discussed in this chapter, a magnetron frequency correction arising from the electrostatic trapping potential and discussed in Chapter 2, and a cavity

[6]Because the noise-free cyclotron line is in the exponential lineshape limit, we actually fit the cyclotron data to the convolution of a Gaussian and an exponential, which is much faster than calculating the convolution with the full lineshape and yields identical results at our precision. Although the anomaly line is near the Lorentzian limit, there is some slight asymmetry in the noise-free line, so we do not make the Lorentzian approximation.

[7]The confidence intervals are calculated by extending the discrete binomial distribution to continuous values of x and integrating to 68.3% probability such that the remaining 31.7% is split evenly below and above the band. This differs from the standard method for estimating binomial confidence intervals, see e.g., [13, p. 308] or [116], which greatly overestimates the interval for low-probability points. For example with $n = 75$ attempts and the low probability $p = 10^{-6}$, the upper limit of a 68.3% confidence interval using our method is $p_+ = 2 \times 10^{-6}$, while the standard interval gives 0.02, which would predict at least one excitation in over 30% of the runs. Other than the plotted bands, these confidence intervals play no role in the data analysis.

shift discussed in Chapter 5. We use single quantum-jump spectroscopy to probe the cyclotron and anomaly resonances, whose expected lineshapes are primarily characterized by the magnetic bottle coupling between the axial energy and the cyclotron and anomaly frequencies. Magnetic field fluctuations add additional noise to these expected lineshapes. A weighted-mean calculation is our primary line-splitting method and uses a property of the expected lineshape, the invariance of its mean to changes in γ_z, to calculate g. Its validity relies on cyclotron and anomaly lines that are unsaturated, taken under identical temperature and drive conditions, and have a symmetric spectrum for any noise. To check these assumptions, we also fit the data to the expected lineshape convolved with a Gaussian noise model using the maximum-likelihood method. The agreement of the two methods quantifies a lineshape model uncertainty, analyzed in Chapter 6. First, we examine the third systematic frequency shift arising from the interaction of the electron cyclotron motion and the electromagnetic modes of the electrode cavity.

Chapter 5

Cavity Control of Lifetimes and Line-Shifts

The metal electrodes alter the density of radiation states away from its free-space value by forming a resonant microwave cavity. Electromagnetic modes of the correct field geometry can couple to the electron cyclotron motion, altering its damping rate [117, 118] and shifting its frequency [79, 1]. Typical cyclotron frequency shifts are at the parts-per-trillion level, and they affect the g-value primarily through the anomaly frequency. With the trap cyclotron eigenfrequency shifted from its free-space value, $\bar{\omega}_c = \omega_c \left(1 + \dfrac{\Delta\omega_c}{\omega_c}\right)$, one must apply a cavity correction to obtain the free-space g-value,[1]

$$\frac{g}{2} = 1 + \frac{\omega_s - \omega_c}{\omega_c} \simeq 1 + \frac{\omega_s - \bar{\omega}_c\left(1 - \frac{\Delta\omega_c}{\omega_c}\right)}{\bar{\omega}_c} = 1 + \frac{\bar{\omega}_a}{\bar{\omega}_c} + \frac{\Delta\omega_c}{\omega_c}. \tag{5.1}$$

[1]Not included here are additional relativistic and magnetron-frequency corrections, discussed in Section 4.1.

(The corresponding cavity shift of the spin frequency is of order $\hbar\omega_s/(2mc^2) \approx 10^{-9}$ smaller than the cyclotron shift and thus negligible [119].) Thus ppt-scale cavity shifts threaten to be a large systematic uncertainty if not understood.

With a cyclotron frequency far from any of these coupled modes, the lack of decay channels greatly inhibits spontaneous emission, giving us longer to detect a cyclotron excitation and providing a probe of the cavity mode structure itself. Our cylindrical electrode geometry [87], invented precisely for this application, allows us to compare measurements of γ_c to an analytic model of electron–cavity coupling [80, 120] in order to determine the frequencies and widths of the relevant cavity modes and to calculate the cyclotron frequency shifts.

We use two independent methods to investigate the cavity mode structure. First, the synchronization of a collective behavior of many electrons is sensitive to γ_c [121], and we measure the degree of synchronization as a function of cyclotron frequency. By mapping the mode locations over a large enough range, we compare their frequencies to those of the modes of an ideal cavity and identify them, and thus their field geometry, using standard identifiers such as TE_{127}. Second, we directly measure the cyclotron damping rate of a single electron as a function of cyclotron frequency, position in the trap, and axial oscillation amplitude. We demonstrate a 165(4) μm axial offset between the electrostatic center of the trap and the center as defined by the modes and place a limit of $\rho < 10$ μm on any radial offset. Using the mode locations determined by these two techniques, we calculate the relative cavity shifts, $\Delta\omega_c/\omega_c$, with uncertainties as low as 0.06 ppt, over six times smaller than the 0.39 ppt of our 2006 measurement [1].

5.1 Electromagnetic Modes of an Ideal Cylindrical Cavity

We begin with an examination of the electromagnetic fields in an ideal cylindrical cavity in order to gain some insight into the mode frequencies and geometries and to see which will couple to an electron or a cloud of many electrons. The boundary conditions for the electromagnetic field at a perfect conductor are

$$E_{\parallel} = 0 = B_{\perp}. \tag{5.2}$$

A right circular cylinder of diameter $2\rho_0$ and height $2z_0$ admits two classes of electromagnetic fields, dubbed "transverse-electric," or TE, and "transverse-magnetic," or TM. As the names suggest, TE and TM modes have no longitudinal component to their respective electric and magnetic fields. Deriving expressions for the electromagnetic fields is straightforward, see e.g., [122, Sec. 8.7],[2] and the result is

[2] In [122], the origin lies at the center of the bottom endcap whereas we put the origin at the center of the cavity.

For TE_{mnp}:

$$\begin{aligned}\mathbf{E} =& E_0 \frac{{}^{(E)}\omega_{mnp}}{c} \left(\frac{\rho_0}{x'_{mn}}\right)^2 \sin(\tfrac{p\pi}{2}(\tfrac{z}{z_0}+1)) \\ & \left[\mp\hat{\boldsymbol{\rho}}\ \frac{m}{\rho}\ J_m(x'_{mn}\tfrac{\rho}{\rho_0})\cos({}^{(E)}\omega_{mnp}t \mp m\phi)\right. \\ & \left. -\hat{\boldsymbol{\phi}}\ \frac{x'_{mn}}{\rho_0}\ J'_m(x'_{mn}\tfrac{\rho}{\rho_0})\sin({}^{(E)}\omega_{mnp}t \mp m\phi)\right] \end{aligned} \tag{5.3a}$$

$$\begin{aligned}\mathbf{B} =& \frac{E_0}{c}\left[\hat{\mathbf{z}}\ J_m(x'_{mn}\tfrac{\rho}{\rho_0})\sin(\tfrac{p\pi}{2}(\tfrac{z}{z_0}+1))\cos({}^{(E)}\omega_{mnp}t \mp m\phi)\right. \\ & + \frac{p\pi}{2z_0}\left(\frac{\rho_0}{x'_{mn}}\right)^2 \cos(\tfrac{p\pi}{2}(\tfrac{z}{z_0}+1)) \\ & \left[\ \hat{\boldsymbol{\rho}}\ \frac{x'_{mn}}{\rho_0}\ J'_m(x'_{mn}\tfrac{\rho}{\rho_0})\cos({}^{(E)}\omega_{mnp}t \mp m\phi)\right. \\ & \left.\left. \pm\hat{\boldsymbol{\phi}}\ \frac{m}{\rho}\ J_m(x'_{mn}\tfrac{\rho}{\rho_0})\sin({}^{(E)}\omega_{mnp}t \mp m\phi)\right]\right] \end{aligned} \tag{5.3b}$$

For TM_{mnp}:

$$\begin{aligned}\mathbf{E} =& E_0\left[\hat{\mathbf{z}}\ J_m(x_{mn}\tfrac{\rho}{\rho_0})\cos(\tfrac{p\pi}{2}(\tfrac{z}{z_0}+1))\cos({}^{(M)}\omega_{mnp}t \mp m\phi)\right. \\ & - \frac{p\pi}{2z_0}\left(\frac{\rho_0}{x_{mn}}\right)^2 \sin(\tfrac{p\pi}{2}(\tfrac{z}{z_0}+1)) \\ & \left[\ \hat{\boldsymbol{\rho}}\ \frac{x_{mn}}{\rho_0}\ J'_m(x_{mn}\tfrac{\rho}{\rho_0})\cos({}^{(M)}\omega_{mnp}t \mp m\phi)\right. \\ & \left.\left. \pm\hat{\boldsymbol{\phi}}\ \frac{m}{\rho}\ J_m(x_{mn}\tfrac{\rho}{\rho_0})\sin({}^{(M)}\omega_{mnp}t \mp m\phi)\right]\right] \end{aligned} \tag{5.3c}$$

$$\begin{aligned}\mathbf{B} =& \frac{E_0}{c}\frac{{}^{(M)}\omega_{mnp}}{c}\left(\frac{\rho_0}{x_{mn}}\right)^2 \cos(\tfrac{p\pi}{2}(\tfrac{z}{z_0}+1)) \\ & \left[\pm\hat{\boldsymbol{\rho}}\ \frac{m}{\rho}\ J_m(x_{mn}\tfrac{\rho}{\rho_0})\cos({}^{(M)}\omega_{mnp}t \mp m\phi)\right. \\ & \left. +\hat{\boldsymbol{\phi}}\ \frac{x_{mn}}{\rho_0}\ J'_m(x_{mn}\tfrac{\rho}{\rho_0})\sin({}^{(M)}\omega_{mnp}t \mp m\phi)\right]. \end{aligned} \tag{5.3d}$$

Each mode is identified by three indices: $m = 0, 1, 2, \ldots$, is the number of nodes as ϕ is swept through π radians; $n = 1, 2, \ldots$, is the number of antinodes in E_ϕ along

the radius; and $p =$ TE: $1, 2, \ldots$; TM: $0, 1, 2, \ldots$, is the number of antinodes along the axis.[3] They have characteristic frequencies given by

$$ {}^{(E)}\omega_{mnp} = c\sqrt{\left(\frac{x'_{mn}}{\rho_0}\right)^2 + \left(\frac{p\pi}{2z_0}\right)^2} \tag{5.4a} $$

$$ {}^{(M)}\omega_{mnp} = c\sqrt{\left(\frac{x_{mn}}{\rho_0}\right)^2 + \left(\frac{p\pi}{2z_0}\right)^2}. \tag{5.4b} $$

Both here and in Eq. 5.3, ${}^{(E)}$ and ${}^{(M)}$ refer to TE and TM modes, x_{mn} is the nth zero of the order-m Bessel function, i.e., $J_m(x_{mn}) = 0$, and x'_{mn} is the nth zero of the derivative of the order-m Bessel function, i.e., $J'_m(x'_{mn}) = 0$. The zeros force the boundary conditions at the cylindrical wall. All but the $m = 0$ modes are doubly degenerate, as indicated by the $\pm$ signs in Eq. 5.3. Physically, the degenerate modes are identical except one rotates clockwise and the other counterclockwise.

Figure 5.1 represents some examples of the fields in Eq. 5.3. Of primary concern is the magnitude of the transverse ($\hat{\boldsymbol{\rho}}$ and $\hat{\boldsymbol{\phi}}$) electric fields, since only these components couple to cyclotron motion. For both TE and TM modes, the transverse components of $\mathbf{E}$ are proportional to

$$ \sin\left(\tfrac{p\pi}{2}\left(\tfrac{z}{z_0}+1\right)\right) = \begin{cases} (-1)^{p/2}\sin\left(\tfrac{p\pi z}{2z_0}\right) & \text{for even } p, \\ (-1)^{(p-1)/2}\cos\left(\tfrac{p\pi z}{2z_0}\right) & \text{for odd } p, \end{cases} \tag{5.5} $$

such that close to the trap center ($z \approx 0$), only modes with odd p have any appreciable coupling. Furthermore, the transverse components are proportional to either the order-m Bessel function times m/ρ or the derivative of the order-m Bessel function,

[3] Here we use the standard notation for TE and TM modes, see e.g., [122]. Other references more concerned about the specific modes that couple to an electron at the center of the trap, e.g., [80, 79, 120], use the notation (n, l) that corresponds to the present notation with $mnp \leftrightarrow 1l(2n+1)$.

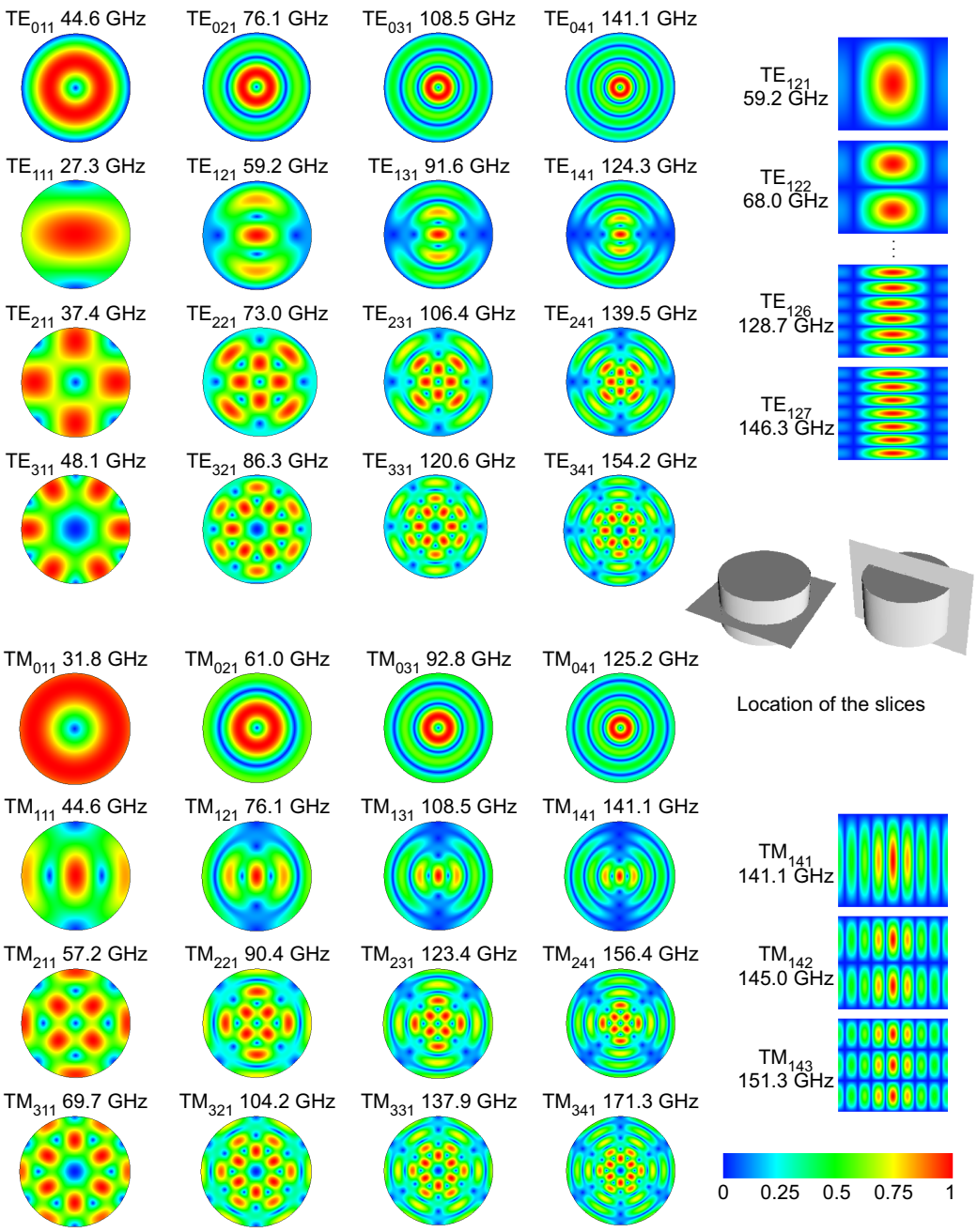

Figure 5.1: Examples of cylindrical cavity modes. Plotted is the magnitude of the transverse electric field, normalized to its maximum value. Both horizontal and vertical cross-sections are taken through the center of the cavity, as shown. The only modes with nonzero transverse electric field at the trap center are $\mathrm{TE}_{1n(\mathrm{odd})}$ and $\mathrm{TM}_{1n(\mathrm{odd})}$. The TM_{mn0} modes have purely longitudinal electric fields and are not shown. The frequencies shown are calculated using Eq. 5.4 and the cavity dimensions in the caption to Table 5.1.

which close to the trap center ($\rho \approx 0$) go as

$$\frac{m}{\rho}\ J_m(x^{(\prime)}_{mn}\tfrac{\rho}{\rho_0}) \sim \begin{cases} \dfrac{1}{(m-1)!}\left(\dfrac{x^{(\prime)}_{mn}}{2\rho_0}\right)^m \rho^{m-1} & \text{for } m > 0 \\ 0 & \text{for } m = 0 \end{cases} \tag{5.6a}$$

$$\frac{x^{(\prime)}_{mn}}{\rho_0} J'_m(x^{(\prime)}_{mn}\tfrac{\rho}{\rho_0}) \sim \begin{cases} \dfrac{1}{(m-1)!}\left(\dfrac{x^{(\prime)}_{mn}}{2\rho_0}\right)^m \rho^{m-1} & \text{for } m > 0 \\ -\dfrac{x^{(\prime)2}_{0n}}{2\rho_0^2}\rho & \text{for } m = 0. \end{cases} \tag{5.6b}$$

In the limit $\rho \to 0$, all but the $m = 1$ modes vanish. To summarize, the only modes that couple to an electron perfectly centered in the trap are $\mathrm{TE}_{1n(\mathrm{odd})}$ and $\mathrm{TM}_{1n(\mathrm{odd})}$.

Coupling the cyclotron motion to the axial motion, such as for sideband cooling (Chapter 7), is facilitated by modes with either an electric field gradient that goes as $z\hat{\boldsymbol{\rho}}$ or $\rho\hat{\mathbf{z}}$ or a z, ρ-independent magnetic field (the coupling then comes from the magnetic Lorentz force, $-e\ \mathbf{v} \times \mathbf{B}$). From the small z, ρ-dependence above, we can see that, at the trap center, the $\mathrm{TE}_{1n(\mathrm{even})}$ and $\mathrm{TM}_{1n(\mathrm{even})}$ modes have a $z\hat{\boldsymbol{\rho}}$ dependence in their electric fields and position-independent transverse magnetic fields. The $\mathrm{TM}_{1n(\mathrm{even})}$ modes have the electric-field $\rho\hat{\mathbf{z}}$ dependence as well. In addition, all the $1n(\mathrm{odd})$ modes have the correct fields at their nodes, which can be reached by offsetting the axial potential minimum.

The cavity formed by the trap electrodes closely matches the ideal cavity described above though it differs in several important ways. First, the electrodes are not perfectly conducting and have a characteristic skin-depth in which they dissipate energy. We will model this phenomenologically below by assigning a quality factor, Q, to the modes. Second, any slight deformation of the cylindrical ring electrode will remove the mode degeneracy and assign separate frequencies to pairs of modes with $m \neq 0$.

In practice, we see little evidence of this splitting. Lastly, the slits between electrodes and machining imperfections can shift the mode frequencies away from their ideal values and modify their widths. Surface currents exist wherever the magnetic field parallel to the surface is nonzero, and one effect of the slits is to impede currents that would normally flow axially along the wall or radially on the endcaps. The TE_{0np} modes should be less susceptible to these shifts because they are the only modes with no such currents. Previous measurements over a large range of cyclotron frequencies indicate good agreement between the predicted and measured frequencies of the TE_{0np} modes [123, 121]. In contrast, the TM_{1np} modes, which should be degenerate with these TE_{0np} modes, are nearly always several linewidths away. Another effect of the slits is to allow microwave power to leak out of the cavity, decreasing the mode Q by amounts that depend on the mode field geometry. To help combat this effect, we have built $\lambda/4$ choke flanges into every trap slit to increase the effective impedance of the slits and reflect stray fields back into the cavity.

5.2 Mode Detection with Synchronized Electrons

In order to accurately calculate the coupling between the cavity modes and a single electron, we must know the mode structure in the real trap cavity. A straightforward but time-consuming method is to measure the electron cyclotron damping rate, γ_c, as a function of cyclotron frequency; we pursue this technique in Section 5.4. A faster method, originally discussed in [124], uses the synchronized axial motion of many electrons as a sensitive probe of γ_c and is the subject of this section.

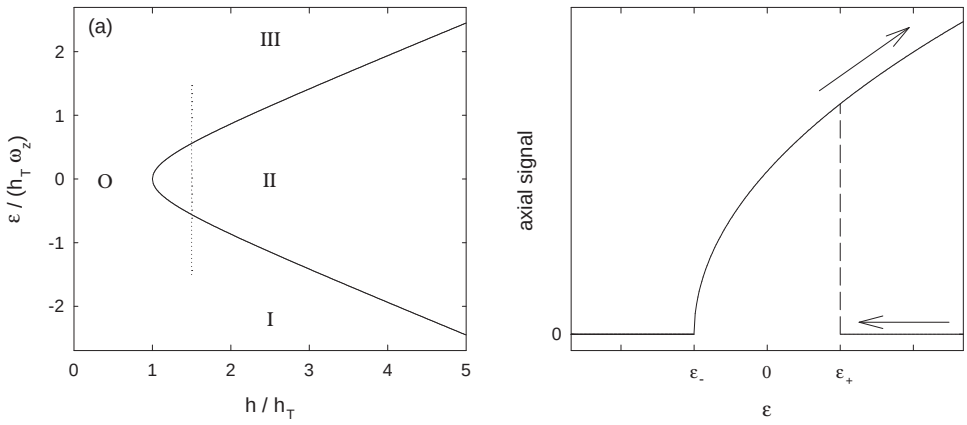

Figure 5.2: The damped Mathieu equation for a drive of strength h and detuned ε from twice the resonant frequency has four regions (a) characterized by threshold phenomena, phase bistability, and hysteresis. The parametric lineshape (b) displays hysteresis in the direction of the frequency-sweep. The dotted line in (a) indicates the sweep range of (b).

5.2.1 The parametric resonance

A parametric resonance can occur when the parameters of a system are themselves functions of time. In this case, we modulate the trapping potential on the bottom endcap at a frequency near twice the axial frequency. One can write this as a frequency modulation of an ω_z carrier. For an electron with axial position z, the motion is governed by the differential equation

$$\ddot{z} + \gamma_z \dot{z} + \omega_z^2 \left\{1 + h\cos\left[(2\omega_z + \varepsilon)t\right]\right\} z + \frac{2C_4}{1+C_2}\omega_z^2 \frac{z^3}{d^2} + \frac{3C_6}{1+C_2}\omega_z^2 \frac{z^5}{d^4} = 0, \qquad (5.7)$$

where the drive is parameterized with a dimensionless strength h (see Section 2.3.2) and is detuned by ε from $2\omega_z$. The anharmonic terms play an important role at high oscillation amplitudes; the anharmonicity coefficients, C_i, and characteristic trap dimension, d, are defined in Chapter 2. At low amplitudes ($z \ll d$), these terms may be ignored, and Eq. 5.7 is the damped Mathieu equation with well-documented solutions for various ranges of h and ε, see e.g., [125].

Figure 5.2 summarizes the characteristic solutions. For low drive strength, region O, all oscillations are damped away by the amplifier and there is no motion. Above a threshold drive strength,

$$h_T = \frac{2\gamma_z}{\omega_z}, \tag{5.8}$$

the solution breaks into three characteristic regions depending on the detuning, with the boundary between the regions determined by

$$\varepsilon_\pm = \pm\frac{1}{2}\omega_z\sqrt{h^2 - h_T^2} \tag{5.9}$$

In region II ($\varepsilon_- < \varepsilon < \varepsilon_+$), the quiescent state is unstable and the electron oscillates at the axial frequency with an exponentially-growing amplitude. The anharmonic components of Eq. 5.7 arrest this growth and force the motion into limit-cycle oscillations. There are two such limit-cycles that are 180° out of phase with each other. For $C_4 > 0$, region I ($\varepsilon < \varepsilon_-$), has the same properties as region O and only the quiescent state is stable. In region III ($\varepsilon > \varepsilon_+$), all three states, the quiescent and both limit-cycles, are stable and the electron motion displays hysteresis, remaining in the quiescent state if entered by changing h from region O and an excited state if entered by sweeping the drive frequency from region II. For $C_4 < 0$, regions I and III interchange. Figure 5.2b displays an example of the parametric resonance and the lineshape hysteresis as the drive is swept among regions I, II, and III.

5.2.2 Spontaneous symmetry breaking in an electron cloud

The axial equation of motion for each electron in a cloud is similar to Eq. 5.7 but the damping is proportional to the cloud center-of-mass (CM) velocity and a Coulomb

term couples the axial and radial degrees of freedom [123, Sec. 3.4]. With the radius no longer explicitly zero, the anharmonic terms gain a ρ-dependence and the radial equation of motion, including the cyclotron damping rate, comes into play. If one sums the equations for all electrons, the result does not factor into an equation for the CM because of the radii and the anharmonic terms, e.g., $\sum z_i^3 \neq (\sum z_i)^3$.

In a remarkable and not-yet fully understood effect, there exists a parameter space where the cloud displays the threshold and hysteretic phenomena described in the single-electron case with a CM amplitude proportional to the cyclotron damping rate, as indicated by a Lorentzian profile of the axial signal when ν_c is swept across a cavity mode [123, 124, 121]. The electrons behave as if they form a pair of clouds, one in each limit-cycle of region II. With equal numbers of electrons in each cloud, there would be no net CM motion and, since our amplifier detects CM velocity, no signal. The observed CM motion means that the increased cooling from a cavity mode breaks the symmetry, creating an excess of electrons in one phase. This synchronization of electrons has been seen in clouds from a hundred thousand electrons down to only two [126]. (The single electron also oscillates in one limit-cycle instead of both [127], but this is due to decoherences in any two-limit-cycle superposition rather than a synchronization effect.) The actual dynamics is more complicated, as 180° phase-fluctuations are seen in the resulting signal, indicating that electrons switch between limit-cycles at a rate that depends on electron number, electrostatic anharmonicity, parametric drive strength, and cyclotron damping rate [123, Ch. 5] and [121]. The threshold energy, however, is independent of γ_c.

How does increasing γ_c lead to symmetry-breaking in the parametric resonance,

and what stops the synchronization before all electrons are in one of the two phases? While one can write down the full equations of motion for N electrons [121, App.], a detailed solution showing the observed collective behavior remains underived. Presumably, increased cyclotron damping has a cooling effect on the cloud, which is heated by the parametric drive and the Johnson noise of the detection circuit. Since the heating mechanisms both affect the axial motion, while γ_c damps the transverse motion, the cooling relies on collisions to transfer energy between the two degrees of freedom. The symmetry-breaking may arise from the increased collisions in one large cloud rather than two smaller ones, with fluctuations in electron number between the two limit-cycles coming from the axial noise sources. Additional clues may be found in the detailed study of these fluctuations as well as the Fourier spectra of the CM signal [123, Ch. 5].[4]

5.2.3 Parametric mode maps

Insofar as the axial CM signal is a probe of γ_c, we may use it to map out the resonant modes of the cavity. Figure 5.3 shows three examples of such parametric mode maps made by monitoring the axial CM signal while sweeping the cyclotron frequency, i.e., the magnetic field. Such a sweep takes several hours. Map *a* is reproduced from [83, Fig. 5.5] and is included here for comparison because it was taken in the same trap under similar conditions as the others. We discuss the striking

[4]The observed electron synchronization inspired a related series of experiments at Seoul National University in which neutral atoms in a magneto-optical trap were parametrically excited by intensity-modulating the trapping beams. The bifurcation of the quiescent state into two equally-occupied limit-cycle states was directly imaged [128], as was spontaneous symmetry-breaking between these two states [129]. There, the broken symmetry arises from a "shadow effect," where one cloud blocks the cooling laser from the other, and the symmetry-breaking is limited before total synchronization by a repulsive "reradiation effect," whereby one atom absorbs a photon emitted by another.

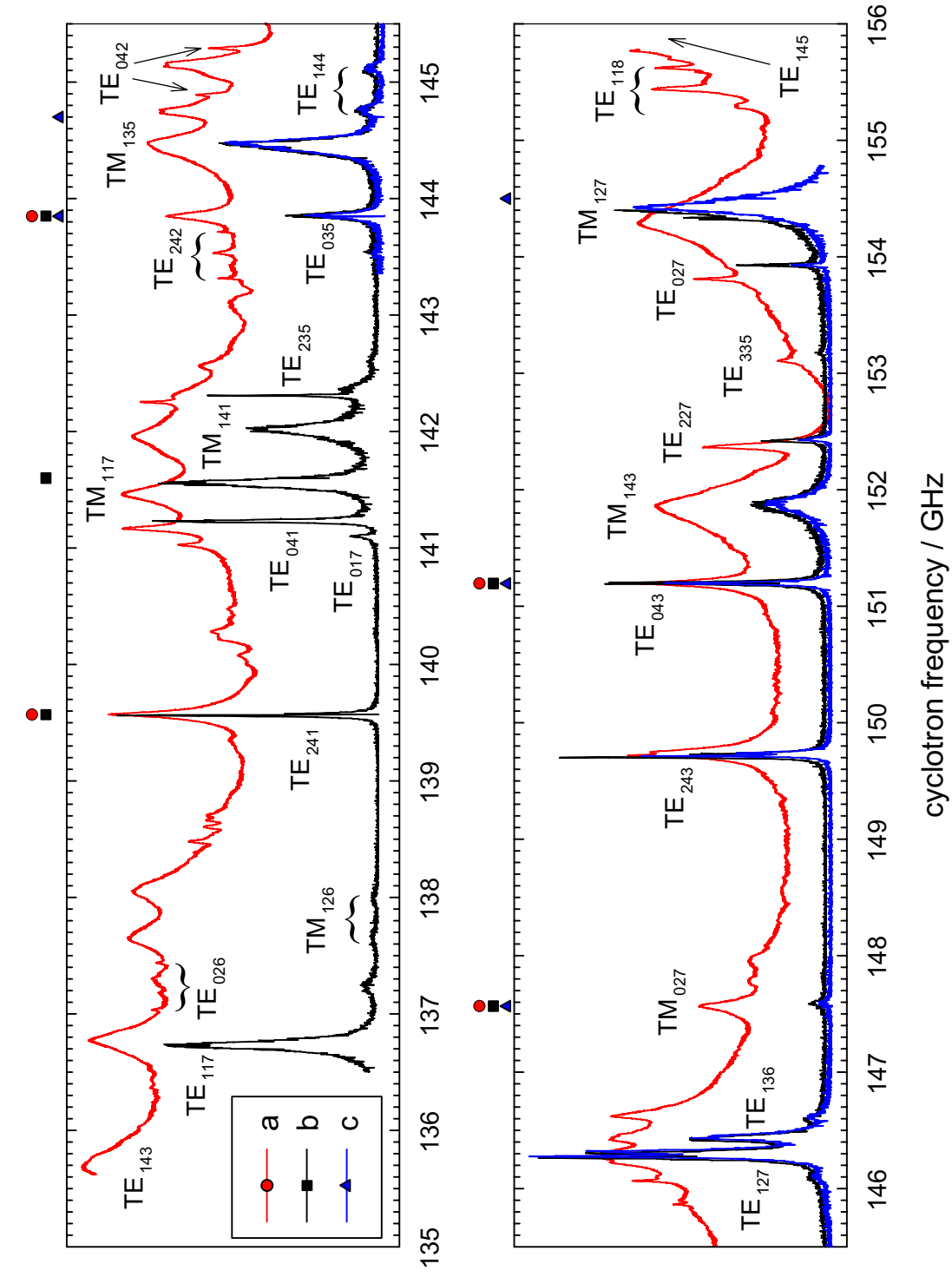

Figure 5.3: Three parametric mode maps. Map *a* reproduces [83, Fig. 5.5] and was taken in the same trap as the others under similar conditions; its striking difference is discussed in the text. The calibration frequencies are indicated with symbols above the plots, and some calibration dips are visible in maps *b* and *c*.

difference between map a and maps b and c below but turn first to a discussion of the features found in all three.

Calibrating the mode maps

Map a is calibrated by moving the magnetic field to the locations indicated by red circles and measuring the cyclotron frequency directly. Maps b and c are calibrated during the sweep by applying a strong cyclotron drive at discrete frequencies, indicated by black squares and blue triangles. When the electrons come into resonance with the drive, the magnetic bottle shifts their axial frequency far enough that the parametric drive is no longer resonant and the signal disappears, producing a sharp dip in the map. One such dip may clearly be seen on TE_{241}, near 139.6 GHz. The cyclotron frequencies for the remainder of each map are assigned with a linear interpolation function between these discrete calibration points.

Comparing the mode frequencies with those of an ideal cylinder with dimensions similar to the trap dimensions allows us to identify the modes. In the frequency range shown, all TE modes with $m = 0, 1, 2$ and all TM modes with $m = 1$ are identified with two exceptions: TE_{217} at $\nu \approx 138.9$ GHz, which has n much lower than the observed TE_{2np} modes, and TM_{142} at $\nu \approx 145$ GHz, which is weakly coupled because of its low, even p. Table 5.1 summarizes the measured mode frequencies and Qs based on Lorentzian fits to mode maps b and c. It includes frequencies calculated from the cylinder dimensions that give the closest agreement to the measured frequencies of the TE_{0np} modes, whose frequency should be closest to that of an ideal cavity because their purely-azimuthal electric fields produce no surface currents that are impeded by

mode	calculated frequency / GHz	measured frequency / GHz	measured Q
TE_{117}	136.568	136.729(8)	1500(100)
TE_{026}	137.276		
TM_{126}	137.276	137.818(10)	730(90)
TE_{241}	139.502	139.563(8)	7500(600)
TE_{017}	141.044	141.097(8)	5000(1000)
TE_{041}	141.095	141.231(8)	5600(500)
TM_{117}	141.044	141.557(8)	1760(140)
TM_{141}	141.095	142.014(8)	1080(90)
TE_{235}	142.347	142.307(8)	14100(1400)
TE_{242}	143.457		
TE_{035}	143.926	143.8518(6)	2500(150)
TM_{135}	143.926	144.458(4)	1250(60)
TE_{144}	145.078	144.933(7)	1500(200)
TE_{042}	145.007		
TE_{127}	146.307	146.289(7)	4600(900)
TE_{136}	146.449	146.436(7)	2200(60)
TM_{027}	147.075	147.5893(9)	2100(90)
TE_{243}	149.817	149.720(6)	10000(4000)
TE_{043}	151.301	151.1970(4)	5900(400)
TM_{143}	151.301	151.865(4)	890(10)
TE_{227}	152.403	152.426(5)	5100(200)
TE_{335}	153.269		
TE_{027}	153.928	153.928(1)	8800(600)
TM_{127}	153.928	154.432(8)	980(80)

Table 5.1: Measured mode frequencies and Qs for the modes identified in the maps of Fig. 5.3 along with their frequencies calculated using Eq. 5.4 and the trap dimensions from a least-squares fit to the TE_{0np} mode locations ($\rho_0 = 4548.41$ μm, $z_0 = 3880.58$ μm). The measured frequencies are based on Lorentzian fits to maps b and c (modes only appearing in map a are left blank) and account for normal mode splitting by averaging the frequencies of the two peaks. The fitted Qs are influenced by strong coupling and should be treated only as estimates of the actual mode Qs.

the trap slits.

These three maps were taken using the same trap over the course of 18 months, during which time the electrodes were thermally cycled to room temperature several times, the refrigerator was inserted and removed, and the magnet was quenched with the electrodes inside. At no point were the electrodes themselves disassembled or adjusted. The general alignment of the features and the precise alignment of the calibration points indicate that the trap cavity and its resonant modes are robust against stresses and thermal cycles. Any misalignments in the location of a particular mode may be attributed to the calibration process, specifically to nonlinear charging rates from the power supplies, rather than to real shifts in the mode frequencies. Thus, once we have determined the locations of the cavity modes, we need not fear that they shift over time and may confidently apply cavity-shift corrections to g-value data even though the cavity and g-value data may have been taken months apart.

5.2.4 Mode map features

Strong plasma–cavity coupling

Three important features aid the understanding of the maps. First, the criterion for Lorentzian lineshapes is that the probe of the cyclotron damping rate only weakly couples to the cavity mode, that is, any energy transfered from the cloud to the mode is damped quickly through resistive losses in the walls. Failure to satisfy this criterion allows the energy to transfer back into the cyclotron motion, ringing several times between electrons and mode before damping away. This oscillation splits the Lorentzian response into a pair of normal modes. The figure-of-merit, η, for this

effect relates the coupling rate between N electrons and the mode, $N\lambda_{\rm M}$ (defined in Section 5.3), to the mode width, $\Gamma_{\rm M}$, or quality factor, $Q_{\rm M}$, [121]

$$\eta = \frac{2N^2\lambda_{\rm M}^2}{\Gamma_{\rm M}^2} = \frac{2N^2\lambda_{\rm M}^2 Q_{\rm M}^2}{\omega_{\rm M}^2}. \tag{5.10}$$

Maps a, b, and c had $N = 26\,000$, $18\,000$, and $17\,000$, leading to $\eta \gg 1$ for most high-Q modes and clear normal mode splitting. This splitting is most obvious in TE_{127} in Fig. 5.3 and Fig. 5.4, but is clear in others when plotted on an enlarged scale. The cavity QED community often refers to this effect as "strong coupling" or "vacuum Rabi splitting," and various papers on the effect note that the mode frequency is midway between the two peaks and that the Q of the split peaks is higher than the mode Q, see e.g., [130, 131, 132, 133].

Motional sidebands

A second feature arises from the axial motion of the cloud during the measurement. Since the axial oscillation amplitude is limited only by trap anharmonicities, it can be quite large. Large axial oscillations across the cosine or sine electric field profile of a mode will amplitude-modulate γ_c, a topic fully explored in Section 5.3.3 and Appendix A. For a cloud oscillating about the trap center, modes with nodes at the center (even p) have a response entirely in the odd-order sidebands at $\omega_{\rm M} \pm \omega_z$, $\omega_{\rm M} \pm 3\omega_z$, and so on, while those with central antinodes (odd p) have a primary response at $\omega_{\rm M}$ with sidebands at $\omega_{\rm M} \pm 2\omega_z$ and the even multiples of ω_z. In both cases, the coupling to the sidebands will depend on the oscillation amplitude and the wavelength of the mode standing-wave pattern, with more prominent sidebands at higher amplitudes and shorter wavelengths (larger p). These motional sidebands are

clearly visible at TE_{144}, near 145 GHz in Fig. 5.3.

Coupling to modes beyond the trap center

A third set of features arises from either the non-zero cloud size or a relative offset between the electrostatic center and the mode center. For a cloud of hundreds or thousands of electrons, the size of the plasma allows it to couple to modes beyond just $1n$(odd). As the cloud extends in radius, it couples to modes with $m \neq 1$. Since the transverse electric field of a mode goes as ρ^{m-1} (ρ for $m = 0$, see Eq. 5.6), we would expect to couple more strongly to modes with m close to 1. Indeed, in Fig. 5.3, we see coupling to modes with $m = 0, 2$ in addition to $m = 1$. Additionally, a larger n increases the number of antinodes along the radius, pushing the nearest one closer, which should increase the coupling to the plasma. We see this effect in the stronger coupling to TE_{027} ($\nu \approx 154$ GHz) than to TE_{017} ($\nu \approx 141$ GHz).

Nonzero size along the axis requires a modification to the sideband discussion of the previous section because not all electrons oscillate precisely about a node or antinode of the mode standing wave. This offset allows coupling to all modes at all axial sidebands, including at the central peak for modes with nodes at the trap center (even p).

Both the coupling to modes with $m \neq 1$ and the presence of additional axial sidebands could occur if the cloud were offset radially or axially from the center of the cavity modes, and determining whether we see the effects because of finite cloud size or an offset will be important when we turn to the single-electron cavity coupling. In the single-electron case, only the offset effects will remain.

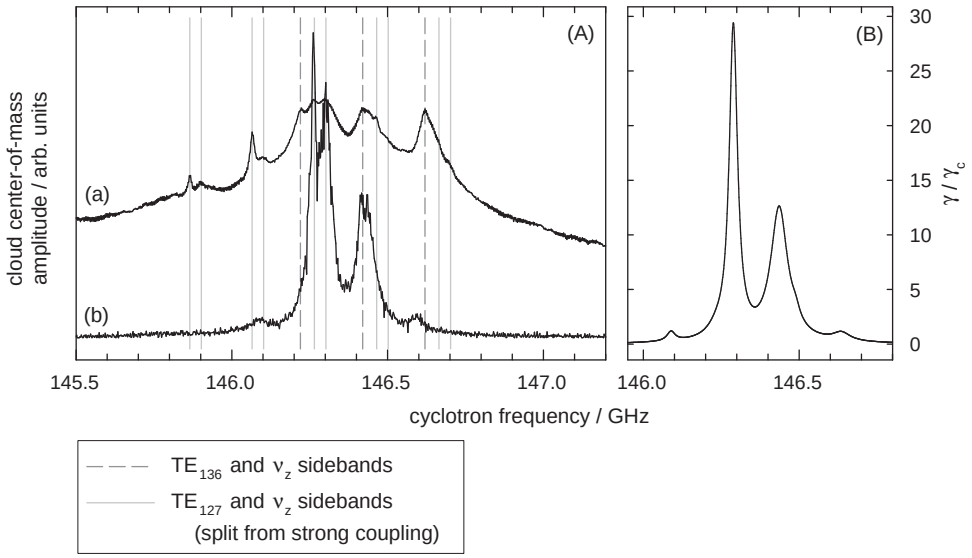

Figure 5.4: Modes TE_{127} and TE_{136} with sidebands. The data (A) are from maps *a* and *b* of Fig. 5.3. The left pair of prominent peaks near 146.3 GHz are TE_{127}, which is split from strong coupling between the plasma and the cavity. The peak near 146.4 GHz is TE_{136}. Vertical bars spaced one axial frequency (200 MHz) apart indicate the expected sideband separation. The existence of the $\pm\nu_z$ sidebands of TE_{127} and of the central peak of TE_{136} suggest that the cloud is not centered axially with respect to the modes. Plot B shows the calculated cyclotron damping rate for a cloud offset 250 μm axially and oscillating with a 100 μm amplitude.

Figure 5.4A gives an expanded view of the region around TE_{127} and TE_{136}, revealing that both modes have central peaks and first-order sidebands (note that TE_{127} also shows normal-mode splitting). Second-order sidebands appear as well for TE_{127} on the upper mode map (map *a* of Fig. 5.3). In order to determine whether the central peak of TE_{136} and the odd-order sidebands of TE_{127} arise from nonzero cloud size or from an axial offset, we can model the coupling to the two modes using the discussion of single-mode coupling with axial oscillations in Section 5.3.3. Using the mode frequencies and Qs of Table 5.1, if the electron cloud is approximated as a sphere of uniform density and centered in the trap, it would need a radius of nearly 600 μm to

have the observed relative peak-heights of TE_{127} and TE_{136}. By contrast, a zero-size cloud would need an offset of approximately 250 μm; the calculated coupling at such an offset is shown in Fig. 5.4B. Both of these estimates are heavily Q-dependent, but different Qs will change both lengths in the same way, e.g., a higher Q for TE_{136} would reduce the estimates for both the 600 μm radius and the 250 μm offset. In both estimates, we use an axial amplitude of 100 μm, which reproduces the observed axial sideband amplitudes.

We may check the reasonableness of a 600 μm radius by calculating the expected plasma radius, which, for a spheroidal cloud of N electrons with radius a, half-height b, and aspect ratio $\alpha \equiv b/a$, is [134]

$$a^3 = \frac{3N}{4\pi\epsilon_0}\frac{e^2 f(\alpha)}{\alpha m \omega_z^2}, \tag{5.11}$$

where the function

$$f(\alpha) = \frac{1}{\alpha^2 - 1}\left[\frac{\alpha}{\sqrt{1-\alpha^2}}\arctan\left(\frac{\sqrt{1-\alpha^2}}{\alpha}\right) - 1\right] \tag{5.12}$$

indicates the square of the ratio of the axial frequency to the plasma frequency (the frequency at which charge density perturbations oscillate in the plasma) and equals 1/3 for a sphere ($\alpha = 1$). For our electron numbers, $N \approx 20,000$, a spherical cloud should have a 150 μm radius, suggesting that either the cloud is not spherical or that it is offset axially from the mode center. We shall see in Section 5.4.3 that the latter is indeed the case.

Mode map consistency

As discussed in Section 5.2.2, the mechanism responsible for translating γ_c into a center-of-mass signal in a parametrically driven cloud is not yet understood. Since

many parameters, including drive strength and frequency, anharmonicity of the trapping potential, and electron number, influence the behavior of the parametric resonance, one might imagine finding the regime in which the collective motion is controlled by the cyclotron damping rate, as is necessary for mapping the cavity modes, would be a difficult task. Early studies [123, 121] found just the opposite—the degree of cloud synchronization closely followed γ_c for wide ranges of parameters, yielding Lorentzian mode profiles except in cases of strong coupling or motional sidebands. Subsequent uses of the technique, including in this thesis, have failed to reproduce this robustness [135, 83].

Figure 5.3 shows two of the three styles of mode maps we have seen: the "good" style of maps *b* and *c*, with Lorentzian mode profiles and no CM motion far from modes, and the "always-synchronized" style of map *a*, where the CM motion never disappears but increases and decreases with γ_c. The third and most common style of map, "doesn't-work," is characterized by a synchronization (or lack thereof) that does not change with magnetic field. We have investigated a range of the parameter space without being able to reproducibly switch among the three map styles. Some clues as to why the previously robust method is no longer so may be found in the primary differences between our apparatus and that of [123, 121]: a forty-times lower cavity temperature and ten-times deeper axial potential increase the inter-particle Coulomb interaction and enhance collective motion [136, 137] and [96, App. B], while ten-times larger electron clouds (we found that smaller clouds rapidly saturated with all electrons in one of the two phases) and a more heavily filtered and noise-free electrical environment should reduce the fluctuations between the bistable states.

We emphasize, however, that although we are unable to create a clean mode map on demand, the ones that we have made are consistent with each other in both the location of the modes and the presence of an offset between the electrostatic and mode centers. This consistency despite the variety of parametric results indicates that the cavity itself is quite stable.

5.3 Coupling to a Single Electron

Having discussed a many-electron method of characterizing the frequency and Q of the cavity modes, we turn to a detailed analysis of the coupling of these modes to a single electron. The importance of such an analysis is twofold: first, measurements of γ_c will allow an independent characterization of the cavity mode structure, and second, it is required for the calculation of the cavity shifts, $\Delta\omega_c$, themselves.[5] In this first of the single-electron-coupling sections, we present an analytic expression for the cyclotron frequency shift and damping rate due to the interaction of the electron with the cavity modes. This expression has been derived before for a centered electron $(z, \rho = 0)$ [80], and we extend it to arbitrary position in the trap in order to include any misalignment between the trap electrostatic and mode centers. In addition, we model the cyclotron damping rate as measured at the rather large amplitudes achieved with our self-excited oscillator (SEO) detection. The results for any misalignment will be important in calculating the g-value shift arising from the cyclotron frequency shift; the high-axial-amplitude corrections will not affect the g-value, which is measured at a much lower axial amplitude with both the SEO and the amplifiers off.

[5]The cavity shift, $\Delta\omega_c$, is not to be confused with the linewidth parameter, $\Delta\omega$, of Eq. 4.7.

5.3.1 Single-mode approximation

Before beginning the full calculation, it is worth modeling the interaction between the electron and a single nearby mode, here denoted M, to give an indication of the character of the electron–mode coupling. This approximation will eventually be the starting point for modeling the coupling including axial motion in Section 5.3.3. The interaction may be approximated as that of two coupled oscillators with the resulting electron frequency shift and damping rate given by [120]

$$\Delta\omega_c = \frac{\gamma_\mathrm{M}}{2}\frac{\delta}{1+\delta^2} \tag{5.13a}$$

$$\gamma = \gamma_\mathrm{M}\frac{1}{1+\delta^2}. \tag{5.13b}$$

Here, γ_M is the cyclotron damping rate when the electron is exactly resonant with the mode and δ is the relative detuning, defined as

$$\delta = \frac{\omega_c' - \omega_\mathrm{M}}{\Gamma_\mathrm{M}/2}. \tag{5.14}$$

The mode full-width at half-maximum, Γ_M, arises because of losses in the cavity and may be written in terms of a quality factor, Q_M, with the usual definition: $Q_\mathrm{M} = \omega_\mathrm{M}/\Gamma_\mathrm{M}$. The cyclotron frequency is maximally-shifted by $\pm\gamma_\mathrm{M}/4$ at $\delta = \pm 1$. Furthermore, provided the cyclotron frequency is detuned far enough from a mode that $\delta \gg 1$, i.e., $(\omega_c - \omega_\mathrm{M})/\omega_\mathrm{M} \gg 1/(2Q_\mathrm{M})$, the shift is Q-independent.

We define a coupling constant λ_M in terms of the mode Q_M and the electron damping rate:

$$\frac{\gamma_\mathrm{M}}{\omega_\mathrm{M}} = 2Q_\mathrm{M}\left(\frac{\lambda_\mathrm{M}}{\omega_\mathrm{M}}\right)^2. \tag{5.15}$$

In the next section, we derive analytic expressions for these coupling constants for

arbitrary axial and radial positions with the results

$$ {}^{(E)}\lambda_{mnp}^2 = \frac{2r_0c^2}{z_0\rho_0^2}\frac{-(1+\mathrm{sgn}(m))}{J_m''(x'_{mn})J_m(x'_{mn})}\sin^2(\tfrac{p\pi}{2}(\tfrac{z}{z_0}+1))R_J(m;x'_{mn}\tfrac{\rho}{\rho_0}) \tag{5.16a} $$

$$ {}^{(M)}\lambda_{mnp}^2 = \frac{2r_0c^2}{z_0\rho_0^2}\frac{1+\mathrm{sgn}(m)}{J'_m(x_{mn})^2}\left(\frac{p\pi}{2z_0}\frac{c}{{}^{(M)}\omega_{mnp}}\right)^2\sin^2(\tfrac{p\pi}{2}(\tfrac{z}{z_0}+1))R_J(m;x_{mn}\tfrac{\rho}{\rho_0}), \tag{5.16b} $$

where $r_0 = \dfrac{1}{4\pi\epsilon_0}\dfrac{e^2}{mc^2}$ is the classical electron radius, ${}^{(E)}$ and ${}^{(M)}$ refer to TE and TM modes, $x_{mn}^{(\prime)}$ are the previously mentioned zeros of the Bessel functions and their derivatives, and the signum function,

$$ \mathrm{sgn}(m) = \begin{cases} -1 & \text{for } m<0 \\ 0 & \text{for } m=0\,, \\ 1 & \text{for } m>0 \end{cases} \tag{5.17} $$

accounts for the double degeneracy of modes with $m > 0$. The entire radial dependence of the coupling is contained in the R_J function, defined by

$$ R_J(m;x) = \frac{m^2}{x^2}J_m(x)^2 - J'_m(x)^2. \tag{5.18} $$

For zero radius, R_J equals $1/2$ if $m = 1$ and zero otherwise. We may now rewrite the frequency shift and damping rate of Eq. 5.13 in terms of the mode coupling constant as

$$ \Delta\omega_c - i\frac{\gamma}{2} = \frac{\omega\lambda_M^2}{\omega^2 + i\omega\Gamma_M - \omega_M^2}, \tag{5.19} $$

where ω is the shifted cyclotron frequency.

It is tempting to expand on the single-mode approximation above by adding the contributions of many modes. This mode-sum approach is fundamentally flawed because the real part is infinite [80]. A linear divergence arises from the inclusion of

the electron self-field contribution to the cavity radiation rather than only the field reflected from the walls. A calculation that explicitly removes the electron self-field from the cavity standing wave, i.e., "renormalizes" the field, yields a finite result and is the subject of the next section.

5.3.2 Renormalized calculation

In this derivation of the frequency shifts and damping rates, as a function of arbitrary electron position, we follow closely the calculation of [80], which contains the result for a fully-centered particle ($z, \rho = 0$) as well as many details omitted here. While it is possible to tackle the full cylindrical cavity directly, removing the electron self-field from such a calculation is difficult. Thus, we begin with a calculation for two parallel conducting plates, i.e., the cylindrical cavity with $\rho_0 \to \infty$. Here, the result may be written as a series of image charges. Renormalizing this sum is trivial—we simply omit the electron and leave the image charges, a result we will call Σ_P. We then proceed to the calculation of the full cylindrical cavity and omit the contribution from the endcaps, leaving only the correction from the cylindrical wall, a result we will call Σ_S. The final result will be the sum of the contributions from the endcaps and the wall. At a cyclotron frequency ω, the frequency shift, $\Delta\omega_c$, and damping rate, γ, will be given in terms of these two contributions, the free space damping rate, γ_c, and a quality factor, Q, for all modes:

$$\Delta\omega_c - \frac{i}{2}\gamma = -\frac{i}{2}\gamma_c + \omega\left\{\Sigma_S\left[\omega(1+\tfrac{i}{2Q}), z, \rho\right] + \Sigma_P\left[\omega(1+\tfrac{i}{2Q}), z\right]\right\}. \tag{5.20}$$

The effect of the cavity on the electron may be modeled as an electric field $\mathbf{E}'(\mathbf{r})$ arising from image charges in the walls. It modifies the transverse equation of motion

to read

$$\dot{\mathbf{v}} - \boldsymbol{\omega_c} \times \mathbf{v} + \frac{e}{m}\nabla V(\mathbf{r}) + \frac{1}{2}\gamma_c \mathbf{v} = \frac{e}{m}\mathbf{E}'(\mathbf{r}). \tag{5.21}$$

The longitudinal part of $\mathbf{E}'(\mathbf{r})$ gives a negligible correction to the trapping potential $V(\mathbf{r})$ [80, Sec. II], but the transverse part generates the anticipated effects. Using the radiation gauge, $\nabla \cdot \mathbf{A} = 0$, the electric field may be written as the time derivative of the vector potential. This vector potential satisfies the wave equation with a transverse current source and thus may be written as the convolution of that source, the moving electron, and a Green's function subject to the appropriate boundary conditions, see e.g., [122, Sec. 6.3-6.4]. Combining the two transverse velocity components as $v = v_x - iv_y = v_0 e^{-i\omega t}$, one can then write Eq. 5.21 as[6]

$$\Delta\omega_c - \frac{i}{2}\gamma + \frac{i}{2}\gamma_c = -\omega r_0 \tilde{D}'_{xx}(\omega; \mathbf{r}, \mathbf{r}), \tag{5.22}$$

where $r_0 = \dfrac{1}{4\pi\epsilon_0}\dfrac{e^2}{mc^2}$ is again the classical electron radius (Appendix A shows some of the details in transforming Eq. 5.21 into Eq. 5.22). $\tilde{D}'_{kl}(\omega; \mathbf{r}, \mathbf{r}')$ is the Fourier transform of the part of that Green's function that arises due to the presence of the cavity walls. That is, it explicitly excludes the electron self-field. Note that $\tilde{D}'_{xx}(\omega; \mathbf{r}, \mathbf{r})$ is in general complex, with the real portion corresponding to frequency shifts and the imaginary portion to a modified damping rate.

Parallel-plate calculation

As mentioned before, we begin with the shift from two parallel plates, a straightforward image-charge calculation. The Fourier transform of the Green's function at

[6] In [80], the frequency and damping shifts here called $\Delta\omega_c - i\gamma/2$ are written as $\omega - \omega'_c = R(\omega) - iI(\omega)/2$.

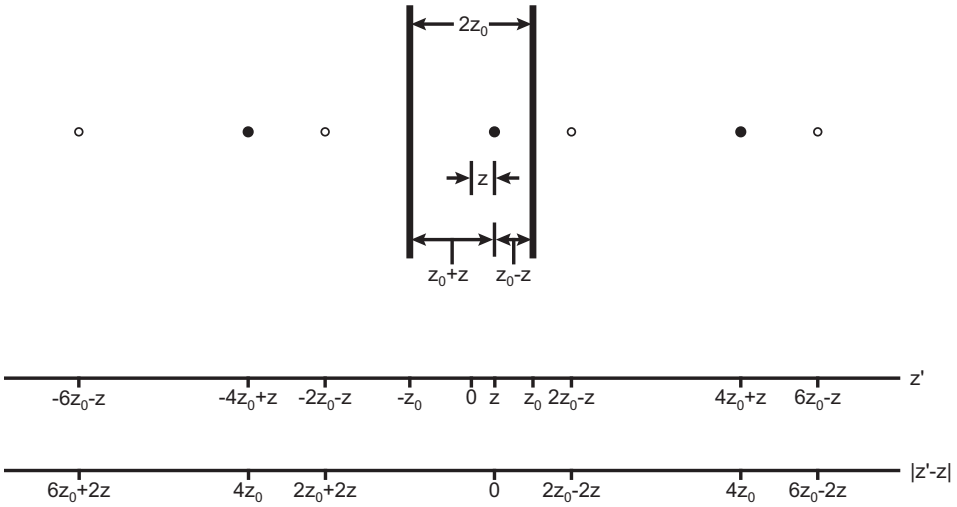

Figure 5.5: Image charges of an electron offset from the midpoint of two parallel conducting plates. The charges alternate sign, as indicated by the open/filled circles.

z' for an electron at z depends only on the distance $|z'-z|$ and is [80, Sec. III]

$$\begin{aligned}\tilde{D}^{(0)}_{xx}(\omega;z'-z) \equiv & F(z'-z) = 4\pi \int \frac{d^3k}{(2\pi)^3}\left(1-\frac{k_x^2}{k^2}\right)\frac{e^{-ik_z(z'-z)}}{k^2-(\omega+i\epsilon)^2/c^2} \\ = & \frac{1}{|z'-z|}\left(e^{i\omega|z'-z|/c}\left(1+\frac{ic}{\omega\,|z'-z|}-\frac{c^2}{(\omega(z'-z))^2}\right)+\frac{c^2}{(\omega(z'-z))^2}\right).\end{aligned} \tag{5.23}$$

For a single conducting plane, the method of images allows us to satisfy the boundary conditions with a single image charge. For two parallel conducting plates, an infinite series is required, as shown in Fig. 5.5. The parallel-plate component of the cavity effect is simply the sum of all the contributions from the image charges:

$$\begin{aligned}\Sigma_P(\omega,z) \equiv & -r_0\tilde{D}'^{(P)}_{xx}(\omega;z,z) = -r_0\left[2\sum_{j=1}^{\infty}F(4jz_0)\right. \\ & \left.-\sum_{j=1}^{\infty}F(2(2j-1)z_0+2z)-\sum_{j=1}^{\infty}F(2(2j-1)z_0-2z)\right].\end{aligned} \tag{5.24}$$

Note that the $j=0$ term has been removed from the first sum. This exclusion of the electron self-field is the explicit renormalization required to avoid an infinite result. Note also that setting $z \to 0$ recovers [80, Eq. 3.7].

The parallel-plate component depends on an axial offset but not a radial one because of the transverse symmetry of two parallel plates. Its imaginary part has a sawtooth form with sharp teeth where the frequency corresponds to an integral number of half-wavelengths between the two endcaps (only the odd integers for $z = 0$ since the even integers have a node there). The real part shows peaks at similar intervals. The nearest such frequency corresponds to eight half-wavelengths at 154.5 GHz, far enough away that the parallel-plate contribution is smooth in our region of interest.

Cylindrical-wall calculation

The cylindrical-wall component is considerably more complicated. The derivation for $z \neq 0$ differs from that of [80, Sec. IV] in a trivial way—we do not substitute $z = 0$ into $\sin(kz)$ and $\cos(kz)$. The inclusion of the ρ-dependence adds a function R_I as well as a sum over the mode-index m. The result is

$$\begin{aligned}\Sigma_S(\omega, z, \rho) = -\frac{r_0}{z_0}\sum_{p=1}^{\infty}\sin^2\left(\tfrac{p\pi}{2}\left(\tfrac{z}{z_0}+1\right)\right) \\ \times\sum_{m=0}^{\infty}(1+\mathrm{sgn}(m))\left[\frac{K'_m(\mu_p\rho_0)}{I'_m(\mu_p\rho_0)}R_I(m;\mu_p\rho)\right. \\ \left.+\left(\frac{p\pi c}{2\omega z_0}\right)^2\left(\frac{K_m(\mu_p\rho_0)}{I_m(\mu_p\rho_0)}R_I(m;\mu_p\rho)-\frac{K_m(\frac{p\pi\rho_0}{2z_0})}{I_m(\frac{p\pi\rho_0}{2z_0})}R_I(m;\tfrac{p\pi\rho}{2z_0})\right)\right]\end{aligned} \tag{5.25}$$

with

$$\mu_p = \sqrt{\left(\frac{p\pi}{2z_0}\right)^2 - \left(\frac{\omega}{c}\right)^2}, \tag{5.26}$$

$$R_I(m;x) = \frac{m^2}{x^2}I_m(x)^2 + I'_m(x)^2, \tag{5.27}$$

and the signum function defined in Eq. 5.17.[7] The sums include modified Bessel functions of the first ($I_\nu(x) = i^{-\nu}J_\nu(ix)$) and second ($K_\nu(x) = \frac{\pi}{2}\frac{I_{-\nu}(x) - I_\nu(x)}{\sin(\nu\pi)}$) kinds as well as their derivatives, see e.g., [113, Ch. 11]. The $K'_m(\mu_p\rho_0)/I'_m(\mu_p\rho_0)$ term comes from the boundary conditions of the TE modes, while the $K_m(\mu_p\rho_0)/I_m(\mu_p\rho_0)$ term comes from the TM modes. For $\rho \to 0$, the R_I functions all go to zero except when $m = 1$, when it goes to $1/2$. For $z \to 0$, only the odd-p terms survive. Combined, these limits reproduce [80, Eq. 4.28].

For a given p, an increasing ω will eventually cross a threshold at which μ_p becomes zero and then imaginary. At that point, we may use the definition of $I_m(x)$ to substitute

$$I_m(\mu_p\rho_0) = i^{-m}J_m(\tilde{\mu}_p\rho_0), \tag{5.28}$$

where $\tilde{\mu}_p$ is the now-real quantity $i\mu_p$. Since $J_m(x)$ and $J'_m(x)$ have a number of zeros, after ω exceeds the p^{th} threshold the sum has poles that may be approximated as

$$\Sigma_S(\omega, z, \rho) \approx \frac{{}^{(E,M)}\lambda^2_{mnp}}{\omega^2 - {}^{(E,M)}\omega^2_{mnp}}. \tag{5.29}$$

For TE modes, the poles occur when $J'_m(\tilde{\mu}_p\rho_0)$ has a zero, that is, when $\omega = {}^{(E)}\omega_{mnp}$ of Eq. 5.4. For TM modes, they occur when $\omega = {}^{(M)}\omega_{mnp}$. Expanding the Bessel functions about their zeros, yields the mode coupling strengths of Eq. 5.16. Given the above, we can see that the summation indices p and m in Eq. 5.25 correspond directly to those in the mode indices, mnp, and the addition of the m, p^{th} term of the sums adds the contributions from all modes of that m and p. The threshold above which

[7] Following the exact procedure in [80, Sec. IV] without taking the $\rho \to 0$ limit will lead to a ϕ-dependence in Σ_S. This is an artifact of the paper's axial-symmetry assumption in using $\tilde{D}'_{xx}$ instead of $\tilde{D}'_{kl}$. One solution is to redo the calculation using the general $\tilde{D}'_{kl}$. Alternately, since the modes physically rotate in time (see Eq. 5.3), it is appropriate to average over this ϕ, which appears only as $\sin^2\phi$ and $\cos^2\phi$ (and not as $m\phi$).

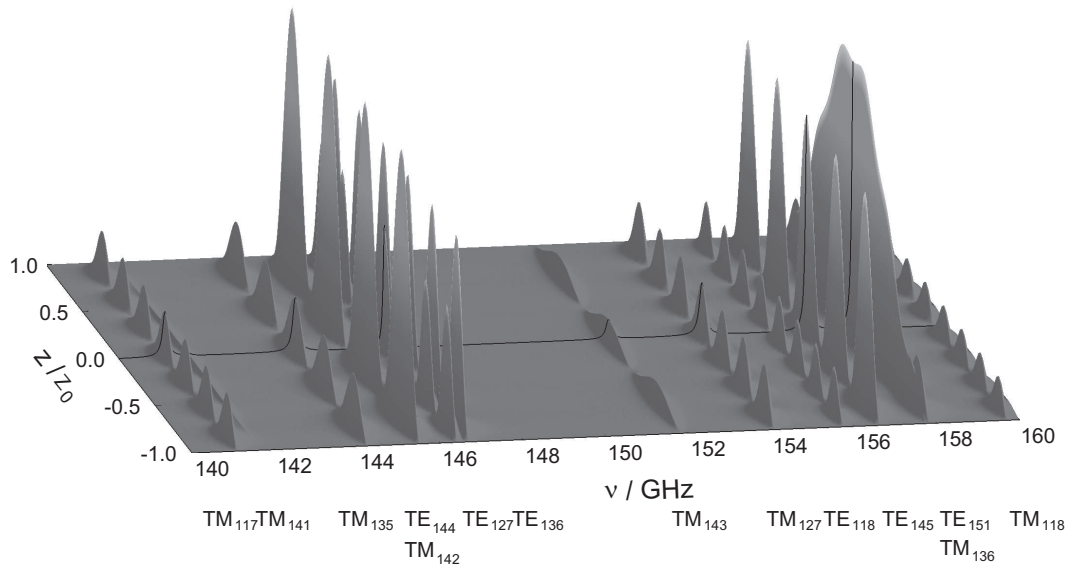

Figure 5.6: Calculated cyclotron damping rates at various z. The black line indicates the mode structure at the trap center. The highest point corresponds to a damping rate approximately fifty times the free-space rate.

μ_p is imaginary corresponds to the frequency whose half-wavelength fits between the endcaps p times.

Total renormalized calculation

The combination of Σ_P and Σ_S in Eq. 5.20 is the result of the renormalized calculation. There, we have included cavity dissipation in the from of a mode Q with the replacement $\omega \rightarrow \omega(1 + \frac{i}{2Q})$. It is possible to include different quality factors for the TE and TM mode classes by using ${}^{(E)}Q$ in the denominator functions $I'_m(\mu_p\rho_0)$ and ${}^{(M)}Q$ everywhere else [80]. It is not possible to include a Q for each mode separately.

The result of a renormalized calculation of the cyclotron damping rate as a function of cyclotron frequency and axial offset (for a radially-centered electron) is shown in Fig. 5.6. Since it is calculated for $\rho = 0$, only the $m = 1$ modes are present. Clearly

observable are the p antinodes between the endcaps and the coupling or lack thereof at the trap center, indicated by a black line.

The strength of the renormalized calculation is its removal of the electron self-energy. It has an important drawback in that the entire calculation has only four input parameters: ρ_0, z_0, ${}^{(M)}Q$, and ${}^{(E)}Q$. It does not allow the input of arbitrary mode frequencies and Qs. If the dominant mode-couplings are to one TE and one TM mode, then the two mode frequencies and Qs can determine the four input parameters. The addition of a third mode, however, over-constrains the problem; unless the three modes happen to have frequencies that correspond to those of an ideal cavity and two happen to share Qs, the renormalized calculation will give an incorrect result.

A hybrid renormalized/mode-sum method

A method for better approximating the cavity-shift given imperfect agreement between measured and calculated mode frequencies is a hybrid renormalized/mode-sum approach. One begins with the renormalized calculation using the two most strongly coupled modes to set the input parameters. Using the single-mode approximation of Eq. 5.19, one then corrects the contribution from any additional mode by subtracting it with its ideal frequency and Q and adding it back in with its measured frequency and Q. Since the coupling strengths of Eq. 5.16 are based on expansions around poles in the renormalized sum, the infinities remain under control.

In this thesis, we must use such a technique because three modes couple to the electron: TE_{127}, TM_{143}, and TE_{136}. Since the electron is close to (but not precisely in) the mode center, the two modes with antinodes at the center (odd p) dominate

the coupling, and we set the four input parameters of the renormalized calculation with the frequencies and Qs of TE_{127} and TM_{143}. We use the mode-moving technique of the previous paragraph for TE_{136} with one alteration: we move the full term, $-\frac{2r_0}{z_0}\sin^2(3\pi(\frac{z}{z_0}+1))\frac{K_1'(\mu_6\rho_0)}{I_1'(\mu_6\rho_0)}R_I(1;\mu_6\rho)$, rather than just the Lorentzian approximation. Although this moves all modes with TE_{1n6} the next-nearest ones are far away: ${}^{(E)}\omega_{126}/(2\pi) \approx 129$ GHz and ${}^{(E)}\omega_{146}/(2\pi) \approx 169$ GHz. Moving the full term has the advantage of a complete cancellation in the mode subtraction rather than leaving artifacts of uncanceled higher-order corrections.

5.3.3 Single-mode coupling with axial oscillations

We have just shown that the coupling strength to the cavity modes depends on the axial position of the electron. In addition to any axial offset, the amplitude of the axial motion itself will modulate the coupling at ω_z. Accounting for this modulation is a nontrivial task, which is intractable for the full renormalized calculation but doable for the single-mode coupling provided that the axial amplitude, A, is much lower than a quarter-wavelength of the mode's axial standing wave ($A \ll z_0/p$). Our typical axial self-excitations fall within this low-amplitude limit with

$$\begin{aligned} A &\approx 50\text{–}150\ \mu\mathrm{m} & \frac{\lambda}{4}_{\mathrm{TE}_{127}} &\approx 550\ \mu\mathrm{m} \\ \frac{\lambda}{4}_{\mathrm{TE}_{136}} &\approx 645\ \mu\mathrm{m} & \frac{\lambda}{4}_{\mathrm{TM}_{143}} &\approx 1300\ \mu\mathrm{m}. \end{aligned} \tag{5.30}$$

All of the z-dependence in the mode-coupling parameters ${}^{(E,M)}\lambda_{mnp}$ of Eq. 5.16 comes in a single sine function:

$${}^{(E,M)}\lambda_{mnp} = \sin(\tfrac{p\pi}{2}(\tfrac{z}{z_0}+1))\tilde{\lambda}_{\mathrm{M}}, \tag{5.31}$$

where we define $\tilde{\lambda}_{\mathrm{M}}$ to be the non-z-dependent part of the coupling. For an electron offset z from the center of the modes and oscillating at frequency ω_z with amplitude $A \ll z_0/p$, we may expand the mode axial-dependence in terms of axial harmonics,

$$\sin(\tfrac{p\pi}{2}(\tfrac{z+A\cos(\omega_z t)}{z_0}+1)) = \sum_{j=0}^{\infty} f_j(z,A)\cos(j\omega_z t), \tag{5.32}$$

where the $f_j(z,A)$ are functions of the axial offset and amplitude. The first three are

$$f_0(z,A) = \sin(\tfrac{p\pi}{2}(\tfrac{z}{z_0}+1))\left[1-\left(\frac{p\pi A}{4z_0}\right)^2+O(A^4)\right] \tag{5.33a}$$

$$f_1(z,A) = \cos(\tfrac{p\pi}{2}(\tfrac{z}{z_0}+1))\left[\frac{p\pi A}{2z_0}-O(A^3)\right] \tag{5.33b}$$

$$f_2(z,A) = \sin(\tfrac{p\pi}{2}(\tfrac{z}{z_0}+1))\left[-\left(\frac{p\pi A}{4z_0}\right)^2+O(A^4)\right]. \tag{5.33c}$$

As derived in Appendix A, including this expansion of the axial oscillation in the transverse equation of motion (Eq. 5.21) yields an amplitude-dependence to the single-mode coupling strength as well as a series of axial harmonics to the mode frequency, ω_{M}:

$$\Delta\omega_c - i\frac{\gamma}{2} = \frac{\tilde{\lambda}_{\mathrm{M}}^2\omega}{2}\sum_{j=0}^{\infty} f_j(z,A)^2\left[\frac{1}{\omega^2-(\omega_{\mathrm{M}}-j\omega_z)^2}+\frac{1}{\omega^2-(\omega_{\mathrm{M}}+j\omega_z)^2}\right]. \tag{5.34}$$

As before, we may include a damping width by substituting $\omega \to \omega(1+\frac{i}{2Q})$ in the two fractions within the brackets. Note that taking the $A \to 0$ limit recovers the usual single-mode coupling of Eq. 5.19.

5.4 Single-Electron Mode Detection

With a good electron–cavity coupling model now in hand, we may use the single-electron cyclotron damping rate as a probe of the cavity mode structure. This probe

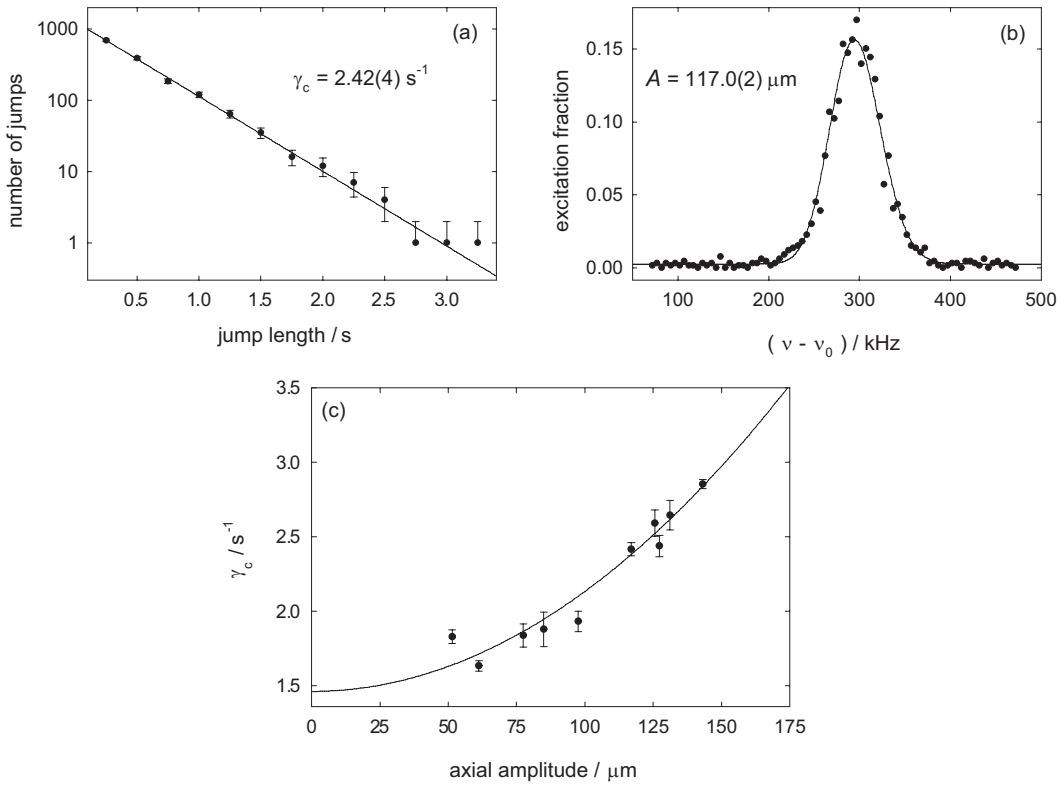

Figure 5.7: Measurement of the cyclotron damping rate at 146.70 GHz, near the upper sideband of TE_{136}. The cyclotron damping rate as a function of axial amplitude (c) extrapolates to the desired lifetime. Each point in (c) consists of a damping rate measured from a fit to a histogram of cyclotron jump lengths (a) as well as an axial amplitude measured from a driven cyclotron line (b).

will determine the mode frequencies and Qs independent of the multi-electron method of Section 5.2. In the sections below, we use measurements of the cyclotron damping rate as a function of cyclotron frequency and of position in the trap to determine the position and Q of the three closest coupled modes and to characterize the alignment of the electrostatic and mode centers.

5.4.1 Measuring the cyclotron damping rate

Since we are able to perform a quantum-nondemolition measurement on the cyclotron state (see Section 2.3.4), measuring the cyclotron damping rate simply consists of making many (typically hundreds) of jumps and fitting the distribution of jump lengths to a decaying exponential with time-constant γ_c^{-1}, as in Fig. 5.7a. A complication arises because, in order to detect the jumps, the electron must be self-excited to a large axial amplitude, A. When ν_c is close to the frequency of a coupled cavity mode, the axial oscillation modulates the coupling as discussed in Section 5.3.3, adding an amplitude-dependence to the lifetime measurement. Therefore, in order to find the zero-amplitude damping rate, we must measure the damping rate as a function of amplitude and extrapolate back to $A = 0$. The amplitude-dependence goes as even powers of A (see Section 5.3.3), and since the amplitude is much less than a quarter-wavelength for the relevant modes, terms of higher-order in A get progressively smaller, allowing extrapolation with a quadratic function,

$$\gamma(A) = \gamma(0) + \gamma_2 A^2. \tag{5.35}$$

We measure the axial amplitude with the driven cyclotron lineshape of Eq. 4.14, where the driven axial motion in the magnetic bottle causes the electron to see a higher average magnetic field, resulting in a cyclotron frequency shift as in Fig. 5.7b. Figure 5.7c shows an example of the measured damping rate as a function of amplitude close to the upper axial sideband of TE_{136} ($^{(E)}\nu_{136} + \nu_z$). It displays a large amplitude-dependence in the cyclotron damping rate because of the proximity of ν_c and the sideband, which becomes more prominent as larger axial oscillations increase the modulation of the mode coupling.

5.4.2 Fitting the cyclotron lifetime data

After repeating such measurements at many cyclotron frequencies, we amass two sets of data: the zero-amplitude cyclotron decay rates, $\gamma(0)$, and the quadratic amplitude-dependence coefficients, γ_2, as functions of ν_c. From these data, we wish to extract the frequencies of the three nearest $m = 1$ modes, TE_{127}, TE_{136}, and TM_{143}. Since the lifetimes are heavily Q-dependent, we must include three Qs, bringing the total number of fit parameters to six.

Building the fit function

The renormalized calculation provides the model for fitting the zero-amplitude cyclotron decay rates. Since it has only four free parameters, we allow it to determine the frequencies and Qs of TE_{127} and TM_{143} and add the TE_{136} parameters by hand, subtracting the TE_{1n6} term in the renormalized calculation for the calculated frequency and Q and adding it back in with the frequency and Q as free parameters, as discussed on page 145.

For the quadratic-amplitude-dependence data, we use the A^2 term in the single-mode coupling expansion of Section 5.3.3 to write

$$\begin{aligned}\gamma_2 = -2\sum_{\mathrm{M}} \mathrm{Im}\Bigg\{ \frac{\tilde{\lambda}_{\mathrm{M}}^2\omega}{2}\Bigg[&\sin^2\left(\tfrac{p\pi}{2}\left(\tfrac{z}{z_0}+1\right)\right)\left(\frac{p\pi}{4z_0}\right)^2 \frac{-4}{\omega^2 + i\frac{\omega\omega_{\mathrm{M}}}{Q_{\mathrm{M}}} - \omega_{\mathrm{M}}^2} \\ &+ \cos^2\left(\tfrac{p\pi}{2}\left(\tfrac{z}{z_0}+1\right)\right)\left(\frac{p\pi}{2z_0}\right)^2 \Bigg(\frac{1}{\omega^2 + i\frac{\omega(\omega_{\mathrm{M}}-\omega_z)}{Q_{\mathrm{M}}} - (\omega_{\mathrm{M}}-\omega_z)^2} \\ &+ \frac{1}{\omega^2 + i\frac{\omega(\omega_{\mathrm{M}}+\omega_z)}{Q_{\mathrm{M}}} - (\omega_{\mathrm{M}}+\omega_z)^2}\Bigg)\Bigg]\Bigg\},\end{aligned} \tag{5.36}$$

where the sum is over the three modes of interest.

	$\mathbf{TE_{127}}$		$\mathbf{TE_{136}}$		$\mathbf{TM_{143}}$	
	$\boldsymbol{\nu_c}$ **/ GHz**	$\boldsymbol{Q}$	$\boldsymbol{\nu_c}$ **/ GHz**	$\boldsymbol{Q}$	$\boldsymbol{\nu_c}$ **/ GHz**	$\boldsymbol{Q}$
lifetime	146.322(13)	4900(300)	146.415(2)	4800(200)	151.811(16)	1270(70)
mode map	146.289 (7)	4600(900)	146.436(7)	2200 (60)	151.865 (4)	890(10)

Table 5.2: Comparison of the mode parameters from the single-electron lifetime fits and the multi-electron parametric mode maps.

We may thus form a $\chi^2_{\gamma(0)}$ using the zero-amplitude data and the renormalized calculation and a $\chi^2_{\gamma_2}$ using the quadratic-amplitude-dependence data and Eq. 5.36. Our fit will consist of minimizing the two χ^2s. Although each depends on the same six fit parameters, it is not immediately clear how to combine the two to get the best parameter values. Since the electron is close to centered axially (we discuss the offset fully in Section 5.4.3 and include the measured offset in the fits), the zero-amplitude data is more sensitive to the two odd-p modes and the amplitude-dependence data to the sidebands of the even-p mode. Thus we expect the best fit to be some combination of the two χ^2s and minimize

$$(1-a)\chi^2_{\gamma(0)} + a\chi^2_{\gamma_2} \tag{5.37}$$

for various values of a from zero to one.

Fit results

Figure 5.8 displays one such fit with $a = 0.75$. The upper plot shows the zero-amplitude cyclotron damping rates and the fit from the renormalized calculation with TE_{136} moved; the lower plot shows the fit to the quadratic-amplitude-dependence data. Table 5.2 lists the best-fit values and uncertainties for the six fit parameters. With the exception of fits for only $\chi^2_{\gamma(0)}$ or $\chi^2_{\gamma_2}$, various weightings of the two χ^2s yield

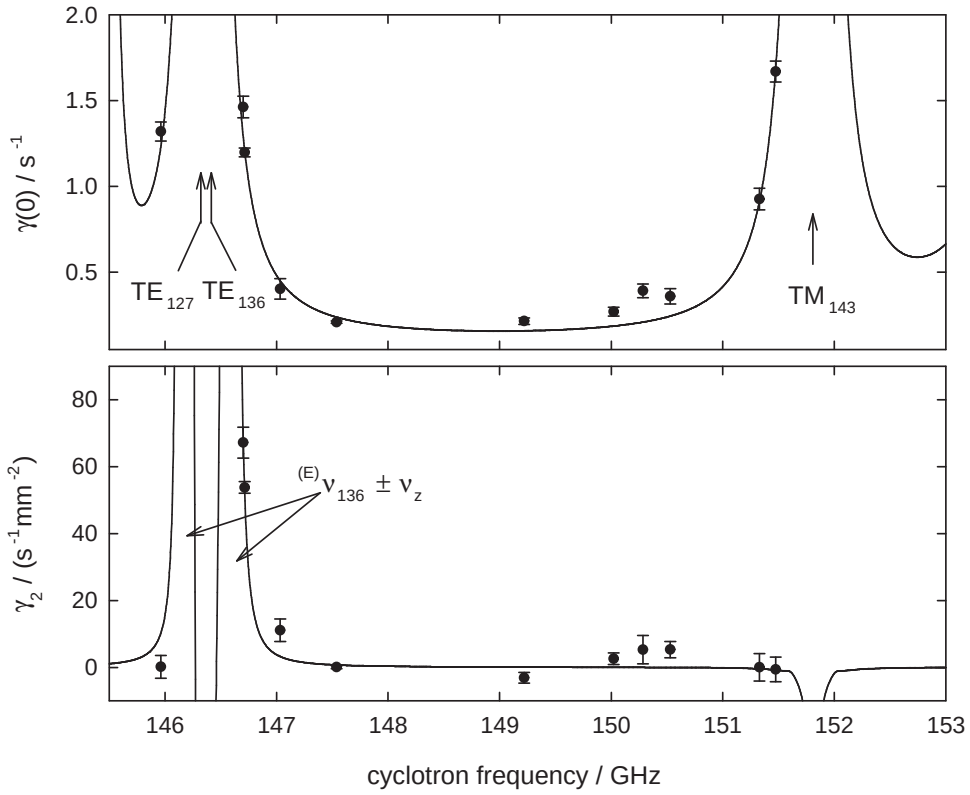

Figure 5.8: Lifetime data with fit. Each cyclotron frequency has a pair of points, one for the zero-amplitude damping rate and one for the quadratic amplitude-dependence, that come from a lifetime-versus-amplitude fit as in Fig. 5.7c.

nearly identical results. Figure 5.9 plots the fitted values of the three frequencies for various weights a. Because nearly all values produce similar results, deciding the most appropriate value of a is unnecessary. We display the parameters and fits for $a = 0.75$ because it gives nearly equal weight to the two χ^2s ($\chi^2_{\gamma(0)}$ is roughly 2.5 times larger than $\chi^2_{\gamma_2}$). The corresponding fit has a total χ^2 per degree of freedom of 2.9.

Both Fig. 5.9 and Table 5.2 also compare the lifetime fit results to those from the mode maps of Section 5.2. The two independent methods should agree but do not. When calculating the cavity shifts, we will assign uncertainties large enough to include both results for the mode frequencies. For the mode Qs, to which the cavity

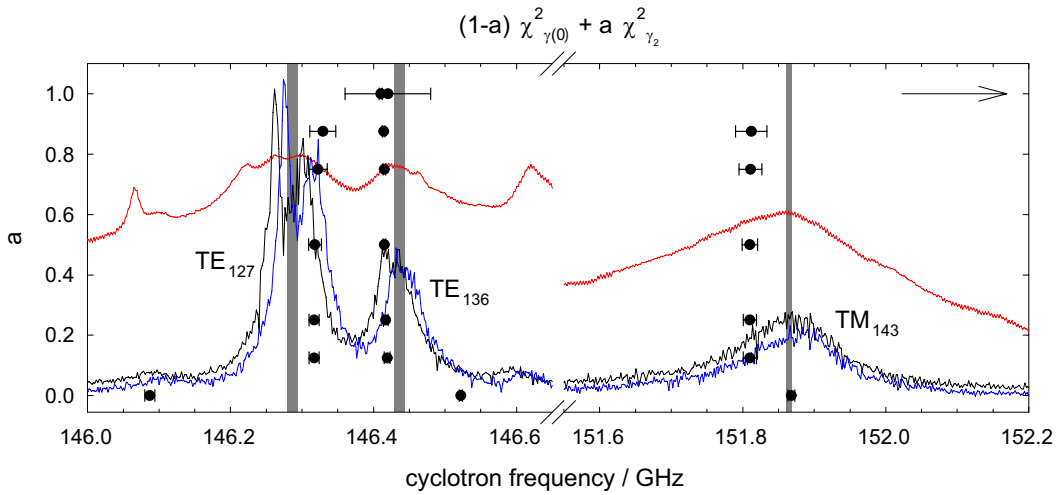

Figure 5.9: Fit results for the three relevant mode frequencies plotted for various a, the weightings between the zero-amplitude and quadratic-amplitude-dependence χ^2s. Also included are the parametric mode maps of Fig. 5.3 as well as gray bands indicating the mode frequencies fit from the maps. The data from the lifetime fits should lie within these bands but do not for unknown reasons.

shifts are much less sensitive, we will use the results from the lifetime fits because of the strong-coupling ambiguity in the mode map values.

5.4.3 Axial and radial (mis)alignment of the electron position

Knowledge of the electron position relative to the cavity modes is important for calculating the electron–mode coupling and thus the cyclotron frequency shift. We have already seen evidence (in Section 5.2.4) that a cloud of electrons couples to modes with nodes at the axial and radial centers and estimated that the observed coupling to TE_{136} is more likely to be caused by an axial offset than an extended cloud. Here, we examine the alignment of the mode center and the electron position,

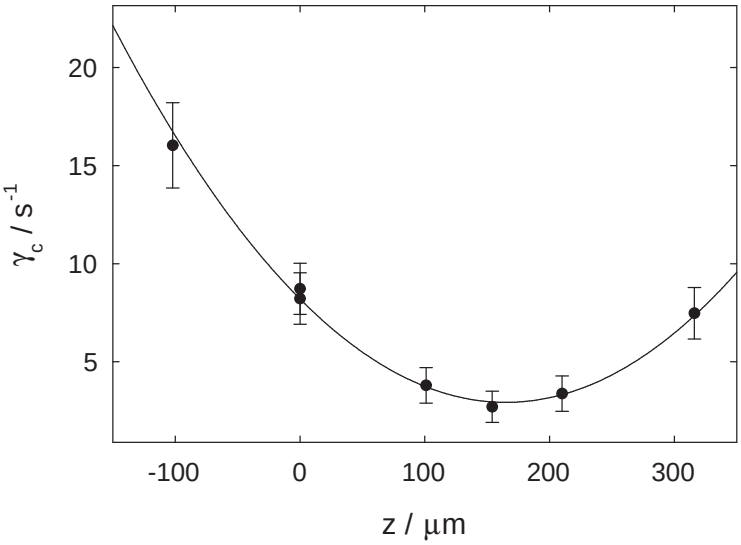

Figure 5.10: Measurement of the offset between the electrostatic and mode centers. Here, z refers to the position relative to the electrostatic center, and the minimum in the cyclotron damping rate corresponds to the mode center.

i.e., the electrostatic center of the trap, and conclude that the electron sits 165(4) μm below the mode center at a radius $\rho < 10$ μm.

Axial misalignment

We determine the axial misalignment by measuring the cyclotron damping rate as a function of z, using antisymmetric endcap potentials to move the electron along the trap axis. Figure 5.10 plots such a measurement with the cyclotron frequency tuned midway between TE_{136} and its upper sideband—close enough to TE_{136} to give a large z-dependence but far enough detuned that the cyclotron lifetime is long enough to see single excitations. Since the mode-couplings are even functions of z, the damping rate should go as z^2 with an extremum at $z = 0$ for the modes. Figure 5.10 shows this extremum, which fits to 165(4) μm. In addition, since the extremum is a minimum,

the nearest coupled mode must have even p, demonstrating that the TE_{127}/TE_{136} identification in Fig. 5.3 is correct.

Because the data for Fig. 5.10 were taken so close to two $m = 1$ modes (TE_{127} couples strongly even when the electron is offset to the node of TE_{136}), the short lifetime prevented the measurement of the zero-axial-amplitude cyclotron frequency and thus the axial amplitude, rendering the extrapolation technique of Section 5.4.1 impossible. We account for this ignorance by estimating the range of cyclotron damping rates one expects from the typical axial amplitudes (50–150 μm) and enlarging the error bars from their statistical values.

The cause of this offset is not known, but several clues are listed below. The offset appears to be stable; the parametric mode maps have consistently shown a central peak for TE_{136} and first-order sidebands for TE_{127}. Measurement of a third trap "center," that of the minimum of the magnetic bottle (see Fig. 2.7), agrees with the electrostatic center (as measured by ν_z versus z and Eq. 2.17). In addition, the ρ_0 dimension from the fit to the TE_{0np} modes (see Table 5.1) agrees with the designed trap radius, after accounting for thermal contraction, to better than a micron (see Table 2.1, which lists the designed dimensions for the cold trap), but the z_0 dimension fits to nearly 50 μm too long, indicating a 100 μm discrepancy in the total trap height ($2z_0$). Since the trap radius is set by one object—the ring electrode—it is not surprising that it agrees better than the effective trap height, which depends on the height of all five electrodes, four spacers, and both pieces of the magnetic bottle. Nevertheless, the 100 μm length disagreement and the measured 165 μm offset are both much larger than the net 25 μm machining tolerances, suggesting that a part

may be bent or misaligned.

Attempts to model the observed offset do not yield a convincing explanation. Simply shifting one endcap away, as if a quartz spacer were too large, could explain the fit to the TE_{0np} modes, but it would move the mode and electrostatic centers nearly identical amounts. Adjusting the spacing among the ring and compensation electrodes, i.e., modeling changes to the gaps between them, should leave the mode center unchanged (it is set by the distance between the endcaps) and can move the electrostatic center. The displacement of the electrostatic center is much less than the displacement of the electrodes, however. For example, if the ≈ 150 μm gaps between the electrodes were closed such that the ring and compensation electrodes were pushed as far down as possible (creating a large gap between the top compensation electrode and the top endcap), the electrostatic center would move down only ≈ 30 μm. Furthermore, because the two halves of the magnetic bottle are spaced by a section of the ring electrode (see Fig. 2.2), any displacement of that electrode would move the bottle as well. Since the electrostatic and magnetic bottle centers agree, displacement of the ring electrode is unlikely. Also, the calculated electrostatic anharmonicity coefficients in Table 2.1 agree well with those measured; for example, the ratio of V_{comp}/V_R at which $C_4 = 0$ agrees to 5%, measurements of $\sqrt{(1+C_2)/d^2}$, which calibrates the axial frequency in terms of the ring voltage in Eq. 2.1, agree to 0.6%, and the value of $c_1 c_3/(1+C_2)^2$, which is measured through axial frequency shifts from antisymmetric endcap biases as in Eq. 2.17, agrees to 0.3%.

It is unclear what the effects are of more exotic trap deformations, such as a tilted endcap or a compensation electrode that protrudes slightly into the cavity. The lack

ν_c / GHz	γ_c / s^{-1}	nearby modes	allowed ρ
143.8495	1.08(3)	TE_{035}, TM_{135}	< 8 μm
147.567	0.182(9)	TM_{027}	0 μm
151.196	0.72(4)	TE_{043}	$1 - 9$ μm

Table 5.3: Limits on the radial alignment between the electrostatic and mode centers, as determined by tuning the cyclotron frequency near resonance with $m \neq 1$ modes.

of a firm explanation for the axial misalignment is worrisome, but the data from the mode-maps and Fig. 5.10 demonstrate that it exists, and we will use the measured offset in calculating the cavity shifts. We build our confidence that this procedure is correct by measuring the g-value at multiple cyclotron frequencies with different cavity shifts and showing the agreement between the predicted and measured shifts.

Radial alignment

We estimate the radial alignment of a single electron by tuning its cyclotron frequency into resonance with three modes that have nodes at the radial center, i.e., have $m \neq 1$, and comparing the measured cyclotron damping rate to that predicted by the renormalized model with $\rho = 0$. Since the $m \neq 1$ modes do not couple to a radially-centered electron, a measured cyclotron damping rate that is faster than the calculated damping rate could indicate a radial misalignment. For the cases where we observe such a discrepancy, we use the full, ρ-dependent renormalized calculation to estimate the range of radial offsets that could explain the observed damping rates. In each of the three cases, we measure damping rates close to that predicted for $\rho = 0$, and we set the limit $\rho < 10$ μm.

The three $m \neq 1$ modes (all were $m = 0$), the measured cyclotron damping

rates, and the radial limits are listed in Table 5.3. Two, TM_{027} and TE_{043}, are within the region in which we measure g; one, TE_{035}, is at a lower frequency.[8] For the renormalized calculation, we include the axial offset of the previous section and use the range of mode parameters determined from the parametric mode maps and lifetime fits and listed in Table 5.4, including the movement of TE_{136} to its observed location (see page 145). We also use the mode-movement technique to put additional nearby modes at their observed locations, as determined by the parametric mode maps and listed in Table 5.1; these additional modes are listed in Table 5.3.

For TE_{035}, having all mode frequencies and Qs at their mean values predicts a cyclotron damping rate faster than the measured rate, leaving no room for a radial offset. By adjusting the mode parameters within their uncertainties to minimize the $\rho = 0$ damping, e.g., shifting the $m = 1$ modes away and increasing their Q, one can bring the calculated $\rho = 0$ damping below the measured one, creating the possibility for a radial offset as large as 8 μm. For TE_{043}, the measured γ_c is consistent with a radial offset in the range 1 $\mu\text{m} < \rho < 9$ μm. For TM_{027}, the cyclotron lifetime is always longer than that calculated by the renormalized method, such that it is never consistent with $\rho \neq 0$.

We did not measure the amplitude of the axial oscillations during these lifetime measurements and are thus not able to extrapolate to zero-amplitude damping rates as we did in Section 5.4.1. Any amplitude corrections are negligible, however, because we are not near resonance with any mode or sideband other than the $m = 0$ modes themselves. Because the electron is nearly centered, the coupling to the $m = 0$

[8] Two of the damping rate measurements appeared previously in [83, Table 5.2], though not in this context.

modes is a small addition on the $\rho = 0$ renormalized calculation, and the amplitude corrections would be small adjustments to that small addition.

None of these three radial-offset tests show evidence of a misalignment as large as the one seen axially, and all are consistent with $\rho < 10$ μm, which we adopt as our limit.

5.5 Cavity-shift Results

With two independent measurements of the relevant mode frequencies as well as quantified trap offsets now in hand, we turn at long last to the cyclotron frequency shifts that directly affect the g-value. In the next two sections, we discuss the methods used for calculating the cavity shift corrections applied in the 2006 g-value publication [1] and in this thesis. The 2006 g-value measurement was the first to use independently measured cavity modes to calculate cavity-shift corrections and included the first measured cavity shift of g between two magnetic fields. The present work adds the independent lifetime measurements and the electrostatic–mode center offsets to improve the cavity-shift precision by more than a factor of six. It includes four new measurements of g with cavity shifts spanning over 10 ppt and uncertainties as low as 0.06 ppt.

5.5.1 2006 cavity shift analysis

For our 2006 publication [1], we assumed that the electron was perfectly centered in the trap. This was wrong, but sensibly chosen error bars were large enough to include the now-measured axial offset. Using the parametric mode maps, we identified

		2006 PRL [1]	**this thesis**
$\mathbf{TE_{127}}$	$\boldsymbol{\nu_c}$ **/ GHz**	146.350(200)	146.309(27)
	$\boldsymbol{Q}$	> 500	4900(300)
$\mathbf{TE_{136}}$	$\boldsymbol{\nu_c}$ **/ GHz**	—	146.428(15)
	$\boldsymbol{Q}$	—	4800(200)
$\mathbf{TM_{143}}$	$\boldsymbol{\nu_c}$ **/ GHz**	151.900(200)	151.832(37)
	$\boldsymbol{Q}$	> 500	1270(70)
electrostatic offset	$\mathbf{z}$ **/** $\boldsymbol{\mu}$**m**	0	165(4)
	$\boldsymbol{\rho}$ **/** $\boldsymbol{\mu}$**m**	0	< 10

Table 5.4: Parameters used in calculating the cavity shifts

all the modes with an antinode at the center, though we remained uncertain about our assignment for the closest TE mode (TE_{127}) and assigned mode-frequency error bars generously to cover any risk of misidentification. The analysis in this chapter demonstrates that we were correct in both our identification and the need for larger error bars because our knowledge was incomplete.

The parameters used for calculating the cavity shifts are listed in Table 5.4. As noted in Section 5.3.1, cavity shifts are independent of mode Q for cyclotron frequencies with relative detunings $(\omega_c - \omega_M)/\omega_M \gg 1/(2Q_M)$. For the two cyclotron frequencies at which we measured g, this detuning requirement is valid for $Q \gg 250$; the mode maps verify that the Qs are at least 500, and we adopt this range. Therefore, without any addition from our uncertainty in the mode Qs, the renormalized calculation for a centered electron takes the uncertainty bands for the mode frequencies to a corresponding cavity-shift uncertainty band. Figure 5.11a,b plots these bands in light gray, and Fig. 5.11c shows the half-width of the cavity-shift band, i.e., the cavity-shift uncertainty.

We measured g at two magnetic fields: one halfway between the two nearest cou-

2006 PRL [1]		**this thesis**	
ν_c / **GHz**	$\Delta\omega_c/\omega_c$ / **ppt**	ν_c / **GHz**	$\Delta\omega_c/\omega_c$ / **ppt**
146.8	12.8 (5.1)	147.5	4.36 (0.13)
149.0	0.06 (0.39)	149.2	-0.16 (0.06)
		150.3	-2.25 (0.07)
		151.3	-6.02 (0.28)

Table 5.5: Calculated cavity shifts

pled modes such that the cavity shift uncertainty was small, 149.0 GHz, and one closer to the modes such that the shift itself was large, 146.8 GHz. Since the uncertainty was much larger at 146.8 GHz, the g-value result was entirely from the centered point, with a cavity-shift uncertainty of 0.39 ppt (see Table 5.5). The 146.8 GHz point allowed the first measurement of a cavity shift of g between two magnetic fields. From Table 5.5, the predicted range of the shift ($g/2$(146.8 GHz) $-$ $g/2$(149.0 GHz)) was -12.7 (5.5) ppt; the measured shift was -9.7 (1.1) ppt, in agreement with the predicted range.

5.5.2 Current cavity shift analysis

Our present analysis of the cavity shifts improves upon the 2006 results and reduces the cavity uncertainty by more than a factor of six. The higher precision comes primarily from three improvements: the independent probe of the cavity modes from single-electron lifetime measurements, including axial-amplitude effects, the discovery and quantification of an offset between the electrostatic and mode centers, and the identification of nearly all modes in the parametric mode maps, which was aided by noticing the effects of strong plasma–mode coupling and of the axial offset.

As in 2006, we calculate a cavity shift uncertainty band from the mode parameters

and their uncertainties via the renormalized calculation. Because of the axial offset, mode TE_{136} affects the shifts, and we calculate with this mode at its observed frequency using the mode-moving technique of page 145. Because fits to the parametric mode maps and to the single-electron lifetime data yield slightly different frequencies for the three nearest coupled modes (see Fig. 5.9), we assign uncertainties large enough to include both. The trap-radius limit only has a significant effect near two modes, TE_{243} and TE_{043}, and we again use the mode-moving technique to place them at their observed frequencies, listed in Table 5.1. Because it appears in the parametric mode map, we include TM_{027} in the calculation, although it does not change the result noticeably.

Figure 5.11 displays the results of this analysis, and Table 5.5 shows the calculated cavity shifts for our four new measurements of g. The shifts span over 10 ppt with uncertainties around 100 times smaller than that range. The measurement is no longer dominated by the results at a single field because the two highest-precision points have comparable uncertainties and a third's uncertainty is only two-times higher. The lowest uncertainties are below a part in 10^{13}, over six times smaller than in 2006 and low enough that this systematic uncertainty is no longer a dominant error in the g-value measurement.

5.6 Summary

The Penning trap electrodes form a microwave cavity whose electromagnetic modes alter the electron's cyclotron frequency and damping rate from their free-space values. By designing trap electrodes with a cylindrical geometry, we may use

an analytic model to describe the coupling of an electron to the modes of an ideal cylindrical cavity. Two independent measurements use sensitivity to γ_c to determine the frequencies and widths of the relevant cavity modes. In the first, the center-of-mass motion of a parametrically-driven cloud of electrons increases with cyclotron damping rate, allowing us to quickly map the modes of the cavity by sweeping the magnetic field. In the second, we measure the damping rate of a single electron at 11 cyclotron frequencies and as a function of axial amplitude. Both methods show modes that correspond closely with those of an ideal cavity, allowing their identification using standard nomenclature, e.g., TM_{143}.

By displacing a single electron along the trap axis, we measure an offset between the electrostatic and mode centers. By tuning its cyclotron frequency into resonance with three modes that have nodes at $\rho = 0$, we set a limit on any radial offset. We calculate the cavity shifts using the measured mode frequencies and trap offsets and a model of the electron–cavity coupling that both removes an infinity from the electron self-field and allows the positioning of the modes at their observed frequencies. The calculated cavity shifts for the four cyclotron frequencies at which we measure g span over 10 ppt and have uncertainties as low as 0.06 ppt. They allow us to correct the measured g to its free-space value in the g-value analysis of the next chapter.

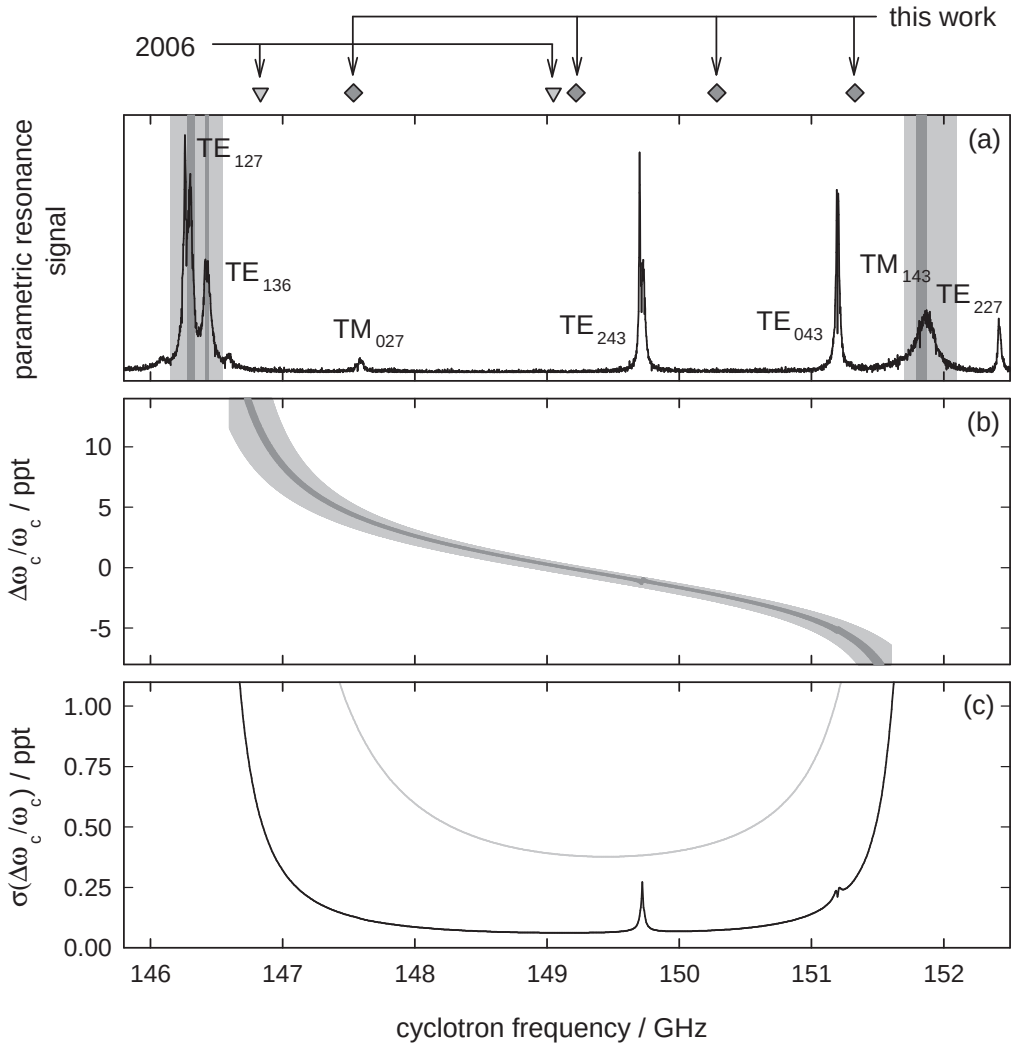

Figure 5.11: Cavity shift results. Uncertainties in the frequencies of the coupled cavity modes (a) translate into an uncertainty band of cavity shifts, $\Delta\omega_c/\omega_c$, (b) whose half-width, i.e., the cavity-shift uncertainty, is plotted in (c). The light gray bands correspond to those used in the 2006 g-value publication [1], while the narrower dark gray bands indicate the analysis presented in this thesis. The triangles at the top indicate the cyclotron frequencies of the two g-value measurements as of 2006; the diamonds show the location of the four new measurements.

Chapter 6

Uncertainties and a New Measurement of g

Combining the techniques and analyses of the previous chapters, we present a new measurement of the electron g-value. With a relative accuracy of 0.28 ppt, it improves the precision of our 2006 result [1] by nearly a factor of three and brings our total improvement compared to the 1987 University of Washington (UW) measurement [2] to a factor of 15.

The uncertainty in g comes primarily from the determination of the cyclotron and anomaly frequencies from their resonance lines. At each field, the weighted means of the cyclotron and anomaly resonances provide a method for splitting lines in the possible presence of magnetic field jitter while requiring only mild assumptions about the noise itself. With an additional assumption about the frequency distribution of the noise, maximum-likelihood fits to the Brownian-motion lineshapes of Chapter 4 with added noise allow a check on the weighted-mean method, and their relative

agreement is used as a lineshape model uncertainty.

Cavity-shifts of the cyclotron and anomaly frequencies, which provided a substantial fraction of our uncertainty in 2006 [1] and dominated the 1987 measurement [2], now give uncertainties well below the lineshape model uncertainties and join the relativistic and magnetron shifts as "routine" corrections. By measuring g at four magnetic fields with cavity shifts spanning over thirty times our final uncertainty, we demonstrate the reliability of the cavity-shift analysis of the previous chapter. The final result comes from a weighted average of the g-value at each of the four fields.

6.1 Lineshape Model Uncertainty and Statistics

The observed cyclotron and anomaly lines are slightly inconsistent with the Brownian-motion lineshapes introduced in Chapter 4 and summarized below. Both lines appear broader than expected, an effect particularly noticeable with the blurring of a sharp feature on the cyclotron line. We attribute this broadening to fluctuations in the magnetic field arising from sources discussed in Chapter 3, such as the relaxation of stresses in the solenoid windings or motion of the trap electrodes in an inhomogeneous magnetic field because of vibration or temperature and pressure fluctuations. To extract resonance frequencies from these noisy lines, we use a property of the noise-free lineshape (unchanged in the presence of noise with a symmetric distribution) and calculate the g-value from the mean values of the cyclotron and anomaly resonances. To check the assumptions of this weighted-mean method, we fit the data to models of their resonance lines. The relative agreement of these two methods quantifies a lineshape model uncertainty. This uncertainty describes how well we know the line-

shape model itself and is different from the statistical uncertainty in determining the weighted mean. We begin with a review of the lineshapes and line-splitting techniques, then describe the analysis for our 2006 g-value measurement [1], and end with the analysis for the present measurement.

6.1.1 Cyclotron and anomaly lineshapes with magnetic field noise

The expected lineshape of Section 4.2 arises from the magnetic field modulation of the electron's axial motion through the inhomogeneous field of the magnetic bottle. The resulting line can take a variety of shapes depending on the ratio of two competing timescales: the timescale for thermal fluctuations of the axial amplitude, γ_z^{-1}, and a coherence timescale, $\approx \Delta\omega^{-1}$. (The linewidth parameter is given by $\Delta\omega = \omega_0 \frac{B_2}{B} \frac{kT_z}{m\omega_z^2}$ for $\omega_0 = \omega_c$ or ω_a.) In addition, for short cyclotron lifetimes the natural linewidth broadens the anomaly lines, which are much narrower than the cyclotron lines in absolute frequency.

At the cyclotron frequency, $\gamma_z \ll \Delta\omega$ ($\gamma_z \approx (200\text{ ms})^{-1}$ and $\Delta\omega \approx (2\text{ ms})^{-1}$) and the axial amplitude fluctuates much slower than the coherence time. The instantaneous lineshape is therefore a natural-linewidth Lorentzian at a cyclotron frequency corresponding to the root-mean-square axial amplitude in the magnetic bottle. Between each excitation attempt, the electron axial motion thermalizes to a new amplitude such that the overall cyclotron lineshape is the narrow Lorentzian convolved with the Boltzmann distribution of axial states. That is, the expected cyclotron line has a sharp edge, corresponding to zero axial amplitude, and an exponential tail whose

width is proportional to the axial temperature.

In all of our data, the cyclotron edge has a width of 0.5 –1 ppb (see Fig. 6.2). This width is far larger than could be explained by adjusting the parameters of the expected lineshape and suggests that some effect remains unaccounted for. Such an effect could be jitter of the magnetic field for any of the reasons discussed in Chapter 3. For example, even with the magnetic field tuned to its specified homogeneity of 10^{-8} over a 1 cm diameter sphere, a 100 μm motion of the trap electrodes would cause a 0.1 ppb field variation. Such a motion could be caused by vibrations that drive the dilution refrigerator like a 2.2 m-long pendulum.

Provided such magnetic field noise fluctuates independent of the axial motion, the resulting lineshape is the convolution of the noise-free one with a noise function, as shown in Section 4.2.5. Attributing the line broadening to field noise assumes that the fluctuation timescale is not so fast that the noise averages away during an excitation attempt. The relevant comparison timescale is the inverse-linewidth coherence time (200 μs for the cyclotron line and 200 ms for the anomaly line), and any line-broadening noise must fluctuate near to or slower than these timescales. Noise-broadening from slow fluctuations is analogous to the exponential limit ($\gamma_z \ll \Delta\omega$) of the noise-free cyclotron line, which takes its shape from the long axial fluctuation time and the distribution of axial energies. Fast noise fluctuations are analogous to the narrower anomaly line, which has $\gamma_z \gg \Delta\omega$; the same axial fluctuations are fast compared to $\Delta\omega^{-1}$ and "average away" to their mean value, approaching a natural-linewidth Lorentzian offset from the zero-axial-amplitude anomaly frequency by $\Delta\omega$. Our edge-tracking technique, used to remove long-term magnetic field drifts and de-

scribed in Section 4.3.3, provides an upper-timescale of minutes for the noise timescale because we see no correlation between adjacent edge-tracking points, which come at intervals of several minutes (see e.g. Fig. 4.6 or Fig. 3.5 for examples of edge-tracking data). This range of allowed timescales constrains the possible fluctuation mechanisms.

The noise-free lineshapes possess the useful characteristic that their mean is equal to $\omega_0 + \Delta\omega$, independent of γ_z. We use this feature in calculating a weighted mean of histograms of the data and thus the cyclotron and anomaly frequencies that correspond to the rms thermal axial motion in the magnetic bottle. Using these frequencies instead of the zero-amplitude frequencies when calculating g should yield identical results at our precision (see Section 4.4.1). Convolving the noise-free lineshape with a noise function, as required when including the magnetic field fluctuations of the previous paragraph, does not change this mean frequency provided the noise fluctuations are symmetric, i.e., the mean frequency of the noise function is zero.

6.1.2 The line-splitting procedure

We use the weighted-mean method as our primary line-splitting technique because it is independent of γ_z and does not require the adoption of a specific model of magnetic field noise. The assumptions inherent in the weighted-mean method are unsaturated lines, identical temperature and drive conditions during cyclotron and anomaly excitations, and a symmetric noise spectrum with fluctuations slower than the inverse-linewidths and faster than several minutes. We assign the resulting error bars (from Eq. 4.32, which assumes binomial uncertainties on the successes in each

histogram bin) as our "statistical" uncertainty. Simulations of g-value data show that the discretization inherent in the weighted-mean method (from a trapezoid-rule integration between histogram bins) does not introduce errors larger than these calculated statistical uncertainties.

To test the assumptions that underly the weighted-mean method, we use maximum-likelihood fits of the data to a lineshape that includes a specific model of the field-noise spectrum—the noise-free lineshape convolved with a Gaussian whose width is left as a fit parameter. The agreement between the g-value calculated from fits to the Gaussian-noise lineshape and that from the weighted mean is our primary check on the lineshape model, and quantifying this agreement provides a systematic, lineshape model uncertainty.

6.1.3 2006 lineshape model analysis

For our 2006 measurement [1], we analyzed each night's data separately. Although we measured g at two cyclotron frequencies, 146.8 GHz and 149.0 GHz, the 6.7 s cyclotron lifetime at 149.0 GHz only allowed an average of 29 sweeps across the resonance lines each night. The statistics after a single night were insufficient for meaningful line fits, so we used only the weighted-mean method to calculate g. The 149.0 GHz data was not included in our lineshape analysis. The 146.8 GHz data, with its shorter 1.4 s lifetime, had an average of 66 measurement cycles per night and therefore much better lineshape statistics. We analyzed each night's data in three ways: a weighted-mean calculation, a maximum-likelihood fit to the noise-free lineshape, and a fit to the Gaussian-noise lineshape with the Gaussian width as a free

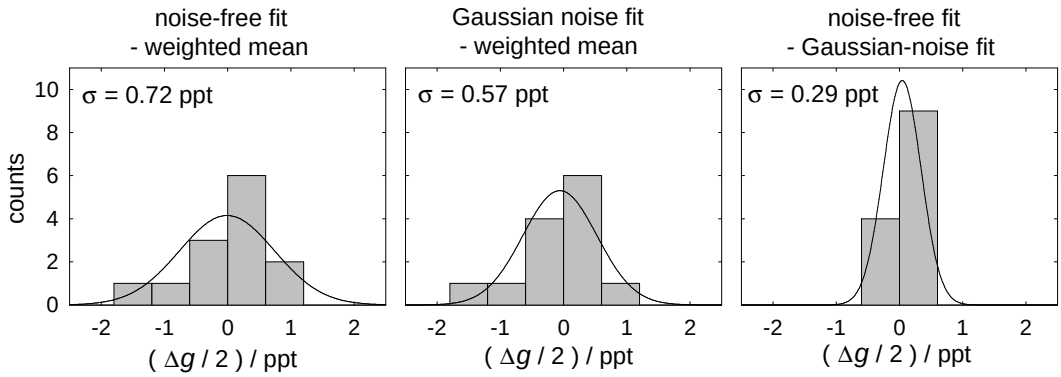

Figure 6.1: Summary of the lineshape model analysis from 2006 [1] based on 13 nights of high-statistics g-value data. Each night was analyzed three different ways, and the plots show the differences between pairs of analysis methods. The Gaussian curves have the mean and standard deviation of the 13 differences. Each histogram shows the distribution of g-value differences. The bin width is equal to our assigned lineshape uncertainty, 0.6 ppt. In all cases, at least 68% of the counts fall within one bin of zero.

parameter.

Figure 6.1 shows the g-value differences between pairs of analysis methods for the 13 nights of data at 146.8 GHz. We assigned a 0.6 ppt lineshape model uncertainty based on the standard deviation of the differences between the weighted-mean and Gaussian-noise lineshape methods, which, given the observed broad cyclotron edge, seem the most likely to give accurate results for g. Even with the noise-free lineshape, however, at least 68% of the differences lie within 0.6 ppt of agreement.

6.1.4 Current lineshape model analysis

For our new measurement, we rely upon our ability to correct for magnetic field drift over long times and analyze all data at a given cyclotron frequency in a pair of composite lines, providing sufficient signal-to-noise to assign a lineshape uncertainty at each field. Although the weighted-mean method is our primary analysis technique,

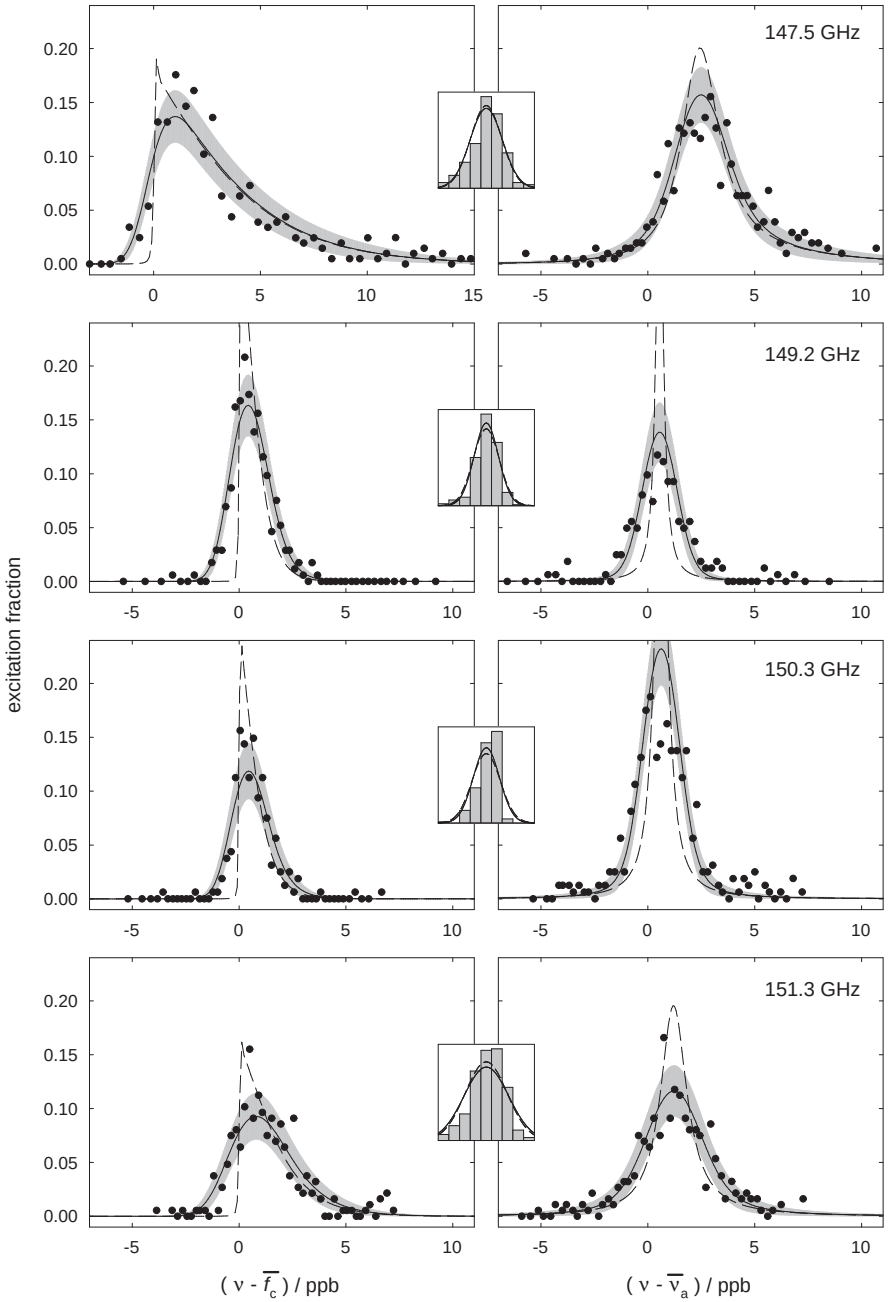

Figure 6.2: Cyclotron (left) and anomaly (right) data from each field. The data are binned into histograms (points) to compare with a maximum likelihood fit to the lineshape with Gaussian-noise (solid); 68% confidence bands (gray) indicate the expected distribution of points. The dashed curves show the best-fit lineshape with its noise-width set to zero. Inset are the edge-tracking data from each field both binned into a histogram and plotted as a Gaussian with the data's mean and standard deviation (solid). The dashed Gaussian shows the noise-width from the best-fit lineshape. All plots share the same relative frequency scale.

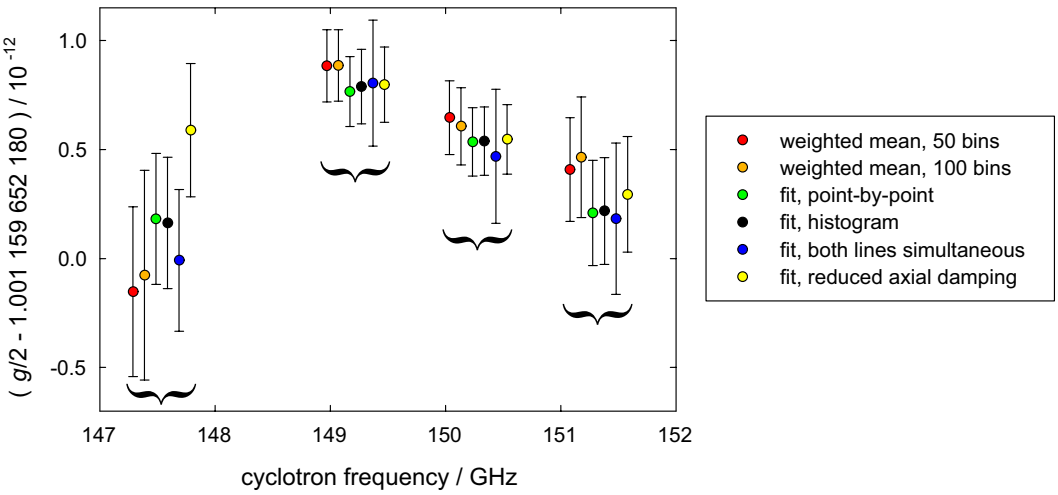

Figure 6.3: Comparing methods for extracting g from the cyclotron and anomaly lines. The data include all corrections (including cavity shifts) so each is a measurement of the free-space g-value, and they should all agree. The error bars reflect only the statistical uncertainty of each analysis method. The lineshape model uncertainty is designed to reflect the range of g-values spanning from the lowest to the highest error bar at each field.

fits make more interesting plots, and we begin by displaying the entire set of g-value data, representing 37 nighttime data runs, in Fig. 6.2. The plots compare a histogram of the data for each line to its maximum-likelihood fit and 68% confidence intervals for the distribution of data about the fit. To indicate the Gaussian-noise width required for the lineshape model to fit the data, they show the lines with the same parameters as before but with this width set to zero. In addition, the inset plots compare the best-fit noise width to the edge-tracking data at each field. Although the precise distribution of edge data depends on the details of the edge-tracking procedure, computer simulations of our procedure indicate that the edge data should be distributed with a width comparable to (within a factor of two of) the Gaussian-noise width. As shown in the figure, the two agree well.

We determine g using six different methods. Because the weighted-mean method

requires binning the data into a histogram, we check that our result is independent of the bin width by using two different numbers of bins per field. The remaining four methods are maximum-likelihood fits to the data:

1. A point-by-point fit (see Section 4.4.2) done sequentially—cyclotron then anomaly,
2. A sequential fit to histogrammed data,
3. A simultaneous fit of both lines with histogrammed data,
4. A sequential fit to histogrammed data with reduced axial damping (1/3 of our measured $\gamma_z/(2\pi) = 1$ Hz).

The last fit is motivated by our difficulty in precisely determining γ_z because of ring voltage drifts while measuring the axial-dip width. Figure 6.3 summarizes the results of these six methods at each field. All systematic corrections are included in the data so that each point is a determination of the free-space g-value. The error bars on the points include only the statistical uncertainty from each analysis method.

At each field, we adopt the 50-bin weighted mean for the g-value result and assign its error bar as the statistical uncertainty. Given the total range of g from the six determinations (highest error bar to lowest), we assign a lineshape uncertainty sufficient to increase the statistical uncertainty to the total range, i.e., the sum in quadrature of the lineshape and statistical uncertainties is the range of g from the six determinations. To establish a baseline that corresponds to our best understanding of the lineshape model, we further sub-divide the lineshape model uncertainty into a "correlated" uncertainty common to all fields and an "uncorrelated" uncertainty to account for any additional discrepancy, and set the correlated uncertainty equal to

ν_c / GHz =	147.5	149.2	150.3	151.3
g-value range	0.73	0.29	0.33	0.45
statistical uncertainty	0.39	0.17	0.17	0.24
		↓		
correlated lineshape model uncertainty	0.24	0.24	0.24	0.24
uncorrelated lineshape model uncertainty	0.56	0	0.15	0.30

Table 6.1: Summary of the lineshape model analysis. All uncertainties are in ppt. The lineshape model uncertainties indicate the agreement between the weighted-mean and line-fit analyses such that their sum in quadrature with the weighted-mean statistical uncertainty equals the total allowed g-value range from all analysis techniques. The lineshape model uncertainty is divided into a correlated part, which establishes a baseline corresponding to our best understanding of the lineshape model, and an uncorrelated part, which indicates any additional uncertainty at a particular frequency.

the smallest lineshape uncertainty of the four fields. For example, the methods at 150.3 GHz give a total range within the error bars of ±0.33 ppt. The 50-bin weighted mean has a statistical uncertainty of 0.17 ppt, and we have assigned a correlated lineshape model uncertainty of 0.24 ppt, so we assign an uncorrelated lineshape model uncertainty of $\sqrt{0.33^2 - 0.17^2 - 0.24^2}$ ppt = 0.15 ppt. Table 6.1 summarizes the statistical and lineshape model uncertainties at the four fields.

6.1.5 Axial temperature changes

The resonance lines at 147.5 GHz and 151.3 GHz appear much broader than those at the other fields. This additional width appears to be stable throughout the data runs at each field (otherwise the narrow lines would be much noisier at high frequencies) but varies between fields. It is consistent with a higher axial temperature, as indicated by the asymmetric broadening of the cyclotron line with a wider exponential

ν_c / GHz	147.5	149.2	150.3	151.3
fitted T_z / K	1.09(8)	0.23(3)	0.23(3)	0.48(5)

Table 6.2: Fitted axial temperatures at each cyclotron frequency.

tail (the fitted temperatures are in Table 6.2), but we have not been able to identify the procedural differences at these fields.

These differences motivate our assignment of separate lineshape model uncertainties at each field. The agreement of the six g-value determinations is much better for the two narrower lines than for the wider ones, which is not surprising because the wider lines rely more on the lineshape model for line-splitting. In particular, because the anomaly line center is offset from the anomaly frequency by $\Delta\omega$, uncertainty in the fitted cyclotron linewidth, i.e., the axial temperature, corresponds to additional uncertainty in the anomaly frequency. Because their g-value data are less consistent, the wider lines will play a smaller role when averaging data from all four fields.

The weighted-mean and line-fit methods should yield g-values independent of axial temperature. In the former, the mean frequency shifts with T_z but in a manner proportional to the magnetic field so the g-value remains unchanged. The line-fit method includes T_z as a fit parameter and any temperature effects are explicitly included in the lineshape. Nevertheless, we check for any systematic trends related to axial temperature by taking an additional set of g-value data at 149.2 GHz with the refrigerator operating at 500 mK instead of 100 mK. The resulting data fit to an axial temperature of 0.55(2) K, in agreement with our deliberate heating. A weighted-mean calculation has a statistical uncertainty of 0.30 ppt, and the maximum-likelihood-fit checks give an uncorrelated lineshape model uncertainty of 0.46 ppt,

both larger than those of the lower-temperature data at 149.2 GHz, in agreement with temperature–uncertainty correlation noted above. Including the statistical and uncorrelated lineshape model uncertainties, the difference between the 149.2 GHz, 500 mK g-value and the 100 mK g-value is 0.5(6) ppt, which is consistent with zero. This check suggests that any temperature shift would be positive, contradicting the trend in Fig. 6.3 that the higher-temperature lines have lower g and suggesting that no temperature shift exists.

6.2 Power Shifts

We expect neither $\bar{\nu}_a$ nor $\bar{f}_c$ to shift with cyclotron or anomaly power, but previous measurements of the electron g-value at the University of Washington (UW) showed unexplained systematic shifts of the cyclotron frequency with both drive powers [2, 99, 81].[1] The origin of these power shifts in the UW measurements remains unknown [81], and extrapolation to zero cyclotron power involved correcting shifts of several ppt in g [2, 81]. We do not see similar shifts in our measurements, most likely because our narrower lines and single-quantum cyclotron technique require much lower drive strengths. The next two sections compare our anomaly and cyclotron excitation techniques to those used at the UW and estimate the size of known shifts. A third section describes our experimental searches for power shifts in both the 2006 measurement and the present one. These searches are consistent with our expectation of no power shifts; in the present measurement, we apply neither power-shift

[1] The UW experiment also saw an axial-power shift, which comes from driving the electron in the magnetic bottle, giving rise to the driven lineshape of Section 4.2.3. It is eliminated (at both the UW and Harvard) by turning off the axial drive during cyclotron and anomaly excitation.

corrections nor any additional uncertainty.

6.2.1 Anomaly power shifts

The UW experiment showed anomaly power shifts of several ppb in the anomaly frequency [81]. An off-resonant anomaly drive during cyclotron excitation shifted the cyclotron line by a similar amount, and the two shifts canceled in the frequency-ratio calculation of g [2]. The origin of these shifts is unknown, although experiments with a variable-strength magnetic bottle showed that they increase with the magnitude of the bottle strength, independent of its sign [81].

Direct comparisons between the anomaly power used in the UW experiment and that used here are difficult because the experiments use different anomaly excitation techniques. The UW excitations were primarily driven with counterflowing current loops in split compensation electrodes, while we drive the electron axially through the $z\rho\hat{\boldsymbol{\rho}}$ gradient of the magnetic bottle. Unlike the current-loop excitation technique, our axial-excitation technique provides a clear mechanism for an anomaly power shift by increasing the average axial amplitude and, therefore, the average magnetic field seen by the electron (because of the $z^2\hat{\mathbf{z}}$ part of the magnetic bottle). We estimate this shift below and expect it to be both smaller than our current precision and canceled in the calculation of g by a similar cyclotron shift from a detuned anomaly drive during cyclotron excitation.

For a driven axial amplitude, z_a, the frequency shift from the motion through the magnetic bottle is

$$\frac{\Delta\omega_a}{\omega_a} = \frac{\Delta\omega_c}{\omega_c} = \frac{B_2}{B}\frac{z_a^2}{2}. \tag{6.1}$$

The axial amplitude is proportional to the rf voltage applied to the bottom endcap [84, 112], so the shift is indeed proportional to power. In order to calculate the expected size of the power shift, we must estimate z_a; only amplitudes over 800 nm will produce shifts at the 0.1 ppb level in frequency. We estimate z_a using two methods: the observed anomaly transition rate and a calibration of the drive voltage. The estimates give similar amplitudes, and neither predicts anomaly power shifts at our precision.

Recalling from Eq. 4.5 that the anomaly transition rate goes as the product of the Rabi frequency squared, Ω_a^2, times the lineshape function, $\chi(\omega)$, and that the anomaly Rabi frequency goes as z_a (Eq. 4.27), we can estimate z_a from a measured peak excitation fraction, P_{pk}, using

$$P_{\mathrm{pk}} = \frac{\pi}{2} T \Omega_a^2 \chi(\omega_{\mathrm{pk}}) = \frac{\pi}{2} T \left(\frac{g}{2} \frac{e\hbar}{2m} B_2 z_a \sqrt{\frac{2n}{m\hbar(\omega_c' - \omega_m)}} \right)^2 \chi(\omega_{\mathrm{pk}}). \tag{6.2}$$

Because the lineshape function is normalized to unity, its value on-peak in the Lorentzian limit is inversely-proportional to the linewidth

$$\chi(\omega_{\mathrm{pk}}) = \frac{2}{\pi} \left(\frac{2\Delta\omega^2}{\gamma_z} + \gamma_c \right)^{-1}. \tag{6.3}$$

For typical experimental parameters, we must drive to $z_a \approx 100$ nm to achieve a 20% excitation fraction.

Alternately, we can estimate the driven amplitude based on the rf voltage on the bottom endcap. An endcap driven with amplitude, V_a, excites the electron to an amplitude given by [84, 112]

$$z_a = \frac{c_1 d^2}{2 z_0} \left[\left(\frac{\omega_a}{\omega_z} \right)^2 - 1 \right]^{-1} \frac{V_a}{V_R}. \tag{6.4}$$

We calibrate the drive amplitude using the anomaly-power-induced axial frequency shifts discussed in Section 6.3.3. They indicate 30 dB of attenuation between the

anomaly frequency synthesizer and the trap electrode. This agrees with the attenuation we measure in the drive line during room-temperature calibrations and seems reasonable given the 20 dB cold attenuator installed at the 1K pot (see Section 2.3.2) and some additional loss in the stainless steel semi-rigid coaxial cable. The highest anomaly power used for g-value data was -16 dBV at the synthesizer, which would attenuate to $V_a = 5$ mV at the bottom endcap and drive the electron to $z_a = 250$ nm.

Driven axial amplitudes around 100–250 nm should only shift the anomaly and cyclotron frequencies at the 1–10 ppt-level, which is far too small to affect the lineshapes (the error in g would be lower by 1000 if the cyclotron and anomaly shifts were uncorrelated, but should be even smaller because the shifts cancel in the frequency ratio).

6.2.2 Cyclotron power shifts

Unlike the anomaly power shifts, the cyclotron power shifts seen in the UW experiments did not cancel in the g-value and added a 1.3 ppt uncertainty to their 1987 result [2]. The shifts appeared as a resonant effect of unknown origin with a resonant drive shifting the cyclotron line several ppb but a detuned cyclotron drive with the same power not shifting the anomaly line. Investigations in a trap with a variable-strength magnetic bottle showed that the shift scaled with B_2 in magnitude and sign. In [81], the authors hypothesize that the shift could have originated in an excitation of the magnetron motion because a typical shift could have been explained by a 10% increase of the magnetron radius.

Our cyclotron excitation technique, injecting microwaves into the trap cavity, is

similar to that used in the UW measurements, so we can compare our technique to theirs. Our lower temperature narrows the lines by a factor of ten, requiring less power to drive transitions. The measured bottle-dependence suggests that our ten-times-stronger magnetic bottle could cancel the advantage of our narrower lines. The overall shifts should still be reduced because our single-quantum-jump spectroscopy only needs to excite to the $n = 1$ state less than 20% of the time. At the UW, typical excitations sustained the electron at energies corresponding to $n \gtrsim 4$ [84, 81]. Naively, exciting to an average energy of $n = 4$ requires 20-times more power than an average energy of $n = 0.2$, and this power reduction alone would reduce several-ppt shifts in g below our precision. The relativistic shifts between cyclotron levels suggest additional power in the UW drives because excitations above $n = 1$ involve driving in the exponential tails of the higher states' resonances. In addition, if the power shift is indeed related to driving a magnetron–cyclotron sideband, our ten-times-higher magnetron frequency and ten-times-narrower cyclotron lines put the closest magnetron sideband, which was fewer than 10 linewidths away at the UW, 100 times farther from the cyclotron resonance.

6.2.3 Experimental searches for power shifts

Although we do not expect any cyclotron or anomaly power shifts of $\bar{\nu}_a$ or $\bar{f}_c$, their existence in the UW measurements makes us proceed with caution and look for them anyway.

2006 power-shift search

For our 2006 measurement [1], we looked for anomaly power systematics by measuring the g-value versus anomaly power. At our 149.0 GHz point, we detected no shift for 5 dB above and 6 dB below our normal anomaly power and assigned a 0.14 ppt uncertainty in g. A similar investigation at 146.8 GHz yielded a 0.4 ppt uncertainty. Each anomaly power uncertainty was dwarfed by the cavity uncertainty at its field. Further details of these investigations may be found in [83, Sec. 6.2.4].

We studied the cyclotron power systematic by measuring g for a range of cyclotron powers. The data were consistent with no power shift, and we set an uncertainty in g of 0.12 ppt at 149.0 GHz and 0.3 ppt at 146.8 GHz. Further details are in [83, Sec. 6.2.5].

Current power-shift search

For the present measurement, we examine the shifts of each line individually to ensure that no systematic effects (even ones that cancel in g) go unnoticed. We look for a cyclotron frequency shift by running three cyclotron scans: a control, one with double the detuned anomaly power, and one with half the cyclotron power (lower to avoid saturation). The scans are interleaved in the same way we interleave cyclotron and anomaly scans during g-value measurements, alternating single sweeps of each line and including edge-tracking to remove long-term drifts (see Section 4.3.3). The resulting cyclotron lines are shown in Fig. 6.4a. We calculate the cyclotron frequency of each line with the weighted-mean method (the offset from $\bar{f}_c$ cancels when subtracting for a frequency shift). Frequency differences between methods are summarized in

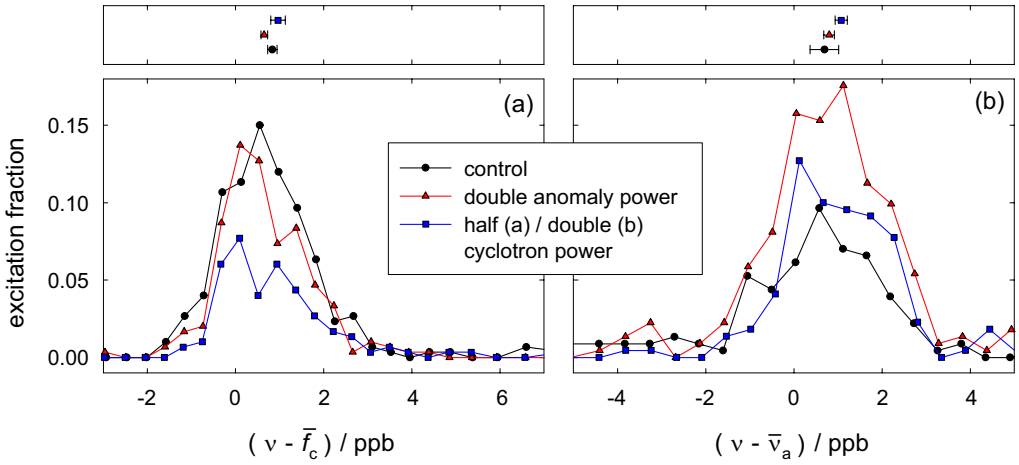

Figure 6.4: The lower plots show cyclotron (a) and anomaly (b) data taken in search of cyclotron and anomaly power shifts. The upper plots compare the weighted-means of these lines.

test	**"shift" / ppb**
$\bar{f}_c$ with double anomaly power	-0.18 (13)
$\bar{f}_c$ with half cyclotron power	0.13 (19)
$\bar{\nu}_a$ with double anomaly power	0.11 (35)
$\bar{\nu}_a$ with double cyclotron power	0.38 (35)

Table 6.3: Summary of power-shift searches

Table 6.3.

To look for anomaly frequency shifts, we run three anomaly scans—a control, one with double the detuned cyclotron power, and one with double the anomaly power (the control power is low enough that we can double the power without saturating)—interleaved and normalized via edge-tracking as before. The resulting anomaly lines are shown in Fig. 6.4b, which includes the frequencies calculated by the weighted-mean method. Table 6.3 summarizes the differences.

The results in Table 6.3 are either consistent with zero or close thereto. The largest "shift" is that of the anomaly frequency with cyclotron power—the only one

of the four *not* seen at the UW. The data of Table 6.3 suggest that any power shift will be $\lesssim 0.35$ ppb in frequency, which is consistent with the limits of our prior studies (summarized in the previous section and detailed in [83, Sec. 6.2]) and with our expectation of no shift at our current precision. The uncertainties are limited by our ability to resolve the lines in a timely manner. (The number of nights spent assembling the data in Fig. 6.4 exceeds twice the number used in an average g-value measurement.) The anomaly line in particular requires the time-consuming discrimination between $|0,\uparrow\rangle$ and $|1,\downarrow\rangle$ after each anomaly pulse (see Section 4.3.3), and any search for a systematic shift in the anomaly frequency multiplies the number of times this must occur.

Because the largest uncertainties of the new measurement are related to resolving the resonances and not to systematic cavity shifts, it is unlikely that even non-existent systematic effects could be constrained better than around 0.2 ppb in $\bar{f}_c$ or $\bar{\nu}_a$ (0.2 ppt in g) in a reasonable amount of time. Since all such tests would be limited by our ability to resolve the lines, including uncertainties for n non-existent systematics in the final result would over-count this resolution uncertainty and increase the final error bar by $\sqrt{n}$. This is not to say that searches for systematic shifts are unimportant but that we should be careful to add uncertainties only when they reflect new (lack of) information and not when they repeat our limits at resolving the lines. For these reasons, in the new measurement we apply neither a correction nor any additional uncertainty from power shifts.

6.3 Axial Frequency Shifts

The Brown–Gabrielse invariance theorem (Section 2.1.2, [90]) allows us to write the magnetron-frequency correction to the anomaly and cyclotron frequencies in terms of the axial frequency. Errors in $\bar{\nu}_z$ will add uncertainty to g with the relative uncertainties given by

$$\frac{\Delta g}{g} \approx -\frac{\bar{\nu}_z^2}{\bar{f}_c^2}\frac{\Delta\bar{\nu}_z}{\bar{\nu}_z} = -1.8\times10^{-6}\frac{\Delta\bar{\nu}_z}{\bar{\nu}_z}. \tag{6.5}$$

To keep the relative uncertainty in g below 0.1 ppt, we must know $\bar{\nu}_z$ to better than 50 ppb, or 10 Hz. This is easily done despite the three shifts to $\bar{\nu}_z$ discussed below.

6.3.1 Anharmonicity

The axial frequency in an anharmonic potential becomes slightly amplitude-dependent, as shown in Eq. 2.5 and reproduced here:

$$\nu_z(A) \approx \nu_z\left[1+\frac{3C_4}{4\,(1+C_2)}\left(\frac{A}{d}\right)^2+\frac{15C_6}{16\,(1+C_2)}\left(\frac{A}{d}\right)^4\right]. \tag{6.6}$$

When self-exciting the electron, we adjust the axial amplitude until the C_4 and C_6 terms cancel and the axial frequency is stable to small amplitude fluctuations. This amplitude is large, typically ≈ 100 μm, giving a high signal-to-noise ratio that is one of the technique's advantages.

As a consequence of deliberately making the axial potential anharmonic, the amplitude-dependence of the axial frequency increases. There is a shift, typically a few hertz, between the axial frequency at the stable self-excitation amplitude and $\bar{\nu}_z$ at the 2 μm thermal amplitudes during cyclotron and anomaly excitation. We must use this SEO-off axial frequency in our g-value calculations. Although we can-

not measure the axial frequency under the anomaly/cyclotron excitation conditions (the amplifier must be on to detect $\bar{\nu}_z$), we can come close by measuring it with the amplifier on and the axial drives off (see Section 4.3.3). The residual frequency shift between the amplifier-on (7 μm) and amplifier-off (2 μm) axial amplitudes is negligible. By measuring the axial frequency under the proper conditions, there is no appreciable uncertainty from anharmonicity.[2]

6.3.2 Interaction with the amplifier

The amplifier tuned circuit interacts with the electron axial motion in the same way as a cavity mode interacts with the cyclotron motion: it damps it and shifts its frequency. In particular, for a relative detuning, δ (with a definition analogous to that in Section 5.3.1), the frequency-pulling is given by Eq. 5.13:

$$\Delta\omega_z = \frac{\gamma_z}{2}\frac{\delta}{1+\delta^2}. \tag{6.7}$$

The maximum axial frequency shifts occur at $\delta = \pm 1$ and equal $\Delta\omega_z = \pm\gamma_z/4$. With $\gamma_z/(2\pi) \approx 1$ Hz, these shifts are negligible.

6.3.3 Anomaly-drive-induced shifts

The anomaly drive induces two shifts on the axial frequency: a frequency-pulling from the off-resonant axial force and a Paul-trap shift from the change in the effective trapping potential [112]. Together, they are

$$\frac{\Delta\bar{\nu}_z}{\bar{\nu}_z} = \frac{V_a^2}{V_R^2}\left\{\frac{3c_1c_3}{8}\left[\left(\frac{\bar{\nu}_a}{\bar{\nu}_z}\right)^2 - 1\right]^{-1} + \frac{C_2^2}{16}\left[\left(\frac{\bar{\nu}_a}{\bar{\nu}_z}\right)^2 - 4\right]^{-1}\right\}, \tag{6.8}$$

[2]For the 146.8 GHz data in the 2006 result, we recorded only the SEO-on axial frequency and thus had to include a shift and an uncertainty from our determination of $\bar{\nu}_z$.

where V_a is the amplitude of the bottom endcap rf drive. We can use these shifts to calibrate the attenuation in the anomaly line. Plugging in the anharmonicity parameters, ring voltage, and frequencies, we calculate that the shift should be $\Delta\bar{\nu}_z/(\bar{\nu}_z V_a^2) = -37\ \mathrm{ppm}\cdot\mathrm{V}^{-2}$. By increasing the output of the anomaly signal generator far above the normal anomaly-excitation levels, we measure a shift (in terms of the output signal generator power) of $-50\ \mathrm{ppb}\cdot\mathrm{V}^{-2}$, indicating a power-loss from signal generator to electrode of $V_{\mathrm{sig.gen.}}^2/V_a^2 \approx 730$, i.e., 29 dB attenuation. Based on the measured shifts in terms of the signal generator power, at the highest anomaly power used for g-value data the axial shift should be approximately -1 ppb or -0.2 Hz. This shift is small enough that we cannot measure it directly, and it does not affect the g-value at our precision.

6.4 Applied Corrections

The free-space g-value may be written in terms of free-space cyclotron and anomaly frequencies:

$$\frac{g}{2} = 1 + \frac{\nu_a}{\nu_c}. \tag{6.9}$$

When measuring g, we must account for three shifts between the free-space frequencies and those accessible to experiment. These shifts are discussed in detail in Section 4.1 and summarized below. Including these corrections, the formula used in calculating the free-space g-value is

$$\frac{g}{2} \simeq 1 + \frac{\bar{\nu}_a - \dfrac{\bar{\nu}_z^2}{2\bar{f}_c}}{\bar{f}_c + \dfrac{3}{2}\delta + \dfrac{\bar{\nu}_z^2}{2\bar{f}_c}} + \frac{\Delta\omega_c}{\omega_c}, \tag{6.10}$$

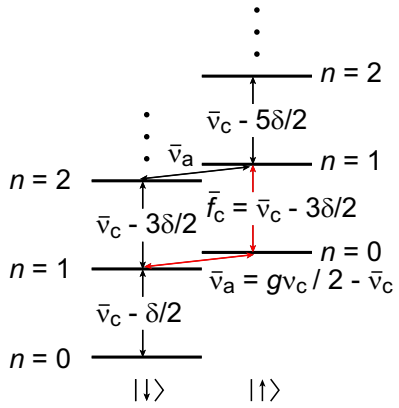

Figure 6.5: The energy levels of an electron in a Penning trap, including ppb-size shifts from special relativity. The red arrows indicate the transitions we measure to determine g.

where the barred frequencies are the ones actually measured and $\Delta\omega_c/\omega_c$ is the calculated relative cavity shift of the cyclotron frequency. The relevant cyclotron and anomaly transitions are shown in Fig. 6.5.

6.4.1 Relativistic shift

Special relativity adds an energy-dependent shift to the cyclotron frequency; left uncorrected, the measured g would depend on both the cyclotron frequency and the particular pair of energy levels used to determine $\bar{\nu}_c$. By choosing always to measure the cyclotron frequency with the $|0,\uparrow\rangle \leftrightarrow |1,\uparrow\rangle$ transition, which we dub $\bar{f}_c$, we may account for the relativistic shift with the replacement

$$\bar{\nu}_c = \bar{f}_c + \frac{3}{2}\delta, \tag{6.11}$$

where

$$\frac{\delta}{\nu_c} = \frac{h\nu_c}{mc^2} \approx 10^{-9}. \tag{6.12}$$

This ppb correction to $\bar{f}_c$ corrects g at the ppt-scale. There is no corresponding shift in $\bar{\nu}_a$ because a similar relativistic shift of ν_s cancels the $\bar{\nu}_c$ one. The energy in the axial and magnetron degrees of freedom also creates relativistic shifts [84, Sec. VII.B], but these corrections are smaller by the ratios of $\bar{\nu}_z$ and $\bar{\nu}_m$ to $\bar{\nu}_c$ (10^{-3}–10^{-6}) and thus negligible.

6.4.2 Magnetron shift

The radial component of the trap's electrostatic quadrupole reduces the free-space cyclotron frequency by the magnetron frequency. Given the hierarchy of frequencies in our trap,

$$\bar{\nu}_c^2 \gg \bar{\nu}_z^2 \gg \bar{\nu}_m^2, \tag{6.13}$$

the Brown–Gabrielse invariance theorem (Section 2.1.2, [90]) allows us to correct for this shift with the replacement

$$\nu_c = \bar{\nu}_c + \frac{\bar{\nu}_z^2}{2\bar{\nu}_c}. \tag{6.14}$$

Because the spin frequency is not affected by the electric field, the anomaly frequency has a corresponding shift that we correct with the replacement

$$\nu_a = \nu_s - \nu_c = \bar{\nu}_a - \frac{\bar{\nu}_z^2}{2\bar{\nu}_c}. \tag{6.15}$$

The ppm shift of $\bar{\nu}_c$ and part-per-thousand shift of $\bar{\nu}_a$ give large corrections to g, but there are no other corrections from the electrostatic quadrupole until a scale given by $(\bar{\nu}_z/\bar{\nu}_c)^4 \approx 10^{-12}$ times the square of any angular misalignment between the electric and magnetic fields or any ellipticity of the quadrupole $\approx (10^{-2})^2$ [84, Sec. II.D],

ν_c / GHz	$\Delta\omega_c/\omega_c$ / ppt
147.5	4.36 (0.13)
149.2	-0.16 (0.06)
150.3	-2.25 (0.07)
151.3	-6.02 (0.28)

Table 6.4: Calculated cavity shifts. $\Delta\omega_c/\omega_c$ is the relative shift of the cyclotron frequency as well as the correction applied to $g/2$.

which is both below our current precision and understood well enough that we could account for it if necessary.

6.4.3 Cavity shift

The resonant electromagnetic modes of the microwave cavity formed by the trap electrodes can shift the cyclotron frequency by several ppt and the anomaly frequency, through its definition in terms of ν_c, by several ppb. Calculating these shifts involves an extensive investigation of the mode structure of the trap cavity and was the subject of the previous chapter. The resulting cyclotron-frequency-dependent corrections to g, $\Delta\omega_c/\omega_c$ in Eq. 6.10, are listed in Table 6.4 (the results from 2006 [1] are in Table 5.5). We measure g at four magnetic fields with diverse cavity corrections to demonstrate our control of this effect. Figure 6.6 shows the g-value data before and after applying the cavity correction. Of the three applied corrections, this is the only one with an uncertainty at a relevant scale. In previous measurements of g, the cavity uncertainty was one of the dominant ones [1, 2], but the techniques presented in this thesis have reduced it to where this is no longer the case.

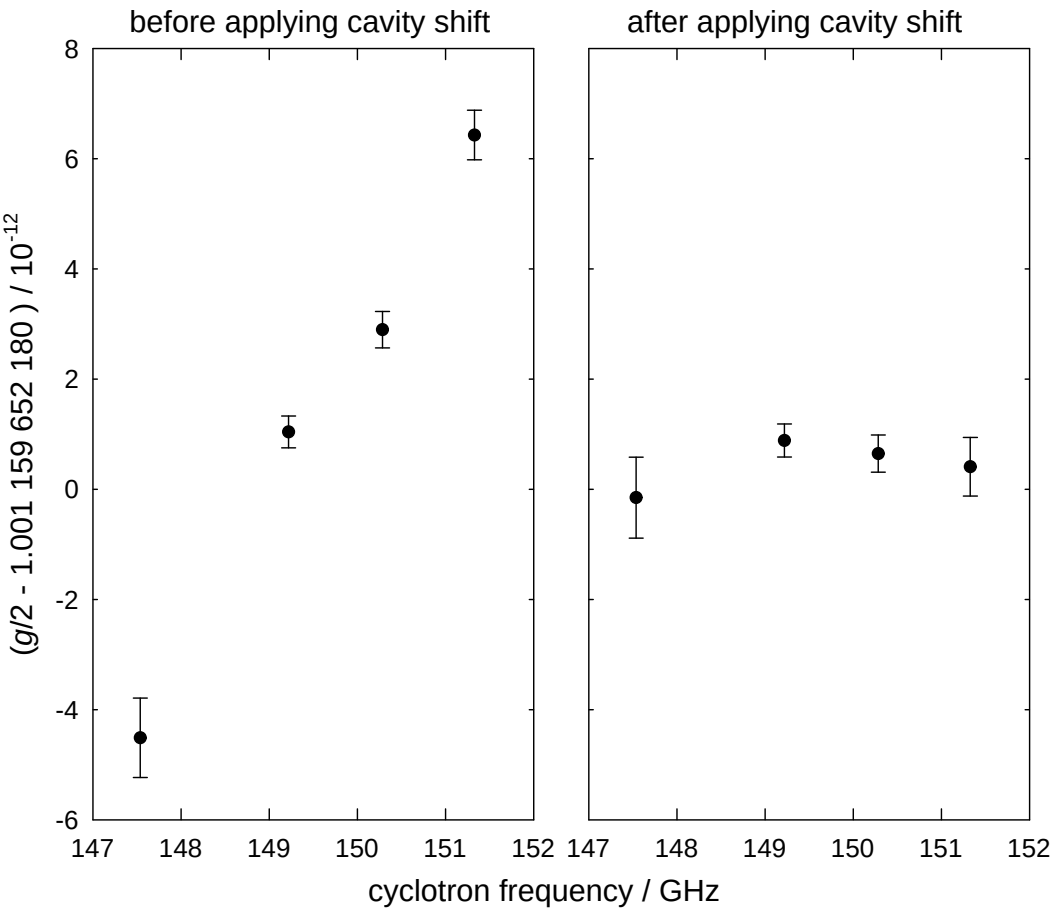

Figure 6.6: g-value data before and after applying the cavity shift

6.5 Results

6.5.1 2006 measurement

Our 2006 g-value measurement [1] improved upon the 1987 UW measurement [2] by almost a factor of six because of numerous innovations including the cylindrical Penning trap [87], quantum cyclotron [85], and self-excited oscillator [88]. It was the first to measure g using solely the lowest cyclotron and spin levels. Lower temperatures narrowed the resonance linewidths over an order of magnitude. In addition,

$\bar{\nu}_c =$	146.8 GHz	149.0 GHz
$g/2$ - 1.001 159 652 180	3.7	0.85
Uncertainties		
$\bar{\nu}_z$ shift	0.3	0.02
Anomaly power	0.4	0.14
Cyclotron power	0.3	0.12
Cavity shift	5.1	0.39
Lineshape model	0.6	0.60
Statistics	0.2	0.17
Total uncertainty	5.2	0.76

Table 6.5: Corrected g and uncertainties in ppt from the 2006 measurement.

the measurement premiered the use of measured cavity modes for predicting and correcting systematic cavity shifts and included the detection of such a shift.

We measured g at two magnetic fields: one far from any modes so the cavity shift and its uncertainty were both small and one near a mode allowing detection of a large cavity shift but having a correspondingly higher cavity shift uncertainty. Table 6.5 summarizes the g-values and uncertainties at each field. Our result,

$$\frac{g}{2}_{(2006)} = 1.001\ 159\ 652\ 180\ 85\ (76)\ [0.76\ \text{ppt}], \tag{6.16}$$

came solely from the 149.0 GHz data because the uncertainty at 146.8 GHz was so much larger. Averaging in the 146.8 GHz data would have shifted it up 0.06 ppt and decreased the uncertainty to 0.75 ppt.

The primary limitations of the 2006 result, both reflected in the uncertainty table, were an incomplete understanding of both the cavity mode structure and the noisy lineshape. Discussed fully in Section 5.5, the cavity shift analysis included error bars stemming from uncertainty in our mode identification. The large lineshape model uncertainty comes from our use of the 146.8 GHz data in assigning the error for both fields. As observed in Section 6.1.4, the disagreement among analysis methods tends

$\bar{\nu}_c =$	147.5 GHz	149.2 GHz	150.3 GHz	151.3 GHz
$g/2$ - 1.001 159 652 180	-0.15	0.88	0.65	0.41
	Uncertainties			
Statistics	0.39	0.17	0.17	0.24
Cavity shift	0.13	0.06	0.07	0.28
Uncorrelated lineshape model	0.56	0.00	0.15	0.30
Correlated lineshape model	0.24	0.24	0.24	0.24
Total uncertainty	0.73	0.30	0.34	0.53

Table 6.6: Corrected g and uncertainties in ppt.

to be larger for wider lines, and the 146.8 GHz data had a linewidth several times that of the 149.0 GHz data (the axial temperature at 146.8 GHz was 0.57(5) K, between that of the new data's two widest lines, while that at 149.0 GHz was 0.16(3) K, below the new data's two narrowest lines). Both limitations are addressed in our new measurement.

6.5.2 New measurement

A new measurement of the electron g-value, presented for the first time in this thesis, improves upon the 2006 result [1] by nearly a factor of three[3] and brings our total improvement compared to the 1987 UW measurement [2] to 15. Several advances lead to the increased accuracy. Two independent probes of the cavity mode structure allow identification of nearly all modes and quantification of an offset between the mode and electrostatic centers. Together with the extension of a renormalized calculation of electron–cavity coupling to arbitrary trap location and a model for the cyclotron lifetime in the presence of axial oscillation through cavity-mode fields, these improvements reduce the cavity shift uncertainty to near-negligible levels at two

[3]It is remarkably close to a factor of e.

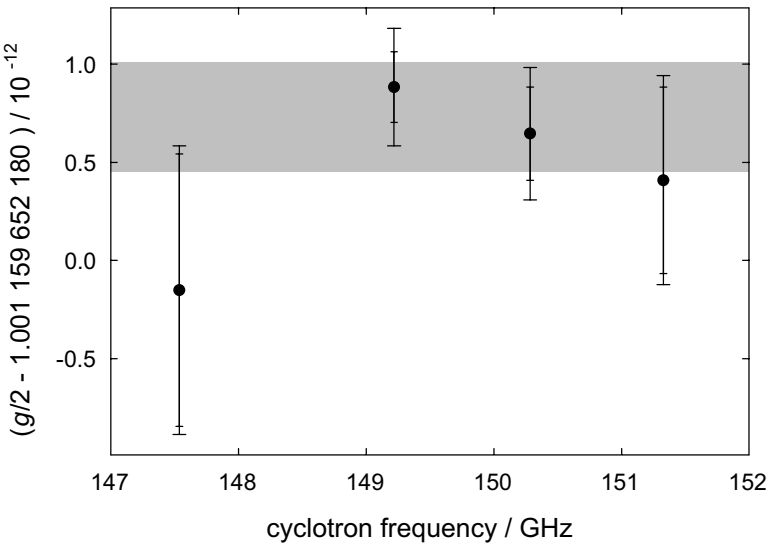

Figure 6.7: Comparison of the new g-value data and their average, indicated in gray as a 68% confidence band. The larger error bars indicate the total uncertainty at each point, while the smaller ones show only the uncorrelated uncertainty.

points (see Chapter 5 for details). By measuring the g-value at four magnetic fields with cavity shifts spanning over thirty times our final error-bar, we precisely test this once-dominant uncertainty.

Analyzing the lineshape model uncertainty at each field allows us to take advantage of the reduced uncertainty for narrower lines. Unlike in 2006, two fields contribute similar amounts to the final g-value, and the remaining two fields contribute more meaningfully than the 146.8 GHz measurement did.

When averaging the four fields, part of the lineshape model uncertainty is treated as correlated in a least-squares analysis (see e.g. [23, App. E] or [115, Ch. 6]); the result is equivalent to leaving it out of a simple weighted average then adding it in quadrature to the resulting uncertainty.

Our result is

$$\frac{g}{2} = 1.001\ 159\ 652\ 180\ 73\ (28)\ [0.28\ \text{ppt}]. \tag{6.17}$$

The average has a χ^2 per degree of freedom of 0.97. (Using the two-digit, rounded values of Table 6.6 gives the same g-value result with a χ^2 per degree of freedom of 0.95.) Figure 6.7 compares the four data points to their average value. Using this result in Eq. 1.6 yields a new value for the fine structure constant,

$$\alpha^{-1} = 137.035\ 999\ 084\ (33)(39) \tag{6.18}$$

$$= 137.035\ 999\ 084\ (51)\ [0.37\ \text{ppb}], \tag{6.19}$$

where Eq. 6.18 separates the uncertainties from experiment and theory to show that the QED uncertainty now exceeds that from the measured g.

Despite more than an order-of-magnitude improvement in the 20 years since 1987, further progress is possible. The largest uncertainty remains that from the lineshape model, and improved understanding (or outright elimination) of magnetic field noise is of primary importance. Chapter 3 discusses a new high-stability apparatus and other improvements that could reduce the noise, and the next chapter includes several promising techniques to enhance the frequency resolution.

Chapter 7

Future Improvements

With cavity-shift uncertainties no longer limiting the g-value measurement, the largest room for improvement lies in the determination of the cyclotron and anomaly frequencies from their lineshapes. The primary source of trouble is the magnetic field noise that blurs the cyclotron edge. For our narrowest lines, the broadening from this noise is comparable to that from the axial temperature. Although our Gaussian noise model agrees well with the weighted mean calculation in our lineshape model uncertainty (Section 6.1), it would be much better to make the noise go away, and a new, high-stability apparatus (Section 3.5) is currently in production with that goal in mind.

Beyond this noise-reduction, there are two main ways to improve the frequency measurements: decrease the linewidth and increase the signal-to-noise ratio. The cyclotron and anomaly lines are broader than their natural linewidth, γ_c, because the magnetic bottle couples their frequency to the axial energy (see Section 4.2), so one narrows the lines by reducing the coupling strength or by lowering the axial

energy. To increase the signal-to-noise, one would shorten the measurement's rate-limiting step, the discrimination between $|0,\uparrow\rangle$ and $|1,\downarrow\rangle$ after applying an anomaly pulse. We discuss some promising techniques below. In addition, we gather from previous chapters four unanswered questions whose solutions could lead to improved measurements.

7.1 Narrower Lines

7.1.1 Smaller magnetic bottle

The linewidth parameter, $\Delta\omega$, is proportional to the magnetic bottle strength, B_2 (see Eq. 4.6). The cyclotron linewidth is $\Delta\omega$, so reducing B_2 will narrow the line. In the Lorentzian limit, the anomaly width is $\gamma_c + 2\Delta\omega^2/\gamma_z$, so a smaller B_2 will greatly reduce its width until it reaches the natural limit.

The axial frequency shifts used to determine the cyclotron and spin states are also proportional to B_2, so any bottle reduction will involve a trade-off between narrower resonance lines and detection efficiency. When contemplating reducing B_2, the three relevant timescales to compare are the signal-averaging time, the cyclotron lifetime, and the axial frequency drift rate. With our current 20 ppb shift, we typically average the axial signal for 1/4 s. (A sample of the signal-to-noise with 1/2 s of averaging may be seen in Fig. 2.8.) Our current averaging time is useful for measuring short cyclotron lifetimes, but could easily be extended by at least a factor of four for measurements at g-value fields, which have cyclotron lifetimes ranging from nearly to greatly exceeding one second. The large axial amplitudes from self-excitation provide

a substantial signal, and we should be able to resolve axial shifts close to the ppb-level with only 1 s of averaging [88]. The longer averaging time would not affect the overall measurement time because our rate-limiting step is governed by the cyclotron lifetime (Section 4.3.3 and Section 7.2) not the axial frequency averaging time. Typical axial frequency drifts are below the ppb-per-second scale, so reducing B_2 by a factor of four seems straightforward; even smaller bottles could be possible after closer study of our axial averaging techniques and stability.

The other use for the magnetic bottle is to drive anomaly transitions with axial motion through its $z\rho\hat{\boldsymbol{\rho}}$ gradient. Although decreasing B_2 reduces this gradient and therefore the transition rate, it also narrows the anomaly line, which increases the rate. Until the anomaly linewidth reaches the natural limit, these two effects cancel, and the transition rate is bottle-independent. We encountered this before in the anomaly power systematic discussion of Section 6.2.1, where we showed that the transition probability on the peak of the anomaly line is

$$P_{\rm pk} = \frac{\pi}{2} T \Omega_a^2 \chi(\omega_{\rm pk}) = \frac{\pi}{2} T \left(\frac{g}{2} \frac{e\hbar}{2m} B_2 z_a \sqrt{\frac{2n}{m\hbar(\omega_c' - \omega_m)}} \right)^2 \frac{2}{\pi} \left(\frac{2\Delta\omega^2}{\gamma_z} + \gamma_c \right)^{-1}. \quad (7.1)$$

For small γ_c, the B_2 dependence of $\Delta\omega$ cancels the B_2 in the Rabi frequency (the squared term in parentheses), and we need not drive harder for having reduced B_2. As the anomaly linewidth approaches γ_c, however, reductions in B_2 must be matched by increases in the driven amplitude, z_a, which could increase anomaly-power systematic effects. At present, the anomaly lines at long-cyclotron-lifetime fields are far from this limit, but the short-lifetime lines have γ_c equal to nearly 25% of the linewidth. If the magnetic bottle were reduced even more, it may require a transition from the axial-excitation technique to the current-loop technique used in previous measurements [2,

81, 99].

7.1.2 Cooling directly or with feedback

Instead of (or in addition to) reducing the magnetic-bottle coupling, lowering the axial energy narrows the lines. The most direct way to reduce the axial energy is with a colder apparatus because the axial motion thermalizes with the amplifier. The transition from 4.2 K liquid-helium cooling in earlier g-value measurements, e.g., [2], to a 0.1 K dilution refrigerator [96, 85] narrowed the lines by over a factor of ten. Although powerful dilution refrigerators are capable of reaching the few-millikelvins range [138], reducing our current 100 mK apparatus temperature by more than a factor of two is impractical because the cooling power of the ^{3}He–^{4}He dilution process decreases as T^2 [138] and we necessarily heat the refrigerator with the detection amplifier and rf and microwave drives. At low enough temperatures, even eddy-current heating from vibration of the refrigerator in the large magnetic field can limit cooling [139].

Using a feedback technique similar to that used for self-excitation, we can cool the electron without further cooling of the apparatus [101]. The self-excited oscillator setup with a gain of less than unity can reduce the axial damping rate (see Eq. 2.31 and Eq. 2.32), which, through the fluctuation-dissipation theorem [100], reduces the axial temperature. Unit gain corresponds to no axial damping and, for a noise-free feedback loop, zero temperature. Noise in the feedback loop limits the minimum temperature by driving a lightly-damped electron to large amplitudes (this is how the self-excited oscillator works) [89, Ch. 5]. In this apparatus, feedback cooling has

been used to reduce the axial temperature from 5.2 K to 850 mK [101]. Additional improvements depend on increasing the signal-to-noise of the feedback loop, which means more power dissipated in the amplifier [89, Ch. 5]. Further pursuit of this technique would require balancing the feedback signal quality with the cooling power available in the dilution refrigerator.

7.1.3 Cavity-enhanced sideband cooling

Sideband cooling the axial motion via the cyclotron degree of freedom is a promising technique because the theoretical cooling limit is equal axial and cyclotron quantum numbers, i.e., the axial ground state. In principle, it proceeds analogously to the magnetron–axial sideband cooling of Section 2.3.7, a routine procedure, but in practice it is difficult to produce sufficient microwave power to achieve appreciable cooling rates. The microwave source described in Section 2.3.5 was designed to output 25 dB more power than the prior source [98] in order to increase these rates. An additional increase in cooling power can be gained by tuning the cooling sideband into resonance with a cavity mode of the correct geometry for cooling, thus admitting more power into the cavity.

Cooling theory

The theory of motional sideband heating and cooling [140] is reviewed in [84, Sec. IV]. It is a classical effect that requires a drive at $\omega_c' \pm \omega_z$ with the correct geometry to produce a force that goes as $x\hat{\mathbf{z}}$, $\dot{x}\hat{\mathbf{z}}$, $z\hat{\mathbf{x}}$, or the equivalent with y. (A force that goes as $\dot{z}\hat{\mathbf{x}}$ will work but is weaker by the ratio ω_z/ω_c'.) The electron motion

through the gradient modulates the sideband drive, producing a resonant force that heats the cyclotron motion and cools ($\omega_c' - \omega_z$) or heats ($\omega_c' + \omega_z$) the axial motion. The cyclotron motion is naturally damped via synchrotron radiation. Any cooling of the axial motion reheats at the axial damping rate, γ_z, so sideband-cooling is most effective when the electron is decoupled from the amplifier, either by detuning the axial potential or by physically decoupling the amplifier from the electrode.

For ions, the sideband frequencies are in the rf range, and applying the sideband drive is straightforward [141]. The required field gradient is achieved by applying the drive to a segment of a compensation electrode, exactly as we do for magnetron–axial sideband cooling. For the electron, the frequencies are microwaves, so we must inject them into the trap electrode cavity. As discussed in Chapter 5, the cavity is a microwave circuit, and the majority of the incident power not resonant with a cavity mode is reflected. This is not a concern for general cyclotron spectroscopy, where we only need sufficient power to excite single transitions; here, however, more power will produce faster cooling rates, so tuning the sideband into resonance with a mode that produces the required force gradients is desirable.

The analysis of the next sections is entirely classical. Achieving the ground states in both cyclotron and axial degrees of freedom is a quantum-mechanical concept and will require a modification to this discussion. In particular, special relativity shifts the cyclotron frequency, and thus the sidebands, depending on the cyclotron state (see Section 4.1); any cooling procedure will need either to move the drive with the frequency-shifts, to power-broaden the drive to span across the shifts, or to account for the decreased cooling rate as the cyclotron frequency shifts into and out of resonance

with the drive.

Traveling wave cooling lines

Although our goal is a description of the cooling rates in the electromagnetic cavity-mode fields, we begin with a simple traveling wave. The results for the cavity modes will be identical up to a geometric factor.

For a drive frequency near the heating (upper sign) or cooling (lower sign) sideband,

$$\omega_d = \omega_c' \pm \omega_z + \varepsilon, \tag{7.2}$$

an electromagnetic wave traveling along $\hat{\mathbf{z}}$ and polarized along $\hat{\mathbf{x}}$ has fields

$$\mathbf{E} = \hat{\mathbf{x}} E_0 \sin(\omega_d(t - \tfrac{z}{c})) \approx \hat{\mathbf{x}} E_0 \left[\sin(\omega_d t) - \frac{\omega_d z}{c}\cos(\omega_d t)\right] \tag{7.3}$$

$$\mathbf{B} = \hat{\mathbf{y}} \frac{E_0}{c} \sin(\omega_d(t - \tfrac{z}{c})) \approx \hat{\mathbf{y}} \frac{E_0}{c} \left[\sin(\omega_d t) - \frac{\omega_d z}{c}\cos(\omega_d t)\right], \tag{7.4}$$

where we have expanded for small $\omega_d z/c \approx 10^{-2}$ because the thermal axial motion is much smaller than the sideband wavelength. These fields produce a force on the electron, and the resonant terms of sizable strength are

$$\mathbf{F} = -e(\mathbf{E} + \mathbf{v} \times \mathbf{B}) = \frac{eE_0}{c}\left(\omega_d \cos(\omega_d t) z\hat{\mathbf{x}} - \sin(\omega_d t)\dot{x}\hat{\mathbf{z}}\right). \tag{7.5}$$

Including this force in the axial and transverse equations of motion gives heating and cooling rates, $\gamma_z^{(\pm)}$, that depend on the detuning, ε, from the sideband [84, Sec. IV.C]:

$$\gamma_z^{(\pm)}(\varepsilon) = \mathrm{Im}\left[(\varepsilon + i\gamma_c/2)\left(1 - \sqrt{1 \mp \frac{\gamma_0\gamma_c}{(\varepsilon + i\gamma_c/2)^2}}\right)\right], \tag{7.6}$$

where the coefficient

$$\gamma_0 = \frac{e^2 E_0^2 \omega_d \omega_c'}{4\gamma_c m^2 c^2 \omega_z(\omega_c' - \omega_m)} \tag{7.7}$$

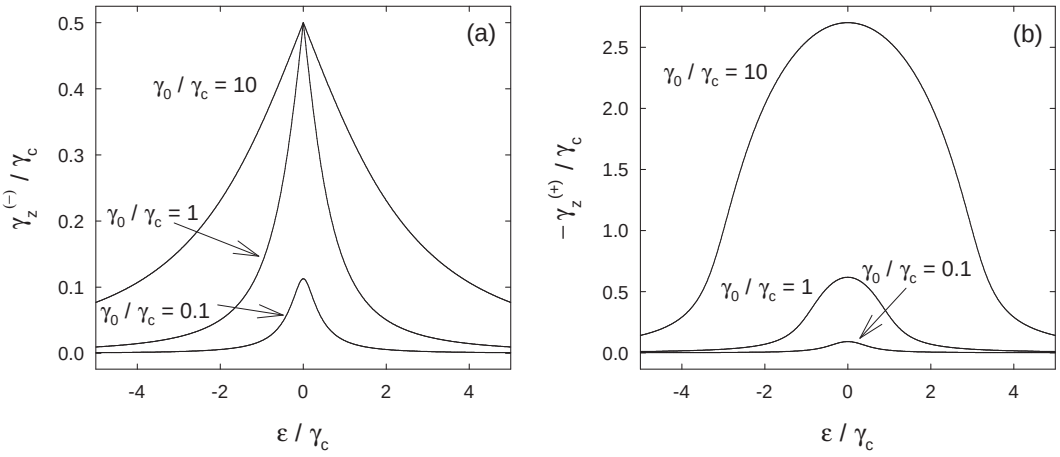

Figure 7.1: Sideband cooling (a) and heating (b) lines, plotted for various γ_0/γ_c.

corresponds to the heating and cooling rates for weak drives on resonance. The heating and cooling lineshapes, plotted for various values of γ_0/γ_c in Fig. 7.1, are nearly Lorentzian for weak drives. For strong drives, the heating rate greatly increases and the line broadens, while the cooling rate saturates at $\gamma_c/2$.

Cavity mode cooling lines

The transverse-electric (TE) and transverse-magnetic (TM) modes of Chapter 5 are the eigenmodes of the electrode cavity, and power is efficiently coupled into the cavity only when resonant with one of these modes. To derive the cooling rates when resonant with one of these modes, we follow the same procedure as with the traveling wave above [84, Sec. IV.C] and expand the electromagnetic fields of Eq. 5.3 for small z and ρ. For both the TE and TM modes, only the modes with $mnp = 1n(\text{even})$ have the appropriate force gradients at $z, \rho = 0$, while the $1n(\text{odd})$ modes have it at $\rho = 0$ and offset a quarter-wavelength along the axis. The resonant forces of sizable

${}^{(E)}\gamma_0/\gamma_0$ for TE_{1np}

$n\backslash p$	1	2	3	4	5	6	7	8
1	1.00	4.00	9.00	16.00	25.00	36.00	49.00	64.00
2	0.12	0.48	1.07	1.91	2.98	4.29	5.84	7.63
3	0.05	0.19	0.42	0.74	1.16	1.67	2.28	2.98
4	0.02	0.10	0.22	0.40	0.62	0.89	1.21	1.58
5	0.02	0.06	0.14	0.25	0.38	0.55	0.75	0.98

${}^{(M)}\gamma_0/\gamma_0$ for TM_{1np}

$n\backslash p$	1	2	3	4	5	6	7	8
1	0.42	1.40	2.75	4.48	6.62	9.20	12.23	15.71
2	0.13	0.49	1.00	1.63	2.35	3.19	4.15	5.22
3	0.06	0.25	0.52	0.87	1.27	1.72	2.22	2.77
4	0.04	0.15	0.32	0.54	0.80	1.09	1.42	1.77
5	0.02	0.10	0.21	0.37	0.55	0.76	0.99	1.24

Table 7.1: Mode geometric factors for cavity-assisted sideband cooling. For odd-p modes, this factor applies when the electron is offset axially by a quarter-wavelength to an electric-field node.

strength are

$$ {}^{(\mathbf{E})}\mathbf{F}_{\mathbf{1np}} = \frac{eE_0}{c}\left(\frac{p\pi\rho_0}{2z_0x'_{1n}}\right)(-1)^{p/2}\left({}^{(E)}\omega_{1np}\sin({}^{(E)}\omega_{1np}t)z\hat{\mathbf{y}} + \cos({}^{(E)}\omega_{1np}t)\dot{y}\hat{\mathbf{z}}\right) \tag{7.8} $$

$$ \begin{aligned} {}^{(\mathbf{M})}\mathbf{F}_{\mathbf{1np}} = eE_0\frac{\rho_0}{x_{1n}}(-1)^{p/2}\Bigg\{&\left(\frac{p\pi}{2z_0}\right)^2\cos({}^{(M)}\omega_{1np}t)z\hat{\mathbf{x}} \\ &+\left[\left(\frac{x_{1n}}{\rho_0}\right)^2\cos({}^{(M)}\omega_{1np}t)x - \frac{{}^{(M)}\omega_{1np}}{c^2}\sin({}^{(M)}\omega_{1np}t)\dot{x}\right]\hat{\mathbf{z}}\Bigg\}. \end{aligned} \tag{7.9} $$

The extra $x\hat{\mathbf{z}}$ force in the TM modes comes from the z-component of the electric field.

For ω_d near resonance with either ${}^{(E)}\omega_{1np}$ or ${}^{(M)}\omega_{1np}$, including one of these forces in the equations of motion gives the same cooling and heating lineshapes of Eq. 7.6, with the coefficients

$$ {}^{(E)}\gamma_0 = \gamma_0\left(\frac{p\pi\rho_0}{2z_0x'_{1n}}\right)^2 \tag{7.10} $$

$$ {}^{(M)}\gamma_0 = \gamma_0\left(\frac{p\pi\rho_0}{2z_0x_{1n}}\right)^2\left[1+\left(\frac{x_{1n}}{\rho_0}\right)^2\frac{c^2}{\omega'_c\omega_d}\right], \tag{7.11} $$

which are identical to the traveling-wave case times a geometric factor. Table 7.1 lists the geometric factors for the trap dimensions fit from cavity modes and listed in Table 5.1. Although some factors are significantly greater than one, the primary benefit in having the sideband resonant with a cavity mode is getting the power into the cavity, and even a mode with a geometric factor less than one provides a substantial enhancement over cooling off a mode.

Cavity-enhanced cooling

The primary advantage to cooling near a mode is the ease with which microwaves are coupled into the cavity. To analyze the resonant cavity as an element in the microwave system, it is useful to model it as an equivalent circuit [142, Ch. 7]. Although a complete description would include the precise method for coupling the power into the cavity, a simple circuit model contains the essential result. In this case, we model a cavity mode as an RLC-parallel circuit, where coupling energy into the cavity is equivalent to dissipation in a large resistance. In terms of the circuit/mode resonant frequency, ω_{M}, quality factor, Q, and equivalent resistance, R, the impedance is

$$Z(\omega_d) = \frac{\dfrac{i\omega_d\omega_{\mathrm{M}}R}{Q}}{\omega_{\mathrm{M}}^2 - \omega_d^2 + \dfrac{i\omega_d\omega_{\mathrm{M}}}{Q}}. \tag{7.12}$$

The magnitude of the electric field in the cavity, E_0 above, goes as this impedance times the electric field incident on the cavity. Since the γ_0 coefficient goes as E_0^2, the squared impedance indicates the cooling power,

$$Z(\omega_d)^2 = Z(\omega_d)^* Z(\omega_d) = \frac{R^2}{1 + Q^2\dfrac{(\omega_d^2 - \omega_{\mathrm{M}}^2)^2}{\omega_d^2\omega_{\mathrm{M}}^2}} \propto \frac{Q^2}{1 + 4Q^2\dfrac{(\omega_d - \omega_{\mathrm{M}})^2}{\omega_{\mathrm{M}}^2}}, \tag{7.13}$$

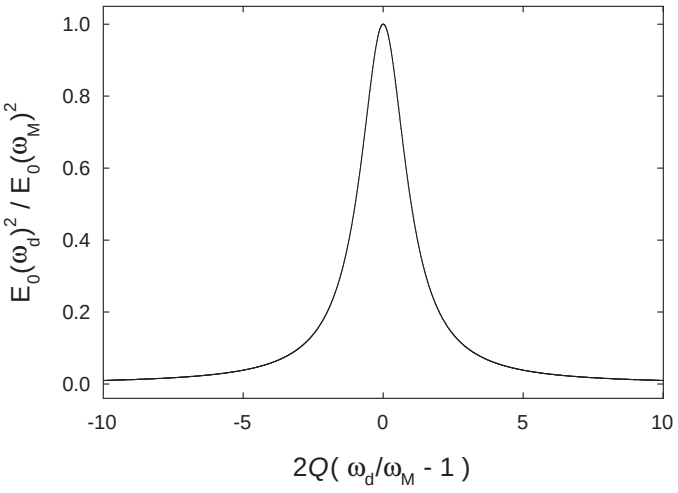

Figure 7.2: Coupling microwave power into the cavity is enhanced near resonance with a mode. The sideband cooling and heating rates are both proportional to the energy in the sideband fields, i.e., $\propto E_0^2$.

where the last statement expands for ω_d close to $\omega_{\rm M}$ and uses the proportionality of the equivalent resistance and the cavity Q (the proportionality constant is the equivalent reactance: R=QX).

The enhanced coupling of the microwave drive to the cavity when near resonance with a cavity mode can be seen in the ratio of the square-magnitude of the electric field at the drive frequency relative to at the mode frequency,

$$\frac{E_0(\omega_d)^2}{E_0(\omega_{\rm M})^2} = \frac{1}{1+\left(2Q(\frac{\omega_d}{\omega_{\rm M}}-1)\right)^2} = \frac{1}{1+\left(\dfrac{\omega_d-\omega_{\rm M}}{\Gamma_{\rm M}/2}\right)^2}, \tag{7.14}$$

where $\Gamma_{\rm M}/2$ is the mode half-width at half-maximum. The Lorentzian dependence is plotted in Fig. 7.2 and is the primary advantage of tuning the sideband cooling frequency near a mode frequency.

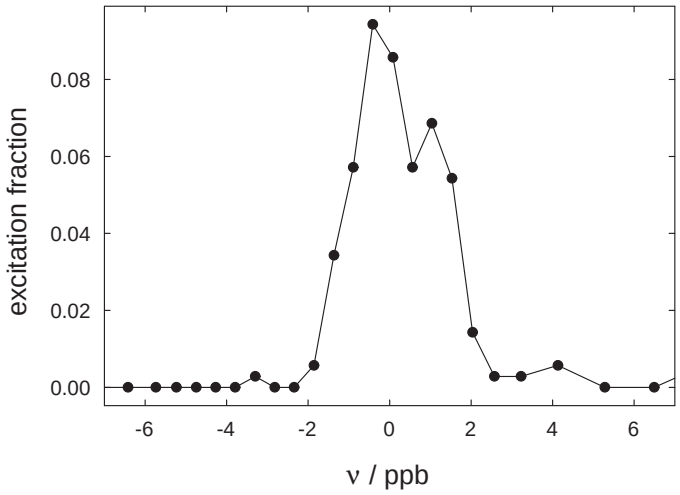

Figure 7.3: Measured axial–cyclotron sideband heating resonance. The zero is an arbitrary offset.

Results and outlook

With the cyclotron frequency at 147.5 GHz, we see cyclotron excitation at both the cooling and heating sidebands despite being detuned 30 linewidths from the nearest cooling mode (TE_{136}). The heating resonance shown in Fig. 7.3 uses the normal cyclotron excitation technique of Section 4.3.1 but with 36 dB more power. Because the axial frequency was left resonant with the amplifier, the heating lineshape of Eq. 7.6 does not apply, and we show the resonance to demonstrate that our microwave system is powerful enough to excite on the sidebands.

Our attempts at cooling the axial degree of freedom are more systematic. With the goal of seeing a lower axial temperature via a narrower cyclotron resonance, we modify the cyclotron excitation scheme used for the g-value data to include detuning the axial frequency from the amplifiers, applying the cooling drive, and retuning the axial frequency after the usual cyclotron pulse. The full sequence follows, beginning with the electron in the $|0,\uparrow\rangle$ state.

1. Turn the self-excited oscillator off and the magnetron cooling drive on. Wait 0.5 s.

2. Turn the amplifiers off. Wait 1.0 s.

3. Turn the magnetron cooling drive off. Wait 1.0 s ($\approx 6\gamma_z^{-1}$).

4. Detune the axial potential $-0.1V_R$ and wait 0.5 s for the endcaps to charge. (There is a 0.1 s RC filter on the endcaps.)

5. Apply the axial cooling drive for 5.0 s then wait 0.1 s.

6. Apply the cyclotron drive and a detuned anomaly drive for 2.0 s.

7. Shift the axial potential to its "pre-retune" value and wait 1.0 s (see Section 2.3.1 for a description of our ν_z detuning technique).

8. Retune the axial potential and wait 0.5 s for the endcaps to charge.

9. Turn the amplifiers on and start the self-excited oscillator. Wait 1.0 s to build up a steady-state axial oscillation.

10. Trigger the computer data-acquisition card (DAQ).

Rather than seeing a narrower cyclotron line after the cooling sequence, we saw a much noisier one because the cooling drive excited the cyclotron motion (as it should), but the cooling rate was so slow that the average cyclotron energy remained above $n = 1$ even when adjusting the length of the cooling pulse up to 15 minutes and cooling at the microwave system's full power (≈ 70 dB above our typical g-value cyclotron excitation power).

Future attempts at sideband cooling should tune the sideband closer to a cooling mode frequency. In the current trap, one could tune to $\nu_c \approx 146.6$ GHz or ≈ 145.1 GHz, each an axial frequency above a cooling mode (TE_{136} at 146.4 GHz and TE_{144} at 144.9 GHz) and both within reach of our current microwave system. The proximity to either of these modes would increase the cooling rate parameter, $\gamma_0 \propto E_0^2$, by a factor of 3600 over its value at $\nu_c = 147.5$ GHz. Neither frequency would be good a location for a g-value measurement, however, because of their proximity to $1n$(odd) modes that create large cavity shift uncertainties. A judicious choice of dimensions in a future trap would have a large range of cyclotron frequencies devoid of any $1n$(odd) modes, which shift ν_c, but peppered with the $1n$(even) modes good for cooling.

Eliminating axial damping is another technical challenge because any axial detuning must be precise enough to calculate the sideband frequency at which we drive; in the future, using this technique in a g-value measurement will require accurate knowledge of the axial frequency for use in calculating the magnetron shift. For both these reasons, decoupling the amplifier from the electrode may be a superior option to detuning the axial potential.

Axial–cyclotron sideband cooling remains—as it has been for some time—a promising technique for the future [84, Sec. IV.C], [123, p. 90–91], [124], [98, p. 120–122], [96, p. 124–125], [89, Sec. 7.1], [83, p. 149]. With our existing, powerful microwave source and a carefully designed new trap, we may finally see the axial motion in its ground-state.

7.2 Better Statistics

Assuming we understand the anomaly and cyclotron lineshapes, increasing the signal-to-noise ratio will reduce the frequency uncertainty when splitting the lines [103]. Although simply running for more nights would work, speeding up the measurement cycle is more efficient. The rate-limiting step of a single sweep of the cyclotron and anomaly lines is the discrimination between $|0,\uparrow\rangle$ and $|1,\downarrow\rangle$ after applying an anomaly pulse. The coupling of these two states to the magnetic bottle produces an axial frequency shift of only 20 ppt (4 mHz), which is too small to detect directly, so we wait several cyclotron lifetimes for the $|1,\downarrow\rangle \rightarrow |0,\downarrow\rangle$ transition, building confidence that the state is actually $|0,\uparrow\rangle$ as $1 - e^{-\gamma_c t}$. Since typical cyclotron lifetimes during g-value measurements are 1–10 s, this wait can be quite long and must occur after *each* anomaly attempt.

We consider two methods to decrease the wait-time: apply a cyclotron π-pulse on the $|1,\downarrow\rangle \leftrightarrow |0,\downarrow\rangle$ transition to drive the electron down or sweep the electron down using an adiabatic-fast-passage technique. Both rely on the different relativistic shift between the two lowest cyclotron transitions.

7.2.1 π−pulse

Special relativity shifts the cyclotron frequency in a state dependent manner, as shown in Fig. 7.4 and given by

$$\Delta\nu_c = -\delta(n + 1 + m_s), \tag{7.15}$$

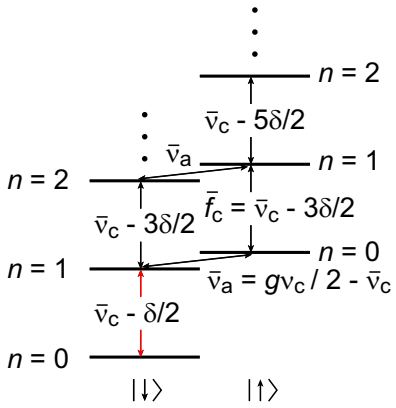

Figure 7.4: The energy levels of an electron in a Penning trap, including ppb-size shifts from special relativity. These shifts make it possible to drive $|0,\downarrow\rangle \leftrightarrow |1,\downarrow\rangle$ without exciting any other transition.

where $\delta/\nu_c = h\nu_c/(mc^2) \approx 10^{-9}$ and $m_s = \pm\frac{1}{2}$. A π-pulse at $\bar{\nu}_c - \delta/2$ can drive the $|1,\downarrow\rangle \rightarrow |0,\downarrow\rangle$ transition without exciting $|1,\downarrow\rangle \rightarrow |2,\downarrow\rangle$ or $|0,\uparrow\rangle \rightarrow |1,\uparrow\rangle$. Applying such a pulse could quickly discriminate between $|0,\uparrow\rangle$ and $|1,\downarrow\rangle$; the former would remain in $|0,\uparrow\rangle$, while the latter would drop to $|0,\downarrow\rangle$.

Two complications create conflicting timescales in our current experiment. First, the time required for a π-pulse depends on the strength of the drive, and the Rabi frequency must be much less than the ppb relativistic shift or the resulting power-broadening can drive the adjacent transition (one level up the cyclotron ladder). Second, the magnetic bottle causes $\bar{\nu}_c$ to fluctuate with the axial energy, decohering the pulse, so the pulse must be much shorter than γ_z^{-1}.

Even on timescales shorter than γ_z^{-1}, during which the axial motion stays in the same state, we have no way of knowing which state that is. Because the linewidth is broader than the relativistic shift, the low-frequency edge of the $\bar{\nu}_c - \delta/2$ line is in the exponential tail of the $\bar{\nu}_c - 3\delta/2$ line, and we could potentially drive the wrong transition. Decoupling from the amplifier would increase γ_z^{-1} and extend the

maximum pulse length, but the ignorance of the axial state would remain. These conflicting timescales thwarted our efforts at seeing Rabi oscillations. Narrower lines are required for this technique.

7.2.2 Adiabatic fast passage

On timescales faster than γ_z^{-1}, the axial motion remains in one state; although we do not know which state that is, we do know that $\nu_c(|0,\downarrow\rangle \leftrightarrow |1,\downarrow\rangle) > \nu_c(|1,\downarrow\rangle \leftrightarrow |2,\downarrow\rangle)$. This knowledge allows us to sweep an electron in the $|1,\downarrow\rangle$ state to the $|0,\downarrow\rangle$ state via adiabatic fast passage. A cyclotron drive swept down in frequency will reach $\bar{\nu}_c - \delta/2$ before $\bar{\nu}_c - 3\delta/2$ and drive the electron into the spin-down ground state. By the time the drive is resonant with the $|1,\downarrow\rangle \leftrightarrow |2,\downarrow\rangle$ transition, the electron will no longer be in the $|1,\downarrow\rangle$ state.

A potential flaw in the technique is the drive's effect on an electron that starts in the $|0,\uparrow\rangle$ state—it sweeps the electron up the cyclotron ladder. An electron in the $|0,\downarrow\rangle$ state, which would occur if the $|1,\downarrow\rangle$ state decays before the drive is swept, would also excite high up the cyclotron ladder. Since the whole point of this technique is to avoid waiting for the cyclotron state to decay, deliberately exciting it seems to be exactly the wrong thing to do. It is possible, however, that a second sweep—*up* in frequency—could de-excite the electron to the ground state.

One complication is the rapid decay of highly excited cyclotron states, which may be lifetime-broadened beyond the relativistic shift. They may decay so fast ($\gamma(n) = n\gamma_c$) that this is not a concern, however, and one could hold the drive at a frequency where the levels are well-separated by the relativistic shift, "catch"

the falling electron, and rapidly sweep it the rest of the way down. The concern, expressed above with the π-pulse, that the Rabi frequency not power-broaden the drive beyond the relativistic shift applies to adiabatic fast passage as well. Since the technique requires the Rabi frequency to greatly exceed the sweep rate, which must be faster than any decoherence time, decoupling from the amplifier will be required. While developing techniques for such decoupling by detuning the axial potential, we were able to sweep the electron up and down the cyclotron ladder via adiabatic fast passage. Our pursuit of a more robust technique was short-lived as we turned our attention to attempts at sideband cooling (presented in Section 7.1.3); further efforts towards adiabatic fast passage are warranted.

This would not be the first use of an adiabatic fast passage technique on a trapped electron. It has been used to demonstrate the relativistic mass increase of the electron through the anharmonic cyclotron resonance [143] as well as to differentiate between the two spin states in a trap with very small magnetic bottle coupling [144, 127]. In the latter cases (both at Harvard and the University of Washington), a drive swept down in frequency starting between $\bar{\nu}_c - \delta/2$ and $\bar{\nu}_c - 3\delta/2$ excites a spin-up electron to high cyclotron states but not a spin-down electron. Adiabatic fast passage has been studied theoretically for the damped anharmonic oscillator (such as the relativistic electron cyclotron motion), including in the case of stochastic fluctuations of the oscillator frequency (corresponding here to axial energy fluctuations in the magnetic bottle) [145, 146].

7.3 Remaining questions

Throughout the thesis, there are four unanswered questions, which we collect here. Answering any of these questions could lead to either an improved g-value measurement or an interesting result with emergent phenomena in many-body systems.

What causes the magnetic field fluctuations? The field noise that broadens the cyclotron edge is the primary source of the lineshape model uncertainty. Characterizing the noise would allow the creation of a more realistic lineshape model. Eliminating it would narrow the lines and remove the lineshape model concern.

Why do the resonance lines have different widths at each field (Section 6.1.4)? The lineshape parameters appear stable throughout the measurements at a particular field but change between fields. The differences are consistent with different axial temperatures, but we have not identified what changed among the procedures. This leads to an increased lineshape model uncertainty for the wider lines.

Why is there an offset between the electrostatic and mode centers (Section 5.4.3)? We observe such an offset in the multi-electron mode maps and with the single-electron damping rate. Estimates of simple shifts among the electrodes are unable to account for the discrepancy, suggesting a more exotic trap deformation. Although the agreement of the cavity-shift-corrected g-values at four magnetic fields reassures us that we account for the offset correctly, understanding its cause could allow for more sturdy trap designs in the future.

How does increasing γ_c lead to symmetry-breaking in the parametric resonance of an electron cloud, and what limits it (Section 5.2)? The electron-cloud mode detection technique relies on synchronization of the axial motion in a parametrically

driven cloud in a manner that is sensitive to γ_c. Although one can write down the full equations of motion, a solution showing the observed collective behavior remains underived. In addition to providing an interesting result in many-body physics, such a solution could suggest a set of parameters that enhance the sensitivity to γ_c, making the faster of our two mode-detection techniques more robust.

7.4 Summary

Future electron g-value experiments should focus on improving the measurement precision of the cyclotron and anomaly frequencies. Foremost, magnetic field noise should be reduced until the resonance lines conform to the Brownian-motion shapes of Section 4.2, [86], and [89, Ch. 3]. The new high-stability apparatus of Section 3.5 should aid in this respect. Additional advantages will come from narrowing the resonance lines and increasing their signal-to-noise ratio. Narrower lines will result from reducing the magnetic-bottle coupling between the axial energy and resonance frequencies as well as from lowering the axial energy itself via cavity-assisted axial–cyclotron sideband cooling. An increased signal-to-noise ratio will result from speeding-up the detection of a spin-flip after an anomaly excitation by driving the $|1,\downarrow\rangle \rightarrow |0,\downarrow\rangle$ transition via a π-pulse, which will require cyclotron linewidths narrower than the ppb relativistic shift, or via adiabatic fast passage. Answering outstanding questions regarding axial temperature changes, the offset between electrostatic and mode centers, and parametric mode-mapping will increase the procedural robustness. Finding the source of any magnetic field noise and eliminating it can remove the lineshape model uncertainty, which dominates both the 2006 and present

g-value measurements. Except for this noise, there is no obvious limitation to future measurements, and substantial improvements from our quantum cyclotron are likely.

Chapter 8

Limits on Lorentz Violation

8.1 The Electron with Lorentz Violation

The high accuracy of our g-value measurement provides several tests of the Standard Model. In Chapter 1, we reviewed tests that rely on a comparison of the measured g-value to that predicted by QED and an independent measurement of the fine structure constant, including searches for electron substructure, for light dark matter, and for modifications to the photon propagator from Lorentz symmetry violation. In this chapter, we focus on temporal variations in g, specifically those showing modulation related to the Earth's rotational frequency; such modulation could arise from a violation of Lorentz symmetry that defines a preferred direction in space.

These modulations would appear as daily variations in the cyclotron and anomaly frequency, and we search for both simultaneously using the cyclotron frequency to normalize the anomaly frequency to a drifting magnetic field and searching for variations in this drift-normalized ν_a with the rotation of the Earth. We limit the amplitude

of these modulations to $|\delta\nu_a| < 0.05$ Hz, which improves upon the prior measurement at the University of Washington (UW) by a factor of two [56].[1] Through the parameterization of a Standard Model extension that allows for violations of Lorentz invariance, we compare this result to those from other experiments and astrophysical observations, finding that the others set much tighter limits. The simplicity of the single-electron system provides a reassuring confirmation of these other limits, and the substitution of a positron will allow further tests of CPT-violation that are inaccessible through other means.

8.1.1 Energy levels and frequency shifts

The Kostelecký Standard Model extension (SME) [51], introduced in Section 1.1.5, provides a framework for extending the Standard Model to include spontaneous breaking of Lorentz symmetry, resulting in CPT violation in some cases. It allows the comparison of tests from diverse experiments and suggests which measurements should be most sensitive to effects beyond the Standard Model. We are most concerned with the extension of the QED Lagrange density; the SME terms are typically parameterized as a_μ, b_μ, $c_{\mu\nu}$, $d_{\mu\nu}$, $H_{\mu\nu}$, $(k_{\mathrm{AF}})^\kappa$, and $(k_{\mathrm{F}})_{\kappa\lambda\mu\nu}$ in

$$\begin{aligned}\mathcal{L}^{\mathrm{SME}} = &-a_\mu\bar{\psi}\gamma^\mu\psi - b_\mu\bar{\psi}\gamma_5\gamma^\mu\psi + c_{\mu\nu}\bar{\psi}\gamma^\mu\left(i\hbar c\partial^\nu - qcA^\nu\right)\psi \\ &+ d_{\mu\nu}\bar{\psi}\gamma_5\gamma^\mu\left(i\hbar c\partial^\nu - qcA^\nu\right)\psi - \frac{1}{2}H_{\mu\nu}\bar{\psi}\sigma^{\mu\nu}\psi \\ &+ \frac{1}{2\hbar}\left(k_{\mathrm{AF}}\right)^\kappa\epsilon_{\kappa\lambda\mu\nu}\sqrt{\frac{\epsilon_0}{\mu_0}}A^\lambda F^{\mu\nu} - \frac{1}{4\mu_0}\left(k_{\mathrm{F}}\right)_{\kappa\lambda\mu\nu}F^{\kappa\lambda}F^{\mu\nu}.\end{aligned} \tag{8.1}$$

[1] We do not get the same order-of-magnitude improvement here that we had for the g-value because the UW result came from a dedicated Lorentz-violation experiment, optimized for detecting ν_a at the expense of poor precision of ν_c.

The a_μ, b_μ, $H_{\mu\nu}$, and $(k_{\rm AF})^\kappa$ terms have units of energy, while $c_{\mu\nu}$, $d_{\mu\nu}$, and $(k_{\rm F})_{\kappa\lambda\mu\nu}$ are dimensionless. The parameter values may differ from particle to particle, and we concern ourselves only with those related to the electron.

No Lorentz violation has been found to date, and the current limits on the SME parameters are much less than one, so they may be used perturbatively in calculations. The leading term in a perturbative expansion about the cyclotron energies of an electron or positron in a Penning trap shows shifts equal to [54]

$$\begin{aligned}\delta E^{\pm}_{n,m_s} \approx{}& \mp a_0 - c_{00}mc^2 - 2m_s(b_3 \pm d_{30}mc^2 \pm H_{12}) \\ &- (c_{00}+c_{11}+c_{22})(n+\tfrac{1}{2}\mp m_s)\hbar\omega_c \\ &- (\tfrac{1}{2}c_{00}+c_{33}\pm 2m_s(d_{03}+d_{30}))\frac{p_z^2}{m},\end{aligned} \tag{8.2}$$

for cyclotron level n and spin state $m_s = \pm\frac{1}{2}$. The $\pm$ in $\delta E^{\pm}_{n,m_s}$ refers to positrons and electrons, and p_z is the axial momentum. The indices refer to a local coordinate system with $\hat{\mathbf{z}}$ (3) parallel to the experiment quantization axis (the magnetic field), $\hat{\mathbf{x}}$ and $\hat{\mathbf{y}}$ (1,2) lying in the transverse plane, and 0 indicating time. The cyclotron and anomaly frequencies are defined by energy differences,

$$\hbar\omega_c^{\pm} = E_{1,\pm\frac{1}{2}} - E_{0,\pm\frac{1}{2}} \tag{8.3}$$

$$\hbar\omega_a^{\pm} = E_{0,\mp\frac{1}{2}} - E_{1,\pm\frac{1}{2}}, \tag{8.4}$$

and show shifts from any CPT or Lorentz violation, given to leading-order by

$$\delta\omega_c^{\pm} \approx -\omega_c(c_{00}+c_{11}+c_{22}) \tag{8.5}$$

$$\delta\omega_a^{\pm} \approx 2(\pm b_3 + d_{30}mc^2 + H_{12})/\hbar. \tag{8.6}$$

Again, the $\pm$ refers to positrons and electrons.

8.1.2 Experimental signatures

The frequency shifts of Eq. 8.5 and Eq. 8.6 are written in terms of a laboratory-based coordinate system that rotates with the Earth. The spatial terms, therefore, are modulated at multiples of the Earth's rotational frequency, Ω, depending on the multipolarity of the term; we explore the precise Ω-dependence in the next section. In principle, we can look for modulations of the anomaly and cyclotron frequencies separately. In practice, we use the cyclotron edge-tracking technique of Section 4.3.3 to remove magnetic field drifts and look for modulations of a drift-normalized ν_a. By using the cyclotron frequency to correct drifts in the anomaly frequency, any modulation of ν_c is transferred onto ν_a.

To see this transfer explicitly, we examine the equation used to correct the drifts,

$$\nu_a(t) = \nu_{a,0}(t) - \frac{g-2}{2}\left(\nu_{c,0}(t) - \nu_c\right), \tag{8.7}$$

where the "0" subscript here indicates the co-drifting frequencies, ν_c the normalization cyclotron frequency, and ν_a the drift-normalized anomaly frequency that is our probe of Lorentz violation. The "(t)" indicates potential time-dependence from Lorentz violation. Combining the leading terms for Lorentz-violation in Eq. 8.5 and Eq. 8.6 with this normalization procedure adds an overall SME-dependence to the drift-normalized anomaly frequency of

$$\delta\nu_a = -\frac{2\tilde{b}_3}{h} + \nu_a(c_{00} + c_{11} + c_{22}). \tag{8.8}$$

Here, we have combined several terms using a conventional shorthand (see e.g. [55]),

$$\tilde{b}_j \equiv b_j - d_{j0}mc^2 - \frac{1}{2}\epsilon_{jkl}H_{kl}. \tag{8.9}$$

Our figure-of-merit is $\delta\nu_a$, which includes modulation of the drift-normalized anomaly frequency as well as offsets between the measured anomaly frequency and that predicted by QED and an independent α.

8.1.3 The celestial equatorial coordinate system

In order to compare our results to those of other experiments, we must rewrite our figure-of-merit, Eq. 8.8, in terms of a rotation-free coordinate system. The customary choice is celestial-equatorial coordinates [147], which defines a position on the celestial sphere in terms of two angles: declination, the angle above the celestial equator, and right ascension, the angle east of the vernal equinox point. This defines a coordinate system where $\hat{\mathbf{Z}}$ points along the rotation axis of the earth (declination 90°), $\hat{\mathbf{X}}$ points towards the vernal equinox point (right ascension and declination 0°), and $\hat{\mathbf{Y}} = \hat{\mathbf{Z}} \times \hat{\mathbf{X}}$ (declination 0°, right ascension 90°).

The rotation matrix to take the $(\hat{\mathbf{X}}, \hat{\mathbf{Y}}, \hat{\mathbf{Z}})$ non-rotating coordinates to the $(\hat{\mathbf{x}}, \hat{\mathbf{y}}, \hat{\mathbf{z}})$ laboratory coordinates is [147]

$$M(\phi, t) = \begin{pmatrix} \sin\phi\cos\Omega t & \sin\phi\sin\Omega t & -\cos\phi \\ -\sin\Omega t & \cos\Omega t & 0 \\ \cos\phi\cos\Omega t & \cos\phi\sin\Omega t & \sin\phi \end{pmatrix}, \tag{8.10}$$

where Ω is the Earth's rotation frequency and ϕ is the latitude of the laboratory, 42.377°, and equal to 90° minus the angle between $\hat{\mathbf{Z}}$ and $\hat{\mathbf{z}}$.[2] Recalling that vectors

[2]Because the system is cylindrically symmetric, $\hat{\mathbf{x}}$ and $\hat{\mathbf{y}}$ enter on equal footing, e.g., $c_{11} + c_{22}$. In the conversion to $(\hat{\mathbf{X}}, \hat{\mathbf{Y}}, \hat{\mathbf{Z}})$, we adopt the convention of [147], with $\hat{\mathbf{x}}$ lying in the z–Z plane and equal to $\hat{\mathbf{z}}\tan\phi - \hat{\mathbf{Z}}\sec\phi$ and $\hat{\mathbf{y}}$ in the plane of the Earth's equator and equal to $\hat{\mathbf{z}} \times \hat{\mathbf{x}}$.

and tensors transform as

$$V^{(x,y,z)} = MV^{(X,Y,Z)} \tag{8.11}$$

$$T^{(x,y,z)} = MT^{(X,Y,Z)}M^{-1}, \tag{8.12}$$

we may express the coefficients in Eq. 8.8 as

$$\tilde{b}_3 = \tilde{b}_Z \sin\phi + \cos\phi\left(\tilde{b}_X \cos\Omega t + \tilde{b}_Y \sin\Omega t\right) \tag{8.13}$$

$$\begin{aligned} c_{11} + c_{22} =& \frac{1}{2}\left(c_{XX} + c_{YY}\right)\left(1 + \sin^2\phi\right) + c_{ZZ}\cos^2\phi \\ & - \cos\phi\sin\phi\left[\left(c_{XZ} + c_{ZX}\right)\cos\Omega t + \left(c_{YZ} + c_{ZY}\right)\sin\Omega t\right] \\ & - \frac{1}{2}\cos^2\phi\left[\left(c_{XX} - c_{YY}\right)\cos 2\Omega t + \left(c_{XY} + c_{YX}\right)\sin 2\Omega t\right]. \end{aligned} \tag{8.14}$$

The c_{00} term in Eq. 8.8 and several of the terms when written in the $(\hat{\mathbf{X}}, \hat{\mathbf{Y}}, \hat{\mathbf{Z}})$ coordinate system have no modulation. They serve as offsets between the measured and predicted anomaly frequencies and would be candidates for physics beyond the Standard Model if our data disagrees with that predicted by QED and an independent α. Our limits of Eq. 1.18 suggest that these terms have $|\delta\nu_a|_{\text{offset}} \approx \nu_c\,|\delta g/2| \lesssim 10^{-14}$ eV/h. The remainder of this chapter investigates the modulation terms.

8.2 Data Analysis

To search for Lorentz variations, we take the data from the four magnetic fields used to measure the g-value in Chapter 6, separate it into several groups based on the Earth's rotation angle, analyze each group separately, and look for variations at one and two times the sidereal frequency.

8.2.1 Local Mean Sidereal Time

We keep track of the Earth's rotation using local mean sidereal time (LMST), which divides a full rotation into 24 hours;[3] 0 h LMST corresponds to the meridian of the vernal equinox overhead, i.e., $\hat{\mathbf{z}}$ lies in the positive-X half of the X–Z plane. The Earth's revolution around the sun creates a discrepancy between the mean solar day and LMST such that one rotation of the Earth (24 h LMST) occurs in approximately 23.93 solar hours, and the two timescales are generally out of phase with each other, rephasing once a year. By running over the course of several months, this relative phase allows us to take data at all 24 sidereal hours despite our limitation to "nighttime" runs (Chapter 3 describes the daytime noise).

Since we time-stamp every excitation attempt, we can bin them by LMST. We calculate LMST as an offset to Greenwich mean sidereal time (GMST), which is given in hours by

$$\text{GMST} = 18.697\ 374\ 827 + 24.065\ 709\ 824\ 279\ D \pmod{24}, \tag{8.15}$$

where D is the number of solar days (including fractions) from 1 January 2000, noon UT (see e.g. [148]). Eq. 8.15 includes a small correction for the Earth's $\approx$ 26 000-year precession but not for its nutation, which never adds more than 1.2 s. The LMST is the GMST offset by the laboratory longitude, $\lambda = -71.118°$,

$$\text{LMST} = \text{GMST} + \frac{\lambda}{15°\text{h}^{-1}} \pmod{24}. \tag{8.16}$$

Figure 8.1 shows the anomaly excitations at each field binned by LMST. Although the data were mostly obtained during the night, the several-month delay among scans

[3] LMST is the conventional choice, but we could just as easily track the rotation angle in radians.

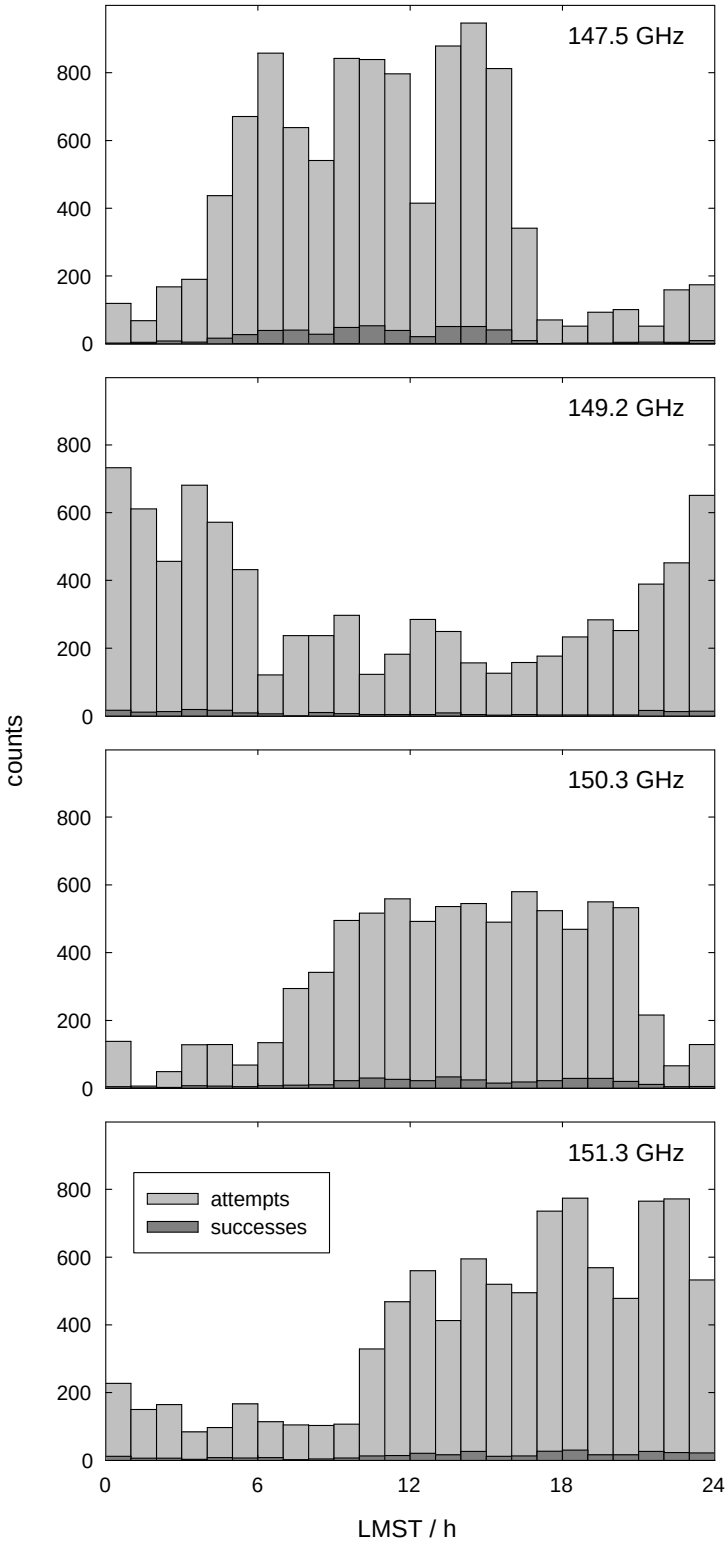

Figure 8.1: Anomaly excitation attempts and successes binned by sidereal time. The attempts greatly outnumber the successes because most tries are off-resonance.

provides broad coverage of LMST.[4]

8.2.2 Fitting the data

After calculating the LMST for each anomaly excitation attempt, we separate the data by time into several bins (we repeat the procedure for 6–24 bins to ensure the binning does not affect the result) and analyze each bin separately. Because the data at each of the four fields was taken under slightly different conditions, e.g., different axial temperatures (see Section 6.1.5), we analyze each field separately as well and combine them in a weighted average for each bin. Using Eq. 8.7, the anomaly excitation attempts are normalized to a common magnetic field. The non-relativistic, free-space, co-drifting frequencies used for normalization, $\nu_{a,0}$ and $\nu_{c,0}$, are calculated from the actual anomaly excitation frequencies, $\bar{\nu}_a$, and the edge-tracking frequencies, $\bar{\nu}_{\text{edge}}$, using the relativistic, magnetron, and cavity corrections (Section 4.1):

$$\nu_{a,0} = \bar{\nu}_a - \frac{\bar{\nu}_z^2}{2\bar{f}_c} + \bar{f}_c \frac{\Delta\omega_c}{\omega_c} \tag{8.17}$$

$$\nu_{c,0} = \bar{\nu}_{\text{edge}} + \Delta_{\text{edge}} + \frac{3}{2}\delta + \frac{\bar{\nu}_z^2}{2\bar{f}_c}. \tag{8.18}$$

Here, Δ_{edge} is a procedure-dependent offset between the edge-tracking and cyclotron frequencies. We measure this offset during the fits that quantify the lineshape model uncertainty and use the measured offset (40–95 Hz depending on the field) and its uncertainty (around 15 Hz) in this analysis.

A weighted-mean calculation using the normalized anomaly attempts provides a measurement of the anomaly frequency offset by $\Delta\omega$, which is subtracted using

[4]The 147.5 GHz, 149.2 GHz, 150.3 GHz, and 151.3 GHz data were taken in February, September, May, and June, 2007.

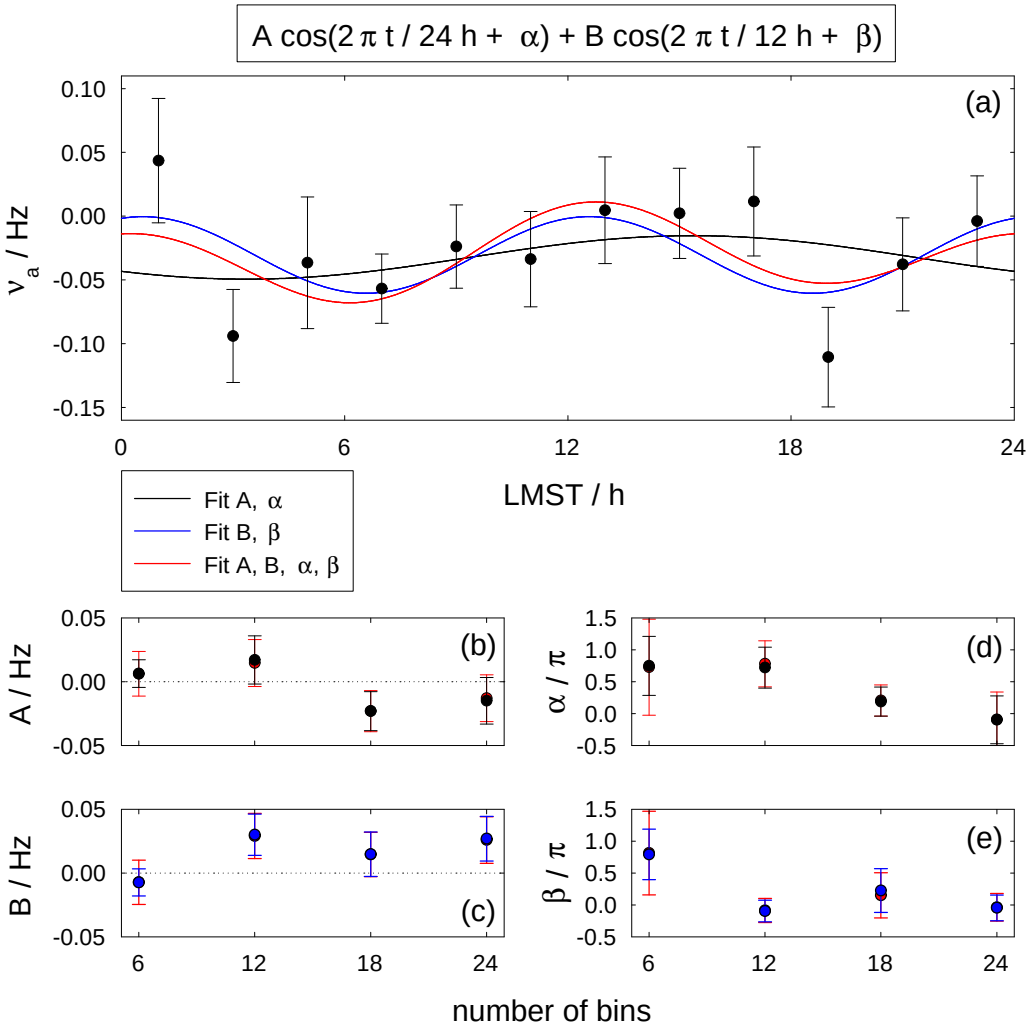

Figure 8.2: Results of analyzing the anomaly frequency versus LMST. Part (a) shows the data separated into 12 2-hour bins and fit to modulations with periods 24 h, 12 h, or both. Parts (b) and (c) show the best-fit amplitudes for four different bin widths. Parts (d) and (e) show the best-fit phases.

the axial temperature at each field (again, from the lineshape model analysis fits) to obtain the anomaly frequency itself. The anomaly frequency in a given time-bin comes from the weighted average of the anomaly frequencies at all fields. In the average, we include uncertainties from the weighted-mean calculation, the axial temperature, the cavity shift (Table 6.4), the edge offset, and the uncorrelated part of the lineshape model (Table 6.1). The correlated lineshape model uncertainty affects neither the weighted average nor the uncertainty in the $\delta\nu_a$ figure of merit, which is essentially a differential measurement.

With the data analyzed into frequency-versus-time, we fit a five-parameter model,

$$\nu_a = \nu_0 + A\cos(2\pi t/24\text{ h} + \alpha) + B\cos(2\pi t/12\text{ h} + \beta), \tag{8.19}$$

where A is the amplitude of the sidereal variation and B is the amplitude of the semi-sidereal variation. We also fit the model with A and B alternately set to zero to analyze the case where only one modulation exists.

The result of such fits for 12 bins (2 h wide) appears in Fig. 8.2a. Figure 8.2b and Fig. 8.2c compare the modulation amplitudes for several different time bin widths. While not all are consistent with zero, they lie within

$$|\delta\nu_a| < 0.05\text{ Hz} = 2\times10^{-16}\text{ eV}/h, \tag{8.20}$$

which we adopt as our result.

8.2.3 Comparisons with other experiments

The limit of Eq. 8.20 is two times better than the 0.10 Hz limit of the previous single-electron result [56]. It provides confirmation of other results but does not set

the limit for any SME coefficients. If the sidereally variant coefficients of c_{ij} are all zero, then the figure of merit, $\delta\nu_a$, sets the limit

$$\left|\tilde{b}_\perp\right| = \left|\sqrt{\tilde{b}_X^2 + \tilde{b}_Y^2}\right| = \frac{h\ |\delta\nu_a|}{2\cos\phi} < 1.4 \times 10^{-16}\ \text{eV}, \tag{8.21}$$

which is stated as the magnitude of $\tilde{b}_j$ perpendicular to the Earth's axis because the cosine fits give little phase information. The best current constraint is $\tilde{b}_\perp$ less than 2.5×10^{-22} eV by a spin torsion-pendulum experiment also at the UW [61], which has a stronger coupling to the $\tilde{b}_j$-field because of 10^{23} more spins.

If instead $\tilde{b}_X$ and $\tilde{b}_Y$ are zero, then $\delta\nu_a$ limits the values of several combinations of c_{ij} coefficients. For rotation purely at the Earth's sidereal frequency, we may limit

$$\left|\sqrt{\left(c_{XZ} + c_{ZX}\right)^2 + \left(c_{YZ} + c_{ZY}\right)^2}\right| = \frac{|\delta\nu_a|}{\nu_a}\frac{1}{\cos\phi\sin\phi} < 6 \times 10^{-10}, \tag{8.22}$$

where again the fits reveal little phase information. For rotation purely at twice the sidereal frequency, we may limit

$$\left|\sqrt{\left(c_{XX} - c_{YY}\right)^2 + \left(c_{XY} + c_{YX}\right)^2}\right| = \frac{|\delta\nu_a|}{\nu_a}\frac{2}{\cos^2\phi} < 1 \times 10^{-9}. \tag{8.23}$$

More stringent limits on these coefficients have been set at the 10^{-15} level using either cryogenic optical resonators [57] or astrophysical observations of electron-emitted radiation [58, 59]. The resonators, which are normally used to place bounds on SME coefficients in the photon sector, look for Lorentz-violating changes in the electronic structure of a crystal resonator. Searching for such violations in the electron sector requires assumptions about negligible violations in the nuclear sector. The astrophysical limit looks at inverse Compton and synchrotron radiation from fast-moving electrons with astrophysical sources, e.g., the Crab nebula, and searches for direction-

dependence in the electron dispersion relations because nonzero $c_{\mu\nu}$ alters the maximum energy or velocity an electron can have.

8.3 Summary and outlook

Searches for modulation of the anomaly frequency with the rotation of the Earth allow us to set a new experimental limit on the modulation amplitude of $|\delta\nu_a| < 0.05$ Hz, a factor of two smaller than the previous single-electron limit [56]. Comparisons using the parameterization of the SME show that experiments with spin torsion-pendulums [61] and optical resonators [57] as well as astrophysical observations [58] yield tighter bounds on Lorentz violation, though with more complicated systems involving estimates of the number of spins in macroscopic material, assumptions about Lorentz violation in the nuclear sector, and astrophysical models. The simplicity of the single-electron system makes the analysis of this chapter worthwhile despite the several orders-of-magnitude difference in the limits.

Additional sensitivity in the single-electron system could be achieved using the same conditions for the entire search, as uncertainties from the axial temperature, the cavity shift, the edge offset, and the lineshape model would then cancel in the analysis.

Other SME coefficients create Lorentz violations from boosts as the Earth revolves around the Sun [149]. Such effects would appear as annual modulations in the anomaly and cyclotron frequencies but would be suppressed by the relativistic factor $\beta_{\mathrm{Earth}} = v_{\mathrm{Earth}}/c \approx 10^{-4}$. The rival experiments mentioned above, however, could also set tighter limits on these boost effects.

The replacement of the single electron with a positron allows the most sensitive test of the CPT-breaking part of $\tilde{b}_j$, i.e., b_j, which creates a difference between the anomaly frequencies of the particle and antiparticle [62]. Unless b_j happened to be parallel to the Earth's axis, this difference would oscillate with the Earth's rotation, so measurements should be taken at all hours of sidereal time. This was not done in the 1987 positron–electron comparison [2, 63], so any new limit comparing the electron and positron frequencies could improve the bound on b_j by more than our order-of-magnitude improvement in g.

Chapter 9

Conclusion

9.1 A New Measurement of g

Using a single electron in a quantum cyclotron, we present a measurement of the electron magnetic moment,

$$\frac{g}{2} = 1.001\ 159\ 652\ 180\ 73\ (28)\ [0.28\ \text{ppt}], \tag{9.1}$$

an improvement of nearly a factor of three over our result of last year [1]. Together, they represent a factor of 15 improvement on the 1987 University of Washington measurement [2]. Among the methods contributing to this enhancement are the use of a cylindrical trap geometry [87] to control the location of cavity modes and allow analytic calculations of their coupling to cyclotron motion [79, 80], lower temperatures to narrow the resonance lines and prepare the cyclotron motion in the quantum-mechanical ground state [85], and a self-excited oscillator [88] to boost the signal-to-noise for quantum nondemolition measurements of single cyclotron jumps and spin flips.

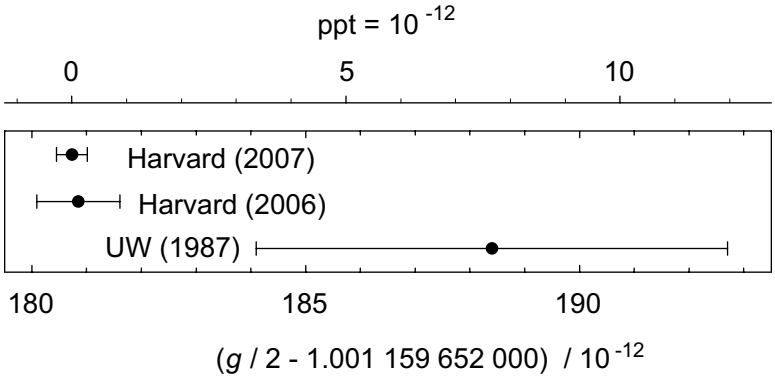

Figure 9.1: Electron g-value comparisons [1, 2].

Using a quantum electrodynamics calculation with small corrections from hadronic and weak loops, we determine an improved value for the fine structure constant,

$$\alpha^{-1} = 137.035\ 999\ 084\ (33)(39) \tag{9.2}$$

$$= 137.035\ 999\ 084\ (51)\ [0.37\ \text{ppb}], \tag{9.3}$$

where Eq. 9.2 separates the experimental and theoretical uncertainties to show that the estimate of the tenth-order coefficient in the QED expansion now contributes more uncertainty than the measured g. Independently measured values of α from atom-recoil measurements are over a factor of ten lower in precision; comparisons between the measured g and that calculated from the atom-recoil fine structure constants and QED provide limits on electron substructure, the existence of light dark matter, and a potential Lorentz-violation by the photon. Searching for modulation of the anomaly frequency as the Earth rotates limits other methods of Lorentz-violation.

9.2 Outlook

The techniques presented in this thesis, especially when augmented with the new high-stability apparatus described in Section 3.5, clear the way for a series of new measurements, several of which have already begun. Among them are the following.

9.2.1 The e^+ g-value and testing CPT

Comparisons of the electron and positron g-values provide high-precision tests of the CPT theorem and constrain possible violations of Lorentz invariance [62]. Except for the loading mechanism and an inverted ring voltage, a positron g-value measurement would proceed identically to the electron measurement presented here. Many methods exist for loading positrons in a cryogenic environment, see e.g., [150, 151], and some are amenable to scaling down to the low loading rates required for trapping only one. Work is underway on a new positron g-value measurement with the goal of exceeding the precision of both the current 4.3 ppt positron g-value limit [2] and the 0.28 ppt electron limit set here [152].

9.2.2 The proton-to-electron mass ratio

The proton-to-electron mass ratio plays an important role in, among other things, atomic hyperfine structure and molecular energy levels. The current 0.5 ppb precision [25] is calculated from the ratio of the proton and electron masses in amu: $A_\mathrm{r}(\mathrm{p})/A_\mathrm{r}(\mathrm{e})$. The former comes from a direct proton–carbon cyclotron frequency comparison in a Penning trap, while the latter is calculated from bound-electron g-value measurements. When combined with existing techniques for 90 ppt resolution

of the proton cyclotron frequency [153], the sub-ppb electron cyclotron frequency resolution presented in this thesis suggests that a direct comparison of the cyclotron frequencies of a proton and a positron should be competitive with the current determination. Since m_p/m_e is currently limited by $A_\mathrm{r}(\mathrm{e})$, any improvement in the ratio would correspond to an improved measurement of the relative electron mass.

9.2.3 The proton and antiproton magnetic moments

The success of the electron magnetic moment measurement has inspired a pair of competing experiments with the goal of direct measurement of the proton and antiproton magnetic moments at the ppb-scale [88, 154]. This precision would represent an order-of-magnitude improvement in the precision of the proton magnetic moment [25] and a million-fold improvement in that of the antiproton, which currently stands at 0.3% [13, p. 955]. Taken individually, these magnetic moment measurements do not serve the same check on theory that the electron moment does because the QCD model for the proton spin is still under investigation [3]. Together, though, they would provide an important test of CPT invariance [54].

Since the antiproton cyclotron frequency can already be measured to the precision required [153], the challenge to applying the techniques of this thesis (especially QND detection with a magnetic bottle) to the antiproton lies in the detection of a spin flip. The absolute axial frequency shift from such a flip is proportional to $\mu/\sqrt{m}$ (see Eq. 2.1 and Eq. 2.26). Both parts increase the measurement difficulty, as the antiproton moment is 658 times smaller than that of the electron, and $\sqrt{m}$ is 43 times larger, making the relative frequency shift 3×10^4 smaller than that of an electron in

the same trap. The proposed solution is to increase the magnetic bottle strength and decrease the trapping potential. Both groups have maximized B_2 by reducing the trap dimensions and by making the ring electrode itself out of ferromagnetic material. In order to reduce the bottle-induced line-broadening (Section 4.2), they employ a dual-trap design, commonly used in bound-electron g-value measurements [31], in which the spin and cyclotron transitions are made in a magnetic-gradient-free trap before the particle is transferred to the large-bottle trap. Decay of excited cyclotron states during the transfer is not a problem because the cyclotron damping rate is greatly reduced for the heavier antiproton (see Eq. 2.11). One of the remaining challenges is keeping the trapping potential stable enough to average the axial frequency and resolve the tiny shift.

9.2.4 A single electron as a qubit

Access to the lowest quantum states of a trapped electron have led to several proposals for using electrons in Penning traps as qubits. When compared to the existing quantum information experiments with ions in linear Paul traps [155], the electron system has three advantages [156]: faster gate times from the higher trap frequencies of the lighter electron, weaker decoherence because only the cyclotron motion has intrinsic damping and the trapping fields are static, and dense coding because each electron can encode information in its spin, cyclotron, and axial degrees of freedom. However, the electron lacks internal degrees of freedom that allow laser-cooling in ions and some electron quantum information proposals rely on challenging techniques such as axial–cyclotron sideband cooling.

Proposals exist for using the cyclotron, spin, and/or axial degrees of freedom as qubits, which could be initialized via natural damping (cyclotron), anomaly transitions (spin) [157], or sideband cooling (axial) [158]. Several gates have been proposed between pairs of degrees of freedom, each forming a single qubit (axial and spin [158, 156] and cyclotron and spin [159]). Scaling the number of qubits could be implemented with a linear array of Penning traps [156] or a 2D array of open-geometry Penning traps [157] with their electrodes in a plane [160]; electrons could be individually addressed by differentiating the trap frequencies, e.g., by introducing a magnetic field gradient or adjusting the electrode potentials. Interaction between electrons via the Coulomb interaction can be controlled by bringing their axial frequencies into resonance. One proposal involves using a magnetic field gradient and the Coulomb interaction to create a pseudo-spin-spin interaction [157]. Others suggest using anharmonicity, either from special relativity or the trap potential, to create state-dependent frequencies useful in conditional gates and to remove the degeneracy of higher cyclotron and axial states, reducing these degrees of freedom to two-level systems. All proposals rely on quantum nondemolition detection of the cyclotron and spin states using the magnetic bottle, and information encoded in the axial state must be transfered to another degree of freedom with a sideband pulse before readout [158].

Steps have been taken toward the demonstration of axial–cyclotron sideband cooling (including the analysis in Chapter 7), electrons have been briefly confined in a planar Penning trap at room temperature [161], and work has begun on a cryogenic planar trap [162]. Nevertheless, a trapped-electron-based quantum computer remains a challenging goal.

9.3 Summary

Precise control of the location of and the coupling to the electromagnetic modes of the electrode cavity has reduced the once-dominant cavity shift uncertainty and led to an improved measurement of the electron magnetic moment. With the measurement limited by the resolution and model of the cyclotron and anomaly lines, future work should focus on enhancing magnetic field stability, narrowing the lines, and building signal-to-noise.

Appendix A

Derivation of Single-Mode Coupling with Axial Oscillations

In Section 5.3.2, we showed that coupling between a cavity mode and an electron depends on the electron position in the trap. Since the electron is oscillating axially, we wish to derive the mode coupling as a function of the axial amplitude. This is trickier than adding a time-dependence to the z-dependent parts of the mode coupling and averaging over an oscillation cycle; one must be careful to keep time and frequency separate by Fourier transforming and time-averaging at the proper points. In principle, one could do a proper calculation for the full renormalized model, though in practice it is difficult. Here, we treat the coupling to a single mode.

We start with the transverse equation of motion (Eq. 5.21),

$$\dot{\mathbf{v}} - \boldsymbol{\omega_c'} \times \mathbf{v} = \frac{e}{m}\mathbf{E}'(\mathbf{r}), \tag{A.1}$$

where we have folded the electrostatic quadrupole into the cyclotron frequency by changing $\boldsymbol{\omega_c} \rightarrow \boldsymbol{\omega_c'}$ and have removed the free-space damping so the electron is

damped only by the mode. We may combine the two transverse components by writing

$$v = v_x - iv_y = v_0 e^{-i\omega t} \tag{A.2}$$

so the equation of motion becomes

$$(\omega - \omega_c')v = i\frac{e}{m}E'(\mathbf{r}), \tag{A.3}$$

where the components of $\mathbf{E}'(\mathbf{r})$ are combined in the manner of Eq. A.2. The quantity $\omega - \omega_c'$ is the same one we have typically referred to as $\Delta\omega_c - i\frac{\gamma}{2}$.

In the radiation gauge, we may write the electric field as the time-derivative of a vector potential, which we write as the convolution of a Green's function, D, with the current source (the electron),

$$i\frac{e}{m}E'(\mathbf{r}) = -i\frac{e}{m}\frac{\partial}{\partial t}\int dt' \frac{\mu_0}{4\pi} D_{xx}(t-t';\mathbf{r},\mathbf{r}')ev_0 e^{-i\omega t'}. \tag{A.4}$$

From the expansion of the renormalized calculation about a mode frequency (Eq. 5.29), we know the Fourier transform of the single-mode Green's function is

$$\tilde{D}_{xx}(\omega;\mathbf{r},\mathbf{r}') = -\frac{1}{r_0}\frac{\lambda_{\mathrm{M}}(\mathbf{r})\lambda_{\mathrm{M}}(\mathbf{r}')}{\omega^2 - \omega_{\mathrm{M}}^2}, \tag{A.5}$$

with $\lambda_{\mathrm{M}}(\mathbf{r}) =^{(E,M)} \lambda_{mnp}$ at position $\mathbf{r}$. After a bit of work, we may inverse Fourier transform to get the time-dependent Green's function

$$\begin{aligned} D_{xx}(t-t';\mathbf{r},\mathbf{r}') &= \int \frac{d\omega}{2\pi} e^{-i\omega(t-t')}\frac{-1}{r_0}\frac{\lambda_{\mathrm{M}}(\mathbf{r})\lambda_{\mathrm{M}}(\mathbf{r}')}{\omega^2 - \omega_{\mathrm{M}}^2} \\ &= \frac{\lambda_{\mathrm{M}}(\mathbf{r})\lambda_{\mathrm{M}}(\mathbf{r}')}{r_0\omega_{\mathrm{M}}}\sin(\omega_{\mathrm{M}}\,|t-t'|), \end{aligned} \tag{A.6}$$

which we substitute into Eq. A.4 to obtain

$$i\frac{e}{m}E'(\mathbf{r}) = -i\frac{\partial}{\partial t}\int dt' v_0 e^{-i\omega t'}\frac{\lambda_{\mathrm{M}}(\mathbf{r})\lambda_{\mathrm{M}}(\mathbf{r}')}{\omega_{\mathrm{M}}}\sin(\omega_{\mathrm{M}}\,|t-t'|). \tag{A.7}$$

We explicitly remove the z-dependence from the coupling parameters as in Eq. 5.31

$$\lambda_{\mathrm{M}}(\mathbf{r}) = \sin(\tfrac{p\pi}{2}(\tfrac{z}{z_0}+1))\tilde{\lambda}_{\mathrm{M}}, \tag{A.8}$$

add the axial time dependence with $z \to z + A\cos(\omega_z t)$, and expand for $A \ll z_0/p$ in terms of axial harmonics as in Eq. 5.32

$$\sin(\tfrac{p\pi}{2}(\tfrac{z+A\cos(\omega_z t)}{z_0}+1)) = \sum_{j=0}^{\infty} f_j(z,A)\cos(j\omega_z t) \tag{A.9}$$

to write

$$i\frac{e}{m}E'(\mathbf{r}) = -i\frac{\partial}{\partial t}\int dt' v_0 e^{-i\omega t'}\frac{\tilde{\lambda}_{\mathrm{M}}^2}{\omega_{\mathrm{M}}}\sum_{j=0}^{\infty}\sum_{k=0}^{\infty} f_j(z,A)f_k(z,A) \tag{A.10}$$
$$\times \cos(j\omega_z t)\cos(k\omega_z t')\sin(\omega_{\mathrm{M}}\,|t-t'|).$$

We may eliminate the absolute value of $t-t'$ in the sine function with a factor of 1 for $t > t'$ and -1 for $t < t'$. Doing this and taking the t-derivative gives

$$i\frac{e}{m}E'(\mathbf{r}) = -\,i\frac{v_0\tilde{\lambda}_{\mathrm{M}}^2}{2}\int dt' e^{-i\omega t'}\sum_{j=0}^{\infty}\sum_{k=0}^{\infty} f_j(z,A)f_k(z,A)\cos(k\omega_z t') \tag{A.11}$$
$$\times\,[\cos((\omega_{\mathrm{M}}+j\omega_z)t-\omega_{\mathrm{M}}t') + \cos((\omega_{\mathrm{M}}-j\omega_z)t-\omega_{\mathrm{M}}t')] \times \begin{cases} 1\ ,\ t > t' \\ \\ -1\ ,\ t < t' \end{cases},$$

where a term of order $\omega_z/\omega_{\mathrm{M}}$ has been dropped. The time integral must be broken

into two at t but is then straightforward with the result

$$\begin{aligned} i\frac{e}{m}E'(\mathbf{r}) = &- i\frac{v_0\tilde{\lambda}_{\mathrm{M}}^2}{2}e^{-i\omega t}\sum_{j=0}^{\infty}\sum_{k=0}^{\infty}f_j(z,A)f_k(z,A) \\ &\times\left[\frac{i\omega\cos((j-k)\omega_z t)-(\omega_{\mathrm{M}}-k\omega_z)\sin((j-k)\omega_z t)}{\omega^2-(\omega_{\mathrm{M}}-k\omega_z)^2}\right. \\ &+\frac{i\omega\cos((k+j)\omega_z t)-(\omega_{\mathrm{M}}+k\omega_z)\sin((k+j)\omega_z t)}{\omega^2-(\omega_{\mathrm{M}}+k\omega_z)^2} \\ &+\frac{i\omega\cos((k+j)\omega_z t)-(\omega_{\mathrm{M}}-k\omega_z)\sin((k+j)\omega_z t)}{\omega^2-(\omega_{\mathrm{M}}-k\omega_z)^2} \\ &\left.+\frac{i\omega\cos((k-j)\omega_z t)-(\omega_{\mathrm{M}}+k\omega_z)\sin((k-j)\omega_z t)}{\omega^2-(\omega_{\mathrm{M}}+k\omega_z)^2}\right]. \end{aligned} \tag{A.12}$$

Now, at long last, we may take the time average and notice that all the terms in the brackets are zero unless $j = k$. We thus recover Eq. 5.34,

$$\Delta\omega_c - i\frac{\gamma}{2} = \frac{\tilde{\lambda}_{\mathrm{M}}^2\omega}{2}\sum_{j=0}^{\infty}f_j(z,A)^2\left[\frac{1}{\omega^2-(\omega_{\mathrm{M}}-j\omega_z)^2}+\frac{1}{\omega^2-(\omega_{\mathrm{M}}+j\omega_z)^2}\right], \tag{A.13}$$

giving the axial-frequency sidebands and amplitude-dependent coupling strengths.

Bibliography

[1] Odom, B., Hanneke, D., D'Urso, B. & Gabrielse, G. New measurement of the electron magnetic moment using a one-electron quantum cyclotron. *Phys. Rev. Lett.* **97**, 030801 (2006).

[2] Van Dyck, Jr., R. S., Schwinberg, P. B. & Dehmelt, H. G. New high-precision comparison of electron and positron g factors. *Phys. Rev. Lett.* **59**, 26–29 (1987).

[3] Bass, S. D. The spin structure of the proton. *Rev. Mod. Phys.* **77**, 1257–1302 (2005).

[4] Pauli, W. Relativistic field theories of elementary particles. *Rev. Mod. Phys.* **13**, 203–232 (1941).

[5] Marciano, W. J. Anomalous magnetic moments. *Int. J. Mod. Phys. A* **19, 2/20/2004 Supplement**, 77–87 (2004).

[6] Tegmark, M., Aguirre, A., Rees, M. J. & Wilczek, F. Dimensionless constants, cosmology, and other dark matters. *Phys. Rev. D* **73**, 023505 (2006).

[7] Uzan, J.-P. The fundamental constants and their variation: observational and theoretical status. *Rev. Mod. Phys.* **75**, 403–455 (2003).

[8] Barrow, J. D. & Tipler, F. J. *The Anthropic Cosmological Principle* (Oxford University Press, New York, 1986).

[9] Guth, A. H. & Kaiser, D. I. Inflationary cosmology: Exploring the universe from the smallest to the largest scales. *Science* **307**, 884–890 (2005).

[10] Hogan, C. J. Why the universe is just so. *Rev. Mod. Phys.* **72**, 1149–1161 (2000).

[11] Peskin, M. E. & Schroeder, D. V. *An Introduction to Quantum Field Theory* (Westview Press, 1995).

[12] Griffiths, D. *Introduction to Elementary Particles* (Wiley-VCH, 2004).

[13] Yao, W.-M. *et al.* Review of particle physics. *J. Phys. G* **33**, 1 (2006).

[14] Schwinger, J. On quantum-electrodynamics and the magnetic moment of the electron. *Phys. Rev.* **73**, 416–417 (1948).

[15] Sommerfield, C. M. Magnetic dipole moment of the electron. *Phys. Rev.* **107**, 328–329 (1957).

[16] Petermann, A. Fourth order magnetic moment of the electron. *Helv. Phys. Acta* **30**, 407–408 (1957).

[17] Sommerfield, C. M. The magnetic moment of the electron. *Ann. Phys.* **5**, 26–57 (1958).

[18] Laporta, S. & Remiddi, E. The analytical value of the electron $(g-2)$ at order α^3 in QED. *Phys. Lett. B* **379**, 283–291 (1996).

[19] Kinoshita, T. & Nio, M. Improved α^4 term of the electron anomalous magnetic moment. *Phys. Rev. D* **73**, 013003 (2006).

[20] Aoyama, T., Hayakawa, M., Kinoshita, T. & Nio, M. Revised value of the eighth-order electron $g-2$ (2007). `arXiv:0706.3496[hep-ph]`.

[21] Kinoshita, T. & Nio, M. Tenth-order QED contribution to the lepton $g-2$: Evaluation of dominant α^5 terms of muon $g-2$. *Phys. Rev. D* **73**, 053007 (2006).

[22] Aoyama, T., Hayakawa, M., Kinoshita, T. & Nio, M. Automated calculation scheme for α^n contributions of QED to lepton $g-2$: Generating renormalized amplitudes for diagrams without lepton loops. *Nucl. Phys. B* **740**, 138–180 (2006).

[23] Mohr, P. J. & Taylor, B. N. CODATA recommended values of the fundamental physical constants: 1998. *Rev. Mod. Phys.* **72**, 351–495 (2000).

[24] Passera, M. Precise mass-dependent QED contributions to leptonic $g-2$ at order α^2 and α^3. *Phys. Rev. D* **75**, 013002 (2007).

[25] Mohr, P. J. & Taylor, B. N. CODATA recommended values of the fundamental physical constants: 2002. *Rev. Mod. Phys.* **77**, 1–107 (2005).

[26] Miller, J. P., de Rafael, E. & Roberts, B. L. Muon $(g-2)$: experiment and theory. *Rep. Prog. Phys.* **70**, 795–881 (2007).

[27] Melnikov, K. & Vainshtein, A. *Theory of the Muon Anomalous Magnetic Moment* (Springer, Berlin, 2006).

[28] Melnikov, K. & Vainshtein, A. Hadronic light-by-light scattering contribution to the muon anomalous magnetic moment reexamined. *Phys. Rev. D* **70**, 113006 (2004).

[29] Hayakawa, M. & Kinoshita, T. Pseudoscalar pole terms in the hadronic light-by-light scattering contribution to muon $g-2$. *Phys. Rev. D* **57**, 465–477 (1998). Ibid. **66**, 019902(E) (2002).

[30] Gabrielse, G., Hanneke, D., Kinoshita, T., Nio, M. & Odom, B. New determination of the fine structure constant from the electron g value and QED. *Phys. Rev. Lett.* **97**, 030802 (2006). Ibid. **99**, 039902(E) (2007).

[31] Beier, T., Häffner, H., Hermanspahn, N., Karshenboim, S. G., Kluge, H.-J., Quint, W., Stahl, S., Verdú, J. & Werth, G. New determination of the electron's mass. *Phys. Rev. Lett.* **88**, 011603 (2002).

[32] Farnham, D. L., Van Dyck, Jr., R. S. & Schwinberg, P. B. Determination of the electron's atomic mass and the proton/electron mass ratio via Penning trap mass spectroscopy. *Phys. Rev. Lett.* **75**, 3598–3601 (1995).

[33] Bradley, M. P., Porto, J. V., Rainville, S., Thompson, J. K. & Pritchard, D. E. Penning trap measurements of the masses of ^{133}Cs, ^{87,85}Rb, and ^{23}Na with uncertainties ≤ 0.2 ppb. *Phys. Rev. Lett.* **83**, 4510–4513 (1999).

[34] Cladé, P., de Mirandes, E., Cadoret, M., Guellati-Khélifa, S., Schwob, C., Nez, F., Julien, L. & Biraben, F. Determination of the fine structure constant based on Bloch oscillations of ultracold atoms in a vertical optical lattice. *Phys. Rev. Lett.* **96**, 033001 (2006).

[35] Cladé, P., de Mirandes, E., Cadoret, M., Guellati-Khélifa, S., Schwob, C., Nez, F., Julien, L. & Biraben, F. Precise measurement of h/m_{Rb} using Bloch oscillations in a vertical optical lattice: Determination of the fine-structure constant. *Phys. Rev. A* **74**, 052109 (2006).

[36] Gerginov, V., Calkins, K., Tanner, C. E., McFerran, J. J., Diddams, S., Bartels, A. & Hollberg, L. Optical frequency measurements of $6s\,^2S_{1/2} - 6p\,^2P_{1/2}$ (D_1) transitions in ^{133}Cs and their impact on the fine-structure constant. *Phys. Rev. A* **73**, 032504 (2006).

[37] Wicht, A., Hensley, J. M., Sarajlic, E. & Chu, S. A preliminary measurement of the fine structure constant based on atom interferometry. *Phys. Scr.* **T102**, 82–88 (2002).

[38] Müller, H., Chiow, S.-W., Long, Q., Vo, C. & Chu, S. A new photon recoil experiment: towards a determination of the fine structure constant. *Appl. Phys.B* **84**, 633–642 (2006).

[39] Becker, P., Cavagnero, G., Kuetgens, U., Mana, G. & Massa, E. Confirmation of the INRiM and PTB determinations of the Si lattice parameter. *IEEE T. on Instrum. Meas.* **56**, 230–234 (2007).

[40] Fujimoto, H., Mana, G. & Nakayama, K. A possible solution for the discrepancy between the INRIM and NMIJ values of the Si lattice-parameter. *IEEE T. on Instrum. Meas.* **56**, 351–355 (2007).

[41] Jentschura, U. D., Kotochigova, S., Bigot, E.-O. L., Mohr, P. J. & Taylor, B. N. Precise calculation of transition frequencies of hydrogen and deuterium based on a least-squares analysis. *Phys. Rev. Lett.* **95**, 163003 (2005).

[42] Gumberidze, A., Stöhlker, T., Banaś, D., Beckert, K., Beller, P., Beyer, H. F., Bosch, F., Cai, X., Hagmann, S., Kozhuharov, C., Liesen, D., Nolden, F., Ma, X., Mokler, P. H., Steck, M., Sierpowski, D., Tashenov, S., Warczak, A. & Zou, Y. Precision tests of QED in strong fields: experiments on hydrogen- and helium-like uranium. *J. Phys.: Conf. Ser.* **58**, 87–92 (2007).

[43] Yerokhin, V. A., Indelicato, P. & Shabaev, V. M. Two-loop self-energy correction in high-Z hydrogenlike ions. *Phys. Rev. Lett.* **91**, 073001 (2003).

[44] Beiersdorfer, P., Chen, H., Thorn, D. B. & Träbert, E. Measurement of the two-loop Lamb shift in lithiumlike U^{89+}. *Phys. Rev. Lett.* **95**, 233003 (2005).

[45] Brodsky, S. J. & Drell, S. D. Anomalous magnetic moment and limits on fermion substructure. *Phys. Rev. D* **22**, 2236–2243 (1980).

[46] Bourilkov, D. Hint for axial-vector contact interactions in the data on $e^+e^- \to e^+e^-(\gamma)$ at center-of-mass energies 192–208 GeV. *Phys. Rev. D* **64**, 071701 (2001).

[47] Boehm, C., Hooper, D., Silk, J., Casse, M. & Paul, J. MeV dark matter: Has it been detected? *Phys. Rev. Lett.* **92**, 101301 (2004).

[48] Jean, P., Knödlseder, J., Lonjou, V., Allain, M., Roques, J.-P., Skinner, G. K., Teegarden, B. J., Vedrenne, G., von Ballmoos, P., Cordier, B., Caraveo, P., Diehl, R., Durouchoux, P., Mandrou, P., Matteson, J., Gehrels, N., Schönfelder, V., Strong, A. W., Ubertini, P., Weidenspointner, G. & Winkler, C. Early SPI/INTEGRAL measurements of 511 keV line emission from the 4th quadrant of the Galaxy. *Astron. Astrophys.* **407**, L55–L58 (2003).

[49] Bœhm, C. & Ascasibar, Y. More evidence in favor of light dark matter particles? *Phys. Rev. D* **70**, 115013 (2004).

[50] Bœhm, C. & Silk, J. A new test of the light dark matter hypothesis (2007). `arXiv:0708.2768[hep-ph]`.

[51] Colladay, D. & Kostelecký, V. A. Lorentz-violating extension of the standard model. *Phys. Rev. D* **58**, 116002 (1998).

[52] Carone, C. D., Sher, M. & Vanderhaeghen, M. New bounds on isotropic Lorentz violation. *Phys. Rev. D* **74**, 077901 (2006).

[53] Tobar, M. E., Wolf, P., Fowler, A. & Hartnett, J. G. New methods of testing Lorentz violation in electrodynamics. *Phys. Rev. D* **71**, 025004 (2005).

[54] Bluhm, R., Kostelecký, V. A. & Russell, N. CPT and Lorentz tests in Penning traps. *Phys. Rev. D* **57**, 3932–3943 (1998).

[55] Bluhm, R. Probing the Planck scale in low-energy atomic physics. In Kostelecký, V. A. (ed.) *Proceedings on the Second Meeting on CPT and Lorentz Symmetry*, 16–25 (World Scientific, 2001).

[56] Mittleman, R. K., Ioannou, I. I., Dehmelt, H. G. & Russell, N. Bound on CPT and Lorentz symmetry with a trapped electron. *Phys. Rev. Lett.* **83**, 2116–2119 (1999).

[57] Müller, H. Testing Lorentz invariance by the use of vacuum and matter filled cavity resonators. *Phys. Rev. D* **71**, 045004 (2005).

[58] Altschul, B. Limits on Lorentz violation from synchrotron and inverse Compton sources. *Phys. Rev. Lett.* **96**, 201101 (2006).

[59] Altschul, B. Synchrotron and inverse Compton constraints on Lorentz violations for electrons. *Phys. Rev. D* **74**, 083003 (2006).

[60] Heckel, B. R. Torsion balance test of Lorentz symmetry violation. In Kostelecký, V. A. (ed.) *Proceedings of the Third Meeting on CPT and Lorentz Symmetry*, 133–140 (World Scientific, 2004).

[61] Heckel, B. R., Cramer, C. E., Cook, T. S., Adelberger, E. G., Schlamminger, S. & Schmidt, U. New CP-violation and preferred-frame tests with polarized electrons. *Phys. Rev. Lett.* **97**, 021603 (2006).

[62] Bluhm, R., Kostelecký, V. A. & Russell, N. Testing CPT with anomalous magnetic moments. *Phys. Rev. Lett.* **79**, 1432–1435 (1997).

[63] Dehmelt, H., Mittleman, R., Van Dyck, Jr., R. S. & Schwinberg, P. Past electron-positron $g-2$ experiments yielded sharpest bound on CPT violation for point particles. *Phys. Rev. Lett.* **83**, 4694–4696 (1999).

[64] Lamoreaux, S. K. & Torgerson, J. R. Neutron moderation in the Oklo natural reactor and the time variation of alpha. *Phys. Rev. D* **69**, 121701 (2004).

[65] Webb, J. K., Murphy, M. T., Flambaum, V. V., Dzuba, V. A., Barrow, J. D., Churchill, C. W., Prochaska, J. X. & Wolfe, A. M. Further evidence for cosmological evolution of the fine structure constant. *Phys. Rev. Lett.* **87**, 091301 (2001).

[66] Ashenfelter, T., Mathews, G. J. & Olive, K. A. Chemical evolution of Mg isotopes versus the time variation of the fine structure constant. *Phys. Rev. Lett.* **92**, 041102 (2004).

[67] Fortier, T. M., Ashby, N., Bergquist, J. C., Delaney, M. J., Diddams, S. A., Heavner, T. P., Hollberg, L., Itano, W. M., Jefferts, S. R., Kim, K., Levi, F., Lorini, L., Oskay, W. H., Parker, T. E., Shirley, J. & Stalnaker, J. E. Precision atomic spectroscopy for improved limits on variation of the fine structure constant and local position invariance. *Phys. Rev. Lett.* **98**, 070801 (2007).

[68] Eidelman, S. & Passera, M. Theory of the τ lepton anomalous magnetic moment. *Mod. Phys. Lett. A* **22**, 159–179 (2007).

[69] Czarnecki, A. & Marciano, W. J. Muon anomalous magnetic moment: A harbinger for "new physics". *Phys. Rev. D* **64**, 013014 (2001).

[70] Abdallah, J. *et al.* Study of tau-pair production in photon-photon collisions at LEP and limits on the anomalous electromagnetic moments of the tau lepton. *Eur. Phys. J. C* **35**, 159–170 (2004).

[71] Bennett, G. W., Bousquet, B., Brown, H. N., Bunce, G., Carey, R. M., Cushman, P., Danby, G. T., Debevec, P. T., Deile, M., Deng, H., Deninger, W., Dhawan, S. K., Druzhinin, V. P., Duong, L., Efstathiadis, E., Farley, F. J. M., Fedotovich, G. V., Giron, S., Gray, F. E., Grigoriev, D., Grosse-Perdekamp, M., Grossmann, A., Hare, M. F., Hertzog, D. W., Huang, X., Hughes, V. W., Iwasaki, M., Jungmann, K., Kawall, D., Kawamura, M., Khazin, B. I., Kindem, J., Krienen, F., Kronkvist, I., Lam, A., Larsen, R., Lee, Y. Y., Logashenko, I., McNabb, R., Meng, W., Mi, J., Miller, J. P., Mizumachi, Y., Morse, W. M., Nikas, D., Onderwater, C. J. G., Orlov, Y., Ozben, C. S., Paley, J. M., Peng, Q., Polly, C. C., Pretz, J., Prigl, R., zu Putlitz, G., Qian, T., Redin, S. I., Rind, O., Roberts, B. L., Ryskulov, N., Sedykh, S., Semertzidis, Y. K., Shagin, P., Shatunov, Y. M., Sichtermann, E. P., Solodov, E., Sossong, M., Steinmetz, A., Sulak, L. R., Timmermans, C., Trofimov, A., Urner, D., von Walter, P., Warburton, D., Winn, D., Yamamoto, A. & Zimmerman, D. Final report of the E821 muon anomalous magnetic moment measurement at BNL. *Phys. Rev. D* **73**, 072003 (2006).

[72] Carey, R., Gafarov, A., Logashenko, I., Lynch, K., Miller, J., Roberts, B., Bunce, G., Meng, W., Morse, W., Semertzidis, Y., Grigoriev, D., Khazin, B.,

Redin, S., Shatunov, Y. M., Solodov, E., Orlov, Y., Debevec, P., Hertzog, D., Kammel, P., McNabb, R., Mülhauser, F., Giovanetti, K., Jungmann, K., Onderwater, C., Dhamija, S., Gorringe, T., Korsch, W., Gray, F., Lauss, B., Sichtermann, E., Cushman, P., Qian, T., Shagin, P., Dhawan, S. & Farley, F. A $(g-2)_\mu$ experiment to ± 0.2 ppm precision: BNL P969 (2004). URL `http://g2pc1.bu.edu/~roberts/Proposal969.pdf`.

[73] Hertzog, D. W., Miller, J. P., de Rafael, E., Roberts, B. L. & Stöckinger, D. The physics case for the new muon $(g-2)$ experiment (2007). `arXiv:0705.4617[hep-ph]`.

[74] Mills, I. M., Mohr, P. J., Quinn, T. J., Taylor, B. N. & Williams, E. R. Redefinition of the kilogram, ampere, kelvin and mole: a proposed approach to implementing CIPM recommendation 1 (CI-2005). *Metrologia* **43**, 227–246 (2006).

[75] Eichenberger, A., Jeckelmann, B. & Richard, P. Tracing Planck's constant to the kilogram by electromechanical methods. *Metrologia* **40**, 356–365 (2003).

[76] Becker, P. Tracing the definition of the kilogram to the Avogadro constant using a silicon single crystal. *Metrologia* **40**, 366–375 (2003).

[77] Rich, A. & Wesley, J. C. The current status of the lepton g factors. *Rev. Mod. Phys.* **44**, 250–283 (1972).

[78] Wineland, D., Ekstrom, P. & Dehmelt, H. Monoelectron oscillator. *Phys. Rev. Lett.* **31**, 1279–1282 (1973).

[79] Brown, L. S., Gabrielse, G., Helmerson, K. & Tan, J. Cyclotron motion in a microwave cavity: Possible shifts of the measured electron g factor. *Phys. Rev. Lett.* **55**, 44–47 (1985).

[80] Brown, L. S., Gabrielse, G., Helmerson, K. & Tan, J. Cyclotron motion in a microwave cavity: Lifetime and frequency shifts. *Phys. Rev. A* **32**, 3204–3218 (1985).

[81] Van Dyck, Jr., R. S., Schwinberg, P. B. & Dehmelt, H. G. Experiments with single electrons. In Hestenes, D. & Weingartshofer, A. (eds.) *The Electron: New Theory and Experiment*, 239–293 (Kluwer Academic Publishers, Netherlands, 1991).

[82] Van Dyck, Jr., R. S., Schwinberg, P. B. & Dehmelt, H. G. Consistency of the electron g-factor in a Penning trap. In Baylis, W. E., Drake, G. W. F. & McConkey, J. W. (eds.) *ICAP-12 Book of Abstracts* (1990).

[83] Odom, B. C. *Fully Quantum Measurement of the Electron Magnetic Moment*. Ph.D. thesis, Harvard University (2004).

[84] Brown, L. S. & Gabrielse, G. Geonium theory: Physics of a single electron or ion in a Penning trap. *Rev. Mod. Phys.* **58**, 233–311 (1986).

[85] Peil, S. & Gabrielse, G. Observing the quantum limit of an electron cyclotron: QND measurements of quantum jumps between Fock states. *Phys. Rev. Lett.* **83**, 1287–1290 (1999).

[86] Brown, L. S. Geonium lineshape. *Ann. Phys.* **159**, 62–98 (1985).

[87] Gabrielse, G. & MacKintosh, F. C. Cylindrical Penning traps with orthogonalized anharmonicity compensation. *Int. J. Mass Spectrom. Ion Processes* **57**, 1–17 (1984).

[88] D'Urso, B., Van Handel, R., Odom, B., Hanneke, D. & Gabrielse, G. Single-particle self-excited oscillator. *Phys. Rev. Lett.* **94**, 113002 (2005).

[89] D'Urso, B. R. *Cooling and Self-Excitation of a One-Electron Oscillator*. Ph.D. thesis, Harvard University (2003).

[90] Brown, L. S. & Gabrielse, G. Precision spectroscopy of a charged particle in an imperfect Penning trap. *Phys. Rev. A* **25**, 2423–2425 (1982).

[91] Gabrielse, G. & Tan, J. Self-shielding superconducting solenoid systems. *J. Appl. Phys.* **63**, 5143–5148 (1988).

[92] Gabrielse, G., Fei, X., Orozco, L. A., Tjoelker, R. L., Haas, J., Kalinowsky, H., Trainor, T. A. & Kells, W. Thousandfold improvement in the measured antiproton mass. *Phys. Rev. Lett.* **65**, 1317–1320 (1990).

[93] Chan, I. H.-Y. *Quantum Dot Circuits: Single-Electron Switch and Few-Electron Quantum Dots*. Ph.D. thesis, Harvard University (2003).

[94] DeMaw, D. (ed.) *The Radio Amateur's Handbook* (The American Radio Relay League, 1968).

[95] Wineland, D. J. & Dehmelt, H. G. Principles of the stored ion calorimeter. *J. Appl. Phys.* **46**, 919–930 (1975).

[96] Peil, S. E. *Quantum Jumps Between Fock States of an Ultracold Electron Cyclotron Oscillator*. Ph.D. thesis, Harvard University (1999).

[97] Rutman, J. & Walls, F. L. Characterization of frequency stability in precision frequency sources. *Proc. IEEE* **79**, 952–960 (1991).

[98] Tseng, C.-H. *Parametric Dark Detection of a Single Electron in a Penning Trap*. Ph.D. thesis, Harvard University (1995).

[99] Van Dyck, Jr., R. S. Anomalous magnetic moment of single electrons and positrons: Experiment. In Kinoshita, T. (ed.) *Quantum Electrodynamics*, 322–388 (World Scientific, Singapore, 1990).

[100] Kubo, R. The fluctuation-dissipation theorem. *Rep. Prog. Phys.* **29**, 255–284 (1966).

[101] D'Urso, B., Odom, B. & Gabrielse, G. Feedback cooling of a one-electron oscillator. *Phys. Rev. Lett.* **90**, 043001 (2003).

[102] Lax, M. Classical noise. v. noise in self-sustained oscillators. *Phys. Rev.* **160**, 290–307 (1967).

[103] Walker, W. F., Sarkar, T. K., Tseng, F.-I. & Weiner, D. D. Carrier-frequency estimation based on the location of the spectra peak of a windowed sample of carrier plus noise. *IEEE T. on Instrum. Meas.* **31**, 239–249 (1982).

[104] Meyer, E. S., Silvera, I. F. & Brandt, B. L. Eddy current shielding and heating: Reduction of dissipation for very low-temperature experiments in the presence of magnetic field ripple. *Rev. Sci. Instrum.* **60**, 2964–2968 (1989).

[105] Gabrielse, G., Tan, J., Clateman, P., Orozco, L. A., Rolston, S. L., Tseng, C. H. & Tjoelker, R. L. A superconducting system which cancels fluctuations in the ambient magnetic field. *J. Mag. Res.* **91**, 564–572 (1991).

[106] Wilson, M. N. *Superconducting Magnets* (Oxford University Press, 1987).

[107] Phillips, D. F. *A Precision Comparison of the $\bar{p} - p$ Charge-to-Mass Ratios.* Ph.D. thesis, Harvard University (1996).

[108] Brunner, S., Engel, T. & Werth, G. Field stabilization of a superconducting magnet by helium pressure control. *Meas. Sci. Technol.* **6**, 222–226 (1995).

[109] Van Dyck, Jr., R. S., Farnham, D. L., Zafonte, S. L. & Schwinberg, P. B. Ultra-stable superconducting magnet system for a Penning trap mass spectrometer. *Rev. Sci. Instrum.* **70**, 1665–1671 (1999).

[110] van Handel, R. *Self-Excited Detection in Geonium: towards an improved $g - 2$ measurement.* Master's thesis, Vrije Universiteit, Amsterdam (2002).

[111] Hoyle, Jr., C. D. *Sub-millimeter Tests of the Gravitational Inverse-Square Law.* Ph.D. thesis, University of Washington (2001).

[112] Palmer, F. L. Excitation of spin flips in geonium at small cyclotron quantum numbers: Transition rates and frequency shifts. *Phys. Rev. A* **47**, 2610–2615 (1993).

[113] Arfken, G. B. & Weber, H. J. *Mathematical Methods for Physicists* (Academic Press, 1995), fourth edn.

[114] Bevington, P. R. & Robinson, D. K. *Data Reduction and Error Analysis for the Physical Sciences* (McGraw-Hill, 2003), third edn.

[115] Barlow, R. *Statistics* (John Wiley & Sons, 1989).

[116] Agresti, A. & Coull, B. A. Approximate is better than "exact" for interval estimation of binomial proportions. *Amer. Statistician* **52**, 119–126 (1998).

[117] Purcell, E. M. Spontaneous emission probabilities at radio frequencies. *Phys. Rev.* **69**, 681 (1946).

[118] Gabrielse, G. & Dehmelt, H. Observation of inhibited spontaneous emission. *Phys. Rev. Lett.* **55**, 67–70 (1985).

[119] Boulware, D. G., Brown, L. S. & Lee, T. Apparatus-dependent contributions to $g - 2$? *Phys. Rev. D* **32**, 729–735 (1985).

[120] Gabrielse, G., Tan, J. & Brown, L. S. Cavity shifts of measured electron magnetic moments. In Kinoshita, T. (ed.) *Quantum Electrodynamics*, 389–418 (World Scientific, Singapore, 1990).

[121] Tan, J. & Gabrielse, G. Parametrically pumped electron oscillators. *Phys. Rev. A* **48**, 3105–3122 (1993).

[122] Jackson, J. D. *Classical Electrodynamics* (John Wiley & Sons, 1999), third edn.

[123] Tan, J. N. *Cooperative Behavior in Cavity-cooled, Parametrically-pumped Electron Oscillators*. Ph.D. thesis, Harvard University (1992).

[124] Tan, J. & Gabrielse, G. Synchronization of parametrically pumped electron oscillators with phase bistability. *Phys. Rev. Lett.* **67**, 3090–3093 (1991).

[125] Nayfeh, A. H. & Mook, D. T. *Nonlinear Oscillations* (John Wiley & Sons, 1979).

[126] Lapidus, L. J., Enzer, D. & Gabrielse, G. Stochastic phase switching of a parametrically driven electron in a Penning trap. *Phys. Rev. Lett.* **83**, 899–902 (1999).

[127] Tseng, C. H., Enzer, D., Gabrielse, G. & Walls, F. L. 1-bit memory using one electron: Parametric oscillations in a Penning trap. *Phys. Rev. A* **59**, 2094–2104 (1999).

[128] Kim, K., Noh, H.-R., Yeon, Y.-H. & Jhe, W. Observation of the Hopf bifurcation in parametrically driven trapped atoms. *Phys. Rev. A* **68**, 031403(R) (2003).

[129] Kim, K., Heo, M.-S., Lee, K.-H., Jang, K., Noh, H.-R., Kim, D. & Jhe, W. Spontaneous symmetry breaking of population in a nonadiabatically driven atomic trap: An Ising-class phase transition. *Phys. Rev. Lett.* **96**, 150601 (2006).

[130] Agarwal, G. S. Vacuum-field Rabi splittings in microwave absorption by Rydberg atoms in a cavity. *Phys. Rev. Lett.* **53**, 1732–1734 (1984).

[131] Zhu, Y., Gauthier, D. J., Morin, S. E., Wu, Q., Carmichael, H. J. & Mossberg, T. W. Vacuum Rabi splitting as a feature of linear-dispersion theory: Analysis and experimental observations. *Phys. Rev. Lett.* **64**, 2499–2502 (1990).

[132] Raizen, M. G., Thompson, R. J., Brecha, R. J., Kimble, H. J. & Carmichael, H. J. Normal-mode splitting and linewidth averaging for two-state atoms in an optical cavity. *Phys. Rev. Lett.* **63**, 240–243 (1989).

[133] Carmichael, H. J., Brecha, R. J., Raizen, M. G., Kimble, H. J. & Rice, P. R. Subnatural linewidth averaging for coupled atomic and cavity-mode oscillators. *Phys. Rev. A* **40**, 5516–5519 (1989).

[134] Bollinger, J. J., Heinzen, D. J., Moore, F. L., Itano, W. M., Wineland, D. J. & Dubin, D. H. E. Electrostatic modes of ion-trap plasmas. *Phys. Rev. A* **48**, 525–545 (1993).

[135] Lapidus, L. J. *Synchronization and Stochastic Behavior of Electrons in a Penning Trap.* Ph.D. thesis, Harvard University (1998).

[136] Malmberg, J. H. & O'Neil, T. M. Pure electron plasma, liquid, and crystal. *Phys. Rev. Lett.* **39**, 1333–1336 (1977).

[137] Ichimaru, S., Iyetomi, H. & Tanaka, S. Statistical physics of dense plasmas: Thermodynamics, transport coefficients, and dynamic correlations. *Phys. Rep.* **149**, 91–205 (1987).

[138] Pobell, F. *Matter and Methods at Low Temperatures* (Springer-Verlag, 1992).

[139] White, G. K. & Meeson, P. J. *Experimental Techniques in Low-Temperature Physics* (Oxford Science, 2002).

[140] Wineland, D. & Dehmelt, H. Line shifts and widths of axial, cyclotron and G-2 resonances in tailored, stored electron (ion) cloud. *Int. J. Mass Spectrom. Ion Phys.* **16**, 338–342 (1975). Ibid. **19**,251(E) (1976).

[141] Cornell, E. A., Weisskoff, R. M., Boyce, K. R. & Pritchard, D. E. Mode coupling in a Penning trap: π pulses and a classical avoided crossing. *Phys. Rev. A* **41**, 312–315 (1990).

[142] Montgomery, C. G., Dicke, R. H. & Purcell, E. M. (eds.) *Principles of Microwave Circuits* (Dover, 1965).

[143] Gabrielse, G., Dehmelt, H. & Kells, W. Observation of a relativistic, bistable hysteresis in the cyclotron motion of a single electron. *Phys. Rev. Lett.* **54**, 537–539 (1985).

[144] Mittleman, R. K., Palmer, F. L. & Dehmelt, H. G. Improving the electron $g-2$ measurement. *Hyperfine Interact.* **81**, 105–113 (1993).

[145] Enzer, D. & Gabrielse, G. Dressed coherent states of the anharmonic oscillator. *Phys. Rev. Lett.* **78**, 1211–1214 (1997).

[146] Enzer, D. G. *Dressed Coherent States of the Anharmonic Oscillator with Damping.* Ph.D. thesis, Harvard University (1996).

[147] Kostelecký, V. A. & Lane, C. D. Constraints on Lorentz violation from clock-comparison experiments. *Phys. Rev. D* **60**, 116010 (1999).

[148] Kaplan, G. H. The IAU resolutions on astronomical reference systems, time scales, and Earth rotation models. Circular 179, U. S. Naval Observatory (2005).

[149] Bluhm, R., Kostelecký, V. A., Lane, C. D. & Russell, N. Probing Lorentz and CPT violation with space-based experiments. *Phys. Rev. D* **68**, 125008 (2003).

[150] Estrada, J., Roach, T., Tan, J. N., Yesley, P. & Gabrielse, G. Field ionization of strongly magnetized Rydberg positronium: A new physical mechanism for positron accumulation. *Phys. Rev. Lett.* **84**, 859–862 (2000).

[151] Schwinberg, P. B., Van Dyck, Jr., R. S. & Dehmelt, H. G. Trapping and thermalization of positrons for geonium spectroscopy. *Phys. Lett.* **81A**, 119–120 (1981).

[152] Fogwell, S. Private communication.

[153] Gabrielse, G., Khabbaz, A., Hall, D. S., Heimann, C., Kalinowsky, H. & Jhe, W. Precision mass spectroscopy of the antiproton and proton using simultaneously trapped particles. *Phys. Rev. Lett.* **82**, 3198–3201 (1999).

[154] Quint, W., Alonso, J., Djekić, S., Kluge, H.-J., Stahl, S., Valenzuela, T., Verdú, J., Vogel, M. & Werth, G. Continuous Stern-Gerlach effect and the magnetic moment of the antiproton. *Nucl. Inst. Meth. Phys. Res. B* **214**, 207–210 (2004).

[155] Leibfried, D., Blatt, R., Monroe, C. & Wineland, D. Quantum dynamics of single trapped ions. *Rev. Mod. Phys.* **75**, 281–324 (2003).

[156] Ciaramicoli, G., Marzoli, I. & Tombesi, P. Scalable quantum processor with trapped electrons. *Phys. Rev. Lett.* **91**, 017901 (2003).

[157] Ciaramicoli, G., Galve, F., Marzoli, I. & Tombesi, P. Array of planar Penning traps as a nuclear magnetic resonance molecule for quantum computation. *Phys. Rev. A* **72**, 042323 (2005).

[158] Mancini, S., Martins, A. M. & Tombesi, P. Quantum logic with a single trapped electron. *Phys. Rev. A* **61**, 012303 (1999).

[159] Ciaramicoli, G., Marzoli, I. & Tombesi, P. Realization of a quantum algorithm using a trapped electron. *Phys. Rev. A* **63**, 052307 (2001).

[160] Stahl, S., Galve, F., Alonso, J., Djekic, S., Quint, W., Valenzuela, T., Verdú, J., Vogel, M. & Werth, G. A planar Penning trap. *Eur. Phys. J. D* **32**, 139–146 (2005).

[161] Galve, F., Fernández, P. & Werth, G. Operation of a planar Penning trap. *Eur. Phys. J. D* **40**, 201–204 (2006).

[162] Goldman, J. Private communication.